Biochemical and biophysical characterization of Ca^{2+} channel complexes in neurotransmission

Yoshitsugu Uriu

2010

Preface

The studies presented in this thesis have been carried out under the direction of Professor Yasuo Mori at the Laboratory of Molecular Biological Chemistry, Department of Synthetic Chemistry and Biological Chemistry, Graduate School of Engineering, Kyoto University during April 2004 to September 2010. This thesis aims to characterize the Ca^{2+} channel complexes in neurotransmission.

It is the greatest pleasure to me to express my sincere gratitude to Professor Yasuo Mori for his guidance, valuable suggestion and encouragement throughout these studies.

I am also deeply grateful to Professor Kevin P Campbell, Associate professor Aaron M Beedle, Dr. Yuji Hara, and Dr. Motoi Kanagawa, Departments of Physiology and Biophysics, Internal Medicine, and Neurology, University of Iowa Roy J. and Lucille A. Carver College of Medicine, Professor Michel De Waard, Inserm U607, Laboratoire Canaux Calciques, Fonctions et Pathologies, Professor Masami Takahashi and Dr. Makoto Itakura, Department of Biochemistry, Kitasato University School of Medicine, Professor Haruhiko Bito and Dr. Mio Nonaka, Department of Neurochemistry, University of Tokyo Graduate School of Medicine, Head Takahisa Furukawa, Vice-head Kazuo Funabiki, Ms. Rikako Sanuki, Ms. Akiko Tani, Departments of Developmental Biology and Systems Biology, Osaka Bioscience Institute, Associate professor Chieko Koike, Department of Pharmacy, Ritsumeikan University, Professor Masao Tachibana and Mr. Takehisa Obara, Department of Psychology, Graduate School of Humanities and Sociology, University of Tokyo, Associate professor Hiroshi Ueda, Department of Biomolecular Science, Faculty of Engineering, Gifu University, Dr. Takuro Numaga-Tomita, Calcium Regulation Group, Laboratory of Signal Transduction, NIEHS, Professor Minoru Wakamori and Assistant Professor Takashi Yoshida, Department of Oral Biology, Graduate School of Dentistry, Tohoku University, Dr. Takafumi Miki, Department of Neurophysiology, Faculty of Life and Medical Sciences, Doshisha University,

Professor Itaru Hamachi, and Dr. Hiroshi Nonaka, Laboratory of Bioorganic Chemistry, Department of Synthetic Chemistry and Biological Chemistry, Graduate School of Engineering, Kyoto University, and Associate Professor Shigeki Kiyonaka, Assistant Professor Tomohiro Numata, Assistant Professor Taketoshi Kajimoto, Laboratory of Molecular Biological Chemistry, Department of Synthetic Chemistry and Biological Chemistry, Graduate School of Engineering, Kyoto University.

The accomplishments described in this thesis could not have been achieved without the efforts of many colleagues. I should be emphasized that the contribution of Ms. Emiko Mori, Mr. Satoshi Akiyama, Mr. Masakuni Yagi, Mr. Akito Nakao, Mr. Hiroshi Nakajima, Mr. Koji Yamazaki, and Mr. Naoto Yokoi, who participated in some work presented here, are greatly appreciated. I should be also express great gratitude to Dr. Shinichiro Yamamoto, Dr. Kenta Kato, Mr. Masahiro Katano, Mr. Nobuaki Takahashi and Mr. Yoshinori Takada for heartwarming assistance.

I owe all members of Professor Mori's laboratory a great depth of gratitude for their constant encouragement throughout this work.

I express great gratitude to parents, my sister and friends who had supported me to complete my thesis, for their kind understanding of my career decision and heartwarming assistance. My sincere thanks my fiancée Yoko for heartwarming encouragement, kind understanding and patience.

Yoshitsugu Uriu

Laboratory of Molecular Biological Chemistry

Department of Synthetic Chemistry and Biological Chemistry

Graduate School of Engineering

Kyoto University

Contents

General Introduction

Physiological significance of Ca^{2+}.

Ca^{2+} influx across the plasma membrane plays a vital role in regulating diverse cellular processes, ranging from ubiquitous activities like gene expression to tissue-specific functions such as neurotransmitter release and muscle contraction, by controlling the cytosolic free Ca^{2+} concentration ($[Ca^{2+}]_i$) (1). The Ca^{2+} entry channels involved in this Ca^{2+} influx are classified into three groups: voltage-dependent Ca^{2+} channels (VDCC), ligand-operated Ca^{2+} channels (neurotransmitter receptors), and non-classical Ca^{2+} channels belonging to neither group.

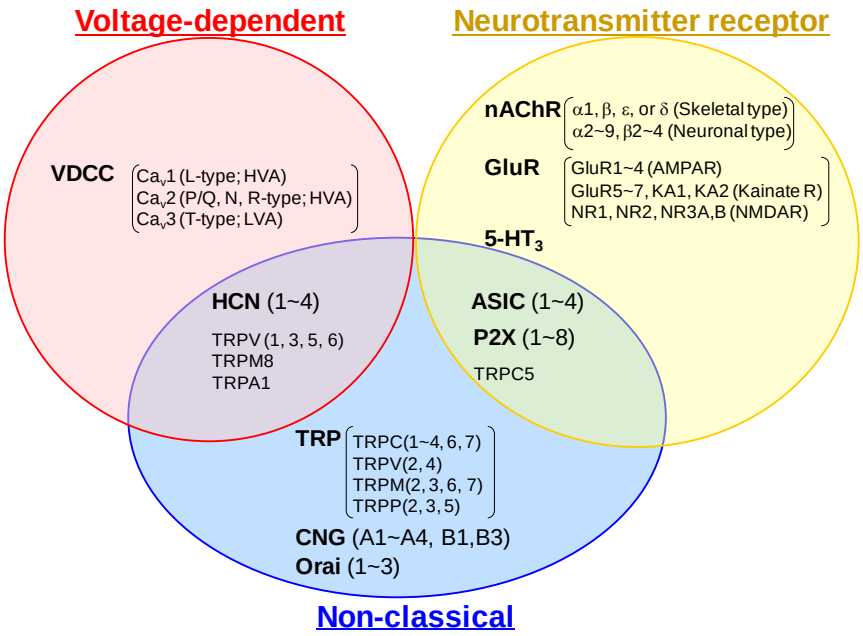

Fig. 1 Classes of Ca^{2+}-permeable ion channels.

Ca^{2+} channels involved in neurotransmission.

Neurotransmission is regulated by presynaptic and postsynaptic Ca^{2+} influx. Ca^{2+} influx into presynaptic nerve terminals via VDCC is an essential step in neurotransmitter release (2). The predominant Ca^{2+} channel species in synaptic nerve terminals are P/Q-type $Ca_V2.1$ and N-type $Ca_V2.2$ channels, with their relative levels of expression varying across the nervous system (3). The different distributions of these two channel subtypes are reflected in their distinct physiological and pathological roles, yet their activity is regulated by common mechanisms and both function as part of larger signaling complexes that enable their precise regulation and subcellular targeting. Ca^{2+} influx into postsynaptic nerve terminals is essential to regulate the

excitability and plasticity of postsynapse. This Ca^{2+} influx involves the three groups of Ca^{2+} entry channels, mentioned above: VDCCs, ligand-operated Ca^{2+} channels (4), and non-classical Ca^{2+} channels including transient receptor potential (TRP) channels (5, 6).

VDCCs.

Multiple types of VDCCs are distinguished on the basis of biophysical and pharmacological properties (7). In neurons, high voltage-activated (HVA) VDCC types such as N-, P/Q-, R-, and L-types are essential for neurotransmitter release from presynaptic terminals (8–10). Furthermore, presynaptic Ca^{2+} channels are considered to serve as the regulatory node in a dynamic, multilayered signaling network that exerts short-term control of neurotransmission in response to synaptic activity (11). Biochemically, VDCCs are known as heteromultimeric protein complexes composed of the pore-forming α_1 and auxiliary subunits α_2/δ, β, and γ (12). The α_1-subunit, designated as Ca_V, is encoded by ten distinct genes, whose correspondence with functional types has already been largely elucidated (13). β-subunits interact with α_1 from the cytoplasmic side to enhance functional channel trafficking to the plasma membrane (14, 15) and to modify multiple kinetic properties (16, 17). Considering the cytoplasmic disposition of β-subunits, it is intriguing to investigate whether β-subunits are involved in targeting specific subcellular machinery to VDCC complexes at presynaptic active zones for neurotransmitter release through as yet unidentified protein interactions.

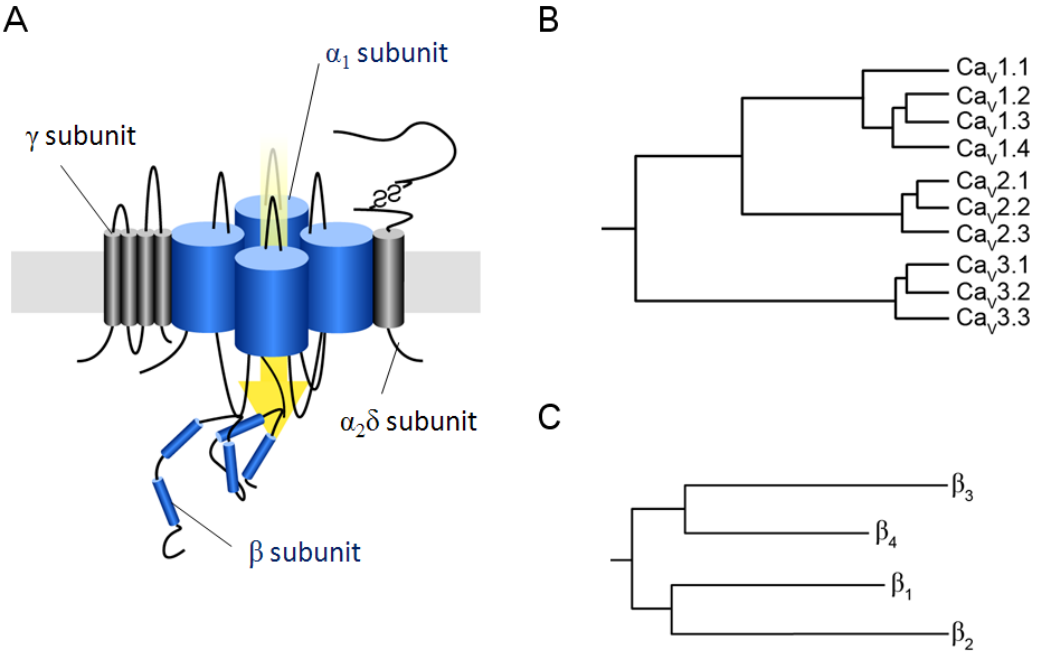

Fig. 2 Voltage-dependent Ca^{2+} channel. A, model of VDCC complex. B, phylogenic tree of α_1-subunits. C, phylogenic tree of β-subunits.

TRP channels.

The largest family of non-classical Ca^{2+} channels is the TRP channel superfamily. The TRP family of ion channels now comprises more than 30 cation channels, most of which are permeable for Ca^{2+}, and some also for Mg^{2+} (18). TRP channels contribute to changes in $[Ca^{2+}]_i$ by providing Ca^{2+} entry pathways, by modulating the driving forces for the Ca^{2+} entry, and very likely also by providing intracellular pathways for Ca^{2+} release from cellular organelles. On the basis of sequence homology, the TRP family can be divided in seven main subfamilies: the TRPC ('Canonical') family, the TRPV ('Vanilloid') family, the TRPM ('Melastatin') family, the TRPP ('Polycystin') family, the TRPML ('Mucolipin') family, the TRPA ('Ankyrin') family, and the TRPN ('NOMPC') family (5, 19–22). The cloning and characterization of members of this cation channel family has exploded during recent years, leading to a plethora of data on the roles of TRP channels in a variety of tissues and species, including mammals, insects, and yeast. TRP channels are activated by a wide range of stimuli including intra- and extracellular messengers, chemical, mechanical, and osmotic stress, and some probably by the filling state of intracellular Ca^{2+} stores (23). In the peripheral nervous system, stimuli including temperature, pressure, inflammatory agents, and receptor activation effect TRP-mediated responses. In the central nervous system, TRPs participate in neurite outgrowth, receptor signalling and excitotoxic cell death resulting from anoxia. TRP channels are emerging as essential cellular switches that allow animals to respond to their environments (5).

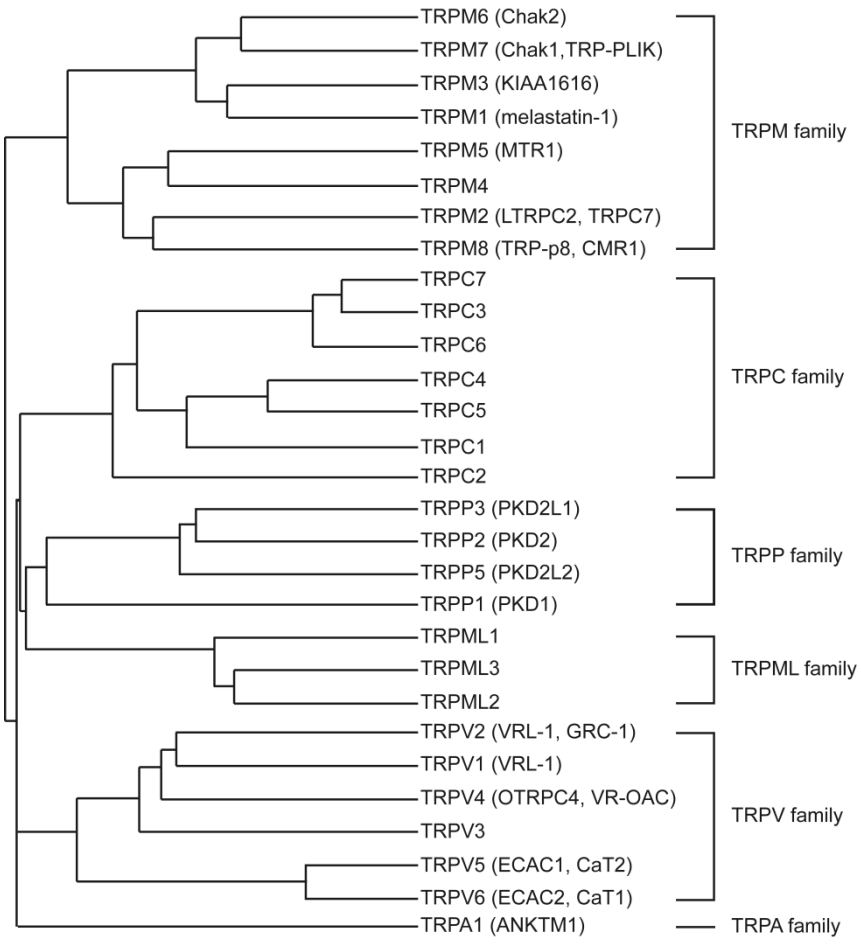

Fig. 3 Phylogenic tree of TRP channels.

Survey of this thesis.

This thesis consists of four chapters on VDCCs. The first three chapters describe the physiological role of novel VDCC complexes, focused on VDCC-β interacting proteins. The last chapter describes the functional characterization and regulatory mechanism of TRPM1, which is all essential postsynaptic TRP channel in retinal bipolar cells.

References

1. Berridge, M. J., Lipp, P., and Bootman, M. D. (2000) *Nat. Rev. Mol Cell Biol.* **1**, 11-21

2. Reid, C. A., Bekkers, J. M., and Clements, J. D. (2003) *Trends in Neurosciences* **26**, 683-687

3. Ishikawa, T., Kaneko, M., Shin, H., and Takahashi, T. (2005) *J. Physiol.* **568**, 199-209

4. Blackstone, C. and Sheng, M. (1999) *Cell Calcium* **26**, 181-192

5. Moran, M. M., Xu, H., and Clapham, D. E. (2004) *Curr. Opin. Neurobiol.* 14, 362-369

6. Koike, C., Obara, T., Uriu, Y., Numata, T., Sanuki, R., Miyata, K., Koyasu, T., Ueno, S., Funabiki, K., Tani, A., Ueda, H., Kondo, M., Mori, Y., Tachibana, M., and Furukawa, T. (2010) *Proc. Nat. Acad. Sci.* **107**, 332–337

7. Tsien, R. W., Ellinor, P. T., and Horne, W. A. (1991) *Trends Pharmacol. Sci.* **12**, 349-354

8. Takahashi, T. and Momiyama, A. (1993) *Nature* **366**, 156-158

9. Wheeler, D. B., Randall, A., and Tsien, R. W. (1994) *Science* **264**, 107-111

10. Catterall, W. A. (1998) *Cell Calcium* **24**, 307-323

11. Catterall, W. A. and Few, A. P. (2008) *Neuron* **59**, 882-901

12. Ertel, E. A., Campbell, K. P., Harpold, M. M., Hofmann, F., Mori, Y., Perez-Reyes, E., Schwartz, A., Snutch, T. P., Tanabe, T., Birnbaumer, L., Tsien, R. W., and Catterall, W. A. (2000) *Neuron* **25**, 533-535

13. Tsien, R. W., Ellinor, P. T., and Horne, W. A. (1991) *Trends Pharmacol. Sci.* **12**, 349-354

14. Mori, Y., Friedrich, T., Kim, M. S., Mikami, A., Nakai, J., Ruth, P., Bosse, E., Hofmann, F., Flockerzi, V., Furuichi, T., Mikoshiba K., Imoto K., Tanabe T., and Numa S. (1991) *Nature* **350**, 398-402

15. Bichet, D., Cornet, V., Geib, S., Carlier, E., Volsen, S., Hoshi, T., Mori, Y., and De Waard, M. (2000) *Neuron* **25**, 177-190

16. Varadi, G., Lory, P., Schultz, D., Varadi, M., and Schwartz, A. (1991) *Nature* **352**, 159–162

17. Lacerda, A. E., Kim, H. S., Ruth, P., Perez-Reyes, E., Flockerzi, V., Hofmann, F., Birnbaumer, L., and Brown, A. M. (1991) *Nature* **352**, 527-530

18. Pedersen, S. F., Owsianik, G., and Nilius, B. (2005) *Cell Calcium* **38**, 233-252

19. Montell, C., Birnbaumer, L., and Flockerzi, V. (2002) *Cell* **108**, 595-598

20. Montell, C., Birnbaumer, L., Flockerzi, V., Bindels, R. J., Bruford, E. A., Caterina, M. J., Clapham, D. E., Harteneck, C., Heller, S., Julius, D., Kojima, I., Mori, Y., Penner, R., Prawitt, D., Scharenberg, A. M., Schultz, G., Shimizu, N., and Zhu, M. X. (2002) *Mol. Cell* **9**, 229-231

21. Corey, D. P. (2003) *Neuron* **39**, 585-588

22. Delmas, P. (2004) *Cell* **118**, 145-14

23. Clapham, D. E. (2003) *Nature* **426**, 517-524

Chapter 1

RIM1 confers sustained activity and neurotransmitter vesicle anchoring to presynaptic Ca^{2+} channels.

Abstract

The molecular organization of presynaptic active zones (AZs) is central to neurotransmitter release triggered by depolarization-induced Ca^{2+} influx. Here, we demonstrate a novel interaction between AZ components, RIM1α and voltage-dependent Ca^{2+} channels (VDCCs), that controls neurotransmitter release. RIM1α associates with VDCC β-subunits via its C-terminus to markedly suppress voltage-dependent inactivation among different neuronal VDCCs. The dominant negative β construct BADN, which disrupts the RIM1α-β association, accelerates inactivation of native VDCC currents. Thus, RIM1α association with β in the AZ may support release via sustaining Ca^{2+} influx through inhibition of channel inactivation.

Introduction

The presynaptic AZ is the specific site for impulse-evoked exocytosis of neurotransmitters at synapses of the nervous system across species (1, 2). Fine regulation of AZ neurotransmitter release is integral to nervous system adaptive functions including learning, memory, and cognition. The molecular organization of AZs, where synaptic vesicles are docked in close vicinity to VDCCs at the presynaptic membrane, is essential for the control of neurotransmitter release triggered by depolarization-induced Ca^{2+} influx. The spacing between VDCCs and vesicles influences the dynamic properties of synaptic transmission (3). However, molecular determinants that maintain vesicles and VDCCs within a physiologically appropriate distance have remained elusive.

RIM1, originally identified as a putative effector for the synaptic vesicle protein Rab3 (ref. 4), is part of the RIM superfamily whose members share a common C_2B domain at their C-termini (5). RIM1α interacts with other AZ protein components, including Munc13, ELKS/CAST, RIM-BP, or Liprins, to form a protein scaffold in the presynaptic nerve terminal (6–10). Mouse knockouts revealed that, in different types of synapses, RIM1α is essential for different forms of synaptic plasticity (9,11). In the CA1-region Schaffer-collateral excitatory synapses and in GABAergic synapses, RIM1α maintains normal neurotransmitter release and short-term synaptic plasticity. In excitatory CA3-region mossy fibre synapses and cerebellar parallel fibre synapses, RIM1α is necessary for presynaptic long-term synaptic plasticity. In autapses, the RIM1α deletion significantly reduces the readily releasable pool of vesicles, alters short-term plasticity and the properties of evoked asynchronous release (12). However, in spite of the progress in understanding RIM1α functions, the mechanisms by which RIM1α acts remain unknown. Moreover, the physiological roles played by other RIM isoforms (RIM2, RIM3, and RIM4) (5) remain unclear.

Multiple types of VDCCs distinguished on the basis of biophysical and pharmacological properties coexist in neurons (13). High voltage-activated types of VDCCs essential for neurotransmitter release include N-, P/Q-, R-, and L-types (14–16). VDCCs are heteromultimeric protein complexes comprised of the pore-forming α_1, designated as Cav, and auxiliary subunits α_2/δ, β, and γ (17). The α1-subunit is encoded by 10 distinct genes, whose correspondence with functional types is largely elucidated (13, 17). VDCC complexes are associated

with presynaptic and postsynaptic proteins including syntaxin, SNAP-25, synaptotagmin, CASK, and Mint primarily via interactions with the α1-subunit (18–25). The β-subunit interacts with the α1-subunit to enhance functional channel trafficking to the plasma membrane (26, 27) and to modify multiple kinetic properties28; it also interacts with other proteins (29–31). Therefore, it is intriguing to investigate whether β-subunits are involved in targeting VDCC complexes to specific subcellular machinery at AZs for neurotransmitter release through yet unidentified interactions. Here, we demonstrate a novel molecular interaction between RIM1α and VDCC β-subunits, both of which are essential AZ proteins. The RIM1α-β interaction supports the function of RIM1α in neurotransmitter release via two distinct mechanisms: the anchoring of neurotransmitter-containing vesicles in the vicinity of VDCCs; and sustaining Ca^{2+} influx through the inhibition of voltage-dependent inactivation.

Results

VDCC β-subunits directly interact with RIM1α

To identify β-subunit interacting proteins that regulate the AZ organization, we performed yeast two-hybrid screening with the combination of a mouse brain complementary DNA library using the full amino acid sequence of the rat β_{4b}-subunit as a bait protein. The β_4-subunit was chosen because spontaneous β_4-mutant mice *lethargic* (32) have clear neurological defects suggesting that β_4-containing VDCCs are physiologically significant in the brain. Screening with VDCC β_{4b}-subunit identified a clone (#2-5) encoding the C-terminal region (1079-1463) of the mouse RIM1α protein (4) including the C_2B domain (Fig. 1*A*). Subsequent two-hybrid assays using a series of deletion and point mutants of β_{4b} revealed that residues 49-410 containing major structural motifs such as Src homology 3 (SH3) domain, α_1-interacting domain known as BID, and guanylate kinase (GK) domain, are required for the interaction of β_{4b} with the RIM1 C-terminus (Fig. 1*B*). *in vitro* pulldown assays using GST fusion proteins for different regions of RIM1 identified the C-terminus (residues 1079-1463) as a major β_4-interaction domain likely formed in concert by two adjacent subdomains (1079-1257 and 1258-1463) in RIM1α (Fig. 1*C*). An *in vitro* binding assay using

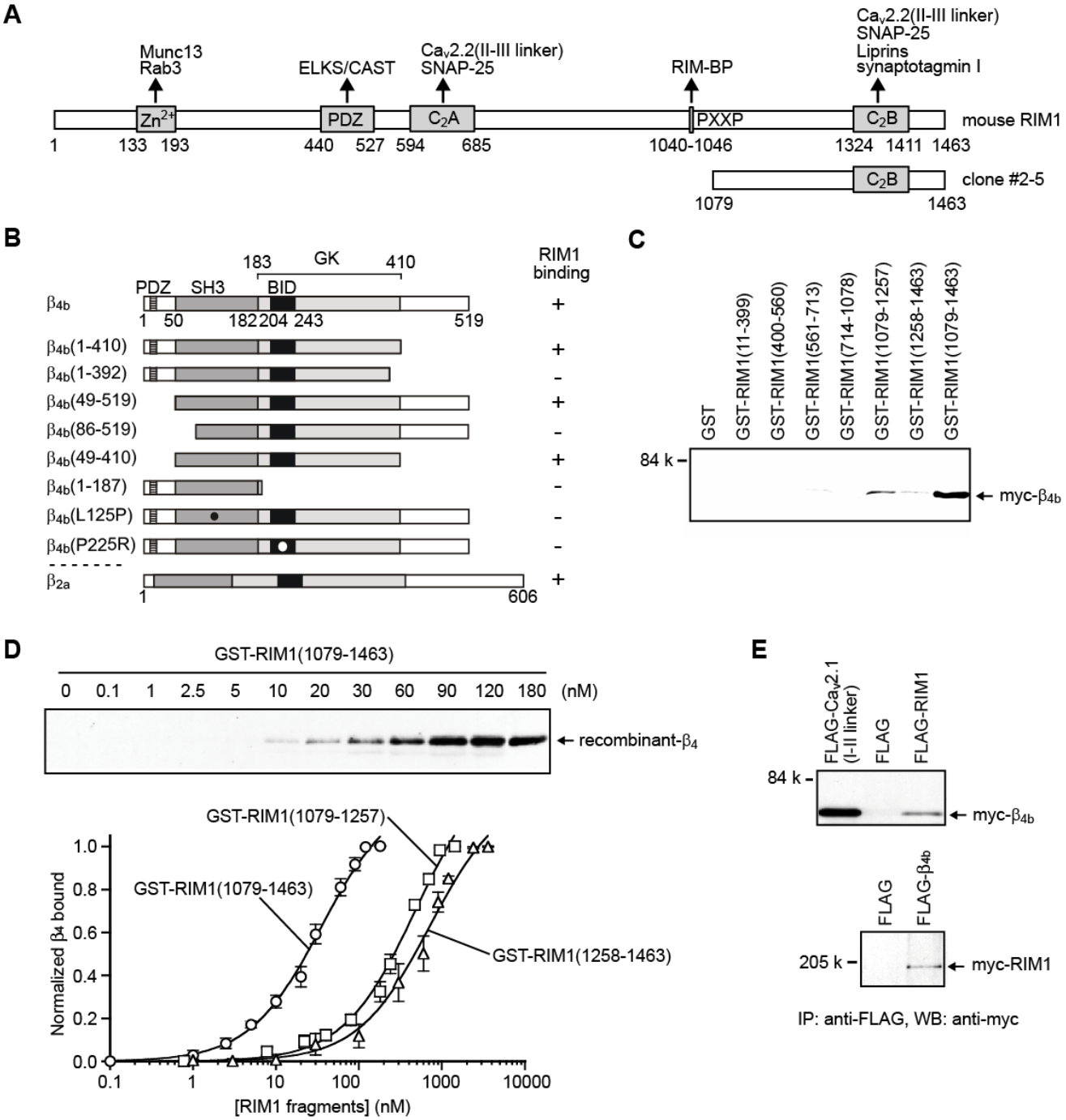

Fig. 1 Direct interaction of RIM1α with the VDCC β_{4b}-subunit.

A. Domain structure of mouse RIM1α. Arrows indicate molecules interacting with RIM1α at the following domains: Zn^{2+}, Zn^{2+}-finger like domain; PDZ, PDZ domain; C_2A and C_2B, first and second C_2 domains; PXXP, proline-rich region (4, 6–10). The protein region encoded by clone #2-5 is also indicated. ***B***. Mapping of RIM1α binding sites on β_{4b} by the yeast two-hybrid assay. Full-length and various mutant β-subunits in bait vectors are tested with RIM1α in the prey vector. The interactions are scored by β-galactosidase activity and His^+ prototrophy. ***C***. Pulldown assay of β_{4b} with GST fusion RIM1α mutants. GST fusion proteins immobilized on glutathione-Sepharose beads are incubated with cell lysate obtained

from myc-β_{4b} cDNA plasmid-transfected HEK293 cells. Bound proteins are analyzed by western blotting (WB) using anti-myc antibody. ***D***. *in vitro* association between the purified preparations of GST-RIM1α fusion constructs and the recombinant β_4-subunit (amino acid residues 47-475). GST-RIM1α proteins at various concentrations, incubated with VDCC β_4 (50 pM), are captured by glutathione-Sepharose beads. Captured β_4 proteins are examined by WB. The bottom panel shows the quantitative densitometric analysis of bands shown in the upper panel. The saturation curves are subjected to the nonlinear least-squares curve-fitting method to evaluate the apparent dissociation constant (K_d). ***E***. Interaction of recombinant β_{4b} and RIM1α in HEK293 cells. The interaction is evaluated by immunoprecipitation (IP) with anti-FLAG antibody, followed by WB with anti-myc antibody. Top: physical association of myc-β_{4b} with FLAG-RIM1α is examined in comparison to a positive control FLAG-$Ca_v2.1$(I-II linker). Bottom: physical association of FLAG-β_{4b} with myc-RIM1α is examined.

---

purified recombinant constructs for β_4 and RIM subfragments revealed a dissociation constant (K_d) of 35.1 nM for RIM1α(1079-1463) significantly lower than 481 nM for RIM1α(1079-1257) and 717 nM for RIM1α(1258-1463) (Fig. 1*D*, Fig. 3*D*). These results, as well as the successful coimmunoprecipitation of full-length RIM1 with β_{4b} (Fig. 1*E*), suggest a direct protein-protein interaction between RIM1 and β_4.

RIM1 physically associates with native VDCCs in the brain

Association between native VDCC β-subunits and RIM1α association was characterized biochemically using VDCC complexes enriched from mouse brains through microsome preparation, KCl wash, solubilization, heparin purification, and sucrose density gradient fractionation (23). Western blot analysis of sucrose gradient fractions showed cosedimentation of RIM1α with $Ca_v2.1$ and β_4 (Fig. 2*A*). Statistical analysis of cosedimentation data plotting the normalized density of each protein as a function of the sucrose density fraction number reveals complete overlap of $Ca_v2.1$ and β_4, confirming their association in the VDCC complex (Fig. 2*B*). RIM1α sedimented in overlapping minor and major peaks. The major peak completely overlapped with VDCC subunits, whereas the smaller peak did not cosediment with VDCC and likely represents a subset of RIM1α in a smaller, non-VDCC complex. Syntaxin, a VDCC interacting protein, showed similar cosedimentation with RIM1 (Fig. 2*A*). To confirm that the cosedimentation of RIM1α is due to its

specific interaction with VDCC subunits, heparin purified samples were subjected to immunoprecipitation analysis (Fig. 2*A*). Anti-β_4 antibody precipitated RIM1α from wild-type mice but not from *lethargic* mice that express truncated β_4 protein lacking the C-terminal region responsible for α_1 interaction (32, 33). It is unlikely that the β_4 isoform exclusively mediates the RIM1α-VDCC association in the brain, since wild-type and *lethargic* mice were indistinguishable in the sucrose gradient profile (Fig. 2*D*). A β_{4b} fusion construct was designed as a dominant negative (beta-AID dominant negative (BADN)) suppressor mutant to dissociate the activity of β-binding proteins such as RIM1 from the functional VDCC complex (Fig. 3*A*-*C*). BADN contains the full-length β_{4b} structure with the β-interacting AID region from $Ca_v2.1$ buried at the α_1-binding site (33). As residues 49-410 of the entire 519 amino acid sequence of β_{4b} are required for RIM1α binding (Fig. 1*B*), we utilized the "full-length" β_{4b} in order to efficiently quench RIM1. The ability of BADN to bind RIM1 was confirmed by *in vitro* binding assay (Fig. 3*D*). Coimmunoprecipitation experiments also showed binding of BADN to RIM1α but not to the AID-containing I-II linker region of $Ca_v2.1$ in HEK cells (Fig. 3*E*). Since the intermolecular association of BADN with VDCC α_1 is thus inhibited by the intramolecular occlusion of the α_1-binding site in BADN, BADN overexpression should deprive native β-subunits of RIM1 without affecting their association with α_1. Importantly, coimmunoprecipitation experiments revealed that the native β-RIM1α association in partially purified brain VDCCs was disrupted by 8 hr coincubation with 100 nM GST fusion proteins for BADN or RIM1α(1079-1463) (Fig. 2*E*). Binding of β_4 to RIM1α(1079-1463) rapidly decayed with the addition of excessive recombinant BADN protein (200 nM) indicating that this disruption is attributable to displacement of binding partners in native association (Fig. 3*E*). These results provide evidence for a physiological association between native RIM1α and P/Q-type VDCCs via the β-subunit in brain.

RIM1 targets to VDCC via the β-subunit at the plasma membrane

In recombinant HEK293 cells, β_{4b} and RIM1α were concentrated at the plasma membrane by coexpression of

the P/Q-type $Ca_v2.1$ α_1-subunit, whereas they were diffusively colocalized throughout the intracellular area in the absence of $Ca_v2.1$ (Fig. 4): F_{PM}/F_{CYT} (ratio of the fluorescent intensity at the plasma membrane to that in the cytoplasm) was 0.52 ± 0.07 and 0.48 ± 0.07 in the presence of $Ca_v2.1$ and 0.10 ± 0.02 and 0.08 ± 0.02 in the absence of $Ca_v2.1$ for β_{4b} and RIM1α, respectively. Importantly, RIM1α localization to the plasma membrane via a membrane-targeted β-binding domain comprised of CD8 and the $Ca_v2.1$ I-II linker was elicited only after β_{4b} coexpression (Fig. 4*B*). F_{PM}/F_{CYT} was 0.29 ± 0.03 and 0.27 ± 0.02 in the presence of β_{4b} and 0.08 ± 0.01 and 0.08 ± 0.02 in the absence of β_{4b} for the $Ca_v2.1$ I-II linker and RIM1α, respectively.

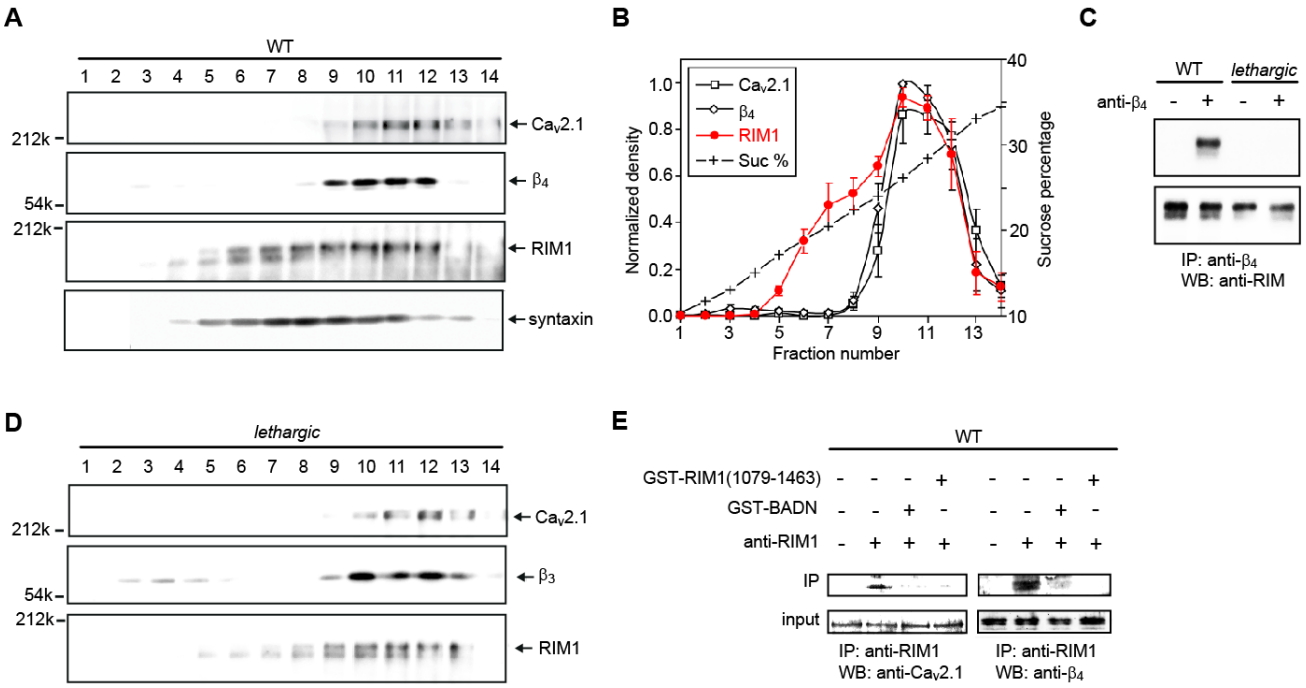

Fig. 2 Association of RIM1 with native neuronal VDCC complexes.

A. Sucrose gradient fractionation of neuronal VDCC complexes from wild-type (WT) mouse brains and subsequent WB demonstrate cosedimentation of RIM1α with $Ca_v2.1$ and β_4. Syntaxin showed similar cosedimentation with RIM1α. ***B***. Densitometry of $Ca_v2.1$, β_4, and RIM1α from western blots of sucrose gradient fractions. ***C***. Coimmunoprecipitation of RIM1α with the β_4-subunit. Immunoprecipitation (IP) using an anti-β_4 antibody and subsequent WB for RIM1α is performed on heparin purified samples. As a negative control, a preparation from *lethargic* mice is used. ***D***. Sucrose gradient fractionation of neuronal VDCC complexes from *lethargic* mouse brains. ***E***. Coimmunoprecipitation of $Ca_v2.1$ with RIM1α. The immunocomplexes are disrupted by GST-BADN or GST-RIM1α(1079-1463). IP using anti-RIM1 antibody and subsequent WB for $Ca_v2.1$ is performed.

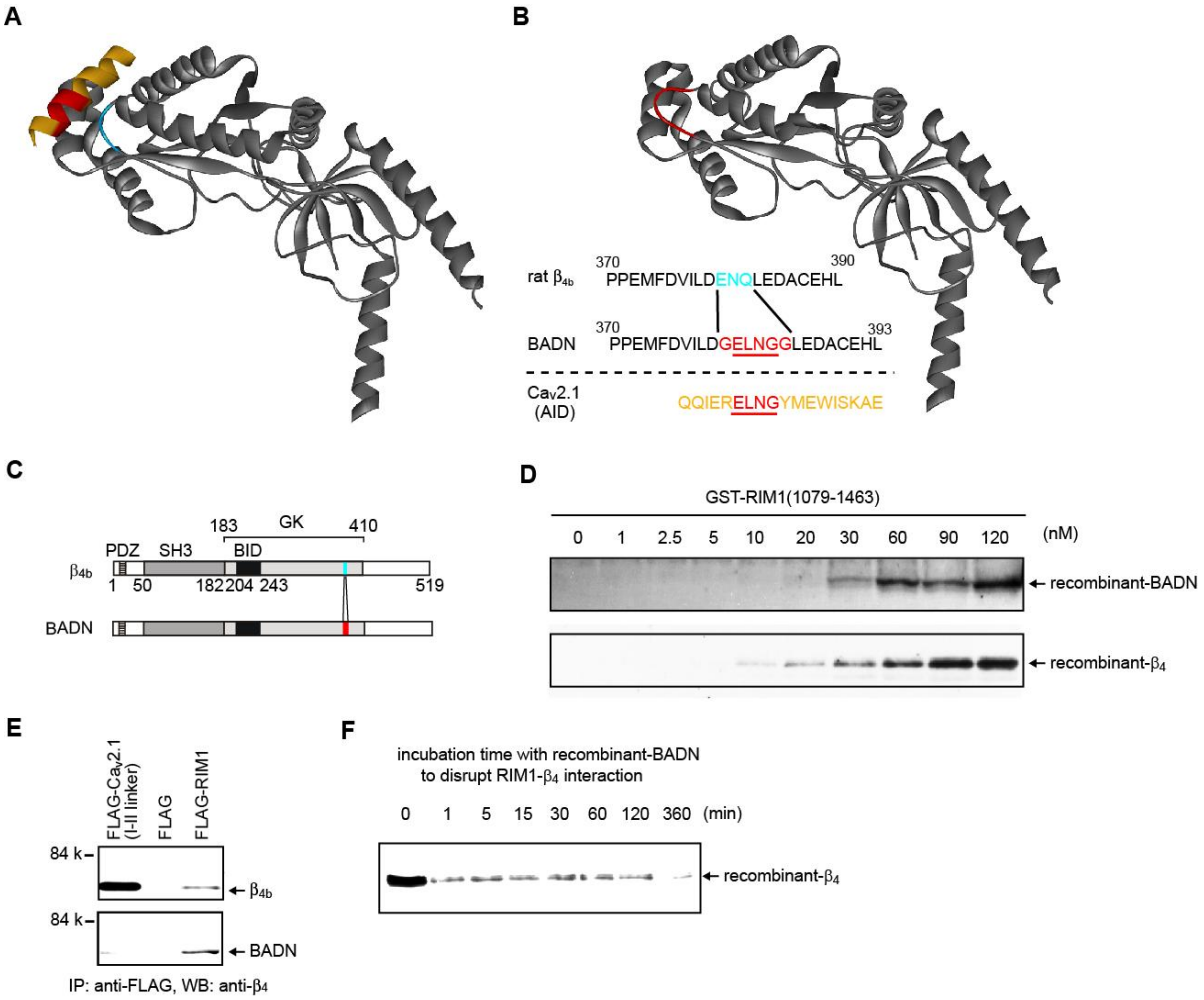

Fig. 3 Molecular modeling and functional characterization of BADN as a dominant-negative mutant for RIM1 function. ***A***. X-ray structure of the b subunit and AID (yellow and red) complex adapted from the previous paper by Opatowsky et al (33). ***B***. Energetically minimized structure of BADN by molecular modeling. BADN is designed to suppress AID binding without destruction of the b subunit 3D structure. Inset indicates the amino acid sequence (370-393) of BADN compared with the sequence of rat b_{4b} and the AID sequence of $Ca_v2.1$. BADN is constructed on the basis of rat β_{4b}, and hexa-peptide (GELNGG (red)) containing the essential region (ELNG) for β subunit binding of AID with flanking glycine residues as spacers replacing the original tri-peptide (ENQ (blue)) to suppress AID binding. ***C***. Domain structure of β_{4b} and BADN. ***D***. Dose-dependent binding of recombinant-BADN to the GST-RIM1α(1079-1463) is shown. This result shows that BADN has affinity to RIM1α(1079-1463) comparable with that of β_4. ***E***. Interaction of recombinant BADN and RIM1α in HEK293 cells. The interaction is evaluated by IP with anti-FLAG antibody, followed by WB with anti-b_4 antibody. Top: HEK293 cells co-transfected with b_{4b} and FLAG-RIM1α. FLAG-$Ca_v2.1$(I-II linker) is used as a positive control. Bottom: HEK293 cells co-transfected with BADN and FLAG-RIM1α. ***F***. Rapid disruption of the RIM1α-β_{4b} interaction by BADN. The dissociation is measured in the presence of excessive BADN protein (200 nM). This result suggests that virtually complete disruption of the RIM1α-β_{4b} interaction is attained within 6 h of incubation.

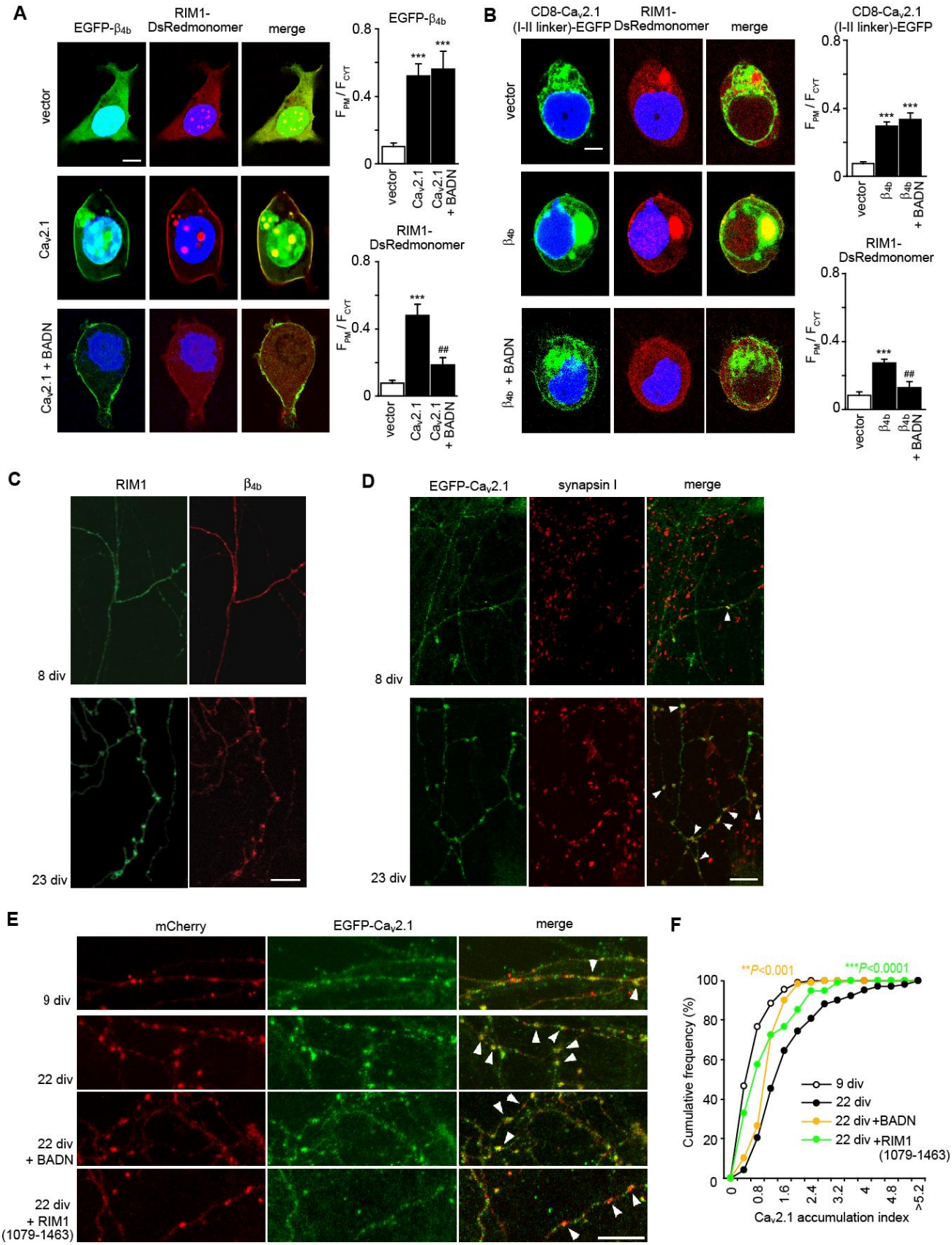
A
EGFP-β4b
RIM1-DsRedmonomer
merge
vector
Cav2.1
Cav2.1 + BADN
EGFP-β4b
RIM1-DsRedmonomer
FPM / FCYT
vector
Cav2.1
Cav2.1 + BADN
B
CD8-Cav2.1 (I-II linker)-EGFP
RIM1-DsRedmonomer
merge
vector
β4b
β4b + BADN
CD8-Cav2.1 (I-II linker)-EGFP
RIM1-DsRedmonomer
vector
β4b
β4b + BADN
C
RIM1
β4b
8 div
23 div
D
EGFP-Cav2.1
synapsin I
merge
8 div
23 div
E
mCherry
EGFP-Cav2.1
merge
9 div
22 div
22 div + BADN
22 div + RIM1 (1079-1463)
F
**P<0.001
***P<0.0001
Cumulative frequency (%)
9 div
22 div
22 div +BADN
22 div +RIM1 (1079-1463)
Cav2.1 accumulation index

Fig. 4 RIM1α clusters with the VDCC α_1- and β-subunits near presynaptic termini in cultured hippocampal neurons.

A. The $Ca_v2.1$ α_1-subunit elicits colocalization of β_{4b} with RIM1α at the plasma membrane. The colocalization is disrupted by BADN. Left: confocal imaging of HEK293 cells co-transfected with EGFP-β_{4b} and RIM1α-DsRedmonomer in the presence vector (top), $Ca_v2.1$ (middle), or $Ca_v2.1$ plus BADN (bottom). Scale bar: 5 μm. Nuclei are stained with Hoechst 33342. Right: statistical analysis of subcellular location of EGFP-β_{4b} or RIM1α-DsRedmonomer distributed in 1 μm widths plasma membrane regions (PM) and in the cytosolic area (CYT) (n = 5 cells in each). $^{***}P < 0.001$ vs vector. $^{\#\#}P < 0.01$ vs $Ca_v2.1$. ***B***. The β_{4b}-subunit elicits colocalization of $Ca_v2.1$(I-II linker) and RIM1α on the plasma membrane. The colocalization is disrupted by BADN. Left: confocal imaging of HEK293 cells co-transfected with CD8-$Ca_v2.1$(I-II linker)-EGFP and RIM1α-DsRedmonomer in the presence vector (top), β_{4b} (middle), or β_{4b} and BADN (bottom). Scale bar: 5 μm. Right: stastical analysis of subcellular location of CD8-$Ca_v2.1$(I-II linker)-EGFP or RIM1α-DsRedmonomer (n = 5 cells in each). $^{***}P < 0.001$ vs vector. $^{\#\#}P < 0.01$ vs β_{4b}. ***C***. Immunolocalization studies of tagged-RIM1 and β_{4b} in mouse hippocampal neurons. Clustering of RIM1 and β_{4b} not detected at 8 days *in vitro* (div), but is present at a substantially later stage at 23 div in cultured mouse hippocampal neurons. Scale bar: 10 μm. ***D***. Comparison of localization of EGFP-$Ca_v2.1$ with that of intrinsic synapsin I in hippocampal neurons. Like RIM1 and β_{4b}, $Ca_v2.1$ clusters much later than the onset of synaptogenesis which occurs earlier than 8 div, as synapsin I-positive puncta are already in abundance at 8 div, while $Ca_v2.1$ distribution is still diffuse. ***E, F*** Enrichment of EGFP-$Ca_v2.1$ in presynaptic varicosities is achieved between 9 div and 22 div. However, this maturation process is impaired by coexpression of a C-terminal fragment of RIM1 (+ RIM1α(1079-1463)), or a dominant negative β construct with occluded α_1-binding pocket (+ BADN), indicating that the local concentration of presynaptic Ca^{2+} channels at AZs may be influenced by RIM1α-β-subunit interaction during a postsynaptogenic maturation period, although contributions from other RIM1-C-terminus-interacting proteins cannot be excluded.

Notably, the plasma membrane colocalization of RIM1α and β_{4b} via $Ca_v2.1$ or the β_{4b}-mediated colocalization of RIM1α and the $Ca_v2.1$ I-II linker was efficiently disrupted by BADN (Fig. 4*A*, *B*). In the presence of BADN, F_{PM}/F_{CYT} was 0.56 ± 0.11 and 0.19 ± 0.04 for β_{4b} and RIM1α, respectively; and F_{PM}/F_{CYT} was 0.33 ± 0.04 and 0.13 ± 0.04 for the $Ca_v2.1$ I-II linker and RIM1α, respectively. Thus, the RIM1α-β_{4b} interaction is likely to be essential for assembly of RIM1α with VDCC at the plasma membrane. In cultured mouse hippocampal neurons, RIM1α and β_{4b} both became enriched near presynaptic termini, in parallel with the clustering of $Ca_v2.1$. These events had a substantially later onset than synaptogenesis

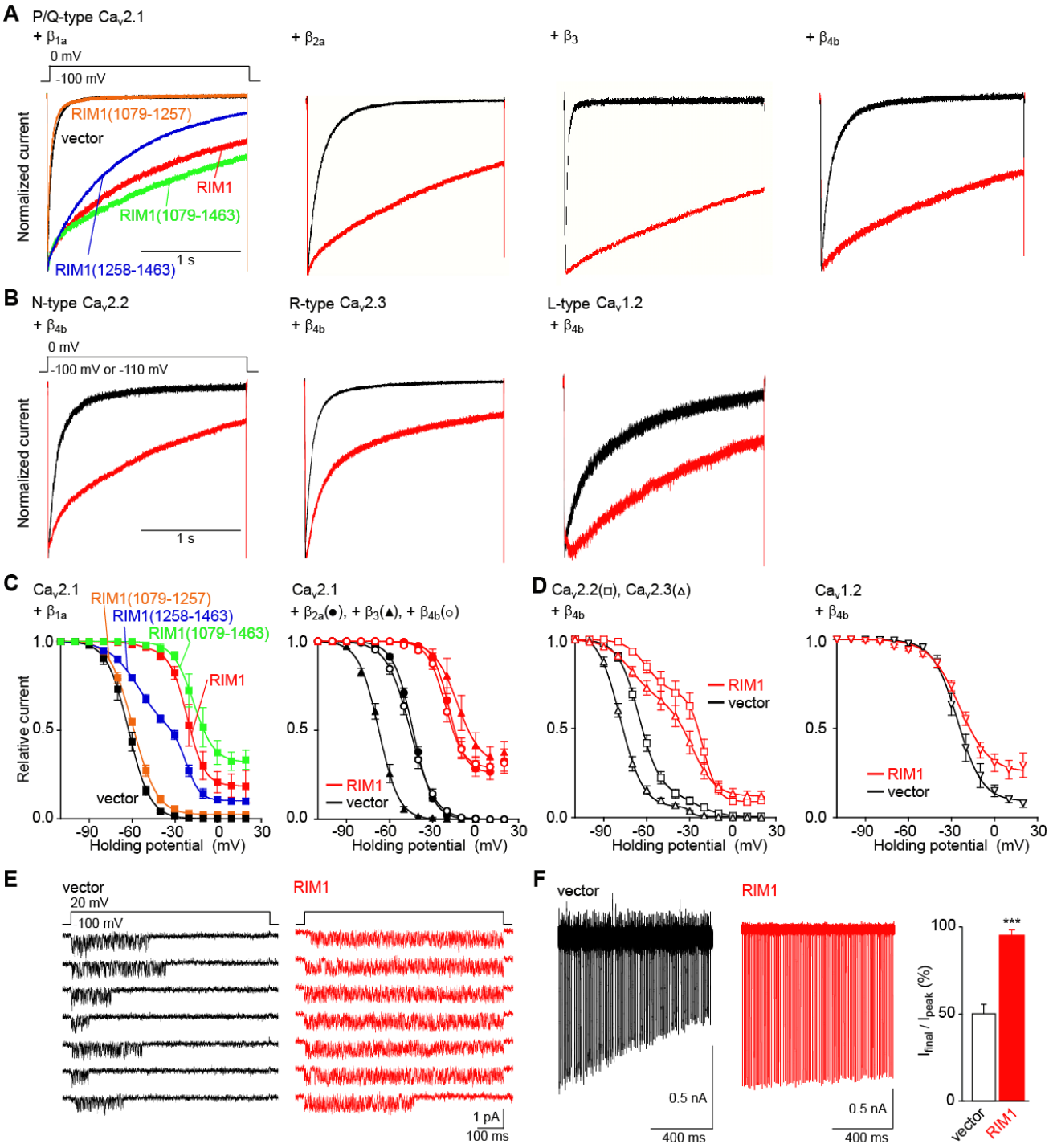

Fig. 5 Effects of RIM1 on the inactivation properties of recombinant neuronal VDCCs.

A. Inactivation of P/Q-type $Ca_v2.1$ currents in BHK cells expressing α_2/δ and β-subunits. For comparison of inactivation time courses before and after expression of RIM1 constructs, the peak amplitudes are normalized for Ba^{2+} currents elicited by 2-s pulses to 0 mV from a holding potential (V_h) of –100 mV. ***B***. Inactivation of N-type $Ca_v2.2$, R-type $Ca_v2.3$, or L-type $Ca_v1.2$ currents in BHK cells expressing α_2/δ and β_{4b}. The V_h is –100 mV for $Ca_v2.2$ or $Ca_v1.2$, and –110 mV for $Ca_v2.3$. ***C***. Left: inactivation curves for $Ca_v2.1$ in BHK cells expressing α_2/δ and β_{1a}. See **Table 3** for statistical significance of the differences

between vector and RIM1, RIM1(1079-1463), or RIM1(1258-1463). Right: inactivation curves for $Ca_v2.1$ in BHK cells expressing α_2/δ and different β-subunits. See **Table 2** for statistical significance of the differences between vector and RIM1 in the presence of β_{2a}, β_3, or β_{4b}. ***D***. Inactivation curves for $Ca_v2.2$, $Ca_v2.3$ (left), or $Ca_v1.2$ (right) in BHK cells expressing α_2/δ and β_{4b}. See **Table 1** for statistical significance of the difference between vector and RIM1 for $Ca_v2.2$, $Ca_v2.3$, or $Ca_v1.2$. ***E***. RIM1 prolongs the time between first channel opening and last closing within a single-channel trace of $Ca_v2.1$ in BHK cells expressing α_2/δ and β_{4b}. Seven consecutive unitary traces are shown. The mean values for the time of each trace are 184.2 ± 33.3 ms (n = 117 traces) for vector and 502.8 ± 33.3 ms, (n = 101) for RIM1. The time for traces without opening is counted as 0 ms. ***F***. Left: $Ca_v2.1$ currents induced by 100 Hz AP trains for 1 s in BHK cells expressing α_2/δ and β_{1a}. Right: percentage of currents in response to the last stimulus compared to the peak current (n = 6 for vector and n = 4 for RIM1). Data points are mean ± S.E.M. $^{***}P < 0.001$.

---

indicated by synapsin I clustering observed at 8 days *in vitro* (Fig. 4*C*, *D*). Quantitative analysis using confocal imaging demonstrated that overexpression of either BADN or the RIM1α C-terminal domain impaired the clustering of the $Ca_v2.1$ α_1-subunit in presynaptic varicosities in cultured hippocampal neurons, (Fig. 4*E*, *F*). The coincident targeting of RIM1α and β_{4b}, as well as the blockade of the $Ca_v2.1$ enrichment in presynaptic varicosities by quenching of RIM1α and βs, suggests that the RIM1α-β interaction regulates localization of VDCCs at the presynaptic membrane. Since RIM1α is known to interact with multiple proteins (Fig. 1*A*) (ref. 6-10), we cannot exclude the possibility that the RIM1αeffect observed in neurons using BADN and the RIM1α C-terminus was due to the quenching of other RIM-dependent interactions at different subcellular locations. However, recent immunostaining at the giant calyx-type synapse of the chick ciliary ganglion by Khanna et al. (34) revealed that the staining intensities for $Ca_v2.2$ and RIM co-vary. This is consistent with the idea that they are both components of transmitter release sites.

RIM1-β interaction modulates inactivation properties of VDCCs

To elucidate the functional significance of direct RIM1-β_4 coupling, we characterized whole-cell Ba^{2+} currents through recombinant VDCCs expressed as $\alpha_1\alpha_2/\delta\beta$ complexes in BHK cells. RIM1α was tested with VDCC containing various neuronal α_1-subunits, N-type $Ca_v2.2$, P/Q-type $Ca_v2.1$, R-type $Ca_v2.3$, and L-type $Ca_v1.2$.

Table 1 Effects of RIM1 constructs on current density, activation, and inactivation of $Ca_v2.1$, $Ca_v2.2$, $Ca_v2.3$, or $Ca_v1.2$ channel in BHK cells expressing α_2/δ and β_{4b}[1].

Subunit combination		Current density (pA / pF)[2]	Activation parameters			Inactivation parameters					
			$V_{0.5}$ (mV)	k (mV)	τ_{act} (ms)[3]	a	$V_{0.5}{}^{1st}$ (mV)	k^{1st} (mV)	b	$V_{0.5}{}^{2nd}$ (mV)	k^{2nd} (mV)
$Ca_v2.1$	vector	−14.0 ± 2.9 (15)	−7.2 ± 1.2 (9)	5.7 ± 0.1 (9)	0.53 ± 0.05 (9)	1.00 ± 0.00 (12)	−45.9 ± 1.8 (12)	−7.5 ± 0.3 (12)			
+ β_{4b}	RIM1	−27.8 ± 4.9 (18)*	−9.1 ± 1.6 (13)	5.6 ± 0.2 (13)	0.59 ± 0.04 (13)	0.70 ± 0.04 (6)***	−21.3 ± 1.2 (6)***	−5.6 ± 0.7 (6)			
$Ca_v2.2$	vector	−50.8 ± 11.9 (12)	−4.1 ± 1.0 (11)	6.8 ± 0.2 (11)	0.67 ± 0.06 (11)	0.91 ± 0.03 (7)	−64.5 ± 1.6 (7)	−7.8 ± 0.5 (7)	0.09 ± 0.04 (7)	−22.4 ± 2.1 (7)	−5.1 ± 1.7 (7)
+ β_{4b}	RIM1	−96.4 ± 18.5 (10)*	−7.0 ± 1.0 (7)	6.8 ± 0.4 (7)	0.73 ± 0.02 (7)	0.30 ± 0.06 (5)***	−59.7 ± 1.2 (5)	−7.7 ± 0.7 (5)	0.61 ± 0.06 (5)***	−20.8 ± 1.8 (5)	−4.9 ± 1.0 (5)
$Ca_v2.3$	vector	−23.0 ± 7.7 (10)	−10.3 ± 1.5 (7)	8.4 ± 0.5 (7)	0.47 ± 0.03 (7)	0.91 ± 0.02 (5)	−78.2 ± 1.3 (5)	−6.7 ± 0.7 (5)	0.08 ± 0.04 (5)	−36.2 ± 3.3 (5)	−6.1 ± 2.9 (5)
+ β_{4b}	RIM1	−23.4 ± 5.4 (12)	−5.3 ± 1.4 (6)*	9.4 ± 0.6 (6)	0.67 ± 0.07 (6)*	0.35 ± 0.05 (6)***	−71.0 ± 1.6 (6)*	−9.1 ± 0.9 (6)	0.53 ± 0.05 (6)***	−27.9 ± 2.3 (6)	−7.5 ± 0.4 (6)
$Ca_v1.2$	vector	−18.6 ± 3.6 (10)	−13.6 ± 1.3(12)	8.4 ± 0.4 (12)	0.46 ± 0.03 (6)	0.93 ± 0.02 (6)	−24.6 ± 3.1 (6)	−8.3 ± 1.3 (6)			
+ β_{4b}	RIM1	−17.1 ± 2.3 (13)	−8.0 ± 1.3 (11)**	10.2± 0.3 (11)**	0.62 ± 0.04 (7)*	0.75 ± 0.07 (5)*	−24.7 ± 1.6 (5)	−10.1 ± 0.6 (5)			

1) $^{*}P < 0.05$, $^{**}P < 0.01$, $^{***}P < 0.001$ vs vector.

2) Ba^{2+} currents evoked by depolarizing pulse to 0 mV from a V_h of −100 or −110 mV are divided by capacitance.

3) Activation time constants obtained from currents elicited by 5-ms test pulse to 20 mV. The activation phases are well fitted by a single exponential function.

The most prominent RIM1α effect on VDCC currents was observed on inactivation parameters. The rate of inactivation was dramatically decelerated in N-, P/Q-, R-, and L-type channels (Fig. 5*A*, *B*). The same set of VDCC types also showed a significant depolarizing shift in the voltage dependence of inactivation (Fig. 5*C*, *D*). In P/Q-types ($Ca_v2.1$ + β_{4b}), RIM1α coexpression shifted the half inactivation potential by +24.6 mV eliciting an inactivation curve with a component susceptible to inactivation induced at high voltages ($V_{0.5}$ (vector) = –45.9 mV, $V_{0.5}$ (RIM1α)= –21.3 mV; $V_{0.5}$ is the potential to give a half-value of inactivation) and a non-inactivating component (Table 1). In N- and R-types, RIM1α coexpression provoked a switch in the major phase of a biphasic inactivation curves from low voltage-induced ($V_{0.5}$ and ratio; –64.5 mV and 0.91 for N, and –78.2 mV and 0.91 for R) to high voltage-induced ($V_{0.5}$ and ratio; –20.8 mV and 0.61 for N, and –27.9 mV and 0.53 for R). L-type inactivation curve remained monophasic, however the non-inactivating component was significantly augmented by RIM1 (from 0.07 to 0.25). In P/Q-type channels, RIM1α effects on kinetics and voltage-dependent equilibrium of inactivation were observed with all other β-subunits tested (Fig. 5*A*, *C*, and Table 2). Furthermore, the C-terminal truncated mutants RIM1α(1079-1463) and RIM1α(1258-1463), but not RIM1α(1079-1257), successfully slowed P/Q-type (with β_{1a}) current inactivation (Fig. 5*A*, *C*, and Table 3). After RIM1α coexpression, single-channel currents clearly demonstrated prolongation of mean time between first channel opening and last closing within a trace during 750-ms depolarizations to 20 mV without significant changes in single-channel amplitude (0.59 pA) (Fig. 5*E*). This observation corresponds well with the whole-cell data and suggests that RIM1α predominantly stabilizes the non-inactivating mode (35) in P/Q-type channels. Currents evoked by trains of action potential (AP)

waveforms, a more physiological voltage-clamp protocol used particularly to reveal closed-state inactivation (36), further support the profound suppression of voltage-dependent inactivation by RIM1α (Fig. 5*F*). The observed effect of RIM1α on VDCC inactivation is attributable to its association with the β-subunit, since replacement of β_4 with a C-terminal truncation construct β_4-GK, that directly interacts with α_1 (37) but lacks the SH3 domain necessary for the RIM binding (Fig. 1*B* and Fig. 6*A*, *B*), failed to significantly affect inactivation in N-type channels (Fig. 6C, D, and Table 4). In addition, BADN, the dominant negative form to quench RIM1 interaction with the β-subunit, significantly on P/Q channel inactivation (Fig. 6*E*, *F*, and

Table 2 Effects of RIM1 or C-terminal truncated mutants of RIM1 on inactivation of $Ca_v2.1$ channel in BHK cells expressing α_2/δ and β_{1a}[1)2)].

	Inactivation parameters					
	a	$V_{0.5}^{1st}$ (mV)	k^{1st} (mV)	*b*	$V_{0.5}^{2nd}$ (mV)	k^{2nd} (mV)
vector	1.00 ± 0.00 (7)	−62.6 ± 1.9 (7)	−7.0 ± 0.3 (7)			
RIM1	0.83 ± 0.07 (5)**	−21.6 ± 2.5 (5)***	−6.1 ± 0.9 (5)			
RIM1(1079-1257)	1.00 ± 0.00 (4)#	−58.9 ± 0.7 (4)###	−8.0 ± 0.8 (4)			
RIM1(1258-1463)	0.51 ± 0.03 (6)***###	−55.2 ± 1.5 (6)*###	−9.6 ± 0.9 (6)*##	0.41 ± 0.02 (6)	−22.3 ± 1.0 (6)	−5.1 ± 0.9 (6)
RIM1(1079-1463)	0.70 ± 0.05 (5)***#	−15.8 ± 3.7 (5)***	−5.9 ± 0.9 (5)			

1) $^{*}P < 0.05$, $^{**}P < 0.01$, $^{***}P < 0.001$ vs vector.

2) $^{\#}P < 0.05$, $^{\#\#}P < 0.01$, $^{\#\#\#}P < 0.001$ vs RIM1.

Table 3 Effects of RIM1 on inactivation of $Ca_v2.2$ channel in BHK cells expressing α_2/δ and β_4-GK.

	Inactivation parameters					
	a	$V_{0.5}^{1st}$ (mV)	k^{1st} (mV)	*b*	$V_{0.5}^{2nd}$ (mV)	k^{2nd} (mV)
vector	0.75 ± 0.08 (5)	−48.9 ± 1.5 (5)	−8.1 ± 0.6 (5)	0.20 ± 0.05 (5)	−5.0 ± 2.2 (5)	−3.9 ± 1.0 (5)
RIM1	0.78 ± 0.07 (5)	−44.0 ± 1.8 (5)	−8.1 ± 0.6 (5)	0.11 ± 0.05 (5)	1.4 ± 0.4 (5)	−4.5 ± 0.4 (5)

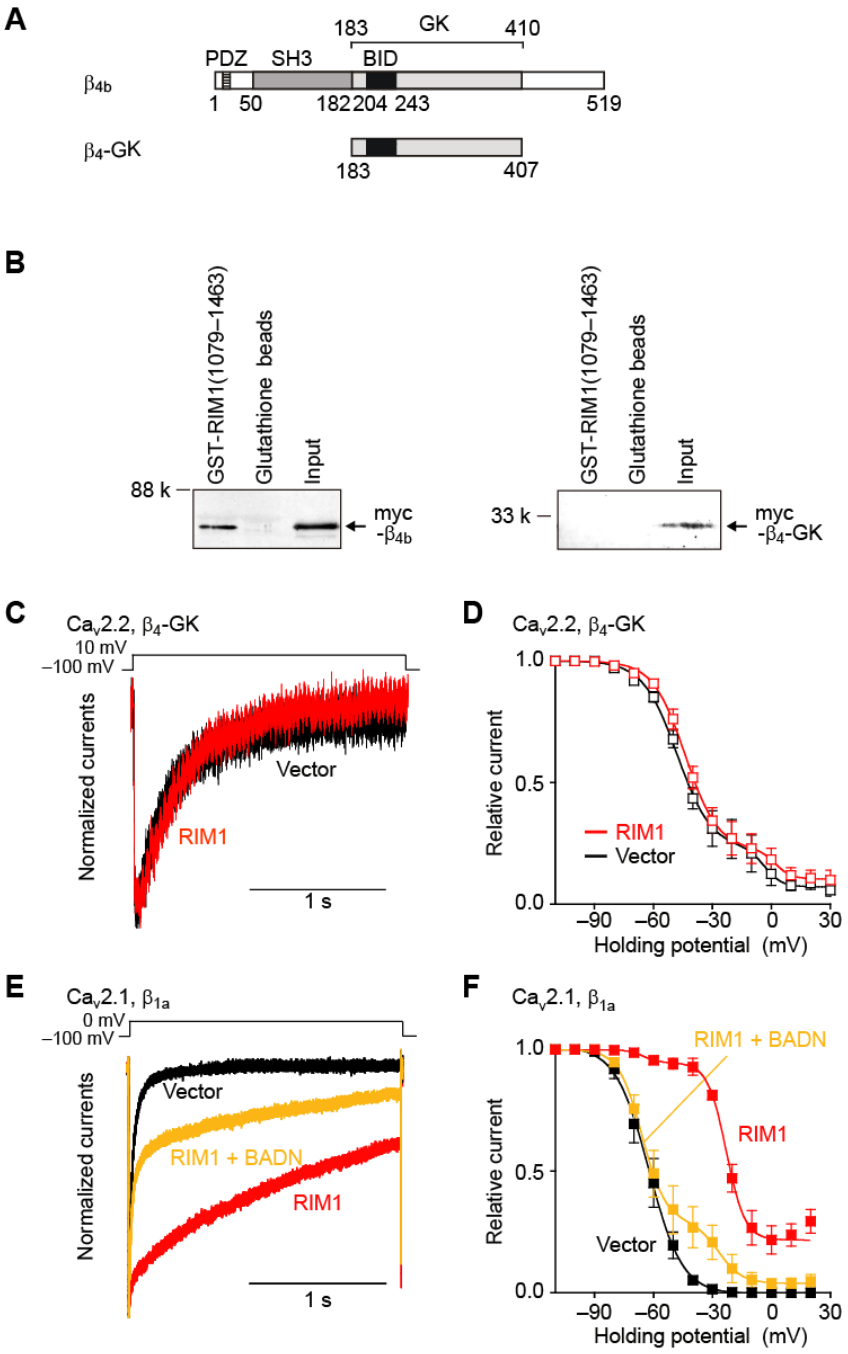

Fig. 6 Disruption of the RIM1α effects on VDCC inactivation by the b_4 GK domain and BADN. ***A***. Structure of β_4-GK in comparison with the WT β_{4b}. β_4-GK corresponds to 183-407 of rat β_{4b}. ***B***. Pulldown assay of β_4-GK constructs with RIM1α(1079-1463) GST fusion protein demonstrates that β_4-GK does not interact with RIM1α(1079-1463). cDNA of β_4-GK is subcloned in the expression plasmid pCMV-tag3. GST fusion proteins immobilized on glutathione-Sepharose beads are incubated with cell lysate obtained from myc-β_4-GK-expressing HEK293 cells. Bound proteins are analyzed by WB using anti-myc antibody. ***C***. Inactivation of $Ca_V2.2$ currents in BHK cells expressing $\alpha_2\delta$ and β_4-GK. For comparison of inactivation time courses before and after expression of RIM1α constructs, the peak amplitudes are normalized for Ba^{2+} currents elicited by 2-s pulses to 10 mV from a V_h of –100 mV. 10 mM Ba^{2+} is used as a charge carrier. ***D***. Inactivation curves of $Ca_V2.2$ currents in BHK cells expressing $\alpha_2\delta$ and β_4-GK. *E*. Dominant-negative effect of BADN for RIM1α effects on inactivation properties of VDCCs. Inactivation kinetics of $Ca_V2.1$ currents in BHK cells expressing a_2d and β_{1a}. ***F***. Inactivation curves of $Ca_V2.1$ in BHK cells expressing $\alpha_2\delta$ and β_{1a}. The differences at > –80 mV between vector and RIM1α, or those between RIM1α plus BADN and RIM1α are significant ($P < 0.05$).

Table 4 Effects of RIM1 or BADN on inactivation of $Ca_v2.1$ channel in BHK cells expressing α_2/δ and β_{1a}.

	Inactivation parameters					
	a	$V_{0.5}^{1st}$ (mV)	k^{1st} (mV)	*b*	$V_{0.5}^{2nd}$ (mV)	k^{2nd} (mV)
RIM1	0.06 ± 0.02 (4)***	−64.3 ± 1.9 (4)	−3.8 ± 0.8 (4)**	0.73 ± 0.07 (4)	−22.3 ± 0.9 (4)	−5.1 ± 0.8 (4)
vector	1.00 ± 0.00 (6)	−62.0 ± 3.1 (6)	−6.7 ± 0.2 (6)			
RIM1 + BADN	0.73 ± 0.08 (5)***###	−64.6 ± 2.4 (5)	−6.0 ± 0.8 (5)#	0.24 ± 0.06 (5)**	−29.2 ± 3.8 (5)	−8.4 ± 2.8 (5)

1) $^{**}P < 0.01$, $^{***}P < 0.001$ vs vector.

2) $^{\#}P < 0.05$, $^{\#\#\#}P < 0.001$ vs RIM1.

Table 5 Effects of RIM1 on inactivation of $Ca_v2.1$ channel in HEK cells expressing α_2/δ and β_1[1)].

	Inactivation parameters					
	a	$V_{0.5}^{1st}$ (mV)	k^{1st} (mV)	b	$V_{0.5}^{2nd}$ (mV)	k^{2nd} (mV)
vector (Ca^{2+})	1.00 ± 0.00 (5)	−41.0 ± 0.7 (5)	−5.8 ± 0.3 (5)			
RIM1 (Ca^{2+})	0.22 ± 0.05 (5)***	−35.5 ± 1.7 (5)	−7.4 ± 1.1 (5)	0.79 ± 0.05 (5)	−10.8 ± 1.4 (5)	−3.0 ± 0.2 (5)
vector (Ba^{2+})	1.00 ± 0.00 (5)	−48.5 ± 1.0 (5)	−5.8 ± 0.3 (5)			
RIM1 (Ba^{2+})	0.23 ± 0.02 (5)***	−45.5 ± 2.4 (5)	−6.4 ± 0.6 (5)	0.58 ± 0.01 (5)	−16.3 ± 1.7 (5)	−4.0 ± 0.6 (5)

1) $^{***}P < 0.001$ vs vector

Table 6 Effects of RIM1 or BADN on inactivation of VDCCs in PC12 cells[1)2)].

	Inactivation parameters					
	a	$V_{0.5}^{1st}$ (mV)	k^{1st} (mV)	*b*	$V_{0.5}^{2nd}$ (mV)	k^{2nd} (mV)
vector	0.23 ± 0.04 (5)	−42.7 ± 0.6 (5)	−7.0 ± 0.9 (5)	0.48 ± 0.04 (5)	−6.9 ± 0.9 (5)	−5.2 ± 0.5 (5)
RIM1	0.07 ± 0.01 (5)**	−40.7 ± 4.5 (5)	−6.4 ± 2.3 (5)	0.54 ± 0.03 (5)	−7.7 ± 1.3 (5)	−5.3 ± 0.4 (5)
BADN	0.36 ± 0.03 (6)**###	−48.5 ± 2.6 (6)	−7.8 ± 0.7 (6)	0.48 ± 0.04 (6)	−11.7 ± 1.3 (6)*#	−5.5 ± 0.6 (6)
siControl	0.21 ± 0.04 (6)	−36.8 ± 1.7 (6)	−7.9 ± 1.4 (6)	0.37 ± 0.04 (6)	−5.3 ± 1.0 (6)	−3.9 ± 0.5 (6)
siRIM1&RIM2	0.39 ± 0.04 (8)**	−38.6 ± 1.8 (8)	−8.4 ± 0.6 (8)	0.32 ± 0.02 (8)	−6.4 ± 1.5 (8)	−5.1 ± 0.6 (8)

1) $^{*}P < 0.05$, $^{**}P < 0.01$ vs vector.

2) $^{\#}P < 0.05$, $^{\#\#\#}P < 0.001$ vs RIM1.

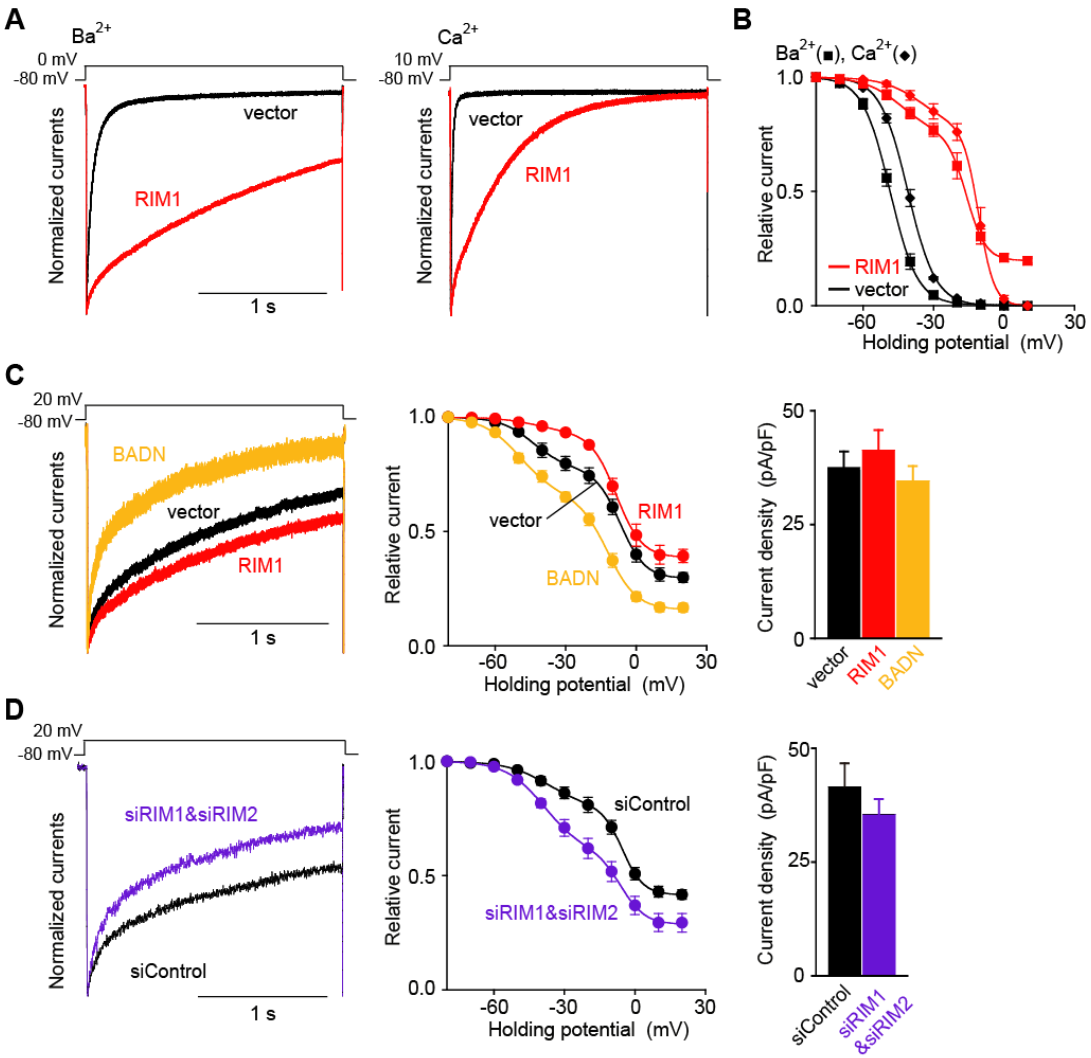

Fig. 7 Physiological relevance of effects of RIM1α on inactivation properties of VDCCs.

A. Effects of RIM1α on inactivation time courses of Ba^{2+} and Ca^{2+} currents in HEK cells expressing $Ca_v2.1$, α_2/δ and β_1. For comparison of inactivation time courses before and after expression of RIM1 constructs, the peak amplitudes are normalized for Ba^{2+} (left) and Ca^{2+} currents (right) elicited by 2-s pulses to 0 and 10 mV, respectively, from a V_h of –80 mV. ***B***. Inactivation curves for Ba^{2+} and Ca^{2+} currents in HEK cells expressing $Ca_v2.1$, α_2/δ and β_1. See **Table 6** for statistical significance of the differences between vector and RIM1. ***C***. Effects of RIM1 and BADN on the inactivation properties of native VDCCs in PC12 cells maintained for 7-9 culture passages. Left: normalized currents recorded from PC12 cells transfected with vector, RIM1α, and BADN. Middle: inactivation curves induced by 2-s holding potential (V_h) displacement. See **Table 7** for statistical significance of the differences among vector, RIM1, and BADN. Right: comparison of current densities at 10 mV (n = 18, 15, and 9 cells for vector, RIM1α, and BADN, respectively). ***D***. Acceleration of inactivation by coapplication of siRNAs specific for RIM1 and RIM2 (siRIM1 & siRIM2) in VDCC currents recorded from PC12 cells. PC12 cells were maintained for 2-3 culture passages. Left: normalized currents evoked by step pulses to 20 mV. Middle: inactivation curves

induced by 2-s V_h displacement. See **Table 7** for statistical significance of the differences between control GAPDH siRNA (siControl) and siRIM1 & siRIM2. Right: comparison of current densities at 10 mV (n = 6 and 8 cells, for siControl and siRIM1 & siRIM2, respectively). Data points are mean ± S.E.M.

Table 5). When 5 mM Ca^{2+} was used as a physiological charge carrier capable of inducing both Ca^{2+}-dependent and voltage-dependent inactivation (38), RIM1α still exerted prominent suppressive effects on inactivation, slowing the speed and shifting the voltage dependence toward depolarizing potentials in P/Q-type currents expressed in HEK cells (Fig 7*A*, *B*; and Table 6). Importantly, in rat pheochromocytoma PC12 neuroendocrine cells in which diverse high voltage-activated types of VDCCs have been characterized in detail (35, 42) (Fig. 8*C*, *D*), BADN or co-application of siRNAs specific for RIM1 and RIM2 accelerated inactivation and shifted the inactivation curve toward the hyperpolarizing direction (Fig. 7*C*, *D*, Table 7, see Fig. 8*A* for the expression suppression of RIMs in PC12 cells). This supports a physiologically significant role for RIM-mediated VDCC modulation via the β subunit. Notably, as observed in RIM1α-expressing cells, voltage-dependent inactivation of presynaptic VDCC currents at membrane potentials ≥ –40 mV was demonstrated in a previous report (39). Thus, RIM1α exerts strong effects on the kinetics and voltage dependence of inactivation of VDCC currents.

RIM1α effects on other functional current parameters such as voltage dependence of activation (Fig. 9*A*), activation kinetics (Fig. 9*B*), and current densities at different voltages in current-voltage relationships (Fig. 9*C*, *D*), distinguish VDCCs into two different groups (Table 1). In β_{4b}-expressing BHK cells, the current densities of N- and P/Q-type channels were significantly augmented by RIM1α (Fig. 9*C*, *D*), while those of the R- and L-type ($Ca_v1.2$) channels were unaffected by RIM1α (Fig. 9*D*). In P/Q-type, the RIM1α C-terminal region (1079-1463), that carries the β-association site, was sufficient to enhance current density (Fig. 9*C*). By contrast, activation speeds were significantly decelerated (Fig. 9*B*) and activation curves were shifted toward positive potentials by RIM1α in R- and L-type, but not in N- and P/Q-type currents (Fig. 9*A*). When β_{4b} was replaced with other β isoforms, the augmentation of P/Q-type current densities by RIM1α was

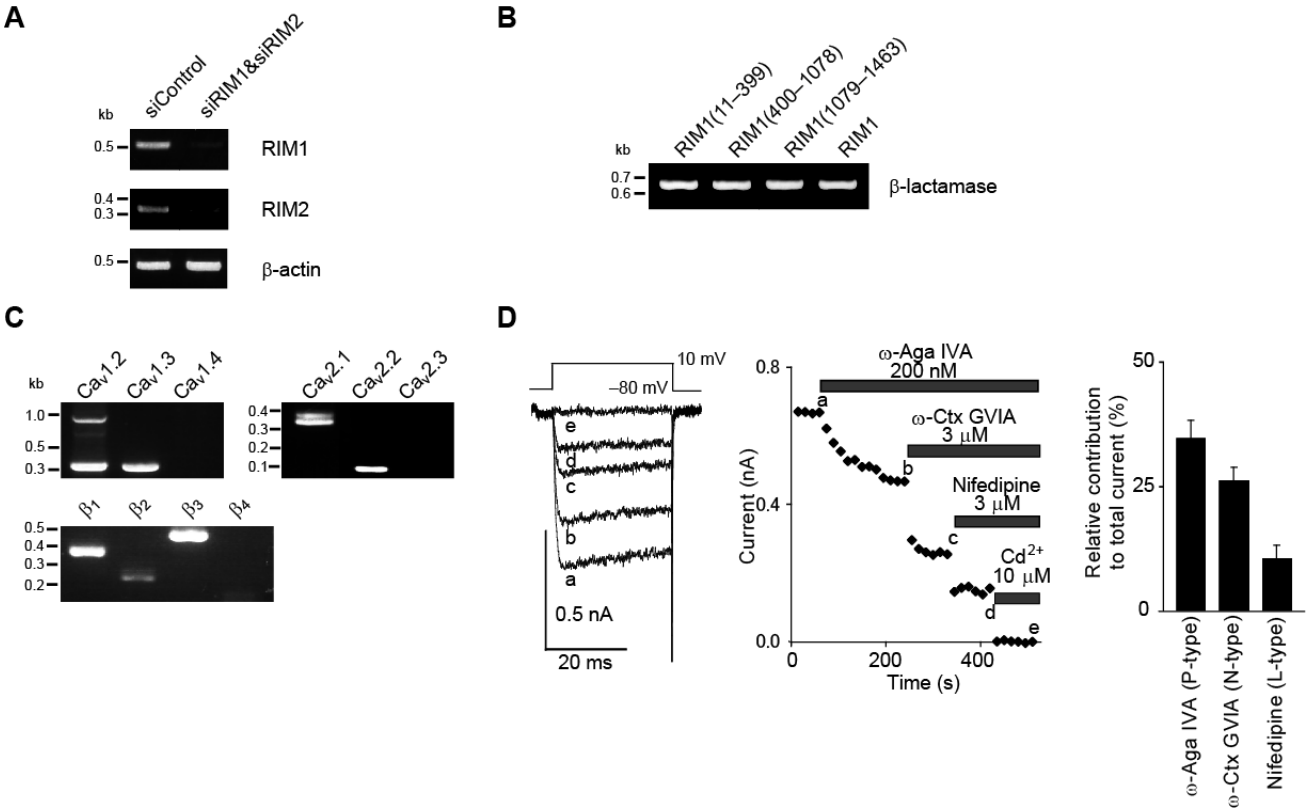

Fig. 8 Molecular and physiological characterization of PC12 cells. ***A***. RT-PCR analysis of RIM1 and RIM2 RNA expression in PC12 cells treated with GAPDH siRNA (siControl) and combination of RIM1- and RIM2-specific siRNAs (siRIM1 and siRIM2). Primer sequences are indicated in **Table 9**. RT-PCR was performed using LA-PCR kit (TaKaRa), according to the manufacturer's information. ***B***. Transfection levels of cDNAs of RIM constructs are examined using PCR in PC12 cells. Primers are designed to amplify the lactamase gene in the pCI-neo vector (**Table 9**). PCR was carried out using LA-PCR kit. ***C***. RNA expression analysis of α_1 and β subunits using RT-PCR in PC12 cells. ***D***. Pharmacological dissection of high voltage-activated Ca^{2+} channel currents in PC12 cells. Left & Middle: time course of blockage of Ca^{2+} current by serial application of 200 nM ω-Aga IVA, 3 mM ω-Ctx GVIA, 3 mM Nifedipine, and 10 mM Cd^{2+} in PC12 cell. Right: summary of relative contributions of each current type.

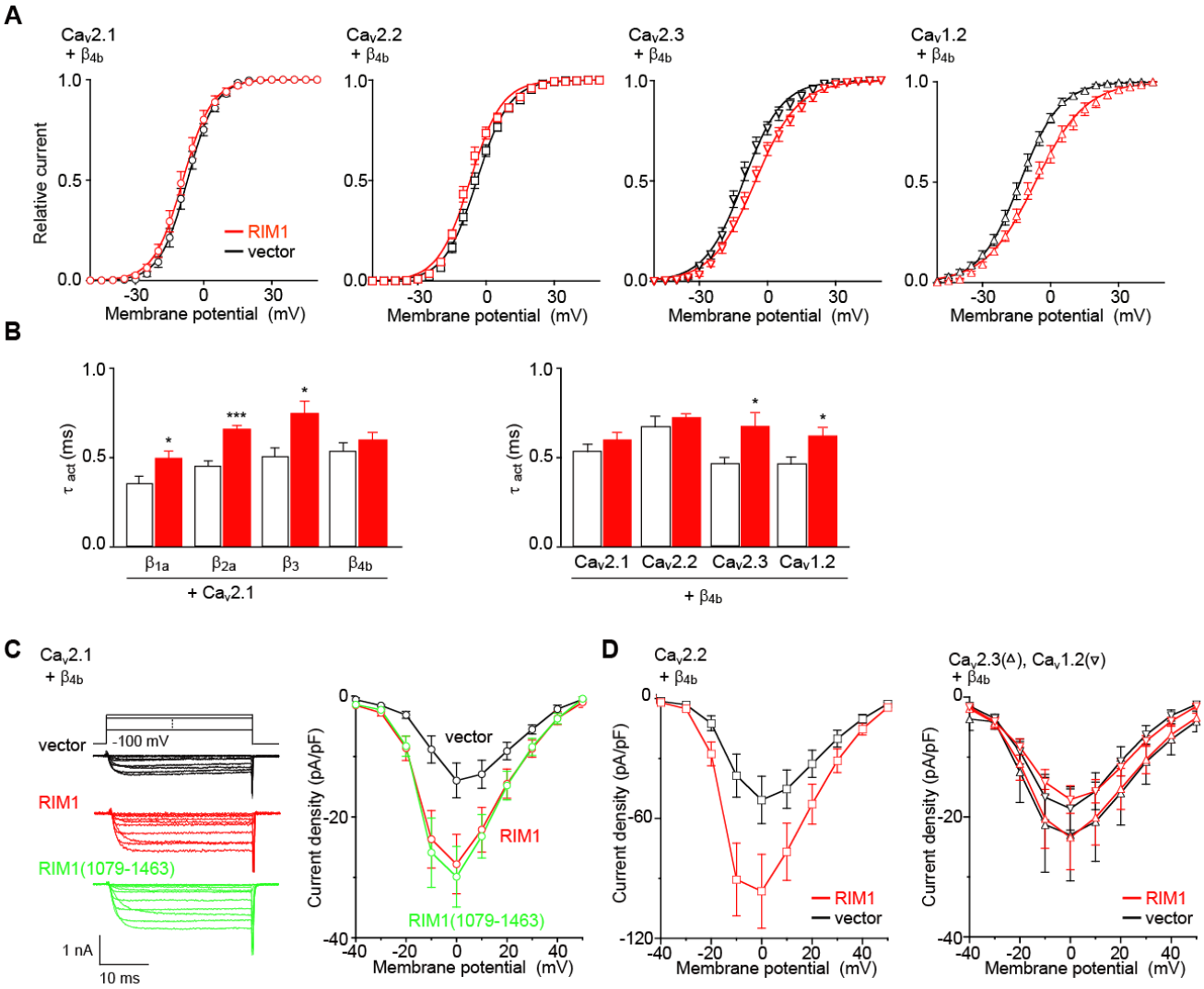

Fig. 9 Effects of RIM1α on the activation properties of VDCCs.

A. Effects of RIM1α on activation curves of Ca_v currents elicited in BHK cells expressing α_2/δ and β_{4b}. Tail currents elicited by repolarization to –60 mV after 5-ms test pulse from –50 to 50 mV are used to determine activation curves. See **Table 1** for statistical significance of the differences between vector and RIM1α. ***B***. Left: effects on activation speed of $Ca_v2.1$ channels containing various β-subunits. Time constants are obtained by fitting the activation phase of currents elicited by 5-ms test pulse to 20 mV with a single exponential function. Right: effects of RIM1α on activation speed of Ca_v currents at 20 mV in various VDCC types. $^{*}P < 0.05$ and $^{***}P < 0.001$. ***C***. Effects of RIM1α proteins on P/Q-type $Ca_v2.1$. Left: representative traces for Ba^{2+} currents upon application of test pluses from –40 mV to 50 mV with 10-mV increments in BHK cells expressing α_2/δ and β_{4b}. Right: current density-voltage (*I-V*) relationships of $Ca_v2.1$. The V_h is –100 mV. See **Table 2** for statistical significance of the differences between vector and RIM1α, or RIM1α(1079-1463). ***D***. *I-V* relationships of $Ca_v2.2$ (left) and $Ca_v2.3$ or $Ca_v1.2$ (right) in BHK cells expressing α_2/δ and β_{4b}. The V_h is –100 mV for $Ca_v2.2$ or $Ca_v1.2$, and –110 mV for $Ca_v2.3$. **Table 1** for statistical significance of the differences between vector and RIM1α for $Ca_v2.2$.

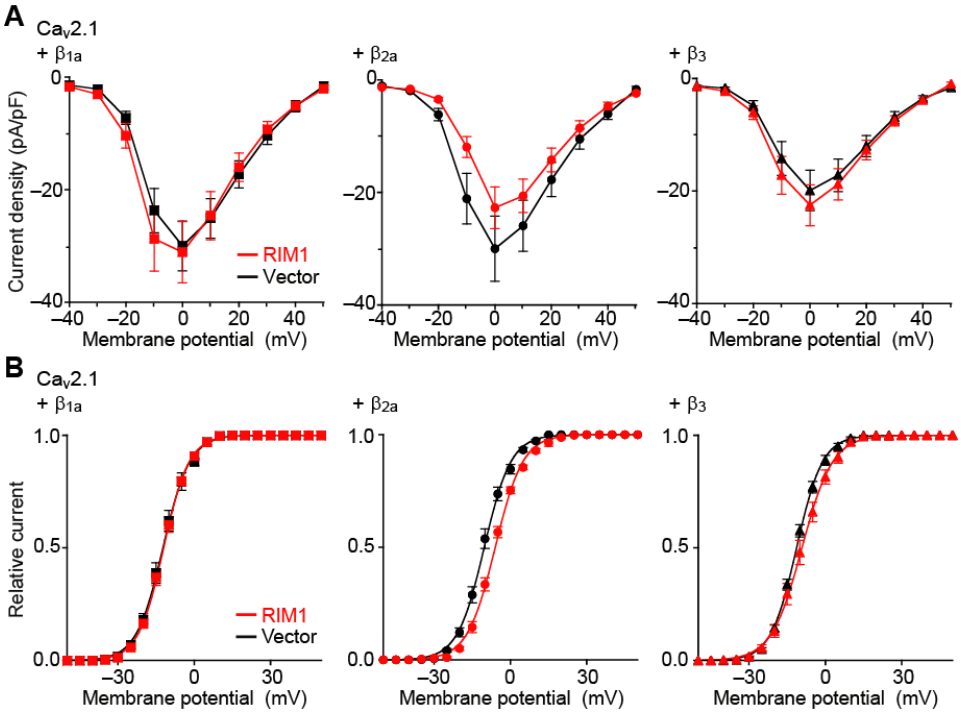

Fig. 10 Effects of RIM1 on the activation properties of VDCCs. ***A***. *I-V* relationships of $Ca_v2.1$ channels in BHK cells expressing $\alpha_2\delta$ and various β subunits. The V_h is –100 mV. ***B***. Activation curves. The differences between vector control and RIM1α are significant at membrane potentials from –25 to +5 mV for β_{2a} are significant (P < 0.05).

abolished (Fig. 9*A*), whereas the effect of RIM1 on activation speed of P/Q-type was induced by the β-subunits other than β_{4b} (Table 2): activation was decelerated in the presence of β_{1a}, β_{2a}, and β_3 (Fig. 9*B*, left panel). The effect of RIM1 shifting the activation curve toward positive potentials was also elicited by β_{2a} in P/Q-type (Fig. 10*B*). Thus, N- and P/Q-type currents responded differently than R- and L-type ($Ca_v1.2$) currents to RIM1 in terms of activation kinetics, voltage dependence of activation, and current densities, perhaps reflecting different subcellular localizations or functions of these channel subsets.

Table 7 Effects of RIM1 constructs on current density, activation, and inactivation of $Ca_v2.1$ channel in BHK cells expressing α_2/δ and various β-subunits[1)].

Subunit combination		Current density (pA / pF)[2)]	Activation parameters			Inactivation parameters		
			$V_{0.5}$ (mV)	k (mV)	τ_{act} (ms)[3)]	a	$V_{0.5}$ (mV)	k (mV)
$Ca_v2.1$	vector	−30.0 ± 4.4 (11)	−12.3 ± 1.0 (6)	5.0 ± 0.2 (6)	0.35 ± 0.04 (5)	1.00 ± 0.00 (7)	−62.6 ± 1.9 (7)	−7.0 ± 0.3 (7)
+ β_{1a}	RIM1	−31.1 ± 5.5 (7)	−12.0 ± 0.7 (7)	4.9 ± 0.2 (7)	0.49 ± 0.04 (6)*	0.83 ± 0.07 (5)***	−21.6 ± 2.5 (5)***	−6.1 ± 0.9 (5)
+ β_{2a}	vector	−30.0 ± 5.8 (15)	−10.3 ± 0.9 (8)	5.0 ± 0.2 (8)	0.45 ± 0.03 (8)	1.00 ± 0.00 (13)	−47.4 ± 0.9 (13)	−6.2 ± 0.2 (13)
	RIM1	−22.7 ± 3.7 (6)	−6.0 ± 0.5 (6)***	5.4 ± 0.2 (6)	0.65 ± 0.02 (6)***	0.73 ± 0.05 (6)***	−18.4 ± 1.4 (6)***	−5.3 ± 0.6 (6)
+ β_3	vector	−19.9 ± 3.6 (16)	−11.3 ± 0.6 (8)	5.0 ± 0.3 (8)	0.50 ± 0.05 (8)	1.00 ± 0.00 (7)	−67.5 ± 1.4 (7)	−6.8 ± 0.3 (7)
	RIM1	−22.5 ± 3.6 (23)	−9.2 ± 1.3 (9)	5.6 ± 0.2 (9)	0.74 ± 0.07 (7)*	0.66 ± 0.05 (5)***	−13.2 ± 3.3 (5)***	−6.0 ± 0.5 (5)
+ β_{4b}	vector	−14.0± 2.9 (15)	−7.2 ± 1.2 (9)	5.7 ± 0.1 (9)	0.53 ± 0.05 (9)	1.00 ± 0.00 (12)	−45.9 ± 1.8 (12)	−7.5 ± 0.3 (12)
	RIM1	−27.8 ± 4.9 (18)*	−9.1 ± 1.6 (13)	5.6 ± 0.2 (13)	0.59 ± 0.04 (13)	0.70 ± 0.04 (6)***	−21.3 ± 1.2 (6)***	−5.6 ± 0.7 (6)
	RIM1(1079-1463)	−29.9 ± 5.0 (10)*						

1) $^{*}P < 0.05$, $^{***}P < 0.001$ vs vector.

2) Ba^{2+} currents evoked by depolarizing pulse to 0 mV from a V_h of -100 mV are divided by capacitance.

3) Activation time constants obtained from currents elicited by 5-ms test pulse to 20 mV. The activation phases are well fitted by a single exponential function.

Discussion

The present investigation reveals a novel physical association between the presynaptic AZ proteins RIM1 and VDCC β-subunits. The results of yeast two hybrid assay, *in vitro* binding assay, and coimmunoprecipitation experiments have identified a RIM1-VDCC complex formed by direct protein-protein interaction of the β-subunit with the α_1-subunit AID region and the RIM C-terminus 1079-1463 (Fig. 1). The colocalization of RIM1α with VDCC subunits at the plasma membrane and the presynapse, and the disruption of such localization and complex formation by the BADN protein (Fig. 3) strongly support physiological roles for the RIM1α-VDCC β-subunit complex. Further biochemical and functional analyses (Fig. 1 and Fig. 5) suggest that RIM1α(1079-1257) and RIM1α(1258-1463) are the primary β-subunit binding site and modulatory region, respectively, in the RIM1 protein. While the RIM1-β_4 interaction was shown in our experiments, RIM1 of wild-type and *lethargic* brains was indistinguishable by sucrose gradient profile (Fig. 2*A*, *D*). It has been previously reported that immunolocalization of $Ca_v2.1$ and $Ca_v2.2$ in the brain and properties of P-type VDCC currents in Purkinje neurons are indistinguishable between wild-type and *lethargic* mice (43). This has been attributed to the rescue of β_4 deficiency by reshuffling of remaining β_1, β_2, and β_3. We expect a similar compensatory mechanism may also occur in the RIM1-β interaction in *lethargic* mice. Therefore, the β_4 isoform is unlikely to exclusively mediate the RIM1α-VDCC association in the brain.

The RIM1α-β association may enables RIM1α to play a dual physiological role in neurotransmitter release: sustaining Ca^{2+} influx through the functional regulation of VDCCs and anchoring vesicles to VDCCs. Among the functional parameters of VDCCs, those which are related to voltage-dependent inactivation are most prominently modified by RIM1αthrough the β interaction (Fig. 5). Inactivation kinetics are markedly decelerated resulting in the predominance of high voltage inactivation and an inactivation-resistant current component in the 2-s prepulse protocol. It is possibly that inactivation properties of P/Q-type VDCC are similarly modulated by other RIM family members such as RIM2α, RIM3γ, or RIM4γ, which all carry the C_2B domain, suggest that this function is a common feature for the RIM family (5). Suppression by BADN of the RIM1α-mediated inactivation in both the recombinant (Fig. 6*E*, *F*) and native VDCCs (Fig. 7*C*) provides evidence that the RIM1 effect is in fact exerted through the RIM1α-β association, as described in our

model (Fig. 11). This is supported by our finding that the C-terminal β construct, which binds to α_1 (ref. 37) but not to RIM1α, failed to mediate RIM1α effects on N-type channels (Fig. 6). Although detailed molecular mechanisms underlying inactivation are yet to be elucidated, previous mapping of the molecular determinants for voltage-dependent inactivation kinetics to segment S6 of repeat I (IS6) (44) may suggest that RIM1α-β complexes bound to the I-II linker AID further act on adjacent IS6 to hinder its conformational transition to inactivation the inactivated state. Alternatively, RIM1α may immobilize the β-subunit and the process of inactivation by slowing the movement of the I-II loop (45, 46). When voltage-dependent inactivation is thus suppressed, the responses of Ca2+ sensors such as synaptotagmins to Ca2+ influx may be potentiated at depolarizing membrane potentials that induce voltage-dependent inactivation when RIM1 is absent. Interestingly, since RIM1α virtually abolished VDCC inactivation elicited by a train of AP waveforms (Fig. 5*F*), certain forms of synaptic depression via closed-state inactivation (36) may be minimized by the presence of RIM1 at AZs. Furthermore, the impact of the RIM1α-β association to delay VDCC inactivation may explain recent findings using the RIM1α knockout mouse demonstrating that RIM1α is important for the late stage asynchronous neurotransmitter release whereas synaptotagmin I is involved in the earlier synchronous release (12). With P/Q- and N-type channels, the RIM1α-β association significantly affected channel activity as well: current densities were nearly doubled by RIM coexpression (Fig. 9*C*, *D*). Thus, RIM1α can maintain and enhance depolarization-induced Ca^{2+} influx to support neurotransmitter release at presynaptic AZs.

Regarding the role of RIM1α in vesicle anchoring, our model (Fig. 11) proposes that synaptic vesicles may be situated in close proximity to VDCC complexes through simultaneous interactions of RIM1α with vesicle-associated Rab3 / Munc13 via the N-terminal Zn^{2+}-finger domain (41) and with the VDCC β-subunit via the C-terminal C_2B domain. Taking into consideration the direct RIM1α-Rab3 association and the regulation of tethering and/or priming of synaptic vesicles by Rab3 (ref. 41), it is likely that the RIM1α-β interaction underlies, at least in part, the maintenance of a close proximity between VDCCs and vesicles, thereby regulating the dynamic properties of synaptic transmission (3). In fact, it was previously reported (47) that the loss of UNC10/RIM caused a reduction in membrane-contacting synaptic vesicles

within 30 nm of the dense projection at *Caenorhabditis elegans* neuromuscular junctions. In our experiments, RIM1α and β-subunit targeting to the presynaptic site was observed after early synapse formation. It is important to note that the interaction of Mint and CASK with VDCC α_1-subunits via their C-termini have been implicated (24, 25) and may direct early channel targeting that precedes RIM1α-β-subunit complex formation. Furthermore, in RIM1α-defecient mice, the decay of excitatory postsynaptic currents (EPSCs) during 14 Hz trains of presynaptic stimulation is abolished (12), while the rate at which the readily releasable vesicle pool is refilled is indistinguishable between the wild-type and RIM1α mutant mice (12). These data suggest that RIM1α-mediated vesicle anchoring to VDCCs may enable a rapid depletion of vesicle pools such that available vesicles are exhausted leading to EPSC decay. In this scenario, RIM1α knockout would minimize rapid vesicle release enabling the readily releasable pool to be maintained and thus prevent EPSC decay. More recently, Schoch *et al.* (48) have reported mice deficient in both RIM1α and RIM2α show lethality due to, at least in part, defects in Ca^{2+}-triggered release despite normal AZ length and normal spontaneous neurotransmitter release. Combined, these studies support our model (Fig. 11), predicting a dual function for RIM1α in neurotransmitter release by coordinating the molecular constituents and Ca^{2+} signaling at presynaptic AZs via the VDCC β interaction.

Previous reports have demonstrated the functional impact of syntaxin, synaptosome-associated protein (SNAP-25), and synaptotagmin on VDCCs through physical association with the 'synprint' region in the II-III linker of α_1-proteins (19-21). Physical association of RIM directly via the C_2A domain with the synprint (10) (Fig. 1*A*) and indirectly via the RIM-binding protein (RIM-BP) with the C-terminal tail of α_1 have been also reported (49). However, RIM1α regulation of VDCCs may be independent of the synprint-mediated regulation or the RIM-BP-mediated association, because RIM1α(1079-1463), which lacks both the C_2A domain necessary for synprint binding (10) and the PXXP motif for the RIM-BP binding is still sufficient to inhibit VDCC inactivation (Fig. 5*A*, *C*). This is supported by our observation that the dominant negative β construct BADN (Fig. 6*E*, *F*) or replacement of wild-type β with a C-terminal truncation construct (Fig. 6*A-D*), is sufficient to disrupt RIM1α effects on inactivation. Syntaxin and SNAP-25 have been proposed to exert inhibition of VDCC-mediated Ca^{2+} influx via a hyperpolarizing shift of the inactivation curve in the

absence of vesicle docking at VDCC sites (19, 21), while our finding by contrast implies enhancement or maintenance of the Ca^{2+} influx via interaction with RIM1α during the docking of vesicles. Importantly, previous reports suggest that RIM1α is involved in the modification of the release apparatus at a late stage in the vesicle cycle (9), particularly in the post-docking step (50). Thus, the protein associations of VDCC α_1 and the VDCC β-RIM1α association may be distinct interactions that contribute at different stages of vesicle cycling to control the Ca^{2+} supply from the source, namely the VDCC, in addition to regulating the proximity between the Ca^{2+} source VDCC and the target Ca^{2+} sensors at the presynaptic AZ.

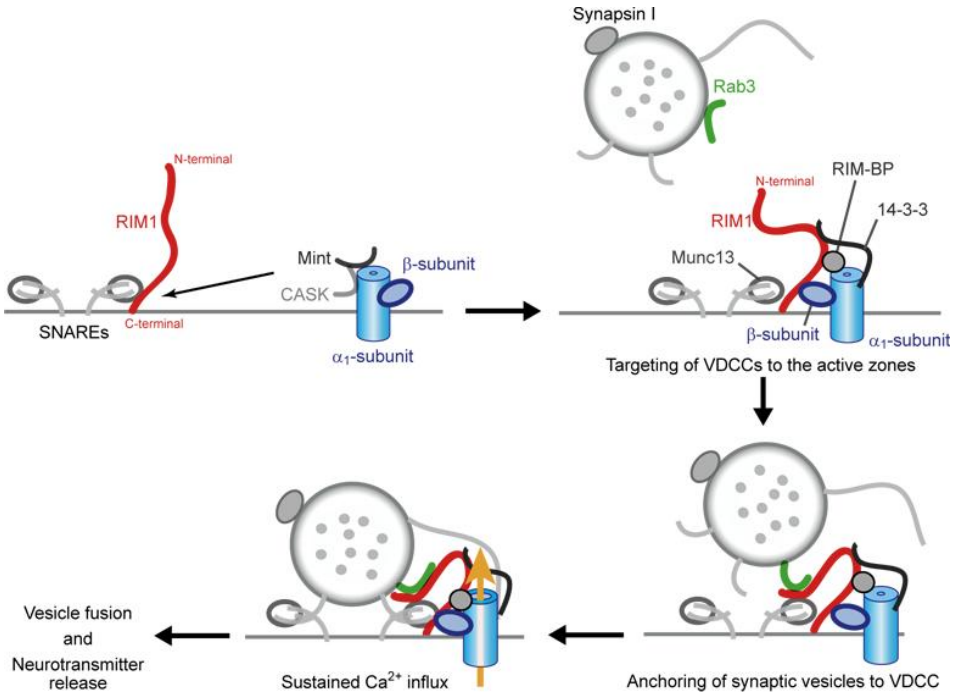

Fig. 11 A model detailing the putative role of the β subunit-RIM1α interaction at presynaptic AZs. Synaptic vesicles are anchored to presynaptic AZs through the association of RIM1α with β subunits, Rab3, and Munc13. Also, functional properties of neuronal VDCCs are significantly modulated by RIM1α through physical association with the β subunit, which can efficiently maintain Ca^{2+} influx through VDCC at AZs. These presynaptic processes regulated by the RIM1α-β complex can involve other important presynaptic proteins such as RIM-BP in the vesicle anchoring by mediating an indirect association of RIM1α with VDCC α_1. 14-3-3, which regulates VDCC inactivation, may contribute to anchoring via the same mechanism. Mint and CASK regulate presynaptic targeting of VDCCs via their association with α_1.

Materials and Methods

Yeast two-hybrid screening and β-galactosidase assay

Rat β_{4b}-subunit (GenBank accession number XM_215742) subcloned into pGBK-T7 was used as a bait to screen a mouse brain pACT2 library (Clontech) in the yeast strain AH109 according to the manufacturer's instructions (Clontech). 1.5 x 10^6 transformants plated to synthetic medium lacking adenine, histidine, leucine, and tryptophan. His^+ colonies were assayed for β-galactosidase activity by a filter assay. Of the transformants, 103 were His^+, of which 21 were also $LacZ^+$. Prey clone #2-5 encoding RIM1α (amino acids 1079-1463) (NM_053270) was isolated. Expression plasmids pGBK-T7 carrying β_{4b} or its mutants were constructed by PCR.

Molecular modeling of BADN

Molecular building and molecular dynamics calculations were performed with Insight II / Discover packaged in the context of the Molecular Simulations Inc (MSI) under the consistent valence force field (CVFF). Biopolymer modules based on the X-ray crystallographic data of β_2-subunit and AID complex (PDB ID: 1T3L) in RSCB protein data bank (PDB) were used. During molecular dynamics minimization around 1000 K, most of the structure except for hexa-peptide (GELNGG, Fig. 3*B*) was restrained. An energetically stabilized conformation was chosen.

Molecular cloning and construction of expression vectors

RIM1α (NM_053270) was cloned from mouse brain Marathon-Ready cDNA (Clontech) using PCR, and was subcloned into pCI-neo (Promega), the FLAG-tagged vector pCMV-tag2 (Stratagene), the myc-tagged vector pCMV-tag3 (Stratagene), the pDsRed-Monomer-N1 (Clontech), and the pIRES2-EGFP (Clontech). Rat β_{4b} (XM_215742) was subcloned into the same vectors. The rat β_{4b} construct, BADN, that carries ELNG (amino acid residues 388-391 of rabbit Cav2.1) with G flanking on both the N- and C-terminal sides for ENQ (380-382 of rat β_{4b}) (Fig.3), was created by using PCR, and was subcloned into pCI-neo. $Ca_v2.1$(I-II linker) (1-435) was constructed by PCR using pK4KBI-2 (ref. 53), and was subcloned into pCMV-tag2. Mouse

VAMP (NM_009497) was cloned using PCR from mouse brain Marathon-Ready cDNA (Clontech), and was subcloned into pEGFP-N1 (Clontech). Human caveolin-1 (NM_001753) was cloned using PCR from human lung Marathon-Ready cDNA (Clontech), and was subcloned into pEGFP-N1 (Clontech).

Cell culture and recombinant expression in HEK293 cells

HEK293 cells were cultured in Dulbecco's modified Eagle's medium (DMEM) containing 10% fetal bovine serum, 30 units/ml penicillin, and 30 μg/ml streptomycin. Transfection of cDNA plasmids was carried out using SuperFect Transfection Reagent (QIAGEN). The cells were subjected to electrophysiological measurements and confocal imaging (see below) 48-72 h after transfection.

Expression of recombinant Ca^{2+} channels in BHK cells

Rabbit β_{2a}-subunit (X64297) and rabbit β_3-subunit (X64300) were subcloned into pCI-neo to yield pCI-β_{2a} and pCI-β_3, respectively. BHK cells cultured as previously described (53) were transfected with pAGS-3a2 (ref. 53) and pCI-β_{2a} or pCI-β_3 using SuperFect (Qiagen), and were cultured in DMEM containing Geneticin (600 μg/ml) (Sigma) and Zeocin (600 μg/ml) (invitrogen), to establish BHK lines stably expressing α_2/δ and β_{2a}, or β_3. BHK lines stably expressing α_2/δ and β_{1a}, or β_{4b} and BHK6-2 stably expressing $Ca_v2.1$, α_2/δ and β_{1a} were described previously (53). These BHK cell lines were co-transfected with pK4K plasmids (53) containing cDNAs for α_1-subunits (pK4KBI-2, pK4KBII, pK4KBIII, pK4KC1) and expression plasmids carrying RIM1 constructs (pIRES2-EGFP-vector, pIRES2-EGFP-RIM1, pIRES2-EGFP-RIM1(1079-1463), pIRES2-EGFP-RIM1(1079-1257), pIRES2-EGFP-RIM1(1258-1463)), using Effectene Transfection Regent (Qiagen). The cells were subjected to measurements 72-96 h after transfection.

Production of GST fusion proteins and purified recombinat β_4-subunit proteins.

For production of GST fusion proteins for RIM1, cDNAs for RIM1 constructs and the GST were subcloned together into the pET23 vector (Novagen). The Rosetta strain (Novagen) of *Escherichia coli* was transformed by the expression vectors, and protein expression/purification was performed according to the

manufacturer's instruction (Novagen, GE Healthcare). For production of recombinant β_4-subunits, the gene encoding residues 47-475 of rat β_{4b}-subunit and the GST were subcloned into the pET23 vector (Novagen). The GST-β_4 proteins were purified by glutathione-Sepharose affinity column (GE Healthcare), and the GST tag was cleaved by incubation with thrombin (4 units/ml, Sigma) for 6 h at 4 °C. Resultant GST and thrombin were removed by glutathione-Sepharose and benzamidine-beads (Sigma) to obtain purified recombinant β_4-subunits. The purified recombinant of residues 47-410 (for disruption experiments) or 47-475 (for *in vitro* binding assay) of BADN was obtained using the same protocol as that for the β_4-subunit. These proteins were stored at –80 °C.

in vitro binding of the purified RIM1 GST fusion and recombinant β_4 proteins

RIM1 GST fusion proteins at various concentrations were incubated with 50 pM purified recombinant β_4-subunits for 3 h at 4 °C in PBS buffer containing 0.1 % NP40 and 50 μg/ml BSA, and then with glutathione-Sepharose beads for 1 h. The beads were centrifuged and washed twice with the PBS buffer. Proteins were boiled in SDS sample buffer and subject to 10 % SDS-PAGE, followed by western blotting (WB) with the anti-β_4 antibody raised against the peptide containing ENYHNERARKSRNRLS, and detected by enhanced chemiluminescence (Pierce). The densities of protein signals, obtained using NIH image under the linear relationship with the applied amount of proteins, were normalized to the densities from the maximal binding. Three independent experiments were performed.

GST-pulldown assay, and coimmunoprecipitation in HEK293 cells.

48 h after transfection, HEK293 cells were solubilized in NP40 buffer containing 150 mM NaCl, 1 % NP40, 50 mM Tris, 1 mM PMSF, 10 μg/ml leupeptin (pH8.0), then centrifuged at 17400 x *g* for 20 min. For pulldown assay, the cell lysate was incubated with glutathione-Sepharose beads bound with purified fusion proteins, then the beads were washed with NP40 buffer at 4 °C. The proteins retained on the beads were characterized by WB with anti-myc antibody (invitrogen). For coimmunoprecipitation, the cell lysate was incubated with anti-FLAG M2 monoclonal antibody (Sigma), then the immunocomplexes were incubated

with protein A-agarose beads (Santa Cruz) and washed with NP40 buffer. Immunoprecipitated proteins were characterized by WB with anti-myc antibody.

Partial purification, sucrose density fractionation, and immunoprecipitation of neuronal Ca^{2+} channel complexes from mouse brains

The Ca^{2+} channel complexes were partially purified from brains of C57B6 mice or *lethargic* mice (B6EiC3Sn-*a*/*A*-*Cacnb4*^{lh}/J, Jackson Laboratory) as previously reported (23). From the 50 mg microsomes, the complexes were extracted with solubilization buffer containing 50 mM Tris, 500 mM NaCl, a mixture of protease inhibitors, 1 % digitonin (Biochemica & Synthetica) (pH 7.4). After centrifugation at 142,000 x *g* for 37 min, solubilized proteins in the supernatant were then mixed with Heparin-agarose beads (Sigma). After washing with Buffer I containing 20 mM HEPES, 300 mM NaCl, a mixture of protease inhibitors, 0.1 % digitonin (pH7.4), and Buffer II containing 20 mM HEPES, 400 mM NaCl, a mixture of protease inhibitors, 0.1 % digitonin (pH 7.4), heparin-bound proteins were eluted with Buffer III containing 20 mM HEPES, 700 mM NaCl, a mixture of protease inhibitors, 0.1 % digitonin (pH 7.4). After elution, concentration of NaCl was diluted to 150 mM by addition of Buffer IV containing 20 mM HEPES, a mixture of protease inhibitors, 0.1 % digitonin (pH 7.4), then the sample was concentrated to 4 ml in an Ultrafree-15 centrifugal filter device (millipore).

The samples were applied to 5-40 % sucrose density gradient (Buffer V containing 50 mM Tris, 150 mM NaCl, a mixture of protease inhibitors, 0.1 % digitonin + 5-40 % sucrose (pH 7.4)). The gradients were centrifuged at 215,000 x *g* for 90 min. WB was performed using anti-RIM antibody (BD bioscience), anti-$Ca_v2.1$ antibody (Alomone), anti-syntaxin antibody (Sigma), or anti-β_4 antibody. The density of protein signals measured using NIH image were normalized through four to five independent experiments.

Anti-RIM1 antibody was prepared according to the paper by Wang *et al.* (4). For immunoprecipitation, partially purified neuronal VDCC complexes were incubated with anti-β_4 or anti-RIM1 antibody-bound protein A-agarose beads. Immunoprecipitated proteins were subject to WB with anti-RIM antibody or anti-$Ca_V2.1$ antibody. To disrupt physiological association of native RIM1 with VDCC β_4, the partially

purified VDCC complexes above were incubated with 200 nM GST fusion proteins for BADN and RIM1(1079-1463) for 8h at 4 °C, and subjected to the immunoprecipitation experiment.

Confocal imaging

PC12 cells were cultured as described previously (43). 32 h after transfection, HEK293 cells or PC12 cells were plated onto poly-L-lysine coated glass coverslips. 56 h after transfection, Hoechst 33342 (1 μg/ml, Dojindo) was added for 30 min to stain nuclei. The imaging was performed in modified Ringer's buffer that contained 130 mM NaCl, 3 mM KCl, 5 mM $CaCl_2$, 1.5 mM $MgCl_2$, 10 mM glucose, 10 mM HEPES (pH 7.4). Fluorescence images were acquired with a confocal laser-scanning microscope (Olympus FV500) using the 405-nm line of an laser diode for excitation and a 430-nm to 460-nm band-pass filter for emission (Hoechst 33342), the 488-nm line of an argon laser for excitation and a 505-nm to 525-nm band-pass filter for emission (EGFP or Venus), or the 543-nm line of a HeNe laser for excitation and a 560-nm long-pass filter for emission (DsRedmonomer). The specimens were viewed at high magnification using plan oil objectives (x60, 1.40 numerical aperture (NA), Olympus).

Total internal reflection fluorescence (TIRF) microscopy

PC12 cells co-transfected with 1 μg pVenus-N1-NPY and of expression plasmids for RIM1 constructs at the equal molar quantity (5.0 μg of RIM1(11-399), 5.7 μg of RIM1(400-1078), 5.0 μg of RIM1(1079-1463), or 7.5 μg of RIM1) and BADN (10 μg) using OptiFect (invitrogen) were plated onto poly-L-lysine-coated coverslips. PCR analysis of the transfection level reveals that the RIM plasmids are transfected at the equal level. The imaging was performed in modified Ringer's buffer. Fluorescence images of NPY-Venus were observed at the single vesicle level as previously reported (40). In brief, a high numerical aperture objective lens (Plan Apochromatic, 100x, numerical aperture = 1.45, infinity-corrected, Olympus) was mounted on an inverted microscope (IX71, Olympus), and incident light for total internal reflection illumination was introduced from the high numerical objective lens through a single mode optical fiber. A diode-pumped solid state 488-nm laser (kyma488, 20 milliwatt, MELLES GRIOT) was used for total internal fluorescence

illumination and 510-nm long pass filter as an emission filter. Images were captured by a cooled CCD camera (EM-CCD, Hamamatsu Photonics) operated with Metamorph (Molecular Devices). Area calculations and counting the number of fluorescent spots were performed using Metamorph softwares. We omitted the cells with disruption of distribution of vesicles by a dark spot with area > 10 μm^2 were omitted, to select the cells, in which vesicles were uniformly distributed, for the analyses. 10 μm^2 was adopted, because 10 μm^2 was the maximal dark circle area that can be located in between vesicles in the images from BADN-transfected cells with uniform vesicle distribution. The statistical analyses were performed using ANOVA followed by Fisher's test.

Immunostaining of cultured hippocampal neurons

Mouse hippocampal neurons were cultured as described (52). Myc-tagged RIM1, FLAG-tagged β_{4b} or EGFP-tagged $Ca_v2.1$ were transfected to neurons by lipofection at either 6 or 7 days *in vitro* (div), and 2 or 16 days later, the cells were fixed and immunostained using anti-FLAG M2 monoclonal and anti-myc polyclonal (Cell Signaling) antibodies, with Alexa488- and Alexa594-conjugated secondary antibodies (Molecular Probes). For quantification of $Ca_v2.1$ accumulation at varicosities, neurons were co-transfected, at 6 or 7 div, with EGFP-tagged $Ca_v2.1$ and mCherry (provided to H.B. by R.Y. Tsien). Immunofluorescent z-stack images for EGFP and mCherry were acquired using a Zeiss LSM510META confocal microscope, and a projection image was obtained from each of confocal z-stack images for EGFP and mCherry using a simple summation algorithm in order to retain all pixel fluorescence information. Somata and varicosities were manually cropped on the projection image of mCherry fluorescence to define individual regions of interests (ROIs). At least 10 adjacent varicosities were selected from a randomly chosen axonal process that could be traced directly from a mCherry-positive soma. Subsequently, fluorescence values of all pixels within each ROI in the image were integrated to calculate the total fluorescence for EGFP-$Ca_v2.1$ and mCherry. Integrated fluorescence at each varicosity was then normalized by dividing against the integrated soma fluorescence, in order to estimate the relative expression per each varicosity. Because this "relative expression factor" is heavily dependent on the sizes of the varicosities and the soma, we further calculated a

ratio between the "relative expression factor" for $Ca_v2.1$ and the "relative expression factor" for mCherry at each varicosity, and designated the ratio as "$Ca_v2.1$ accumulation index". Since mCherry is a space-filling volume marker, this ratio is indicative of volume-independent $Ca_v2.1$ enrichment at each varicosity. Statistical analysis was carried out by a Kolmogorov-Smirnov test between either 22 div and + RIM1(1079-1463) samples, or between 22 div and + BADN samples.

Whole-cell recordings

Whole-cell mode of the patch-clamp technique was performed on BHK cells or PC12 cells at room temperature (22-25 °C) as previously described (53). Pipette resistance ranged from 2 to 3.5 megohm. The series resistance was electronically compensated, and both the leakage and the remaining capacitance were subtracted by a –P/4 method. Currents were sampled at 100 kHz after low pass filtering at 8.4 kHz (3 db) in the experiments of activation kinetics, otherwise sampled at 10 kHz after low pass filtering at 2.9 kHz (3 db). An external solution contained 3 mM $BaCl_2$, 155 mM tetraethylammonium chloride (TEA-Cl), 10 mM HEPES, 10 mM glucose (pH adjusted to 7.4 with tetraethylammonium-OH). For current recordings in PC12 cells, an external solution contained 10 mM $BaCl_2$, 153 mM TEA-Cl, 10 mM HEPES, 10 mM glucose (pH adjusted to 7.4 with TEA-OH). The pipette solution contained 95 mM CsOH, 95 mM Aspartate, 40 mM CsCl, 4 mM $MgCl_2$, 5 mM EGTA, 2 mM $ATPNa_2$, 5 mM HEPES, 8 mM creatine phosphate (pH adjusted to 7.2 with CsOH). To characterize Ca^{2+}-dependent inactivation of $Ca_v2.1$ expressed in HEK cells, external solutions contained 5 mM $CaCl_2$ or $BaCl_2$, 153 mM TEA-Cl, 10 mM HEPES, 10 mM glucose (pH adjusted to 7.4 with tetraethylammonium-OH (TEA-OH)). The pipette solution contained 135 mM Cs-$MeSO_3$, 5 mM CsCl, 0.5 mM EGTA, 5 mM $MgCl_2$, 4 mM $ATPNa_2$ and 10 mM HEPES (pH adjusted to 7.2 with CsOH).

Single-channel recording

The cell-attached patch recording technique was performed (53). Patch electrodes had resistance of 5-8 megohms. The bath solution contained 150 mM KCl, 5 mM HEPES, 0.2 mM EGTA, 10 mM glucose (pH adjusted to 7.4 with KOH). The composition of the pipette solution was 110 mM $BaCl_2$ and 10 mM HEPES

(pH adjusted to 7.4 with $Ba(OH)_2$). Voltage steps with duration of 750 ms were given every 5 s from a V_h of –100 mV. The data, low-passed filtered at 1 kHz (3 db, 8-pole Bessel filter), were digitized at 10 kHz and analyzed using the pCLAMP 6.02 software. The records were corrected for capacitative and leakage currents by subtraction of the average of records without channel activity.

RNA analysis in PC12 cells

RNA expression of the α_1-subunits, β-subunits, RIM1, or RIM2 in PC12 cells was determined by RT-PCR using specific primers listed in Table 5.

Suppression of the action of endogenous RIM1 and RIM2 using specific siRNAs and BADN in PC12 cells

The sense siRNA sequences 5'-AAGAATGGACCACAAATGCTT-3' and 5'-AAGGTGATTGGATGGTATAAA-3' for rat RIM1, and 5'-AAGGCCCAGATACTCTTAGAT-3' and 5'-AAGAACTATCCAACATGGTAA-3' for rat RIM2 were used. To construct siRNA oligomers, the Silencer siRNA Construction Kit (Ambion) was used. The GAPDH siRNA (siControl) used was the control provided with the kit. We transfected the mixture of RIM1 and RIM2 siRNAs to PC12 cells using Lipofectamine^{TM} 2000. Suppression of RNA expression was confirmed using RT-PCR analyses. 8.0 μg pCI-neo-BADN or 8.0 μg pCI-neo-RIM1 was transfected as described above in the TIRF imaging. The cells treated with siRNAs or cDNA constructs were subjected to patch clamp measurements 72-96 h after transfection.

Statistical analysis

All data were expressed as means ± S.E.M. The data were accumulated under each condition from at least three independent experiments. The statistical analyses were performed using Student's *t*-test, Kolmogorov-Smirnov test, or ANOVA followed by Fisher's test.

Table 8 Antisense and sense PCR primers.

Gene	Orientation	Pair of primers for first PCR (5' to 3')	Pair of primers for nested PCR (5' to 3')
$Ca_v1.2$	Sense	AAGAAGAGAAGGAGAGAAAGAAGCTGGC	GATGCGGAGAGCCTGACCTCTGCCC
	Antisense	CATCCTCTTCACCTGCAGTGTCTGGG	CGGGGGCGTGGGCCCACAGGCATCTCG
$Ca_v1.3$	Sense	TGAGACACAGACCAAGCGAAGC	ACCTTCGACAACTTCCCACAGGCGCTCC
	Antisense	GTTGTCACTGTTGGCTATCTGG	GACCTCTGGTTTGTTGTTTTTTTTGTTTTCTAGG
$Ca_v1.4$	Sense	TCTTCATGCTCTGTGCCT	CCTAACCAGAGATTGGTCTATTCTGGGACCC
	Antisense	AGCCCTGCCTGGTCCTGA	CCTGGGATGGGCAAATCCTCACAACTGCCC
$Ca_v2.1$	Sense	CCAGTCTGTGGAGATGAGAGAAATGGG	CTGATGGCTACTCAGACAGCGAACACTACC
	Antisense	TTTGGAGGGCAGGTCACCCGATTG	CATGCTCAGATCTGTCCCCAGGCC
$Ca_v2.2$	Sense	GCCGTCTCAGCCGCGGCCTTTCT	CAATGCCCTGCTCCAGAAAGAGCCC
	Antisense	CAAAGGTGAGTGTATCCTCAGGC	CCAGACGCTGCCCTAGGTAAGGGTC
$Ca_v2.3$	Sense	ATCTTACTGTGGACCTTCGTGC	GCAGTCCTTTAAGGCTCTCCCCTATG
	Antisense	CTAGCGGTGGTGACATGAGAGTCAGC	CATACATCTCAGTGTAATGGATGCGGCC
β_1	Sense	TCCAGGGACCCTACCTTGTTTCC	GGGACCAGCCGCTGGACCGGG
	Antisense	CCTCCAGCTCATTCTTATTGCGC	GGCCCACCACCCTCCGCACAG
β_2	Sense	TCGGATCCGAAGAAGAACCTTGTCTGG	CCCAACACCGTTCTTCCTCAGCCACACACC
	Antisense	TCGAATTCAGTAGCGATCCTTAGATTTATGC	CCTAGTGCGGTGGCGAGGCTCC
β_3	Sense	GTGGTGTTGGATGCTGAC	GCACAGCTAGCCAAGACCTCACTGG
	Antisense	ATTGTGGTCATGCTCCGA	GGTCATGCCCGTTAGCACTGGG
β_4	Sense	CGTGGGCTCCACAGCTCTCTCACC	CTCTGGACTACAGAGTCAGCGGATGAGGC
	Antisense	CCACCAGAGGGTAGTGATCTCGGCTGTGC	GGAGGACAAGCGGTTCCTACTCTTGCGG
RIM1	Sense	CAGCATCAACAGTTATAGCTCGG	
	Antisense	CATCCAATCACCATGCTGGATAG	
RIM2	Sense	GGATCACAAATCCTTTATGGGAGTGG	
	Antisense	CACAGGATGGCTCTTTATCCCTAGAC	
β-actin	Sense	TTCTACAATGAGCTGCGTGTGGC	
	Antisense	CTCATAGCTCTTCTCCAGGGAGGA	
β-lactamase	Sense	GTTACATCGAACTGGATCTCAACAGC	
	Antisense	CGTGTAGATAACTACGATACGGGAG	

References

1. Zhai, R. G. and Bellen, H. J. (2004) *Physiology* **19**, 262-270
2. Atwood, H. L. (2006) *Science* **312**, 1008-1009
3. Neher, E. (1998) *Neuron* **20**, 389-399
4. Wang, Y., Okamoto, M., Schmitz, F., Hofmann, K., and Südhof, T. C. (1997) *Nature* **388**, 593-598
5. Wang, Y. and Südhof, T. C. (2003) *Genomics* **81**, 126-137
6. Wang, Y., Sugita, S., and Südhof, T. C. (2000) *J. Biol. Chem.* **275**, 20033-20044
7. Betz, A., Thakur, P., Junge, H. J., Ashery, U., Rhee, J. S., Scheuss, V., Rosenmund, C., Rettig, J., and Brose, N. (2001) *Neuron* **30**, 183-196
8. Ohtsuka, T., Takao-Rikitsu, E., Inoue, E., Inoue, M., Takeuchi, M., Matsubara, K., Deguchi-Tawarada, M., Satoh, K., Morimoto, K., Nakanishi, H., and Takai, Y. (2002) *J. Cell Biol.* **158**, 577-590
9. Schoch, S., Castillo, P. E., Jo, T., Mukherjee, K., Geppert, M., Wang, Y., Schmitz, F., Malenka, R. C., and Südhof, T. C. (2002) *Nature* **415**, 321-326
10. Coppola, T., Magnin-Luthi, S., Perret-Menoud, V., Gattesco, S., Schiavo, G., and Regazzi, R. (2001) *J. Biol. Chem.* **276**, 32756-32762
11. Castillo, P. E., Schoch, S., Schmitz, F., Südhof, T. C. and Malenka, R. C. (2002) *Nature* **415**, 327-330
12. Calakos, N., Schoch, S., Südhof, T. C. and Malenka, R. C. (2004) *Neuron* **42**, 889-896
13. Tsien, R. W., Ellinor, P. T. and Horne, W. A. (1991) *Trends Pharmacol. Sci.* **12**, 349-354
14. Takahashi, T and Momiyama, A. (1993) *Nature* **366**, 156-158
15. Wheeler, D. B., Randell, A. and Tsien, R. W. (1994) *Science* **264**, 107-111
16. Catterall, W. A. (1998) *Cell Calcium* **24**, 307-323
17. Ertel, E. A., Campbell, K. P., Harpold, M. M., Hofmann, F., Mori, Y., Perez-Reyes, E., Schwartz, A., Snutch, T. P., Tanabe, T., Birnbaumer, L., Tsien, R. W., and Catterall, W. A. (2000) *Neuron* **25**, 533-535
18. Sheng, Z.-H., Rettig, J., Takahashi, M. and Catterall, W. A. (1994) *Neuron* **13**, 1303-1313
19. Bezprozvanny, I., Scheller, R. H. and Tsien, R. W. (1995) *Nature* **378**, 623-626
20. Zhong, H., Yokoyama, C. T., Scheuer, T. and Catterall, W. A. (1999) *Nat. Neurosci.* **2**, 939-941

21. Spafford, J. D. and Zamponi, G. W. (2003) *Curr. Opin. Neurobiol.* **13**, 308-314

22. Nishimune, H., Sanes, J. R. and Carlson, S. S. (2004) *Nature* **432**, 580-587

23. Kang, M., Chen, C., Wakamori, M., Hara, Y., Mori, Y., and Campbell, K. P. (2006) *Proc. Natl. Acad. Sci. U.S.A* **103**, 5561-5566

24. Maximov, A., Südhof, T. C. and Bezprozvanny I. (1999) *J. Biol. Chem.* **274**, 24453-24456

25. Maximov, A. and Bezprozvany I. (2002) *J. Neurosci.* **22**, 6939-6952

26. Mori, Y., Friedrich, T., Kim, M. S., Mikami, A., Nakai, J., Ruth, P., Bosse, E., Hofmann, F., Flockerzi, V., and Furuichi, T. (1991) *Nature* **350**, 398-402

27. Bichet, D., Cornet, V., Geib, S., Carlier, E., Volsen, S., Hoshi, T., Mori, Y., and De Waard, M. (2000) *Neuron* **25**, 177-190

28. Varadi, G., Lory, P., Schultz, D., Varadi, M. and Schwartz, A. (1991) *Nature* **352**, 159-162

29. Béguin, P., Nagashima, K., Gonoi, T., Shibasaki, T., Takahashi, K., Kashima, Y., Ozaki, N., Geering, K., Iwanaga, T., and Seino, S. (2001) *Nature* **411**, 701-706

30. Hibino, H., Pironkova, R., Onwumere, O., Rousset, M., Charnet, P., Hudspeth, A. J., and Lesage, F. (2003) *Proc. Natl. Acad. Sci. U.S.A* **100**, 307-312

31. Vendel, A. C., Terry, M. D., Striegel, A. R., Iverson, N. M., Leuranguer, V., Rithner, C. D., Lyons, B. A., Pickard, G. E., Tobet, S. A., and Horne, W. A. (2006) *J. Neurosci* **26**, 2635-2644

32. Burgess, D. L., Jones, J. M., Meisler, M. H., and Noebels, J. L. (1997) *Cell* **88**, 385-392

33. Opatowsky, Y., Chen, C. C., Campbell, K. P. and Hirsch, J. A. (2004) *Neuron* **42**, 387-399

34. Khanna, R., Li, Q., Sun, L., Collins, T. J. and Stanley, E. F. (2006) *Neuroscience* **140**, 1201-1208

35. Plummer, M. R., Logothetis D. E. and Hess, P. (1989) *Neuron* **2**, 1453-1463

36. Patil, P. G., Brody, D. L. and Yue, D. T. (1998) *Neuron* **20**, 1027-1038

37. De Waard, M., Pragnell, M. and Campbell, K. P. (1994) *Neuron* **13**, 495-503

38. DeMaria, C. D., Soong, T. W., Alseikhan, B. A., Alvania, R. S. and Yue, D. T. (2001) *Nature* **411**, 484-489

39. Stanley, E. F. (2003) *Eur. J. Neurosci.* **17**, 1303-1305

40. Tsuboi, T. and Fukuda, M. (2006) *J. Cell Sci.* **119**, 2196-2203

41. Dulubova, I., Lou, X., Lu, J., Huryeva, I., Alam, A., Schneggenburger, R., Südhof, T. C., nd Rizo, J. (2005) *EMBO J*. **24**, 2839-2850

42. Liu, H., Felix, R., Gurnett, C. A., De Waard, M., Witcher, D. R., and Campbell, K. P. (1996) *J. Neurosci.* **16**, 7557-7565

43. Burgess, D. L., Biddlecome, G. H., McDonough, S. I., Diaz, M. E., Zilinski, C. A., Bean, B. P., Campbell, K. P., and Noebels, J. L. (1999) *Mol. Cell. Neurosci*. **13**, 293-311

44. Zhang, J. F., Ellinor, P. T., Aldrich, R. W., and Tsien, R. W. (1994) *Nature* **372**, 97-100

45. Stotz, S. C., Hamid, J., Spaetgens, R. L., Jarvis, S. E., and Zamponi, G. W. (2000) *J. Biol. Chem*. **275**, 24575-24582

46. Geib, S., Sandoz, G., Cornet, V., Mabrouk, K., Fund-Saunier, O., Bichet, D., Villaz, M., Hoshi, T., Sabatier, J., and De Waard, M. (2002) *J. Biol. Chem.* **277**, 10003-10013

47. Brehm, P. and Eckert, R. (1978) *Science* **202**, 1203-1206

48. Schoch, S., Mittelstaedt, T., Kaeser, P. S., Padgett, D., Feldmann, N., Chevaleyre, V., Castillo, P. E., Hammer, R. E., Han, W., Schmitz, F., Lin, W., and Südhof, T. C. (2006) *EMBO J*. **25**, 5852-5863

49. Hibino, H., Pironkova, R., Onwumere, O., Vologodskaia, M., Hudspeth, A. J., and Lesage, F. (2002) *Neuron* **34**, 411-423

50. Koushika, S. P., Richmond, J. E., Hadwiger, G., Weimer, R. M., Jorgensen, E. M., and Nonet, M. L. (2001) *Nat. Neurosci.* **4**, 997-1005

51. Wakamori, M., Yamazaki, K., Matsunodaira, H., Teramoto, T., Tanaka, I., Niidome, T., Sawada, K., Nishizawa, Y., Sekiguchi, N., Mori, E., Mori, Y., and Imoto, K. (1998) *J. Biol. Chem.* **273**, 34857-34867

52. Nonaka, M., Doi, T., Fujiyoshi, Y., Takemoto-Kimura, S. and Bito, H. (2006) *J. Neurosci.* **26**, 763-774

53. Wakamori, M. et al. Single tottering mutations responsible for the neuropathic phenotype of the P-type calcium channel. (1998) *J. Biol. Chem.* **273**, 34857–34867

Chapter 2

Rab3-interacting molecule γ isoforms lacking the Rab3-binding domain induce long-lasting currents but block neurotransmitter vesicle-anchoring in voltage-dependent P/Q-type Ca^{2+} channels

Abstract

Assembly of voltage-dependent Ca^{2+} channels (VDCCs) with their associated proteins regulates the coupling of VDCCs with upstream and downstream cellular events. Among the four isoforms of Rab3-interacting molecule (RIM1–4), we have previously reported that VDCC β-subunits physically interact with the long α isoform of the presynaptic active zone scaffolding protein RIM1 (RIM1α) *via* its C-terminus containing C_2B domain. This interaction cooperates with RIM1α-Rab3 interaction to support neurotransmitter exocytosis by anchoring vesicles in the vicinity of VDCCs and by maintaining depolarization-triggered Ca^{2+} influx as a result of marked inhibition of voltage-dependent inactivation of VDCCs. However, physiological functions have not yet been elucidated for RIM3 and RIM4, which exist only as short γ isoforms (γ-RIMs), carrying the C-terminal C_2B-domain common to RIMs but not the Rab3-binding region and other structural motifs present in the α-RIMs including RIM1α. Here, we demonstrate that γ-RIMs also exert prominent suppression of VDCC inactivation *via* direct binding to β-subunits. In the pheochromocytoma PC12 cells, this common functional feature allows native RIMs to enhance acetylcholine secretion, whereas γ-RIMs are uniquely different from α-RIMs in blocking localization of neurotransmitter-containing vesicles near the plasma membrane. γ-RIMs as well as α-RIMs show wide distribution in central neurons, but knockdown of γ-RIMs attenuated glutamate release in less extent than that of α-RIMs in cultured cerebellar neurons. The results suggest that sustained Ca^{2+} influx through suppression of VDCC inactivation by RIMs is a ubiquitous property of neurons, while the extent of vesicle-anchoring to VDCCs at the plasma membrane may depend on the competition of α-RIMs with γ-RIMs for VDCC β-subunits.

Introduction

Protein complexes play essential roles in various cellular responses including neurotransmission *via* synapses in the nervous system. In central synapses, the postsynaptic density is formed by protein complexes containing neurotransmitter receptors, signaling and cytoskeletal proteins, and scaffolding proteins such as PSD-95 (1), while active zones are formed by the cytomatrix and other proteins responsible for neurotransmitter release from presynaptic nerve terminals (2–6). For Ca^{2+} influx upon membrane potential depolarization to evoke neurotransmitter release, efficient coupling of VDCCs to protein machineries such as soluble N-ethylmaleimide-sensitive factor attachment protein receptors (SNAREs), mediating fusion of neurotransmitter-containing vesicles with presynaptic membranes, is critical (7–13). Thus, it is extremely important to identify protein associations and their functional significance in understanding neurotransmission.

Multiple types of VDCCs are distinguished on the basis of biophysical and pharmacological properties (14). In neurons, high voltage-activated (HVA) VDCC types such as the N-, P/Q-, R-, and L-types are essential for neurotransmitter release from presynaptic terminals (15–17). Furthermore, presynaptic Ca^{2+} channels were considered to serve as the regulatory node in a dynamic, multilayered signaling network that exerts short-term control of neurotransmission in response to synaptic activity (13). Biochemically, VDCCs are known as heteromultimeric protein complexes composed of the pore-forming α_1 and auxiliary subunits α_2/δ, β, and γ (18). The α_1-subunit, designated as Ca_V, is encoded by ten distinct genes, whose correspondence with functional subtypes has been largely elucidated (14, 18). VDCC complexes are primarily known for association with presynaptic and postsynaptic proteins including syntaxin, SNAP-25, synaptotagmin, CASK and Mint *via* interactions with the α_1-subunit (8, 9, 19–24). It was traditionally believed that anchoring Ca^{2+} channels close to the Ca^{2+} microdomain-dependent release machinery was the main reason for the physical interactions between channels and synaptic proteins. However, it is now becoming clear that these proteins additionally regulate channel activity. β-subunits interact with α_1 from the cytoplasmic side to enhance functional channel trafficking to the plasma membrane (25, 26) and to modify multiple kinetic properties (27, 28). Association with other proteins has also been revealed for β-subunits

(12, 29, 30, 31). Considering the cytoplasmic disposition of β-subunits, it is intriguing to investigate whether β-subunits are involved in targeting specific subcellular machinery to VDCC complexes at presynaptic active zones for neurotransmitter release through as yet unidentified protein interactions.

Originally identified as a putative effector of the synaptic vesicle protein Rab3 (32), RIM1 is part of the RIM superfamily, whose members share a common C_2B domain at their C-termini (33). With regard to RIM1 and RIM2, a long isoform α and short isoforms β and γ that lack the Rab3-interacting Zn^{2+}-finger domain are known, while only short γ forms are known for RIM3 and RIM4 (33, 34). A recent paper identified RIM3γ as a postsynaptic protein (35). RIM1 has been shown to interact with other presynaptic active zone protein components, including Munc13, ELKS (also known as CAST), RIM-binding protein (RIM-BP) and liprins, to form a protein scaffold in the presynaptic nerve terminal (2, 36–39). Recently, we reported that the association of RIM1 with β-subunits that supports neurotransmitter release *via* two distinct mechanisms: sustaining Ca^{2+} influx through inhibition of channel inactivation, and anchoring of neurotransmitter-containing vesicles in the vicinity of VDCCs (12). Importantly, presynaptic VDCC currents manifest resistance to voltage-dependent inactivation and exhibit inactivation largely dependent upon the magnitude of the inward Ca^{2+} current (40, 41), as observed for VDCCs associated with RIM1 (12). Furthermore, we demonstrated that the mouse RIM1 arginine-to-histidine substitution (R655H), which corresponds to the human autosomal dominant cone-rod dystrophy mutation (42), modifies RIM1 function in regulating VDCC currents elicited by the P/Q-type $Ca_V2.1$ and L-type $Ca_V1.4$ channels (43).

Genetic studies using mouse knockouts have shown that RIM1 is essential for different forms of synaptic plasticity in different types of synapses (39, 44, 45). In the CA1-region Schaffer collateral excitatory synapses and GABAergic synapses, RIM1 maintains normal neurotransmitter release and short-term synaptic plasticity. In excitatory CA3-region mossy fiber synapses, cerebellar parallel fiber synapses, and cortico-lateral amygdala synapses, RIM1 is necessary for presynaptic long-term plasticity. Using pharmacological and genetic approaches, a presynaptic signaling pathway *via* cAMP, protein kinase A, and RIM1α was elucidated as a general mechanism that underlies the long-term modulation of transmitter release at both excitatory and inhibitory synapses (46). In autapses, the RIM1α deletion significantly reduces the

readily releasable pool of vesicles, and it alters short-term plasticity and the properties of evoked asynchronous release (47). More recently, severe impairment of mouse survival by deletion of both RIM1α and RIM1β was reported (34). Electrophysiological analyses showed that the deletion of both RIM1α and RIM1β abolished long-term presynaptic plasticity, as does RIM1α deletion alone, but aggravated the impairment in synaptic strength and short-term synaptic plasticity that is caused by the RIM1α deletion. Mice deficient in both RIM1α and RIM2α showed lethality due to defects in Ca^{2+}-triggered release, despite normal presynaptic active zone length and normal spontaneous neurotransmitter release (48). In *Caenorhabditis elegans* (*C. elegans*), the loss of the single RIM homolog, UNC10, caused a reduction in membrane-contacting synaptic vesicles within 30 nm of the dense projection at neuromuscular junctions (49). In support of our hypothesis regarding VDCC-RIM1α association (12), a recent report states that RIM colocalizes with the Ca^{2+} channels and provides a mechanism to target vesicles to the presynaptic density through direct interaction with Rab3 at *C. elegans* presynaptic densities (50). However, despite this progress in genetic studies of RIMs, RIM2, RIM3, and RIM4 have yet to be characterized functionally (33, 35, 36, 51), and physiological roles played by RIM1 remain controversial (52).

Here, we analyze a physical and functional interaction between RIM family members and VDCC β-subunits. γ-RIMs as well as α-RIMs interact with four VDCC β-subunits and markedly suppress the voltage-dependent inactivation of P/Q-type $Ca_V2.1$ VDCC expressed in BHK cells, and are essential for regulation of Ca^{2+}-triggered exocytosis in PC12 cells and in cultured cerebellar neurons. Unlike α-RIMs, γ-RIMs suppress anchoring of neurotransmitter-containing vesicles to VDCCs.

Results

Direct interaction of RIMs with VDCC β-subunits. The C-terminal sequence of RIM1 (RIM1α (1231–1463)) that interacts with VDCCs is highly conserved among RIM family members (83%, 73% and 65% identity with RIM2α (1339–1572), RIM3γ (77–307) and RIM4γ (36–269), respectively) (Fig. 1*A*). We first tested the ability of RIM proteins to bind to the β-subunits of VDCCs. To test the importance of the conserved C-terminus, direct protein-protein interactions between RIMs (RIM1α (1079–1463), RIM2α

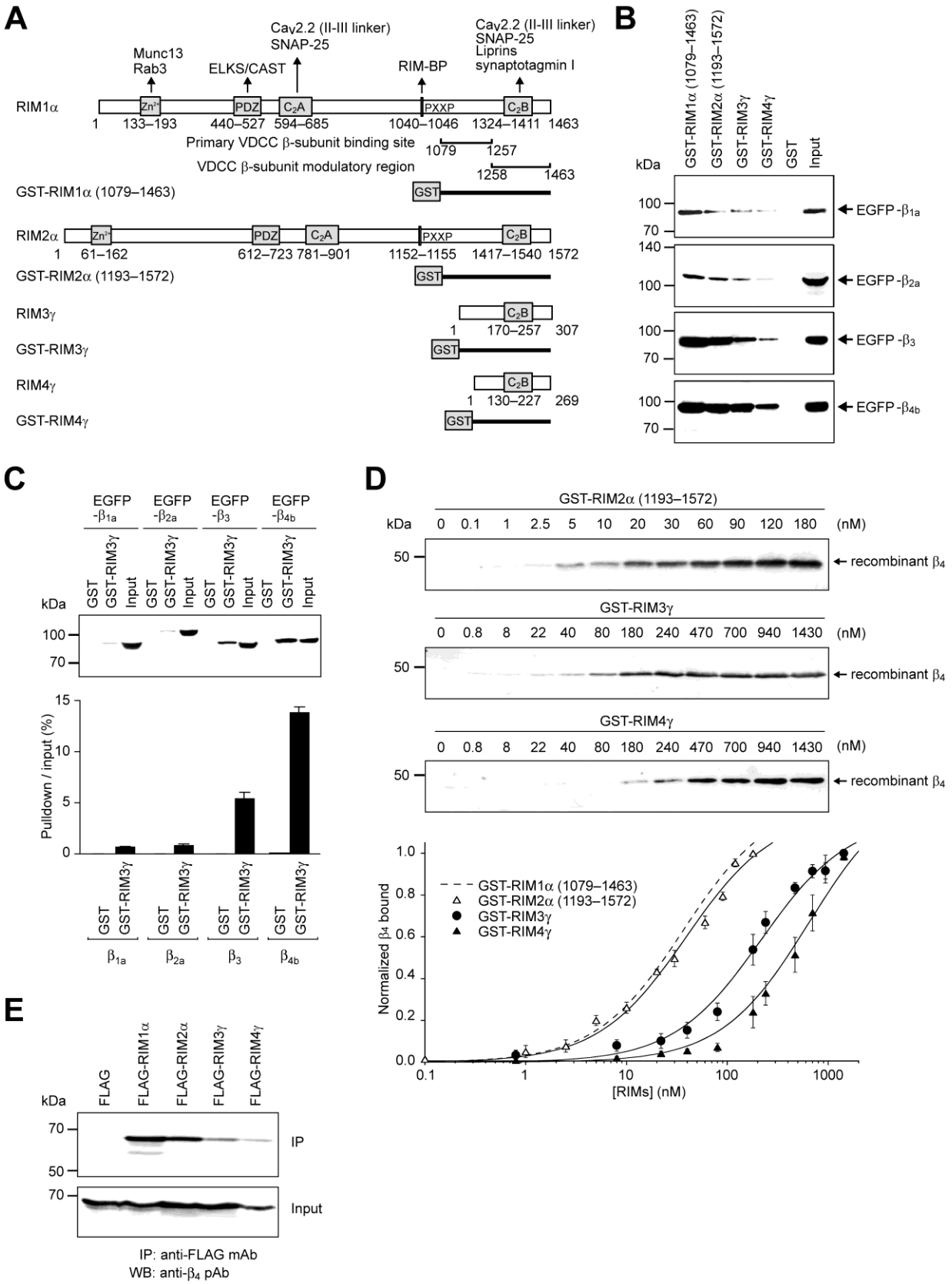
A
Munc13
Rab3
ELKS/CAST
CaV2.2 (II-III linker)
SNAP-25
RIM-BP
CaV2.2 (II-III linker)
SNAP-25
Liprins
synaptotagmin I
RIM1α
Zn2+
PDZ
C2A
PXXP
C2B
1 133–193 440–527 594–685 1040–1046 1324–1411 1463
Primary VDCC β-subunit binding site
1079 1257
VDCC β-subunit modulatory region
1258 1463
GST-RIM1α (1079–1463)
GST
RIM2α
1 61–162 612–723 781–901 1152–1155 1417–1540 1572
GST-RIM2α (1193–1572)
RIM3γ
1 170–257 307
GST-RIM3γ
RIM4γ
1 130–227 269
GST-RIM4γ
B
GST-RIM1α (1079–1463)
GST-RIM2α (1193–1572)
GST-RIM3γ
GST-RIM4γ
GST
Input
kDa
100
70
140
EGFP -β1a
EGFP -β2a
EGFP -β3
EGFP -β4b
C
EGFP -β1a
EGFP -β2a
EGFP -β3
EGFP -β4b
GST
GST-RIM3γ
Input
kDa
100
70
Pulldown / input (%)
15
10
5
0
β1a
β2a
β3
β4b
D
GST-RIM2α (1193–1572)
kDa
0 0.1 1 2.5 5 10 20 30 60 90 120 180 (nM)
50
recombinant β4
GST-RIM3γ
0 0.8 8 22 40 80 180 240 470 700 940 1430 (nM)
GST-RIM4γ
Normalized β4 bound
1.0
0.8
0.6
0.4
0.2
0.0
GST-RIM1α (1079–1463)
GST-RIM2α (1193–1572)
GST-RIM3γ
GST-RIM4γ
0.1
1
10
100
1000
[RIMs] (nM)
E
FLAG
FLAG-RIM1α
FLAG-RIM2α
FLAG-RIM3γ
FLAG-RIM4γ
kDa
70
50
IP
Input
IP: anti-FLAG mAb
WB: anti-β4 pAb

Fig. 1 Direct interaction of RIMs with VDCC β-subunits. *A.* Domain structures and GST fusion constructs of mouse RIMs. Arrows indicate molecules interacting with RIM1 at the following domains: Zn^{2+}, Zn^{2+} finger-like domain; PDZ, PDZ domain; C_2A and C_2B, first and second C_2 domains; PXXP, proline-rich region. Primary VDCC β-subunit binding site (RIM1α (1079–1257)) and VDCC β-subunit modulatory region (RIM1α (1258–1463)) are indicated according to ref. 12. *B.* Pulldown assay of β-subunits with GST fusion RIM constructs. GST fusion proteins immobilized on glutathione-Sepharose beads are incubated with cell lysates obtained from EGFP-β-transfected HEK293T cells. Bound proteins are analyzed by WB using antibody for GFP. *C.* A comparison of RIM3γ binding affinity among VDCC β-subunits. Upper panel: β-subunits are analyzed by GST-pulldown using GST- or GST-RIM3γ-coated beads. Input is 10% of amount used for pulldown. Lower panel: quantification of pulldown results, mean ± S.E.M. of three experiments. *D. In vitro* association between the purified GST-RIM fusion constructs and recombinant β_4-subunit (amino acid residues 47–475). GST-RIM proteins at various concentrations, incubated with β_4 (50 pM), are captured by glutathione-Sepharose beads. Captured β_4 proteins are examined by WB. The lower panel shows the quantitative densitometric analysis of bands shown in the upper panels. The saturation curves are subjected to the nonlinear least-squares curve-fitting method to evaluate the apparent K_d. The saturation curves for GST-RIM1α (1079–1463) is adapted from Kiyonaka *et al.* (12). *E.* Interactions of recombinant β_{4b} and RIMs in HEK293T cells. The interactions are evaluated by immunoprecipitation with antibody for FLAG, followed by WB with antibody for β_4.

(1193–1572), RIM3γ, and RIM4γ) and VDCC β-subunits (β_{1a}, β_{2a}, β_3, and β_{4b}) were examined by *in vitro* pulldown assays. GST fusion RIM proteins (Fig. 1*A*) immobilized on glutathione-Sepharose beads were incubated with cell lysate obtained from HEK293T cells transfected with each EGFP-tagged β-subunit. Bound proteins analyzed by WB using anti-GFP antibody revealed that the respective RIM isoforms bind to four VDCC β-subunit isoforms (Fig. 1*B*). To compare the affinity of binding to RIM3γ among VDCC β-subunits, amounts of β proteins bound to GST-RIM3γ were quantified and normalized to those of input β-subunits. The relative amounts of β-subunits pulled down by GST-RIM3γ suggested that RIM3γ has a higher binding affinity to β_3 and β_{4b}, the brain-type β-subunits (62, 63), compared with the skeletal and cardiac muscle-type β-subunits, β_{1a} and β_{2a} (64, 65) (Fig. 1*C*). Subsequent *in vitro* binding assays using purified preparation of recombinant β_4-subunit (amino acid residues 47–475) and GST-RIM proteins revealed a dissociation constant (K_d) of 39.3 ± 3.9 nM (n = 4) for RIM2α (1193–1572), which was similar to that for RIM1α (1079–1463) (35.1 nM) (adapted from Kiyonaka *et al.* (12)), while the K_d values for RIM3γ (233 ± 57

nM, n = 4) and RIM4γ (566 ± 63 nM, n = 3) were almost an order of magnitude higher than those of α-RIMs (Fig. 1*D*). Furthermore, coimmunoprecipitation experiments revealed an association between recombinant VDCC β_{4b}-subunit and FLAG-tagged RIMs in HEK293T cells (Fig. 1*E*). RIM1α and RIM2α were more efficiently coimmunoprecipitated with the β_{4b}-subunit compared with RIM3γ and RIM4γ, which is consistent with the results of the GST-pulldown assays. These results suggest that γ-RIMs directly interact with VDCC β-subunits with a lower binding affinity than those of α-RIMs.

Functional effects of RIMs on P/Q-type VDCC currents. To elucidate the functional significance of the direct interaction between RIMs and VDCC β-subunits, we examined whole-cell Ba^{2+} currents through recombinant P/Q-type VDCCs expressed as $\alpha_1\alpha_2/\delta\beta$ complexes containing the BI-2 variant of $Ca_V2.1$ (25) and β_{1a} in BHK cells. Prominent effects of RIMs on P/Q-type VDCC currents were observed for the parameters of voltage-dependent inactivation. Inactivation was markedly decelerated (Fig. 2*A*), while the voltage dependence of the inactivation was significantly shifted toward depolarizing potentials by RIMs: the inactivation curve showed a component susceptible to inactivation at high voltages (the half-inactivation potentials ($V_{0.5}$) ranged from –28 to –23 mV) and a non-inactivating component (Fig. 2*B* and Table 1). Furthermore, we coexpressed BADN, a dominant-negative suppressor β_{4b} fusion construct designed to disrupt the association of β-binding proteins such as RIMs with the functional VDCC complex without interfering with the α_1-β interaction (12). BADN significantly diminished the effect of RIMs on P/Q channel inactivation. The inactivation kinetics were markedly accelerated and biphasic inactivation curves were elicited (Fig. 2). In the presence of BADN, we observed components susceptible to inactivation at low voltages in inactivation curves ($V_{0.5}$ values ranged from –72 to –63 mV) and at high voltages ($V_{0.5}$ values ranged from –27 to –19 mV) (Fig. 2*B* and Table 1). Thus, the strong suppressive effect on voltage-dependent inactivation of P/Q-type VDCCs *via* interaction with β-subunits is a functional feature common to RIMs. RIM proteins differently modulated the activation kinetics of P/Q-type VDCCs (Fig. 3*A*). The time constant ($\tau_{activation}$) obtained by fitting the activation time course of inward currents with a single exponential was "bell-shaped" when plotted against different voltages. Activation showed the slowest speed at –15 mV in vector-, RIM1α-, and RIM2α-expressing cells and at –10 mV in RIM3γ- and RIM4γ-expressing cells.

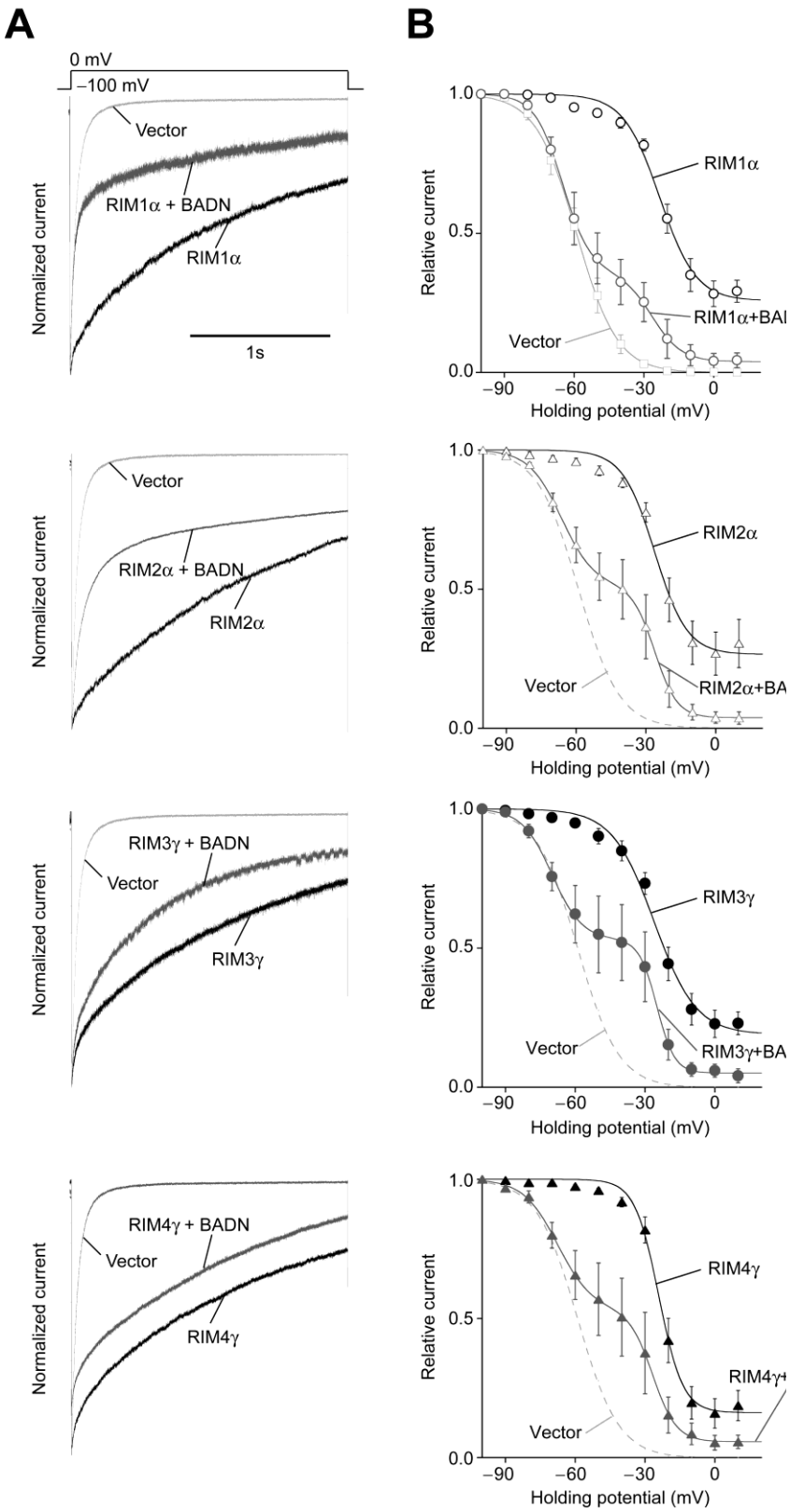

Fig. 2 Effects of RIMs on the inactivation properties of P/Q-type $Ca_V2.1$ channels. *A.* Effects of RIMs and BADN on inactivation of P/Q-type $Ca_V2.1$ currents in BHK cells expressing α_2/δ and β_{1a}-subunit. The peak amplitudes are normalized for Ba^{2+} currents elicited by 2-s pulses to 0 mV from a V_h of –100 mV. *B.* Effects of RIMs and BADN on voltage dependence of inactivation of $Ca_V2.1$. To determine the voltage dependence of inactivation, currents are evoked by 20-ms test pulse to 5 mV after the 10-ms repolarization to –100 mV following 2-s V_h displacements (conditioning pulses) from –100 mV to 20 mV with 10-mV increments. See Table 1 for statistical significance of the differences.

Table 1 Effect of RIMs or BADN on inactivation properties of P/Q-type VDCC in BHK cells expressing $Ca_v2.1$, α_2/δ and β_{1b}[1) 2) 3)].

	Inactivation parameters						
	a	$V_{0.5}^{Low}$ (mV)	K^{Low} (mV)	*b*	$V_{0.5}^{High}$ (mV)	K^{High} (mV)	1–*a*–*b*
Vector	1.00 ± 0.00 (12)	–58.8 ± 2.5 (12)	–7.1 ± 0.2 (12)	0.00 ± 0.00 (12)			0.00 ± 0.00 (12)
RIM1α	0.00 ± 0.00 (6) ***			0.73 ± 0.04 (6)***	–23.4 ± 0.9 (6)	–7.8 ± 1.3 (6)	0.27 ± 0.04 (6)***
RIM1α + BADN	0.67 ± 0.06 (4) ***###	–63.6 ± 2.9 (4)	–6.2 ± 1.0 (4)	0.29 ± 0.04 (4)***###	–26.7 ± 3.7 (4)	–6.4 ± 2.4 (4)	0.04 ± 0.03 (4)#
RIM2α	0.00 ± 0.00 (6) ***			0.75 ± 0.08 (6)***	–25.8 ± 1.8 (6)	–7.4 ± 1.5 (6)	0.25 ± 0.08 (6)***
RIM2α + BADN	0.52 ± 0.11 (6) ***###	–66.6 ± 2.0 (6)	–7.3 ± 0.3 (6)	0.45 ± 0.10 (6)***#	–26.8 ± 2.8 (6)	–3.4 ± 0.4 (6)	0.04 ± 0.02 (6)#
RIM3γ	0.00 ± 0.00 (5) ***			0.81 ± 0.02 (5)***	–27.6 ± 1.6 (5)	–7.7 ± 1.2 (5)	0.19 ± 0.02 (5)***
RIM3γ + BADN	0.44 ± 0.17 (5) ***###	–72.0 ± 2.5 (5)	–5.2 ± 0.7 (5)	0.49 ± 0.14 (5)***#	–19.3 ± 6.2 (5)	–1.0 ± 2.7 (5)	0.07 ± 0.03 (5)#
RIM4γ	0.00 ± 0.00 (6) ***			0.81 ± 0.04 (6)***	–25.0 ± 1.7 (6)	–6.2 ± 1.7 (6)	0.19 ± 0.04 (6)***
RIM4γ + BADN	0.46 ± 0.15 (5) ***###	–68.9 ± 1.7 (5)	–6.8 ± 0.5 (5)	0.49 ± 0.13 (5)***#	–27.0 ± 3.2 (5)	–4.6 ± 1.2 (5)	0.04 ± 0.02 (5) ***#

1) ***$P < 0.001$ versus vector.

2) #$P < 0.05$, ###$P < 0.001$ versus without BADN.

3) Numbers of cells analyzed are indicated in the parenthesis.

γ-RIMs significantly decelerated the activation kinetics at membrane potentials over –10 mV, while RIM1α only slightly decelerated the activation at membrane potentials over 10 mV, and RIM2α had no significant effect (Fig. 3*A* and Table 2). RIMs failed to exert effects on other functional parameters such

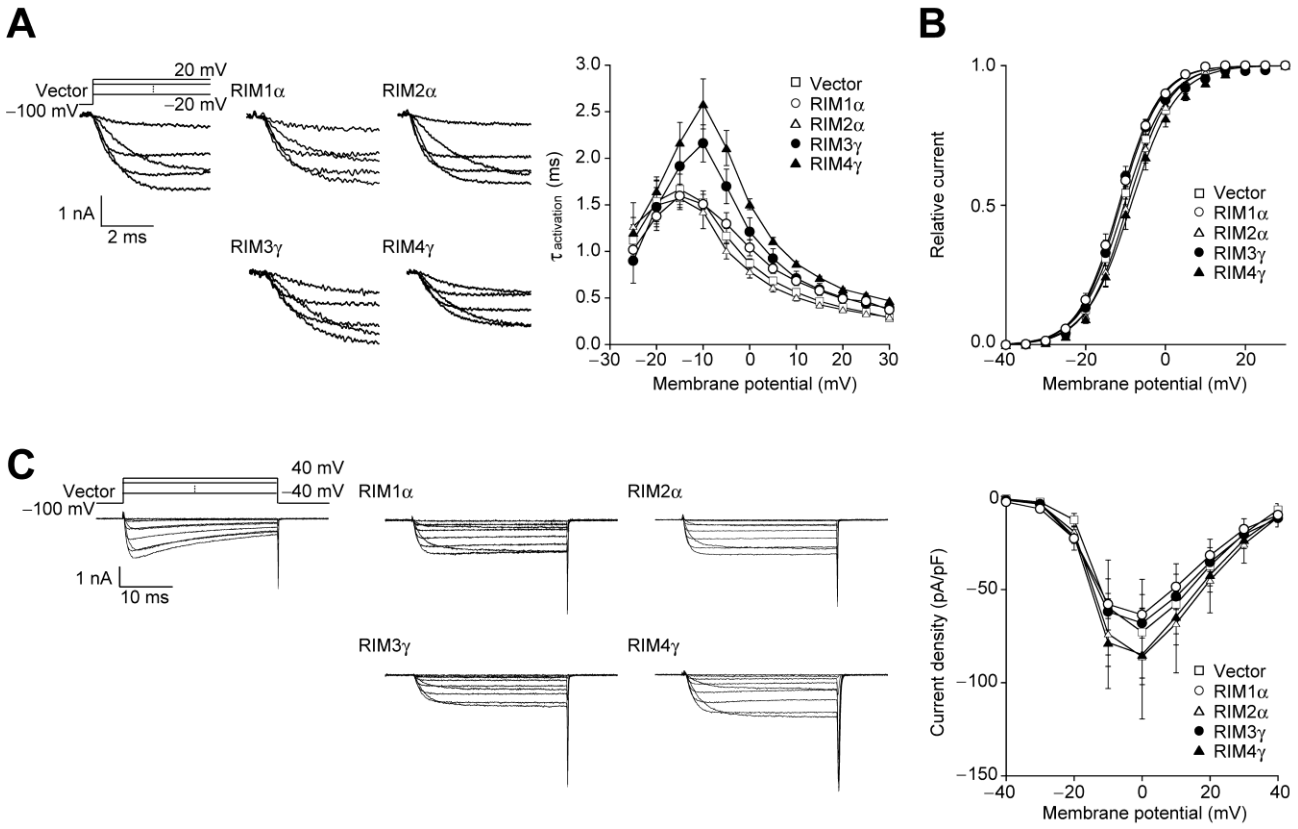

Fig. 3 Effects of RIMs on the activation properties of P/Q-type $Ca_V2.1$. *A.* Activation kinetics of P/Q-type $Ca_V2.1$ currents in BHK cells expressing α_2/δ and β_{1a}-subunit. Left, families of representative Ba^{2+} currents. Currents evoked by 5-ms step depolarization from –20 to 20 mV in 10-mV increments from a V_h of –100 mV are displayed. Right, activation time constants plotted as a function of test potential. The activation phases are well fitted by single exponential function at all potentials. Activation time constants ($\tau_{activation}$) are obtained from currents elicited by 5-ms step depolarization from –25 to 30 mV in 5-mV increments from a V_h of –100 mV. *B.* Activation curves of P/Q-type $Ca_V2.1$ currents. Tail currents elicited by repolarization to –60 mV after 5-ms test pulses from –40 to 30 mV are used to determine activation curves. *C.* Effects of RIMs on P/Q-type $Ca_V2.1$ currents. Left, representative traces for Ba^{2+} currents on application of test pluses from –40 mV to 40 mV with 10-mV increments from a V_h of –100 mV. Right, current density-voltage (*I-V*) relationships of $Ca_V2.1$. See Table 2 for statistical significance of the differences.

---

as the voltage-dependence of activation and the current densities at different voltages (Fig. 3*B*, *C* and Table 2). Thus, γ-RIMs more significantly affect P/Q-type VDCC currents in terms of activation kinetics compared with α-RIMs.

Table 2 Effects of RIMs on current density and activation of P/Q-type VDCC in BHK cells expressing $Ca_v2.1$, α_2/δ and β_{1b}[1) 2)].

	Current density (pA / pF)[3)]	Activation parameters			
		$V_{0.5}$ (mV)	k (mV)	$\tau_{activation\ (-10mV)}$(ms)[4)]	$\tau_{act\ (10mV)}$(ms)[5)]
Vector	−72.7 ± 28.3 (7)	−5.1 ± 0.2 (9)	10.5 ± 0.9 (9)	1.53 ± 0.12 (15)	0.56 ± 0.03 (15)
RIM1α	−63.5 ± 15.4 (11)	−4.9 ± 0.3 (7)	9.6 ± 1.3 (7)	1.54 ± 0.05 (6)	0.71 ± 0.05 (6)*
RIM2α	−86.1 ± 33.4 (7)	−4.9 ± 0.3 (5)	9.6 ± 1.3 (5)	1.43 ± 0.18 (6)	0.51 ± 0.04 (6)
RIM3γ	−68.0 ± 8.0 (12)	−5.4 ± 0.3 (10)	7.4 ± 1.3 (10)	2.16 ± 0.20 (7)*	0.71 ± 0.06 (7)*
RIM4γ	−84.9 ± 12.6 (9)	−5.1 ± 0.2 (12)	8.6 ± 1.1 (12)	2.58 ± 0.27 (10)***	0.87 ± 0.02 (10)***

1) $*P < 0.05$, $***P < 0.001$ versus vector.

2) Numbers of cells analyzed are indicated in the parenthesis.

3) Ba^{2+} currents evoked by depolarizing pulse to 0 mV from a V_h of −100 mV are divided by capacitance.

4) Activation time constants obtained from currents elicited by 5-ms test pulse to −10 mV. The activation phases are well fitted by a single exponential function.

5) Activation time constants obtained from currents elicited by 5-ms test pulse to 10 mV.

Tissue distribution of RIM3 and RIM4 expression. RNA preparations from different mouse tissues and brain regions were subjected to northern blot analyses using cDNA probes specific for RIM1, RIM2, RIM3, or RIM4 (Fig. 4*A*). RIM1 RNA was detected abundantly in the brain and at low levels in the eye. In the brain,

RIM1 RNA was most abundant in the cerebrum and cerebellum. The principal transcripts of RIM2 (~7.0 and ~5.5 kb) were detected at high level in the brain and eye and at lower levels in the kidney and testis. In the brain, RIM2 RNA transcripts were detected at the highest level in the cerebellum. RIM3 RNA was also detected at the highest level in the brain. In the brain, RIM3 RNA was detected at similar levels in the cerebrum, cerebellum, brainstem, and olfactory bulb. RIM4 RNA was also detected at the highest level in the brain. In the brain, RIM4 RNA was detected ubiquitously but at relatively low levels in the brainstem and olfactory bulb. Thus, compared with the relatively selective expression of RIM1 and RIM2, RIM3 and RIM4 are more widely distributed in the brain.

To quantify levels of expression, RNA preparations from different mouse tissues were subjected to real-time PCR analyses using RIM1-, RIM2-, RIM3-, and RIM4-specific primers (Fig. 4*B*). The brain was a tissue with high levels of expression common to all RIMs. This is consistent with northern blot analysis (Fig. 4*A*). Other tissues of high expression were the testis for RIM2, RIM3, and RIM4 and the eye for RIM2. Moderate levels of expression (>10% of the level in the brain) were observed in the dorsal root ganglion (DRG), eye, stomach, large intestine and testis for RIM1, in the DRG, stomach, small intestine, large intestine, kidney, and ovary for RIM2, and in almost all tested tissues except for the stomach and small intestine for RIM3, and in the eye, heart, thymus, and ovary for RIM4. To determine exactly which cell types express RIM3 and RIM4 mRNA in the CNS, sections of 8-week-old C57BL/6 mouse brains were subjected to *in situ* hybridization histochemistry using cRNA probes specific for RIM3 or RIM4. RIM3 and RIM4 RNAs were expressed in neurons throughout the CNS, supporting the widespread distribution of RIM3 and RIM4 (Fig. 5*A*). For both RIM3 and RIM4, regions rich in glial cells (*e.g.*, the white matter of the cerebral cortex and cerebellum) were not significantly labeled (Fig. 5*Aa* and *Ba*). In the hippocampus, pyramidal neurons of the CA1–CA3 region, granule cells of the dentate gyrus and interneurons exhibited positive labeling for RIM3 and RIM4 (Fig. 5*Ab* and *Bb*). In the neocortex, stainings for RIM3 and RIM4 was more intense in layers III and IV of the neocortex, in comparison with that in layers II, V, and VI (Fig. 5*Ac* and *Bc*). In the thalamus, staining for RIM3 was relatively strong (Fig. 5*Ad*), while RIM4 hybridization was relatively weak (Fig. 5*Bd*). These results support our northern blotting data indicating a relatively lower expression of RIM4 in the

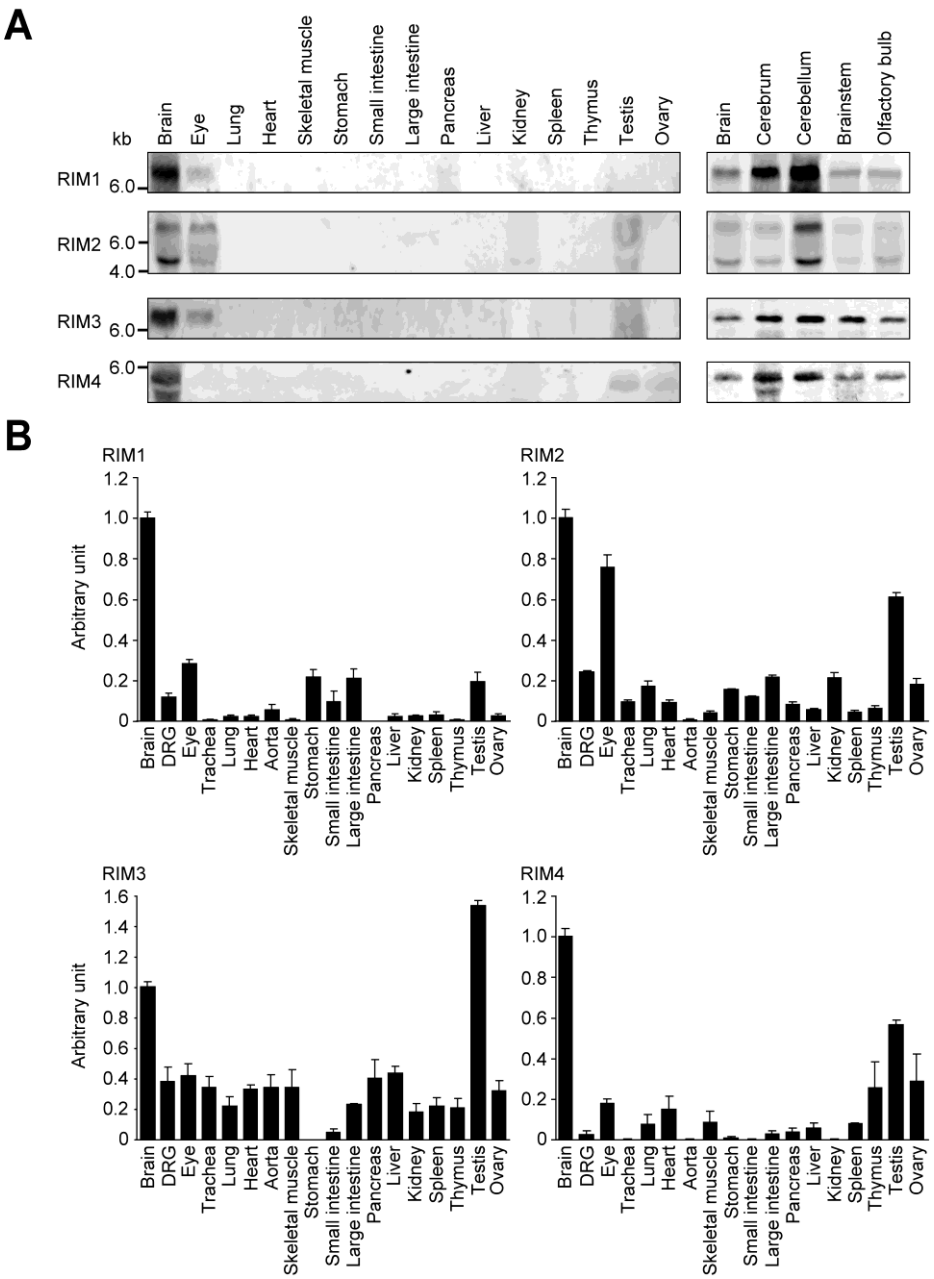

Fig. 4 Tissue distribution of RIMs. *A.* Northern blot analyses show the tissue distribution of RIM1, RIM2, RIM3, and RIM4 RNAs. Positions of molecular size markers are identified on the left. *B.* Real-time PCR analyses of the tissue distribution of RIM1, RIM2, RIM3, and RIM4 RNAs. The expression levels of RIM RNAs are normalized to those of 18S. The results are expressed relative to the brain given the arbitrary value of 1 and are means ± S.E.M. of at least three independent experiments.

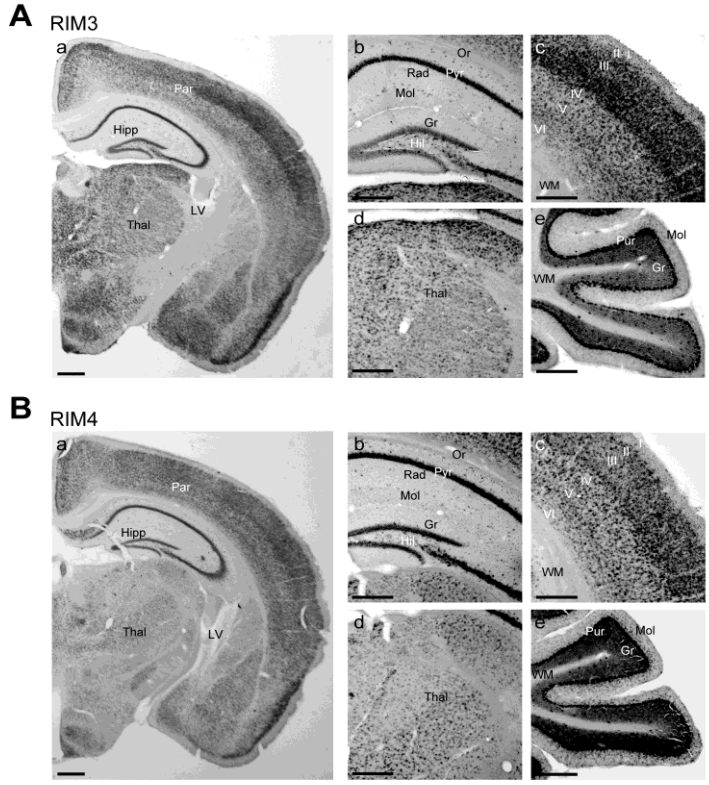

Fig. 5 Distribution of RIM3 and RIM4 RNA in the brain. *In situ* hybridization photomicrographs show expression of RIM3 (*A*) and RIM4 (*B*) RNA in the forebrain (*Aa*, *Ba*), hippocampal formation (*Ab*, *Bb*), cerebral cortex (*Ac*, *Bc*), thalamus (*Ad*, *Bd*), and cerebellar cortex (*Ae*, *Be*). I–VI, layers of cerebral cortex; Gr, granule cell layer of dentate gyrus (*Ab*, *Bb*) or cerebellar cortex (*Ae*, *Be*); Hil, hilar region of hippocampal formation; Hipp, hippocampus; LV, lateral ventricle; Mol, stratum lacunosum-moleculare of hippocampal CA1 (*Ab*, *Bb*) or molecular cell layer of cerebellar cortex (*Ae*, *Be*); Or, stratum orien; Par, parietal cortex; Pyr, stratum pyramidale; Rad, stratum radiatum; Thal, thalamus; WM, white matter. Scale bars, 500 μm in *Aa* and *Ba*; 50 μm in *Ab–e* and *Bb–e*.

brainstem (Fig. 4*A*). In the cerebellar cortex, prominent RIM3 and RIM4 hybridization signals were observed in the granule and Purkinje cell layers (Fig. 5*Ae* and *Be*). The RIM3 distribution, which was consistent with a recent report (35), is similar to the expression pattern of RIM4 in the mouse brain except in the brainstem.

α-RIM and RIM3 physically associate with native VDCCs in the crude synaptic membrane from the mouse brain. Subcellular fractionation analysis of the mouse brain showed that RIM1 and RIM3 were highly concentrated in the crude synaptic membrane (CSM) fraction, which was similar to that for PSD-95 and synaptophysin, established marker proteins of the postsynapse and presynapse, respectively (Fig. 6*A*). In immunoprecipitation analysis of the CSM fraction solubilized with 1% digitonin-containing buffer, the P/Q-type ($Ca_V2.1$) and N-type ($Ca_V2.2$) VDCC α_1-subunits and the VDCC β_4-subunit were coimmunoprecipitated with α-RIM (RIM1 or RIM2) and RIM3 (Fig. 6*B*). Thus, the P/Q-type and N-type channels are physically associated with RIM3 as well as with α-RIM in the CSM fraction of the mouse brain.

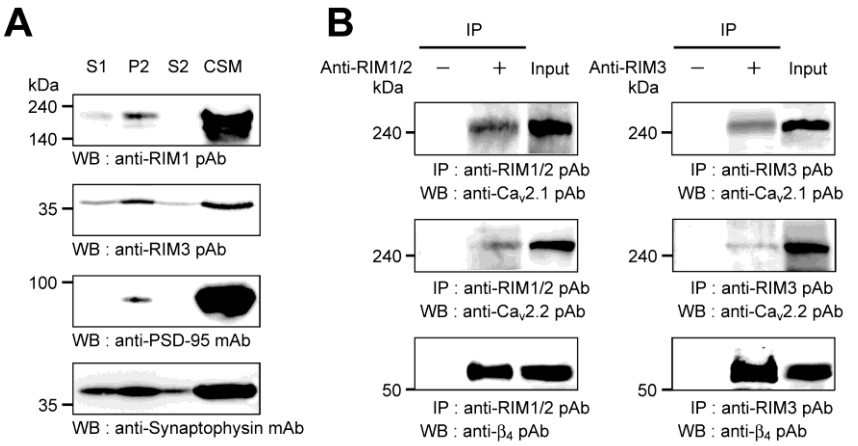

Fig. 6 Association of RIMs with native neuronal VDCC complexes in CSM fraction. *A.* Subcellular fractionation. The homogenate of mouse brain is subjected to subcellular fractionation. An aliquot of each fraction (10 μg of protein each) is analyzed by WB with the indicated antibodies. S1, crude synaptosomal fraction; P2, crude membrane fraction; S2, cytosolic synaptosomal fraction; CSM, CSM fraction. *B.* Coimmunoprecipitation of RIMs with the VDCC subunits. Immunoprecipitation using an antibody for RIMs and subsequent WB for $Ca_V2.1$, $Ca_V2.2$, and β_4 are carried out on CSM fraction.

Physiological relevance of RIM effects on the inactivation properties of VDCCs. To investigate the physiological roles of RIM-β-subunit complexes in native systems, expression of RIM was suppressed by treatment with siRNA (Fig. 7). In rat neuron-like pheochromocytoma PC12 cells, diverse HVA VDCC types have been precisely characterized (66, 67). Previously, we identified P/Q-, N-, and L-type Ca^{2+} currents by pharmacological dissection of HVA Ca^{2+} current, and detected α_1 mRNA species (P/Q-type ($Ca_V2.1$), N-type ($Ca_V2.2$), and L-type ($Ca_V1.2$ and $Ca_V1.3$)) and β-subunits (β_1, β_2, and β_3) in PC12 cells (12). RT-PCR analysis revealed expression of RNA species encoding RIM1, RIM2, RIM3, and RIM4 in PC12 cells (Fig. 7*A*). RT-PCR analysis also showed that combinations of siRNAs specific for RIM1 and RIM2 (siRIM1&2), RIM3 and RIM4 (siRIM3&4), or all four RIMs (siRIM1&2&3&4) effectively suppressed the expression of target genes, while control siRNA (siControl) failed to exert significant effects on RIM RNA expression (Fig. 7*A*). WB also indicated that application of siRNAs for RIMs effectively suppressed expressions of RIM proteins (Fig. 7*B*). siRNAs for RIMs accelerated inactivation of whole-cell Ba^{2+} currents through VDCCs endogenously expressed in PC12 cells (Fig. 7*C* upper). The voltage-dependence of VDCC inactivation in PC12 cells consisted of three phases: a low voltage-induced phase, a high voltage-induced phase, and a non-inactivating phase (Fig. 7*C* lower and Table 3). siRNA application increased the proportion of the low voltage-induced phases (from 0.21 to 0.35 for siRIM1&2, to 0.38 for siRIM3&4, and to 0.46 for

siRIM1&2&3&4) and reduced the proportion of the non-inactivating phases (from 0.42 to 0.30 for siRIM1&2, to 0.26 for siRIM3&4, and to 0.17 for siRIM1&2&3&4) (Fig. 7*C* lower and Table 3). siRIM1&2&3&4 showed a more marked effect than siRIM1&2 or siRIM3&4. These inactivation properties were rescued by siRNA-resistant RIM constructs. Expression of siRNA-resistant (denoted by *) RIM cDNAs reversed the accelerated inactivation in RIM knockdown cells (siRIM1&2 + RIM1*&2* and siRIM3&4 + RIM3*&4*) (Fig. 7*C* middle). The increase of the ratios of low voltage-induced phases and the reduction of ratios of non-inactivating phases were also rescued by the siRNA-resistant RIMs (0.05 and 0.41 for siRIM1&2 + RIM1*&2*, and 0.12 and 0.42 for siRIM3&4 + RIM3*&4*). Other functional current parameters such as current densities and activation kinetics at different voltages were unaffected by siRNA for RIMs (Fig. 8 and Table 4). Thus, RIMs exert suppressive effects on voltage-dependent inactivation of native VDCCs in PC12 cells.

Table 3 Effects of RIM siRNA applications on inactivation properties of VDCC in PC12 cells[1) 2) 3)].

siRNA	Inactivation parameters						
	a	$V_{0.5}^{Low}$ (mV)	K^{Low} (mV)	*b*	$V_{0.5}^{High}$ (mV)	K^{High} (mV)	1–*a*–*b*
siControl	0.21 ± 0.04 (7)$^{\#\dagger}$	−35.2 ± 2.1 (7)	−8.3 ± 1.3 (7)	0.36 ± 0.03 (7)	−4.5 ± 1.2 (7)	−4.0 ± 0.4 (7)	0.42 ± 0.02 (7)$^{\#\dagger\dagger\dagger}$
siRIM1&2	0.35 ± 0.04 (9)*	−37.6 ± 1.9 (9)	−8.7 ± 0.6 (9)	0.31 ± 0.02 (9)	−5.7 ± 1.5 (9)	−4.6 ± 0.8 (9)	0.30 ± 0.04 (9)*
siRIM3&4	0.38 ± 0.02 (6)*	−40.1 ± 2.0 (6)	−8.9 ± 0.9 (6)	0.36 ± 0.01 (6)	−1.8 ± 2.1 (6)	−6.1 ± 1.0 (6)*	0.26 ± 0.03 (6)***
siRIM1&2&3&4	0.46 ± 0.04 (8)***$^{\#\dagger}$	−38.9 ± 1.9 (8)	−8.5 ± 0.7 (8)	0.38 ± 0.05 (8)	−4.8 ± 0.9 (8)	−5.2 ± 0.8 (8)	0.17 ± 0.02 (8)***$^{\#\#\dagger\dagger\dagger}$
siRIM1&2 + RIM1*&2*	0.05 ± 0.02 (9)**$^{\#\#\dagger\dagger\dagger}$	−40.4 ± 2.3 (9)	−6.6 ± 0.1 (9)	0.54 ± 0.02 (9)*$^{\#\#\dagger\dagger}$	−3.7 ± 0.9 (9)	−4.4 ± 0.25 (9)$^{\#}$	0.41 ± 0.01 (9)$^{\#\dagger\dagger\dagger}$
siRIM3&4 + RIM3*&4*	0.12 ± 0.05 (7)$^{\#\#\dagger\dagger\dagger}$	−36.3 ± 4.9 (7)	−9.3 ± 0.6 (7)	0.47 ± 0.05 (7)$^{\#\#}$	−3.4 ± 1.2 (7)	−3.9 ± 0.7 (7)$^{\#}$	0.42 ± 0.05 (7)$^{\#\dagger\dagger\dagger}$

1) $^{*}P < 0.05$, $^{**}P < 0.01$, $^{***}P < 0.001$ versus siControl.

2) $^{\#}P < 0.05$, $^{\#\#}P < 0.01$, $^{\#\#\#}P < 0.001$ versus siRIM1&2

3) $^{\dagger}P < 0.05$, $^{\dagger\dagger}P < 0.01$, $^{\dagger\dagger\dagger}P < 0.001$ versus siRIM3&4.

4) Numbers of cells analyzed are indicated in the parenthesis.

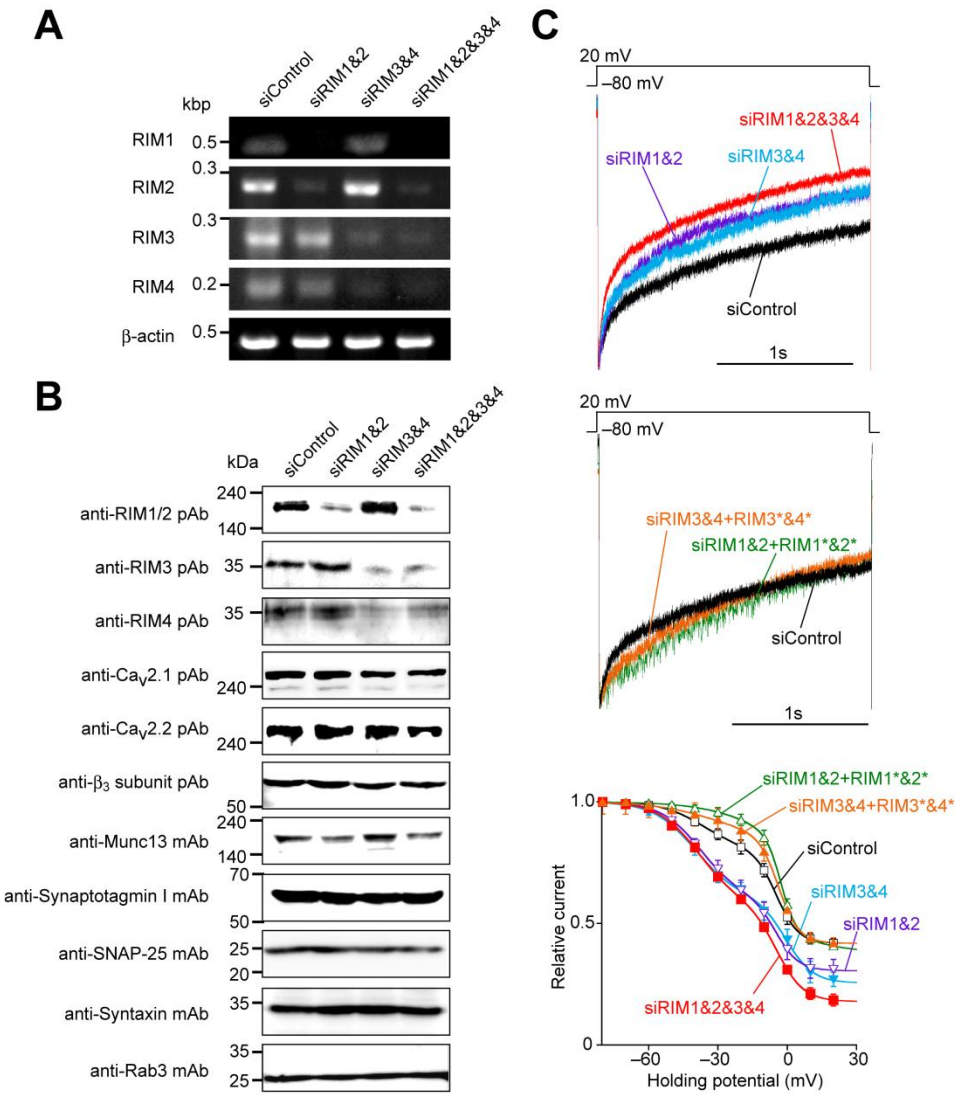

Fig. 7 Physiological relevance of effects of RIMs on inactivation properties of VDCCs. *A.* RT-PCR analysis of RIM1, RIM2, RIM3, and RIM4 RNA expression in PC12 cells treated with GAPDH siRNA (siControl), combination of RIM1- and RIM2-specific siRNAs (siRIM1&2), combination of RIM3- and RIM4-specific siRNAs (siRIM3&4), and combination of RIM1-, RIM2-, RIM3-, and RIM4-specific siRNAs (siRIM1&2&3&4). PCR is performed 29 cycles. β-actin is used as an internal control. *B.* WB of essential components of release machinery and VDCC subunits in PC12 cells transfected with indicated combination of siRNAs. Primary antibodies used are indicated on the left. *C.* Acceleration of inactivation by application of siRNAs specific for RIMs in VDCC currents recorded from PC12 cells. The acceleration of inactivation in RIM knockdown cells is reversed by expression of siRNA-resistant RIM cDNAs (siRIM1&2 + RIM1*&2*, and siRIM3&4 + RIM3*&4*). Upper and middle, normalized current traces. Lower, inactivation curves. See Table 3 for statistical significance of the differences.

γ-RIMs inhibit but α-RIMs support anchoring of neurotransmitter vesicles to VDCCs. Dense-core vesicles were identified by a fusion protein of NPY and the fluorescent protein Venus (NPY-Venus) in PC12 cells. When cotransfected NPY-Venus was used as an siRNA transfection marker, comparison of fluorescence intensities of immunoreactivities to anti-RIM1 and RIM2 antibodies in NPY-Venus-positive PC12 cells with those in NPY-Venus-negative PC12 cells revealed that combination of specific siRNAs

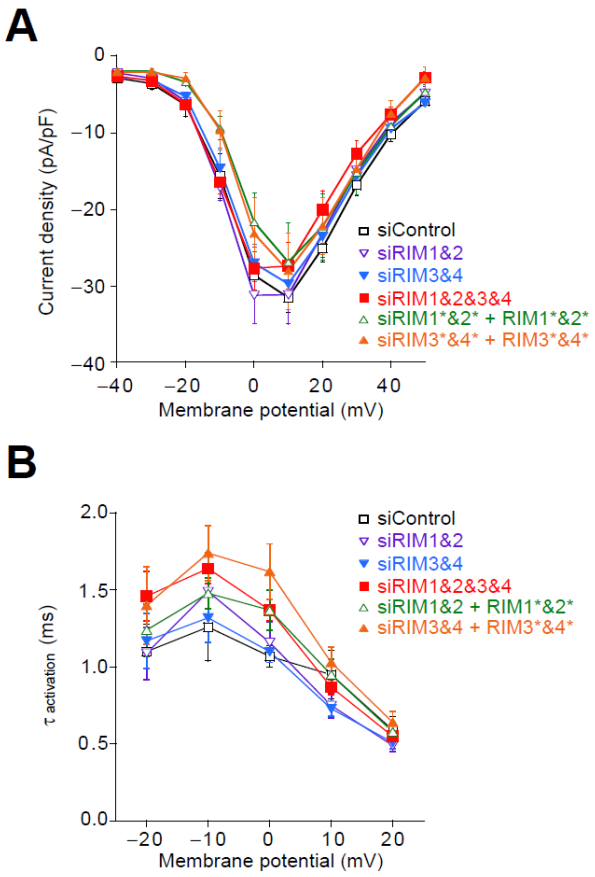

Fig. 8 Effects of siRNA for RIMs on the activation properties of VDCC currents in PC12 cells. *A.* Effects of siRNA for RIMs on I-V relationships in PC12 cells. Ba^{2+} currents elicited by application of 30-ms test pluses from –40 mV to 50 mV with 10-mV increments from a V_h of –80 mV are analyzed. *B.* Activation kinetics of Ba^{2+} currents in PC12 cells. Activation time constants are obtained from currents elicited by 30-ms step depolarization from –20 to 20 mV in 10-mV increments from a V_h of –80 mV and plotted as a function of test potential. See Table 4 for statistical significance of the differences.

TABLE 4 Effects of RIM siRNA applications on activation properties of VDCC in PC12 cells[1].

siRNA	Current density (pA / pF)[2]	Activation parameters	
		$\tau_{activation\ (-10mV)}$(ms)[3]	$\tau_{act\ (10mV)}$(ms)[4]
siControl	−29.6 ± 2.1 (12)	1.26 ± 0.22 (6)	0.95 ± 0.16 (6)
siRIM1&2	−31.1 ± 3.7 (17)	1.49 ± 0.16 (12)	0.75 ± 0.08 (12)
siRIM3&4	−26.9 ± 2.4 (21)	1.32 ± 0.16 (12)	0.73 ± 0.05 (12)
siRIM1&2&3&4	−27.6 ± 2.8 (27)	1.64 ± 0.10 (12)	0.87 ± 0.05 (12)
siRIM1&2 + RIM1*&2*	−21.6 ± 3.8 (11)	1.48 ± 0.10 (11)	0.95 ± 0.10 (11)
siRIM3&4 + RIM3*&4*	−20.9 ± 2.7 (8)	1.74 ± 0.18 (8)	1.03 ± 0.10 (8)

1) Numbers of cells analyzed are indicated in the parenthesis.

2) Ba^{2+} currents evoked by depolarizing pulse to 0 mV from a V_h of –80 mV are divided by capacitance.

3) Activation time constants obtained from currents elicited by 30-ms test pulse to –10 mV. The activation phases are well fitted by a single exponential function.

4) Activation time constants obtained from currents elicited by 30-ms test pulse to 10 mV.

efficiently suppressed RIM1 and RIM2 expression in confocal images (Fig. 9). We directly observed fluorescent images in the plasma membrane area using evanescent wave microscopy, which illuminates only the subcellular area from the surface to a depth of less than 100 nm by TIRF. When cotransfected Ds-Red monomer was used as an siRNA transfection marker, comparison of fluorescence intensities of immunoreactivities to anti-RIM1 and RIM2 antibodies in Ds-Red-positive PC12 cells with those in Ds-Red-negative PC12 cells also revealed that combination of specific siRNAs efficiently suppressed RIM1 and RIM2 expression in TIRF images (Fig. 10). The number of vesicles docked to the plasma membrane

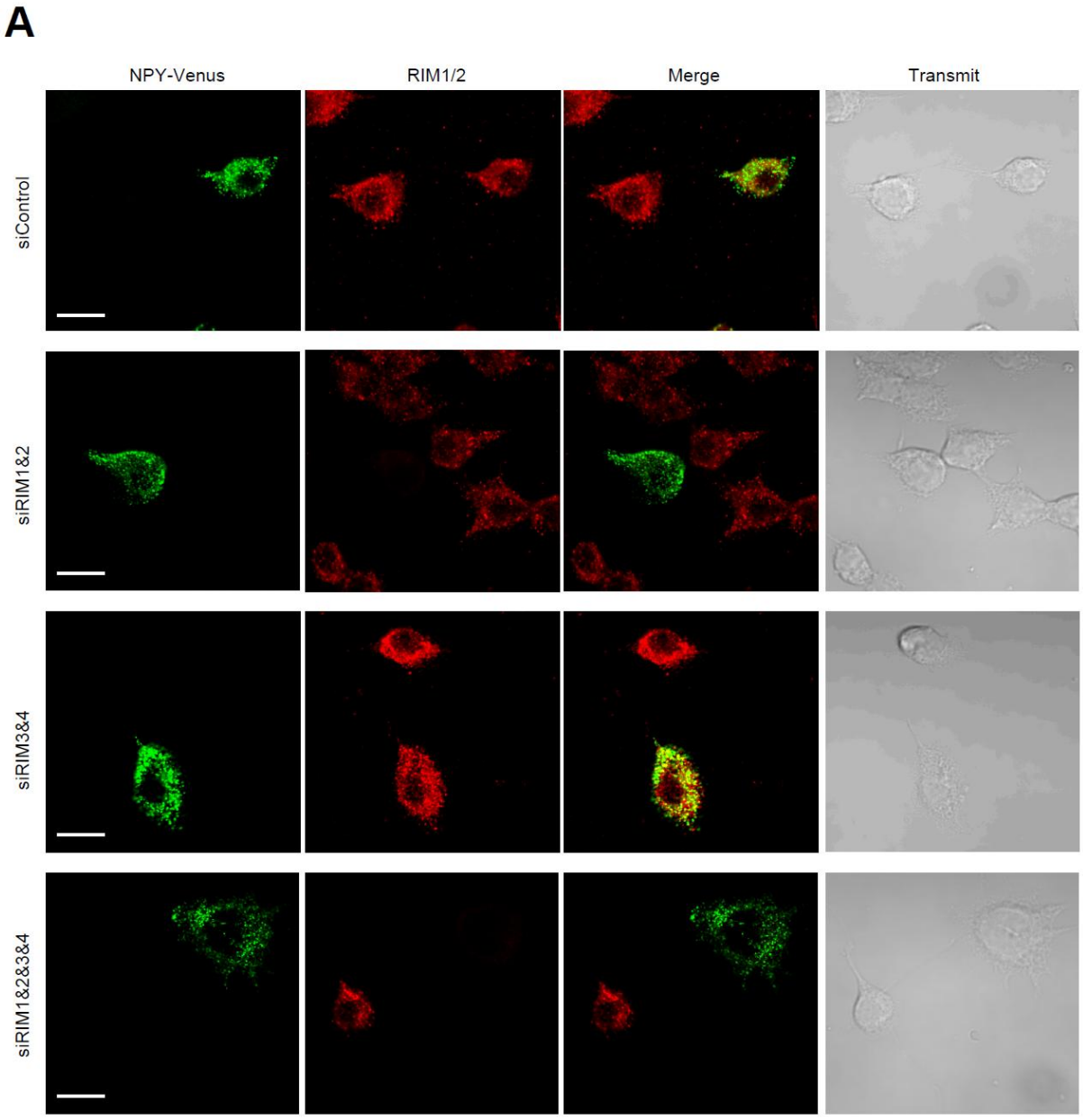
A
NPY-Venus
RIM1/2
Merge
Transmit
siControl
siRIM1&2
siRIM3&4
siRIM1&2&3&4
B
Relative intensity
(Ipositive / Inegative)
1.0
0.5
0
###
***
###
***
siControl
siRIM1&2
siRIM3&4
SiRIM1&2&3&4

Fig. 9 Confocal images demonstrate silencing of RIM1 and RIM2 with siRNA in PC12 cells. A. Silencing of endogenous RIM1 and RIM2 in PC12 cells with siRNA causes reduction of RIM1 and RIM2 immunoreactivity. NPY-Venus and combination of siRNAs (siControl, siRIM1&2, siRIM3&4, or siRIM1&2&3&4) are co-transfected into PC12 cells. Forty-eight h after transfection, cells are fixed, permeabilized, and stained with anti-RIM1/2 polyclonal antibody and Cy3-conjugated anti-rabbit secondary antibody. The fluorescent image is analyzed by confocal laser microscopy. Scale bar, 10 μm. B. Relative intensity of RIM1/2 immunoreactivity. Average intensity of RIM1/2 immunoreactivity in NPY-Venus-positive cells is normalized to that in NPY-Venus-negative cells in the same visual field. Numbers of areas observed are 14, 15, 11, and 9 for transfection of siControl, siRIM1&2, siRIM3&4, and siRIM1&2&3&4, respectively. ***P < 0.001 versus siControl. ###P < 0.001 versus siRIM3&4.

---

was decreased significantly by combinatory application of RIM1 and RIM2 siRNAs, whereas it was increased by RIM3 and RIM4 siRNA (Fig. 11). Importantly, the inhibitory effect of siRIM1&2 and the enhancing effect of siRIM3&4 were reversed by expression of siRNA-resistant RIM cDNAs (siRIM1&2 + RIM1*&2* and siRIM3&4 + RIM3*&4*). Effects of siRIM1&2 or siRIM3&4 are unlikely to be due to altered densities of VDCCs at the plasma membrane in PC12 cells, because the siRNAs used did not affect VDCC current densities and VDCC expression levels (Fig. 7*B*, Fig. 8A, and Table 4). It is important to note that endogenous Rab3 and Munc13 were immunoprecipitated with FLAG-tagged α-RIMs but not γ-RIMs, while Liprin1-α was immunoprecipitated with α-RIMs and γ-RIMs (Fig. 14). This is consistent with the previous report that α-RIMs are associated with Rab3 and Munc13 *via* their N-terminus and with Liprin1-α *via* their C-terminus (32, 37, 39). Thus, γ-RIMs as well as α-RIMs play important roles in regulating neurotransmitter vesicle-anchoring to VDCCs. *γ-RIMs less potently enhance neurotransmitter secretion than α-RIMs in PC12 cells.* We studied the physiological relevance of RIM interactions with the VDCC complexes by assessing neurotransmitter release from PC12 cells. PC12 cells were transfected with RIM cDNAs or with siRNAs for RIMs along with *Chat* encoding choline acetyltransferase, which synthesizes ACh for synaptic vesicles (57). ACh release, triggered by Ca^{2+} influx in response to high-K^+-induced (extracellular K^+ concentration elevated from 5.9 mM to 51.1 mM for 30 s) membrane depolarization, was less potently potentiated by recombinant RIM3γ and RIM4γ than by recombinant RIM1α and RIM2α (Fig.

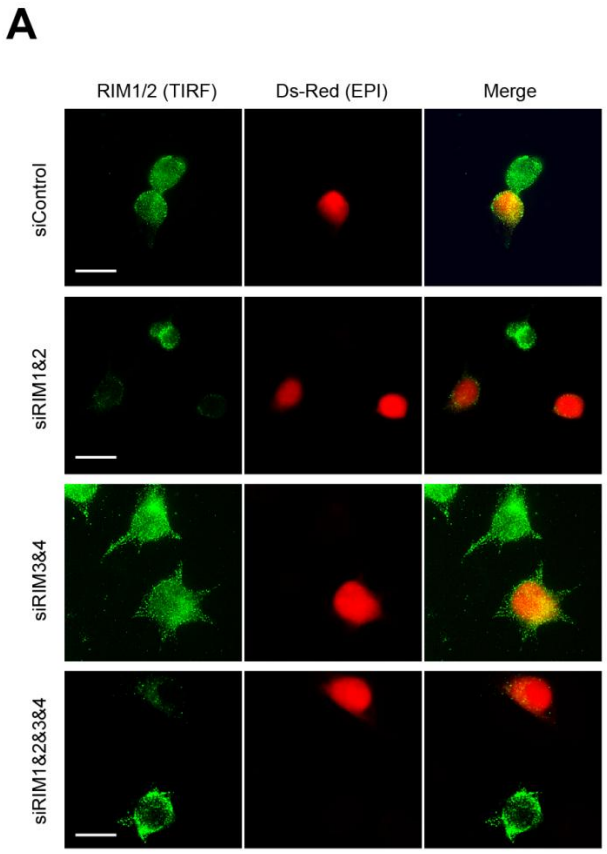

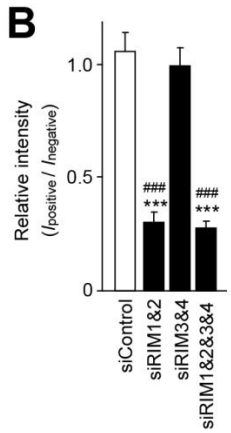

Fig. 10 TIRF images demonstrate silencing of RIM1 and RIM2 with siRNA in the plasma membrane of PC12 cells. A. Typical TIRF images of immunoreactivity of RIM1 and RIM2 in the plasma membrane. Ds-red monomer and combination of siRNAs are co-transfected into PC12 cells. Forty-eight h after transfection, cells are fixed, permeabilized, and stained with anti-RIM1/2 polyclonal antibody and Alexa-Fluor-488-conjugated anti-rabbit secondary antibody. Epi-fluorescent images (EPI) are obtained for Ds-red monomer used as a marker of transfection. Scale bar, 10 mm. B. Relative intensity of RIM1/2 immunoreactivity. Average intensity of RIM1/2 immunoreactivity in Ds-Red-positive cells is normalized to that in Ds-Red-negative cells in the same visual field. Numbers of areas observed are 10, 18, 12, and 21 for transfection of siControl, siRIM1&2, siRIM3&4, and siRIM1&2&3&4, respectively. ***P < 0.001 versus siControl. ###P < 0.001 versus siRIM3&4.

12*A*). A similar result has been reported previously for RIM3γ for the secretion of human growth hormone in PC12 cells (36). siRNAs specific to RIMs significantly decreased ACh release. siRIM1&2&3&4 suppressed ACh secretion more markedly than siRIM1&2 or siRIM3&4. Furthermore, ACh release was abolished in the presence of 0.3 mM Cd^{2+}, a selective blocker of HVA Ca^{2+} channels, in extracellular solutions (Fig. 12*B*). Likewise, ACh release triggered by moderate depolarization (extracellular K^+ concentration elevated from 5.9 mM to 28.4 mM for 2 min) was also significantly decreased by siRNAs specific to

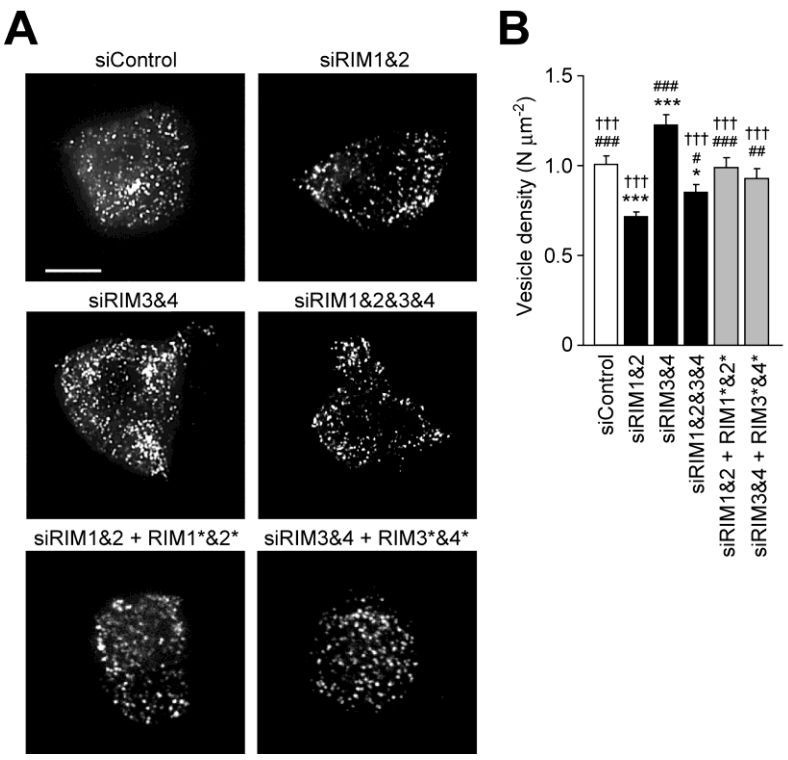

Fig. 11 γ-RIMs reduce the density of vesicles at the plasma membrane in PC12 cells. *A.* Typical TIRF images of plasma membrane-docked vesicles containing NPY-Venus are shown. NPY-Venus, combination of siRNAs and siRNA-resistant RIM cDNAs are cotransfected in PC12 cells and live images of cells are obtained by TIRF microscopy. Scale bar, 10 μm. *B.* The vesicle density (N μm^{-2}) is determined by counting the vesicles in each image. The number of individual fluorescent spots in the area, where vesicles uniformly distributed in TIRF images, is divided by the area. Numbers of area observed are 48, 51, 40, 45, 30, and 29 for transfection of siControl, siRIM1&2, siRIM3&4, siRIM1&2&3&4, siRIM1&2 + RIM1*&2*, and siRIM3&4 + RIM3*&4*, respectively. $^{*}P <$ 0.05 and $^{***}P <$0.001 versus siControl. $^{\#}P < 0.05$, $^{\#\#}P < 0.01$, and $^{\#\#\#}P < 0.001$ versus siRIM1&2. $^{\dagger\dagger\dagger}P <$ 0.001 versus siRIM3&4.

RIMs (Fig. 12*C*). The inhibitory effect of siRIM1&2 and siRIM3&4 on depolarization induced ACh release were rescued by expression of siRNA-resistant RIM cDNAs (Fig. 12*B, C*). Notably, ACh release triggered by 28.4 mM K^+ was more susceptible to suppression by siRIM1&2 than by siRIM3&4. Amount of control ACh secretion by 51.1 mM K^+ solution nearly doubled that by 28.4 mM K^+ solution. The intracellular Ca^{2+} concentration ($[Ca^{2+}]_i$) under stimulation with extracellular K^+ elevation was estimated with fluorescent measurement using fura-2. In 51.1 mM and 28.4 mM K^+-containing extracellular solution, $[Ca^{2+}]_i$ elevations ($\Delta[Ca^{2+}]_i$) were observed and effectively decreased by knockdown of RIMs (Fig. 12*D, E*). Control $[Ca^{2+}]_i$ elevation in 51.1 mM K^+ solution were approximately one order of magnitude higher than those in 28.4 mM K^+ solution. It is important to note that inhibition of ACh secretion by RIM siRNAs is unlikely to be due to their secondary effects that cause a mislocalization or reduction of the release machinery in PC12 cells, because the siRNAs used did not affect the localization of syntaxin (Fig. 13) or the expression levels

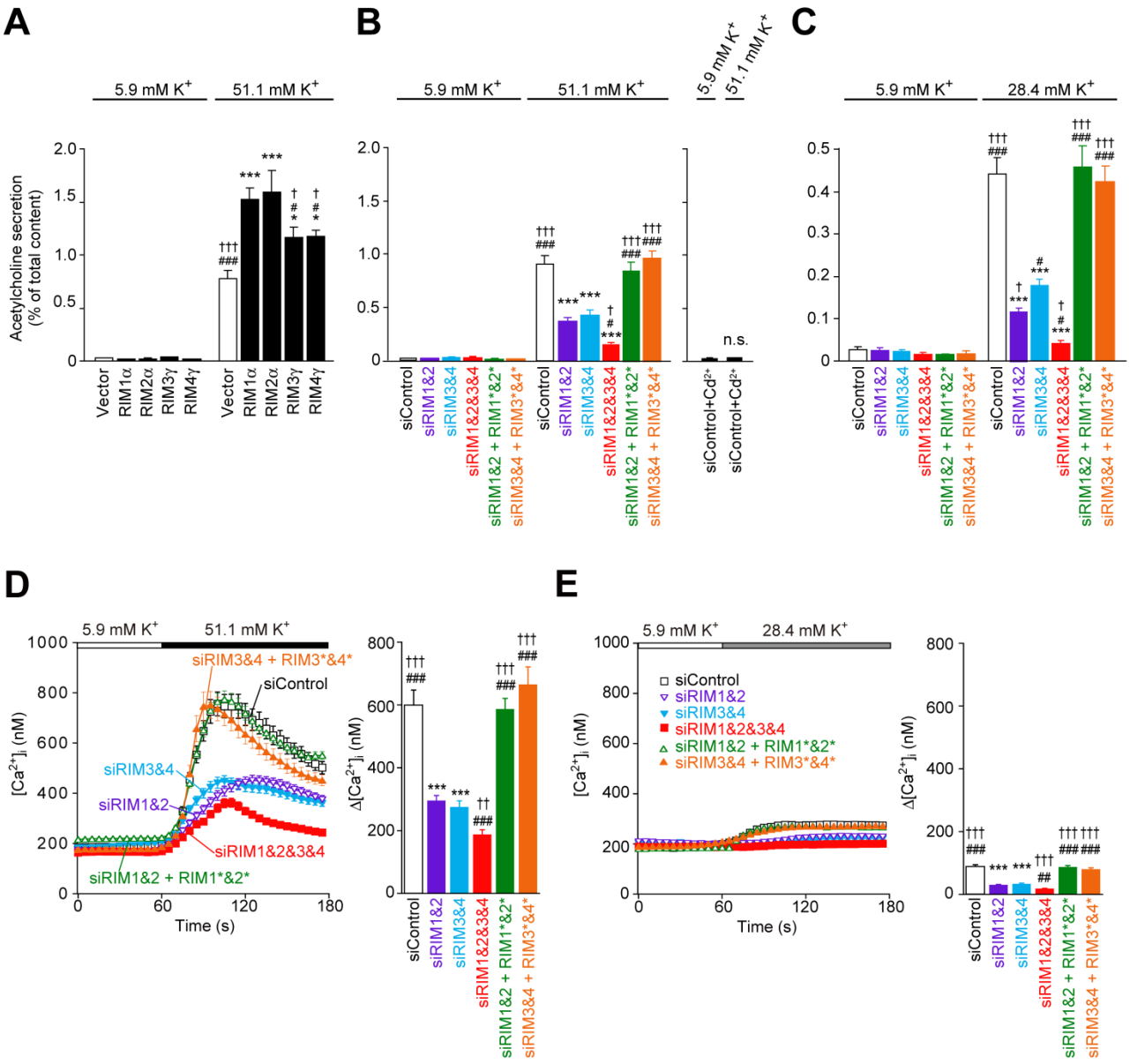

Fig. 12 γ-RIMs enhance neurotransmitter release less potently than α-RIMs in PC12 cells. *A.* Effects of recombinant RIMs on depolarization-dependent release of ACh from ChAT-cotransfected PC12 cells. Transfected PC12 cells are incubated for 30 s with 5.9 mM K^+ solution at 37 °C. The release of ACh during this period is considered to be basal release. To measure depolarization induced ACh release, the cells are then incubated for 30 s with 51.1 mM K^+ solution. The amount of secreted ACh is determined as a percentage of the cellular content for each dish. Numbers of experiments performed are 12, 10, 11, 10, and 12 for transfection of vector, RIM1α, RIM2α, RIM3γ, and RIM4γ, respectively. $^{*}P < 0.05$ and $^{***}P < 0.001$ versus vector. $^{\#}P < 0.05$ and $^{\#\#\#}P < 0.001$ versus RIM1α. $^{\dagger}P < 0.05$ and $^{\dagger\dagger\dagger}P < 0.001$ versus RIM2α. *B.* Left, effects of siRNA for RIMs on depolarization-dependent release of ACh from ChAT-cotransfected PC12 cells. Numbers of experiments performed are 12, 12, 11, 6, 9, and 11 for transfection of siControl, siRIM1&2, siRIM3&4, siRIM1&2&3&4, siRIM1&2 + RIM1*&2*, and siRIM3&4 + RIM3*&4*, respectively. $^{***}P < 0.001$ versus siControl. $^{\#}P < 0.05$ and $^{\#\#\#}P < 0.001$

versus siRIM1&2. $^{\dagger}P < 0.05$ and $^{\dagger\dagger\dagger}P < 0.001$ versus siRIM3&4. Right, effects of 0.3 mM Cd^{2+} on depolarization-dependent release of ACh from ChAT-cotransfected PC12 cells. Number of experiments performed is 4. n.s., not significant. *C.* Effects of siRNA for RIMs on moderate depolarization-dependent release of ACh from ChAT-cotransfected PC12 cells. To measure ACh release, the cells are incubated for 120 s with a 28.4 mM-K^+ solution. Numbers of experiments performed are 9, 10, 11, 7, 7, and 11 for transfection of siControl, siRIM1&2, siRIM3&4, siRIM1&2&3&4, siRIM1&2 + RIM1*&2*, and siRIM3&4 + RIM3*&4*, respectively. $^{***}P < 0.001$ versus siControl. $^{\#}P < 0.05$ and $^{\#\#\#}P < 0.001$ versus siRIM1&2. $^{\dagger}P < 0.05$ and $^{\dagger\dagger\dagger}P < 0.001$ versus siRIM3&4. *D.* Effects of siRIMs on Ca^{2+} responses upon elevation of extracellular K^+ concentration from 5.9 mM to 51.1 mM. Average time courses (left) and maximal $[Ca^{2+}]_i$ rises (right) are shown. Numbers of PC12 cells analyzed are 46, 85, 90, 72, 45, and 49 for transfection of siControl, siRIM1&2, siRIM3&4, siRIM1&2&3&4, siRIM1&2 + RIM1*&2*, and siRIM3&4 + RIM3*&4*, respectively. $^{***}P < 0.001$ versus siControl. $^{\#\#\#}P < 0.001$ versus siRIM1&2. $^{\dagger\dagger}P < 0.01$, $^{\dagger\dagger\dagger}P < 0.001$ versus siRIM3&4. *E.* Effects of siRIMs on Ca^{2+} responses upon elevation of extracellular K^+ concentration from 5.9 mM to 28.4 mM. Numbers of PC12 cells analyzed are 80, 92, 90, 97, 49, and 66 for transfection of siControl, siRIM1&2, siRIM3&4, siRIM1&2&3&4, siRIM1&2 + RIM1*&2*, and siRIM3&4 + RIM3*&4*, respectively. $^{***}P < 0.001$ versus siControl. $^{\#\#}P < 0.01$, $^{\#\#\#}P < 0.001$ versus siRIM1&2. $^{\dagger\dagger\dagger}P < 0.001$ versus siRIM3&4.

---

of essential components of the release machinery such as synaptotagmin, SNAP-25, syntaxin, and Rab3 (Fig. 7*B*). Munc13 was slightly decreased in RIM1 and RIM2 knockdown cells (Fig. 7*B*), as reported in the RIM1 knockout mouse, presumably because Munc13 binds to α-RIMs (Fig. 14) (37) and is destabilized in their absence (39). Thus, native γ-RIMs together with α-RIMs play important roles in neurotransmitter release in the PC12 cells.

γ-RIMs support neurotransmitter secretion in rat cerebellar neurons. To investigate physiological roles of RIMs in neurons, we next examined neurotransmitter release from cultured cerebellar neurons. RT-PCR analyses revealed expression of RNA species encoding RIM1, RIM2, RIM3, and RIM4 in cultured rat cerebellar neurons (Fig. 15*A*). Combinations of shRNAs specific for RIM1 and RIM2 (shRIM1&2), RIM3 and RIM4 (shRIM3&4), or four RIM isoforms (shRIM1&2&3&4) effectively suppressed the expression of target genes, while control shRNA (shControl) failed to exert significant effects on RIM RNA expression in rat cerebellar neurons 10 days after transfection (Fig. 15*A*). Glutamate release from cerebellar neurons,

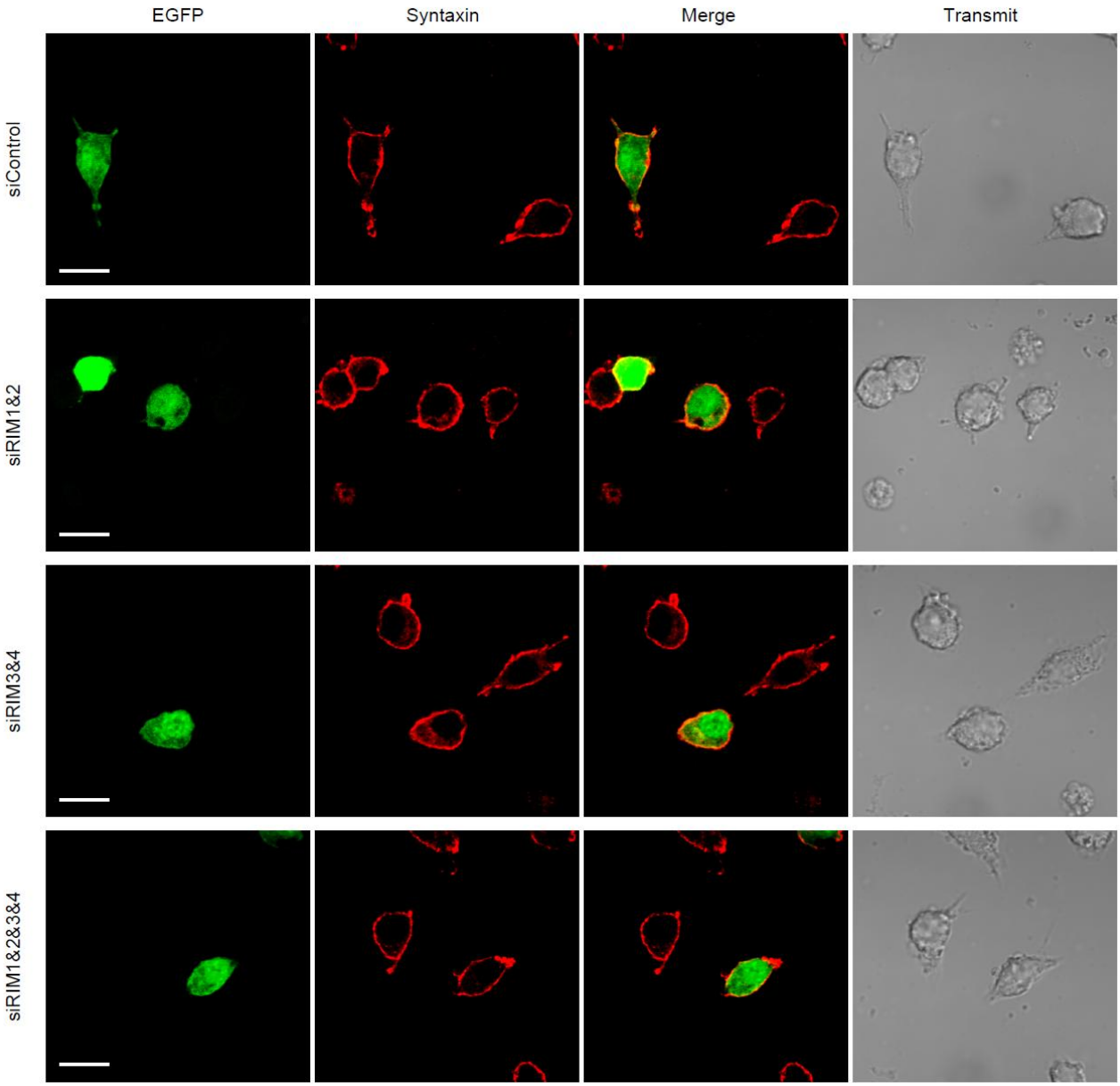

Fig. 13 Localization of syntaxin is intact in RIM knockdown PC12 cells. Silencing of endogenous RIMs in PC12 cells with siRNA fails to affect localization and intensity of syntaxin immunoreactivity. EGFP and combination of siRNAs (siControl, siRIM1&2, siRIM3&4, or siRIM1&2&3&4) are co-transfected into PC12 cells. Forty-eight h after transfection, cells are fixed, permeabilized, and stained with anti-syntaxin monoclonal antibody and Cy3-conjugated anti-mouse secondary antibody. The fluorescent image is analyzed by confocal laser microscopy. Scale bar, 10 μm.

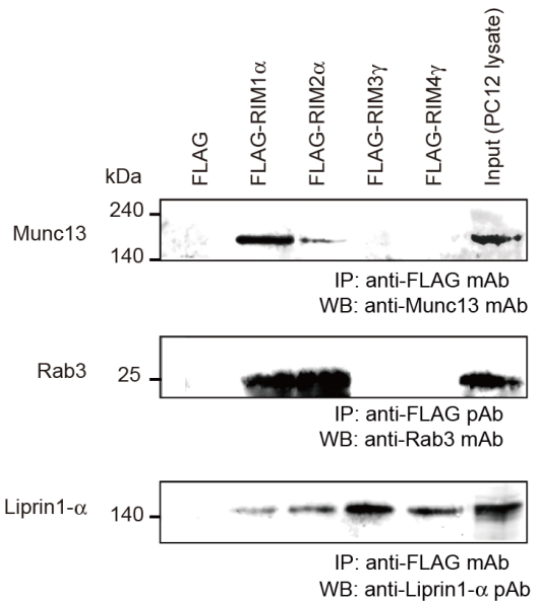

Fig. 14 Characterization of binding of synaptic proteins to RIMs. FLAG-RIMs expressing HEK293T cell lysate is incubated with PC12 cell lysate. FLAG-RIMs are immunoprecipitated with anti-FLAG monoclonal or polyclonal antibody and are analyzed by WB using indicated antibody. Associations between Rab3 and RIMs are evaluated in the presence of GTPγS.

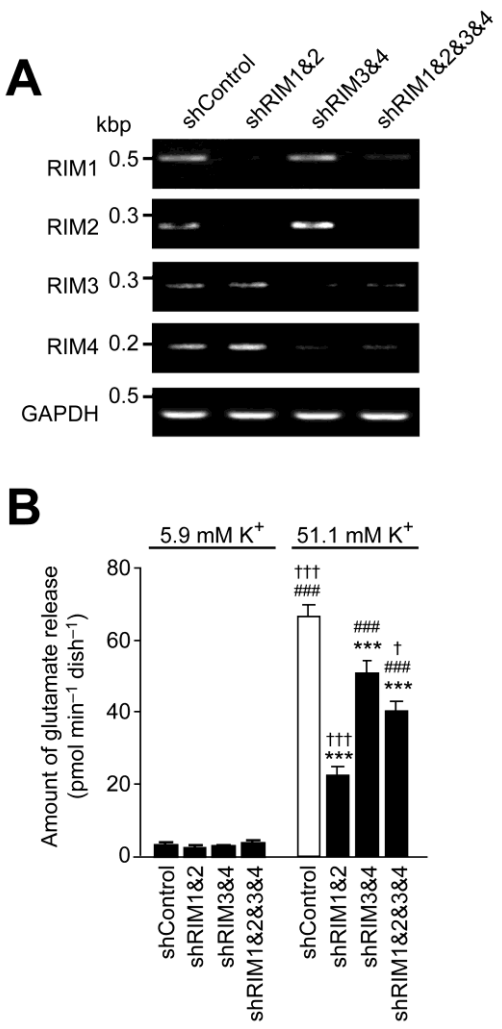

Fig. 15 γ-RIMs support neurotransmitter release in cerebellar neurons. *A.* RT-PCR analysis of RNA expression of RIMs in cultured cerebellar neurons treated with a negative control shRNA vector (shControl), combination of RIM1- and RIM2-targeted shRNA vectors (shRIM1&2), combination of RIM3- and RIM4-targeted shRNA vectors (shRIM3&4), and combination of RIM1-, RIM2-, RIM3-, and RIM4-targeted shRNA vectors (shRIM1&2&3&4). GAPDH is used as an internal control. PCR is performed 26 cycles for RIM1, 30 cycles for RIM2, 36 cycles for RIM3, 36 cycles for RIM4, 30 cycles for GAPDH. *B.* Effects of shRNA for RIMs on depolarization-dependent release of glutamate from cultured cerebellar neurons. Cultured cerebellar neurons transfected with shRNA vectors (10 DIV) are incubated for 1 min with the low-K^+ solution (5.9 mM K^+) at 37 °C. The release of glutamate during this period is considered to be basal release. To measure glutamate release, the cells are then incubated for 1 min with a high-K^+ solution (51.1 mM K^+). Numbers of experiments performed are 11, 11, 16, and 11 for transfection of shControl, shRIM1&2, shRIM3&4, and shRIM1&2&3&4, respectively. $^{***}P < 0.001$ versus shControl. $^{\#\#\#}P < 0.001$ versus shRIM1&2. $^{\dagger}P < 0.05$ and $^{\dagger\dagger\dagger}P < 0.001$ versus shRIM3&4.

triggered by Ca^{2+} influx in response to high-K^+-induced (extracellular K^+ concentration elevated from 5.9 mM to 51.1 mM for 60 s) membrane depolarization was significantly decreased by shRIM1&2, shRIM3&4, and shRIM1&2&3&4 (Fig. 15*B*). Notably, knockdown of α-RIMs (shRIM1&2) more reduced glutamate release than that of γ-RIMs (shRIM3&4) and that of all RIMs (shRIM1&2&3&4). These results suggest that both α-RIMs and γ-RIMs are important for neurotransmitter release, but their contributions to glutamate release from cultured cerebellar neurons are different.

Discussion

An understanding of the physiological roles played by RIMs other than RIM1 has been elusive, despite evolutionary conservation of the C_2B domain-containing C-terminus among all RIM isoforms. The present investigation revealed physical associations of RIM2α, RIM3γ, and RIM4γ with VDCC β-subunits. *In vitro* binding assays and coimmunoprecipitation experiments identified protein complexes formed by direct interactions of VDCC β-subunits with α_1-subunits and with RIMs (Figs. 1 and 6). The interactions between RIMs and VDCC β-subunits decelerated VDCC inactivation to sustain depolarization-induced Ca^{2+} influx (Figs. 2 and 7) and enhanced depolarization-induced ACh release in PC12 cells in cultured cerebellar neurons (Fig. 12, Fig. 15). TIRF imaging of dense-core vesicles indicated that, unlike RIM1α and RIM2α, RIM3γ and RIM4γ inhibit the anchoring of neurotransmitter vesicles in the vicinity of VDCCs (Fig. 11).

K_d values of the binding of RIM1α (1079–1463), RIM2α (1193–1572), RIM3γ and RIM4γ to the β_4-subunit indicate that the binding affinities of RIM3γ and RIM4γ are almost an order of magnitude lower than those of RIM1α and RIM2α (12) (Fig. 1*D*). This is consistent with the fact that the amino acid sequence of the primary β-subunit interaction region in the RIM1α (RIM1α (1079–1257)) (12) is better conserved in RIM2α (60% identity in RIM2α (1193–1366)), than in RIM3γ and RIM4γ (25% and 12% identities for RIM3γ (1–104) and RIM4γ (1–63), respectively). Despite these differences in affinity among the primary interaction regions for β-subunits, kinetic modulation of VDCC inactivation was observed for RIM3γ and RIM4γ as well as for RIM2α. This functional conservation in terms of VDCC regulation may be mainly attributable to the modulatory region (12) well conserved among all RIM proteins: identities with the

RIM1α modulatory region (1258–1463) (Fig. 1*A*) are 84%, 74% and 67% for RIM2α (1367–1572), RIM3γ (105–307) and RIM4γ (64–269), respectively.

While expression of RIM3γ or RIM4γ significantly inhibits inactivation and slows the activation kinetics of recombinant P/Q-type VDCCs in BHK cells, knockdown of endogenous RIM3 and RIM4 promotes inactivation but fails to affect the activation kinetics of native VDCC currents in PC12 cells. In the recombinant BHK cell system, the P/Q-type formed by the $Ca_V2.1$ α_1- and β_{1a}-subunit was the only VDCC type expressed. However, PC12 cells express various VDCC subunits (the P/Q-, N-, and L-type α_1-subunits and the β_1-, β_2-, and β_3-subunits) (12, 66, 67). It is therefore possible that multiple types of VDCCs formed by various α_1- and β-subunits are regulated in a different manner by γ-RIMs in PC12 cells in terms of parameters such as activation. In fact, we previously reported using the recombinant system that RIM1α modulates VDCC activation properties such as current density, voltage dependence of activation, and activation kinetics depending on the subunit combination of the VDCC complex (12). In contrast to these functional parameters, similar RIM1α suppression of inactivation was observed for P/Q-type VDCCs containing a β_{2a}-, β_3-, or β_{4b}-subunit (12). Furthermore, a similar effect on inactivation by RIM1α was shown in N-type ($Ca_V2.2$), R-type ($Ca_V2.3$), and L-type ($Ca_V1.2$) VDCCs containing a β_{4b}-subunit. Thus, considering that the other β-subunits interact with RIMs even more strongly than β_{1a} (Fig. 1*B* and *C*), suppressive effects of RIMs on inactivation are universal among HVA types, whereas effects of RIMs on activation kinetics are variable depending on the subunit combination of the VDCC complex. Since the submission of this manuscript, similar modulation of $Ca_V1.3$ VDCC inactivation has been most recently reported for RIM2 (68).

Previous reports have demonstrated functional impacts of syntaxin, SNAP-25 and synaptotagmin on VDCCs through their physical association with the 'synprint' region in the II-III linker of α_1-proteins (9, 19, 22). It has also been reported that RIM1 and RIM2 associate with the synprint (38, 69) directly *via* the C_2A domain, and with the α_1 C-terminal tail indirectly *via* the RIM-BP (70) (Fig. 1*A*). However, inhibition of VDCC inactivation by RIMs may be independent of the synprint- or RIM-BP-mediated association, because γ-RIMs, which lack both the C_2A domain necessary for synprint binding (38, 69) and the PXXP motif for the

RIM-BP binding, inhibit VDCC inactivation (Fig. 2). This idea is supported by our observation that BADN was sufficient to inhibit the effects of RIMs on inactivation (Fig. 2). In addition, we have observed that replacement of β with the C-terminal truncation construct β_4-GK (71), which directly interacts with α_1 but lacks the ability to bind RIM1, was also sufficient to disrupt the RIM1 effects on inactivation (12). In our previous paper, we discussed that RIM1α may affect a conformational transition to the inactivated state of VDCCs *via* association with the β-subunit (12). Recently, it has been proposed that the HOOK domain, between the conserved SH3 and GK domains of the β-subunit, is an important determinant of inactivation (72). Hence, RIMs may act on HOOK domain to suppress the regulatory function of the β-subunit in VDCC inactivation.

In PC12 cells, biphasic voltage dependence of inactivation was observed for native VDCC currents (Fig. 7*C* lower). In the recombinant expression system, a similar biphasic inactivation curve was observed in the presence of BADN, suggesting that a dominant negative effect of BADN partially dissociates the RIMs from the VDCC complexes. Furthermore, $V_{0.5}$ values of the low voltage-induced phase and the high voltage-induced phase were similar to those of inactivation curves without RIMs and with RIMs, respectively, while the proportions of each phase were affected by RIMs (Fig. 2 and Table 1). These findings suggest that at least two types of VDCC complexes, one with RIMs and the other without RIMs, coexist in PC12 cells. VDCC complexes not associated with RIMs may be weakly and indirectly linked to neurotransmitter release in PC12 cells, because knockdown of all four RIMs markedly decreased but did not completely abolish Ca^{2+} influx-triggered neurotransmitter release (Fig. 12).

When voltage-dependent inactivation of VDCCs is suppressed by RIMs, the responses to depolarizing membrane potentials of Ca^{2+} sensors such as synaptotagmins can be potentiated at presynaptic active zones. RIM-VDCC association can thus support synaptic plasticity by regulating depolarization-dependent neurotransmitter release. In PC12 cells, expression of both α-RIMs and γ-RIMs enhanced depolarization-dependent neurotransmitter release (Fig. 12*A*). Thus, not only α-RIMs but also γ-RIMs may play an important role in Ca^{2+} influx triggered-exocytosis in neuroendocrine cells such as PC12 cells. In the case of α-RIMs such as RIM1α, their association with VDCC β-subunits supports release *via* two distinct

mechanisms: sustaining Ca^{2+} influx as described above, and anchoring neurotransmitter-containing vesicles in the vicinity of VDCCs (12). The former function requires only the RIM1α C-terminus (RIM1α (1258–1463)), which is conserved among RIMs, while the latter function requires the 'full-length' structure of α-RIMs. Because γ-RIMs exert only the former function, they can act as dominant negative suppressors of vesicle docking. In fact, knockdown of RIM3γ and RIM4γ by specific siRNAs increased the number of neurotransmitter vesicles anchored near the plasma membrane in PC12 cells (Fig. 11). In addition, the expression of α-RIMs enhanced neurotransmitter release more significantly than did γ-RIMs upon depolarization elicited by 51.1 mM K^+ (Fig. 12*A*), and knockdown of α-RIMs decreased neurotransmitter release more prominently than γ-RIMs upon moderate depolarization elicited by 28.4 mM K^+ in PC12 cells (Fig. 12*C*). Upon depolarization elicited by 51.1 mM K^+, neurotransmitter release in cells with knockdown of α-RIMs and in cells with knockdown of γ-RIMs was indistinguishable (Fig. 12*B*). This is presumably because the robustness of global $[Ca^{2+}]_i$ elevation upon 51.1 mM K^+ stimulation (Fig. 12*D, E*) masks the vesicle-anchoring effect of α-RIMs in PC12 cells. Importantly, compared with 51.1 mM K^+, 28.4 mM K^+ induced global $[Ca^{2+}]_i$ elevation by an order of magnitude lower (Fig. 12*D, E*) but ACh secretion by only 50% lower (Fig. 12*B, C*), suggesting that 28.4 mM K^+ is a depolarizing stimulation almost sufficient for physiological ACh secretion in PC12 cells. Hence, the presence of two functionally different groups of RIMs, α-RIMs and γ-RIMs, becomes physiologically relevant only at moderate stimulations and $[Ca^{2+}]_i$ elevations in ACh secretion from PC12 cells. By contrast, in cerebellar neurons, contributions of α-RIMs and γ-RIMs to glutamate secretion were differentiated even upon robust depolarization elicited by 51.1 mM K^+ stimulation (Fig. 15*B*). We can therefore hypothesize that a transition of the associating partner of presynaptic VDCCs between α-RIMs and γ-RIMs would modify the tightness of coupling of Ca^{2+} influx with fusion of synaptic vesicles and eventually modulates the efficacy of synaptic transmission.

Relative contributions of α-RIMs and γ-RIMs in neurotransmitter release are very likely different between neurons and PC12 cells. In particular, glutamate release is less reduced by knockdown of all RIMs (shRIM1&2&3&4) than by knockdown of α-RIMs (shRIM1&2) in cerebellar neurons in contrast to ACh release in PC12 cells (Fig. 10*B*), suggesting that contributions to neurotransmitter release of γ-RIMs through

'inhibition' of vesicle-anchoring to VDCCs is greater in cerebellar neurons than in neuroendocrine PC12 cells. This is presumably because knockdown of all RIMs abolish the inhibition of anchoring by γ-RIMs and, at the same time, the enhancement of anchoring by α-RIMs, while knockdown of only α-RIMs allows an effective inhibition of anchoring by γ-RIMs left intact in neurons. In support of this idea, it has been previously demonstrated that Ca^{2+}-triggered release is decreased approximately 10-fold in neurons from mice deficient in both α-RIMs (48). Furthermore, the pre-stimulus docking is thought to facilitate fusion and be a preparatory step for exocytosis in neurons (10). On the other hand, in PC12 cells, which possess small vesicles in addition to large dense-core vesicles, there is little pre-stimulus docking for ACh-containing small vesicles (73). It should be also considered that knockdown efficiency is slightly reduced in shRIM1&2&3&4 as demonstrated by residual expression of RIM1 and RIM3 in Fig. 10*A*. The transfection efficiency of each plasmid can be reduced when four shRNA vectors are simultaneously transfected.

In central neurons, overlapping distributions of RIM isoforms revealed by *in situ* hybridization (Fig. 5) (35, 48) suggested that RIM isoforms coexist in the same neurons in the brain. Redundant functions of RIM1α and RIM2α in Ca^{2+}-triggered neurotransmitter release have been reported, but α-RIMs were not replaceable by γ-RIMs with regard to their role in neurotransmitter release (48). This supports that α-RIMs and γ-RIMs function antagonistically in terms of vesicle-anchoring to VDCCs, and may also suggest that γ-RIMs are involved in physiological functions other than neurotransmitter release in neurons. Different subcellular distributions of RIMs support this hypothesis: while RIM1α is a presynaptic protein (32, 39), RIM3γ is present in many neuronal dendrites and dendritic spines, especially in or near the postsynaptic densities (35). Interestingly, studies on the subcellular localization of the P/Q- and R-type channels have defined both axonal and somatodendritic localizations in contrast to the constrained nerve terminal localization of N-type channels (74–76). Thus, in regulation of VDCC inactivation, the respective RIM isoforms may interact with particular VDCC types at axonal and somatodendritic regions and at presynaptic regions in neurons.

In terms of $Ca_V2.1$, which forms P/Q-type VDCCs, the P-type current characterized by very slow inactivation kinetics was first identified in cerebellar Purkinje cells (77, 78), while the Q-type current characterized by fast inactivation kinetics was later identified in cerebellar granule cells (79, 80). Although

P- and Q-type VDCCs show distinct properties, knockout studies have clearly demonstrated that both are encoded by the same $Ca_V2.1$ gene (80, 81). In addition, recombinant human $Ca_V2.1$ expressed in HEK cells produced the Q-type current, but failed to produce the P-type current (82). However, the P-type current was recorded in knock-in mice that express the human $Ca_V2.1$ instead of mouse $Ca_V2.1$ (83). These results suggest that some additional factors, such as post-translational modification or interaction with other proteins, may be necessary to produce the P-type current. An interesting candidate that determines the channel types of the $Ca_V2.1$-forming channel is RIMs. This idea is supported by the following findings. First, our *in situ* hybridization of cerebellar sections revealed that RIM3γ and RIM4γ are more highly expressed in Purkinje cells than in granule cells (Fig. 5*Ae* and *Be*). Second, RIM3γ has been reported as a postsynaptic protein in the molecular layer of the cerebellar cortex, which contains dendrites of Purkinje cells (35) and P-type has also been located in the dendrites and soma of Purkinje cells (77, 84).

In conclusion, we present a common physiological function for RIM proteins, maintaining Ca^{2+} influx triggered by depolarization through suppression of VDCC inactivation. As observed in PC12 cells and cerebellar neurons, specific physiological roles played by γ-RIMs can weaken the physical coupling of VDCCs with synaptic vesicles. Further studies using γ-RIM knockout mice are necessary to test this hypothesis and reveal its relevance to neural processes.

Materials and Methods

cDNA cloning and construction of expression vectors- RIM1α (GenBank accession no. NM_053270), RIM2α (GenBank accession no. HM015529), RIM3γ (GenBank accession no. NM_182929), and RIM4γ (GenBank accession no. NM_183023) were cloned from mouse brain Marathon-Ready cDNA (Clontech) using PCR. Mouse brain RIM2α is a novel variant which is highly homologous with RIM2α (NM_053945) cloned from the rat brain. The amino acid sequence of mouse RIM2α is slightly different from rat RIM2α mainly in three regions (^{542}GDMEYSWLEHASWHSSEASPMSL^{563} in rat RIM2α is replaced with ^{542}GDSQKGKRKTSEQGVLSDSNTRSERQKKRMYYGGHSLEEDLEWSEPQIKDSGVDTCSSTTLNEEH SHSDK^{611} in mouse brain RIM2α, and ^{733}SQSLSRRTTPFVPRVQ^{748} and ^{1132}MITEDMDSTRKRNS^{1145} in rat

RIM2α is deleted in mouse brain RIM2α). These clones were subcloned into pCI-neo (Promega) and the FLAG-tagged vector pCMV-tag2 (Stratagene). Rat β_{4b} (GenBank accession no. XM_215742) was subcloned into the same vectors.

Production of glutathione S-transferase (*GST) fusion proteins and recombinant β_4-subunit proteins*- For production of GST fusion proteins for RIMs, each cDNA for RIM constructs and cDNA for GST were subcloned together into the pET23 vector (Novagen). The Rosetta strain (Novagen) of *Escherichia coli* was transformed by the expression vectors, and protein expression/purification was performed according to the manufacturer's instruction (Novagen). For production of recombinant β_4-subunits, the gene encoding amino acid residues 47–475 of rat β_{4b}-subunit and cDNA for GST were subcloned into the pET23 vector (Novagen). The GST-β_4 fusion proteins were purified by glutathione-Sepharose beads (GE Healthcare), and the GST tag was cleaved by incubation with thrombin (4 units/ml, Sigma) for 6 h at 4 °C. Resultant GST and thrombin were removed by glutathione-Sepharose beads and by benzamidine-beads (Sigma) to obtain purified recombinant β_4-subunits. These proteins were stored at –80 °C.

GST-pulldown assay and coimmunoprecipitation in HEK293T cells- HEK293T cells were cultured in Dulbecco's modified Eagle's medium (DMEM) containing 10% fetal bovine serum, 30 units/ml penicillin, and 30 μg/ml streptomycin. Forty-eight h after transfection, HEK293T cells were solubilized in NP-40 buffer (150 mM NaCl, 50 mM Tris, 1% NP-40, and protease inhibitors), and then centrifuged at 17400 × *g* for 20 min. For pulldown assay, the cell lysate was incubated with glutathione-Sepharose beads bound with purified fusion proteins at 4 °C, then the beads were washed with NP-40 buffer. The proteins retained on the beads were characterized by WB with anti-GFP antibody (Clontech 632460). For coimmunoprecipitation, the cell lysate was incubated with anti-FLAG M2 monoclonal antibody (Sigma F3165), and then the immunocomplexes were incubated with protein A-agarose beads (Santa Cruz), and the beads were washed with NP-40 buffer. Immunoprecipitated proteins were characterized by WB with anti-β_4 antibody.

In vitro binding of the purified RIM-GST fusion proteins and recombinant β_4 protein- RIM-GST fusion proteins at various concentrations were incubated with 50 pM purified recombinant β_4-subunits for 3 h at 4 °C in PBS buffer containing 0.1% NP-40 and 50 μg/ml BSA, and then incubated with glutathione-Sepharose beads for 1 h. The beads were washed twice with the PBS buffer. The proteins retained on the beads were characterized by western blotting (WB) with the anti-β_4 antibody (12), and detected by enhanced chemiluminescence (Thermo scientific). The densities of protein signals, obtained using NIH image under the linear relationship with the applied amount of proteins, were normalized to the densities from the maximal binding.

Cell culture and cDNA expression in BHK cells- Baby hamster kidney BHK6-2 cell line stably expressing $Ca_V2.1$, α_2/δ and β_{1a} was described previously (53). BHK6-2 cells were cultured in DMEM containing 10% fetal bovine serum, 30 units/ml penicillin, and 30 μg/ml streptomycin. Transfection of cDNA plasmids was carried out using Effecten Transfection Reagent (QIAGEN). The cells were subjected to electrophysiological measurements 48 h after transfection.

Current recordings- Whole-cell mode of the patch-clamp technique was carried out at 22–25 °C with EPC-9 (*HEKA Elektronik*) patch-clamp amplifier as previously described (54). Patch pipettes were made from borosilicate glass capillaries (1.5 mm outer diameter, 0.87 mm inner diameter; Hilgenberg) using a model P-87 Flaming-Brown micropipette puller (Sutter Instrument Co.). The patch electrodes were fire-polished. Pipette resistance ranged from 2 to 3.5 megohm when filled with the pipette solutions described below. The series resistance was electronically compensated to > 60%, and both the leakage and the remaining capacitance were subtracted by –P/4 method. Currents were sampled at 100 kHz after low pass filtering at 8.4 kHz (3 db) in the experiments of activation kinetics, otherwise sampled at 20 kHz after low pass filtering at 3.0 kHz (3 db). Data were collected and analyzed using the Pulse v8.77 (HEKA Elektronic). An external solution contained (in mM): 3 $BaCl_2$, 155 tetraethylammonium chloride (TEA-Cl), 10 HEPES, and 10 glucose (pH 7.4 adjusted with TEA-OH) for BHK cells, and 10 $BaCl_2$, 153 TEA-Cl, 10

HEPES, and 10 glucose (pH 7.4 adjusted with TEA-OH) for PC12 cells. The pipette solution contained (in mM): 95 CsOH, 95 aspartate, 40 CsCl, 4 $MgCl_2$, 5 EGTA, 2 disodium ATP, 5 HEPES and 8 creatine phosphate (pH 7.2 adjusted with CsOH).

Voltage-dependence of inactivation- To determine the voltage-dependence of inactivation (inactivation curve) of VDCCs, Ba^{2+} currents were evoked by 20-ms test pulse to 5 mV after the 10-ms repolarization to –100 mV (–80 mV for PC12) following 2-s holding potential (V_h) displacement (conditioning pulse) from –100 mV to 20 mV (from –80 mV to 20 mV for PC12) with 10-mV increments. Amplitudes of currents elicited by the test pulses were normalized to those elicited by the test pulse after a 2-s V_h displacement to –100 mV (–80 mV for PC12). The mean values were plotted against potentials of the 2-s V_h displacement. When the inactivation curve was monophasic, the mean values were fitted to the single Boltzmann's equation: $h(V_h) = (1–a)+a/\{1+\exp[(V_{0.5}–V_h)/k]\}$, where a is the rate of inactivating component, $V_{0.5}$ is the potential to give a half-value of inactivation, and k is the slope factor. Otherwise, the mean values were fitted to the sum of two Boltzmann's equations: $h(V_h) = (1–a–b)+a/\{1+\exp[(V_{0.5}^{Low}–V_h)/k^{Low}]\}+b/\{1+\exp[(V_{0.5}^{High}–V_h)/k^{High}]\}$, where a, b and $(1–a–b)$ are the ratios of a low voltage-induced phase, a high voltage-induced phase, and a non-inactivating phase, $V_{0.5}^{Low}$ and $V_{0.5}^{High}$ are the potentials give a half-value of components susceptible to inactivation at low voltages in inactivation curves and at high voltages, and k^{Low} and k^{High} are the slope factors.

Voltage-dependence of activation- Tail currents were elicited by repolarization to –60 mV after 5-ms test pulse from –40 to 30 mV with 5-mV increments. Currents were sampled at 100 kHz after low pass filtering at 8.4 kHz. Amplitude of tail currents were normalized to the tail current amplitude obtained with a test pulse to 30 mV. The mean values were plotted against test pulse potentials, and fitted to the Boltzmann's equation: $n(V_m) = 1/\{1+\exp[(V_{0.5}–V_m)/k]\}$, where V_m is membrane potential, $V_{0.5}$ is the potential to give a half-value of conductance, and k is the slope factor.

RNA preparation, northern blot analysis, and real-time PCR- Total RNA was prepared from various tissues of 2-month-old C57BL/6 mice with ISOGEN total RNA isolation reagent (Nippon Gene) according to the manufacturer's instructions. For northern blot analysis, 30 μg of total RNA was separated by electrophoresis in a denaturating gel and blotted onto nylon membrane (Roche). The probes used to detect RIM1 and RIM2 RNA were cDNA fragment corresponding to nucleotides 1035–1491 of mouse RIM1α and nucleotides 592–1490 of mouse RIM2α, respectively. The probes used to detect RIM3 and RIM4 were cDNA fragment corresponding to coding sequence of mouse RIM3γ and RIM4γ , respectively. The cDNA probes were labeled with digoxigenin (DIG) using the PCR DIG Labeling kit (Roche). The hybridization, washing, and detection were performed according to the manufacturer's instructions. Equal loading of total RNA was estimated by ethidium bromide staining of ribosomal RNAs. For real-time PCR, reverse-transcription of RNA to cDNA was performed using RNA LA PCR kit (TaKaRa). Quantification was performed by real-time PCR (LightCycler Instrument, Roche) using the LightCycler FastStart DNA Master HybProbe Kit (Roche). Primer sequences are indicated in Table 5. Temperature cycles were as follows: initial 95 °C for 10 min was followed by 40 cycles at 95 °C for 10 s, 60 °C for 10 s, 72 °C for 30 s for RIM1, at 95 °C for 10 s, 60 °C for 10 s, 72 °C for 30 s for RIM2, at 95 °C for 10 s, 60 °C for 10 s, 72 °C for 30 s for RIM3, at 95 °C for 10 s, 60 °C for 10 s, 72 °C for 30 s for RIM4, and at 95 °C for 10 s, 57 °C for 5 s, 72 °C for 5 s for 18S–ribosomal RNA (18S). The results were analyzed with LightCycler software. The identity of the PCR product was confirmed by automated determination of the melting temperature of the PCR products. The results for each gene were normalized relative to 18S as described previously (55) and were expressed relative to the brain given the arbitrary value of 1.

In situ hybridization histochemistry- For histological staining of the central nervous system (CNS), adult mice (C57BL/6, body weight 20–25 g) were deeply anesthetized with an overdose of Nembutal and then transcardially perfused by 0.9% NaCl, followed by 3% paraformaldehyde in 0.1 M phosphate buffer (pH 7.4). The brains of the animals were dissected. Cryoprotection of the tissue blocks in 30% sucrose for 24 h at 4°C was followed by histological sectioning on a cryostat (Leica). For details about in situ hybridization

histochemistry, refer to Kagawa et al. (56). Briefly, *in-vitro*-transcribed DIG-labeled cRNA probe was generated against template RIM3γ or RIM4γ cDNA fragment corresponding to cording sequence of mouse RIM3γ or RIM4γ using DIG High Prime kit (Roche). The probe (0.3 μg/ml) was hybridized overnight to mouse CNS histological 35-μm-thick sections at 50°C. Positive signals were detected by alkaline phosphatase-conjugated antidigoxigenin antibody and the nitro-blue tetrazolium (NBT) 5-bromo-4-chloro-3'-indolylphosphate (BCIP) reaction.

Biochemistry of native neuronal VDCC complexes- To obtain crude synaptic membrane (CSM) fraction, subcellular fractionation was performed based on a previously described method (24), with slight modification. Whole mouse brains (8 g) were homogenized in a homogenization buffer containing 4 mM HEPES, 0.32 M sucrose, 5 mM EDTA, 5 mM EGTA, and protease inhibitors (pH 7.4). Cell debris and nuclei were removed by centrifugation at 800 × *g* for 10 min. The supernatant (S1) was centrifuged at 9,000 × *g* for 15 min to obtain crude synaptosomal fraction as pellet (P2). The supernatant was stored as S2. The crude synaptosomes were resuspended in the homogenization buffer and centrifuged at 10,000 × *g* for 15 min. The washed crude synaptosomes were lysed by hypoosmotic shock in water, rapidly adjusted to 1 mM HEPES/NaOH (pH 7.4), and stirred on ice for 30 min. After centrifugation of the lysate at 25,000 × *g* for 20 min, the pellet was resuspended in 0.25 M buffered sucrose. The synaptic membranes were then further enriched through a discontinuous sucrose gradient containing 0.8/1.0/1.2 M sucrose. After centrifugation at 65,000 × *g* for 2 h, the CSM fraction was collected from 1.0/1.2 M sucrose interface. S1, P2, S2 and CSM fractions were analyzed by WB using rabbit anti-RIM1 polyclonal antibody raised against amino acid residues 11-399 of mouse RIM1, anti-RIM3 polyclonal antibody raised against the peptide containing GSQQAGGGAGTTTAKK, anti-PSD-95 monoclonal antibody (Thermo scientific MA1-045), and anti-synaptophysin monoclonal antibody (Sigma S5768).

Synaptic membrane proteins were extracted from the CSM with solubilization buffer containing 50 mM Tris, 500 mM NaCl, a mixture of protease inhibitors, and 1% digitonin (Biosynth) (pH 7.4). After centrifugation at 147,600 × *g* for 37 min, supernatant was diluted with a buffer containing 50 mM Tris and 1%

digitonin to adjust NaCl concentration to 150 mM and incubated overnight at 4 °C. After centrifugation at 6,654 × *g* for 15 min, the supernatant was incubated with protein A-agarose coupled to anti-RIM1/2 antibody (Synaptic Systems 140-203) or anti-RIM3 polyclonal antibody for 6 h at 4 °C. Immunoprecipitated proteins were subjected to WB with anti-$Ca_V2.1$ antibody (alomone ACC-001), anti-$Ca_V2.2$ antibody (alomone ACC-002), or anti-β_4 antibody.

PC12 cell culture and siRNA suppression of endogenous RIMs in PC12 cells- PC12 cells were cultured as described previously (57). The siRNA sequences for rat RIM1 and RIM2 were described previously (12). The sense siRNA sequences 5'-AAGCTCCGAGGGCACGTTTAT-3' and 5'-AACTGGCTGGTACAAACTCTT-3' for RIM3, and 5'-AACTATGGAGGAGTTTGTCTA-3' and 5'-AACTGCCAGCTGCCTATATCA-3' for RIM4 were used. To construct siRNA oligomers, the Silencer siRNA Construction Kit (Ambion) was used. The GAPDH siRNA (siControl) used was the control provided with the kit. Transfection of siRNAs to PC12 cells was carried out using Lipofectamine^{TM} 2000 (invitrogen). Cells were transfected with combinations of 0.5 μg each of siRNAs in 35 mm culture dish. Suppression of RNA expression was confirmed by reverse transcription PCR (RT-PCR) analyses (29 cycles) using specific primers listed in Table 5 and WB analyses. RT-PCR was performed using the LA-PCR kit (TaKaRa), according to the manufacturer's instructions. The cells treated with siRNAs were subjected to WB analyses, patch-clamp measurements, imaging of secretory vesicles, or release assay 48h after transfection. To generate expression vectors (pCI-neo) for siRNA-resistant RIMs (denoted by *), silent mutations were introduced in the siRNA-binding regions of RIM. Silent mutations of RIM1 were introduced by substituting the nucleotide sequence ^{4198}aga atg gac cac aaa tgc^{4217} for ^{4198}ag**g** atg ga**t** ca**t** aa**g** tg**t**^{4217} and ^{4267}gtg att gga tgg tat aaa^{4284} for ^{4267}gt**a** at**c** gg**c** tgg ta**c** aa**g**^{4284}. Silent mutations of RIM2 were introduced by substituting the nucleotide sequence ^{4429}gcc cag ata ctc tta gat^{4446} for ^{4429}gc**g** ca**a** at**c** ct**t** tt**g** ga**c**^{4446} and ^{4453}gaa cta tcc aac^{4464} for ^{4453}ga**g** ct**t** tc**g** aa**t**^{4464}. Silent mutations of RIM3 were introduced by substituting the nucleotide sequence ^{346}agc tcc gag ggc acg ttt^{363} for ^{346}ag**t** tcc ga**a** gg**t** ac**a** tt**c**^{363} and ^{811}ggc tgg tac aaa^{822} for ^{811}gg**t** tgg ta**t** aa**g**^{822}. Silent mutations of RIM4 were introduced by substituting the nucleotide sequence ^{244}tat gga gga gtt tgt^{258} for

^{244}ta**c** gg**c** gg**c** gt**a** tg**c**^{258} and ^{445}ctg cca gct gcc tat atc^{462} for ^{445}ct**a** cc**t** gc**a** gc**t** ta**c** at**a**^{462}. Letters in bold indicate mutated nucleotides. In rescue experiments, rescue plasmids were cotransfected with siRNAs using Lipofectamine^{TM} 2000. 1.0 μg each of siRNA-resistant RIM1* and RIM2* and/or 0.4 μg each of siRNA-resistant RIM3* and RIM4* were cotransfected with 0.5 μg each of siRNA in 35 mm culture dish.

WB analysis of PC12 cells transfected with siRNAs- PC12 cells transfected with siRNAs were solubilized and analyzed by WB using anti-$Ca_V2.1$ polyclonal antibody, anti-$Ca_V2.2$ polyclonal antibody, anti-β_3 antibody (Abcam ab16717), anti-RIM1/2 polyclonal antibody, anti-RIM3 polyclonal antibody, anti-RIM4 polyclonal antibody (Santa Cruz Biotechnology sc-85885), anti-Munc13 monoclonal antibody, anti-Synaptotagmin I monoclonal antibody (WAKO 017-15761), anti-SNAP-25 monoclonal antibody (BD Transduction Laboratory S35020), anti-Syntaxin monoclonal antibody, and anti-Rab3 monoclonal antibody (BD Transduction Laboratory 610379).

Total internal reflection fluorescence (TIRF) imaging of secretory vesicles- PC12 cells cotransfected with pVenus-N1-NPY carrying a DNA construct for the fusion protein of neuropeptide Y (NPY) and the fluorescent protein Venus (NPY-Venus) and mixture of RIM siRNAs using OptiFect (invitrogen) were plated onto poly-L-lysine-coated coverslips. The imaging was performed in modified Ringer's buffer that contained (in mM): 130 NaCl, 3 KCl, 5 $CaCl_2$, 1.5 $MgCl_2$, 10 glucose, and 10 HEPES (pH 7.4). Fluorescence images of NPY-Venus in large dense core vesicles were observed as previously reported (12, 58). In brief, a high numerical aperture objective lens (Plan Apochromatic, 100×, numerical aperture = 1.45, infinity-corrected, Olympus) was mounted on an inverted microscope (IX71, Olympus), and incident light for total internal reflection illumination was introduced from the high numerical objective lens through a single mode optical fiber. A diode-pumped solid state 488-nm laser (kyma488, 20 milliwatt, MELLES GRIOT) was used for total internal fluorescence illumination and 510-nm long pass filter as an emission filter. Images were captured by a cooled CCD camera (EM-CCD, Hamamatsu Photonics) operated with Metamorph (Molecular Devices). Densities of vesicles were assessed by counting the number of individual fluorescent spots in the

area where vesicles show uniform distribution in TIRF images, and obtained numbers were divided by areas. Area calculations were performed using Metamorph softwares. The cells with distribution of vesicles by a dark spot with area > 10 μm^2 were omitted, to select the cells, in which vesicles were uniformly distributed, for the analyses. Ten μm^2 was adopted, because 10 μm^2 was the maximal dark circle area that can be located in between vesicles in the images from siRIM1&2-transfected cells with uniform vesicle distribution.

Release assay in PC12 cells- Acetylcholine (ACh) secretion experiments were performed as previously reported with slight modifications (57). PC12 cells were plated in poly-D-lysine-coated 35-mm dishes (BD bioscience) with 5×10^5 cells per dish. Cells were cotransfected with 5 μg of each RIM plasmid and 1 μg of pEFmChAT encoding mouse ChAT cDNA using Lipofectamine^{TM} 2000. Three days after transfection, PC12 cells were washed with a 5.9 mM K^+ solution that contained (in mM): 0.01 eserine, 140 NaCl, 4.7 KCl, 1.2 KH_2PO_4, 2.5 $CaCl_2$, 1.2 $MgSO_4$, 11 glucose, and 15 HEPES (pH 7.4 adjusted with NaOH) and incubated for 30 s with the 5.9 mM K^+ solution at 37 °C. The release of ACh during this period was considered as basal release. To measure K^+-stimulated release of ACh, the cells were then incubated for 30 s with a 51.1 mM K^+ solution that contained (in mM): 0.01 eserine, 94.8 NaCl, 49.9 KCl, 1.2 KH_2PO_4, 2.5 $CaCl_2$, 1.2 $MgSO_4$, 11 glucose, and 15 HEPES (pH 7.4 adjusted with NaOH) or for 2 min with a 28.4 mM K^+ solution that contained (in mM): 0.01 eserine, 94.8 NaCl, 27.2 KCl, 1.2 KH_2PO_4, 2.5 $CaCl_2$, 1.2 $MgSO_4$, 11 glucose, and 15 HEPES (pH 7.4 adjusted with NaOH). Supernatant from cells solubilized in NP-40 buffer and centrifuged at 17400 × *g* for 20 min at 4 °C was taken as the cellular ACh that was not secreted. ACh was measured using HPLC with electrochemical detection (HTEC-500, EiCOM).

Fluorescent $[Ca^{2+}]_i$ measurements- PC12 cells cotransfected with pEGFP-N1 and mixture of RIM siRNAs using OptiFect (invitrogen). Thirty-six h after transfection, PC12 cells were plated onto poly-L-lysine coated glass coverslips. Forty-eight h after transfection, cells on coverslips were loaded with fura-2 by incubation in DMEM containing 10 μM fura-2/AM (Dojindo Laboratories), 0.04% Pluronic F-127 (Biotium), and 10% fetal bovine serum at 37 °C for 40 min and washed with the 5.9 mM K^+ solution. The

coverslips were then placed in a perfusion chamber mounted on the stage of the microscope. Fluorescence images of the cells were recorded and analyzed with a video image analysis system (AQUACOSMOS, Hamamatsu Photonics). The fura-2 fluorescence at an emission wavelength of 510 nm was observed at 37 ± 1 °C by exciting fura-2 alternately at 340 and 380 nm. Measurement was carried out in 5.9 mM K^+ solution, 51.1 mM K^+ solution, and 28.4 mM K^+ solution. The 340:380 nm ratio images were obtained on a pixel by pixel basis and were converted to Ca^{2+} concentrations by in vivo calibration using 40 μM ionomycin (59).

Construction of short hairpin RNA (shRNA) vectors- shRNA vectors were constructed based upon a pSUPER.neo+GFP vector (OligoEngine). To create shRIM2, shRIM3, and shRIM4, two complementary 60-bp oligonucleaotides carring antisense and sense sequence for GGCCCAGATACTCTTAGAT (19-bp corresponding to nucleotides 4554-4572 of rat RIM2), CTGGCTGGTACAAATTCTT (nucleotides 1252-1270 of rat RIM3), and CTGCCAGCTGCCTATATCA (nucleotides 445-463 of rat RIM4) were annealed and ligated to pSUPER.neo+GFP vectors in accordance with OligoEngine's instructions. To create shRIM1, 60-bp oligonucleaotides carrying GTAATAAATGAAGAGGTTTAAACTTCTTCGTTTGTTGC and its complementary sequence were annealed and ligated to pSUPER.neo+GFP vectors. In construction of shRIM1, we inserted mutation in the stem sequence of shRNA according to the previous report (60) for better silencing efficiency. shControl was generated similarly except that an artificial 19-mer sequence (ATCCGCGCGATAGTACGTA) was used as a target. This sequence was based upon a commercially available negative control siRNA sequence (B-Bridge International), and we confirmed it had no significant identity to any known mammalian gene based on a BLAST search.

Rat cerebellar neuron primary cultures and transfection- Primary cerebellar neuron cultures were prepared as previously described (61) with minor modifications. Briefly, cerebella from 7–9-day-old Wister rat pups were digested with 1% trypsin (Difco). The solution was removed after a brief centrifugation, and the tissue was mechanically dissociated by repeated pipetting in DMEM containing 10% fetal calf serum (FCS) (GIBCO). The cell suspension was centrifuged at 200 × *g* for 3 min. The pellet was resuspended in

DMEM containing 10% FCS and filtered through a 70-μm cell strainer. After centrifugation at 100 × *g* for 5 min, 5×10^6 cells were re-suspended in 100 μl rat neuron nucleofector solution (Amaxa) with 3 μg shRNA vector (total amount of DNA was 4 μg in all cases). The cell suspension was electroporated using the G-13 program (Amaxa). The cells were diluted with DMEM containing 10% FCS, and seeded onto polyethyleneimine-coated 15-mm diameter four-well multidish (Nunc) at a density of 1×10^6 per well. Two h after initial plating, the medium was removed and gently replaced with Neurobasal medium containing 0.5 mM glutamine, 26 mM KCl, 60 U/ml penicillin, 60 μg/ml streptomycin, and 2% B-27 (Invitrogen). The cultures were maintained at 37 °C with 5% CO_2. The medium was very gently replaced with fresh medium every 3 days.

Glutamate release assay- After the transfection with shRNA vectors, cerebellar neurons (10 days in vitro (DIV)) were washed briefly with pre-warmed low-K^+ solution that contained (in mM): 140 NaCl, 4.7 KCl, 1.2 KH_2PO_4, 2.5 $CaCl_2$, 1.2 $MgSO_4$, 11 glucose, and 15 HEPES-NaOH (pH 7.4), and were incubated for 1 min with the low-K^+ solution at 37 °C. The release of glutamate during this period was considered as basal release. To measure K^+-stimulated release of glutamate, the cells were then incubated for 1 min with a high-K^+ solution that contained (in mM): 94.8 NaCl, 49.9 KCl, 1.2 KH_2PO_4, 2.5 $CaCl_2$, 1.2 $MgSO_4$, 11 glucose, 15 HEPES-NaOH (pH 7.4). Glutamate was determined by reverse-phase HPLC on an Eicompak SC-5ODS (EiCOM), using precolum derivatization with *o*-phthalaldehyde and electrochemical detection (HTEC-500, EiCOM).

Confocal imaging- PC12 cells were co-transfected with pVenus-N1-NPY or pEGFP-N1 and mixture of RIM siRNAs using OptiFect (invitrogen). Thirty-six h after transfection, PC12 cells were plated onto poly-L-lysine coated glass coverslips. Forty-eight h after transfection, cells were fixed, permeabilized, and stained with anti-RIM1/2 polyclonal antibody (Synaptic Systems 140-203) or anti-Syntaxin monoclonal antibody (Sigma S0664) and Cy3-conjugated secondary antibody (Invitrogen). Fluorescence images were acquired with a confocal laser-scanning microscope (Olympus FV500) using the 488-nm line of an argon laser

for excitation and a 505-nm to 525-nm band-pass filter for emission (Venus and EGFP), or the 543-nm line of a HeNe laser for excitation and a 560-nm long-pass filter for emission (Cy3). The specimens were viewed at high magnification using plan oil objectives (× 60, 1.40 numerical aperture (NA), Olympus).

TIRF imaging of RIM1 and RIM2 immunoreactivity- pDsRed-monomer-N1 (Clontech) and mixture of RIMs siRNAs were transfected into PC12 cells. Thirty-six h after transfection, PC12 cells were plated onto poly-L-lysine coated glass coverslips. Forty-eight h after transfection, cells were fixed, permeabilized, and stained with anti-RIM1/2 polyclonal antibody (Synaptic Systems 140-203) and Alexa Fluor-488-conjugated anti-rabbit secondary antibody (Invitrogen). TIRF images were obtained using 100 x 1.45-numerical-aperture TIRF objective fitted to an inverted microscope system (Olympus IX71) and a 488-nm laser line (kyma488, 20 milliwatt, MELLES GRIOT), and images were acquired using a cooled CCD camera (EM-CCD Hamamatsu Photonics) and recorded with Metamorph software (Molecular Devices). Area and fluorescent intensity calculations were also performed using Metamorph software. Relative intensities of RIM1/2 immunoreactivity were estimated by normalizing average intensity in Ds-Red positive cells to that in Ds-Red negative cells in the same visual field.

Coimmunoprecipitation using PC12 cell lysate- HEK293T cells were transfected with pCMV-tag2-RIMs. Forty-eight h after transfection, HEK293T cells were solubilized in NP-40 buffer, and then centrifuged at 17400 × *g* for 20 min. The supernatant was incubated with PC12 cell lysate for 6 h at 4 °C. For coimmunoprecipitation, the mixture was incubated with anti-FLAG M2 monoclonal antibody (Sigma F3165) or polyclonal (Sigma F7425) antibody. The immunocomplexes were incubated with protein A-agarose beads (Santa Cruz), and the beads were washed with NP-40 buffer. Immunoprecipitated proteins were characterized by WB. Association between Rab3 and RIMs are evaluated in the presence of 0.5 mM Guanosine-5'-O-(3-thiotriphosphate) (GTPγS). Mouse anti-Munc13 monoclonal antibody (BD Transduction Laboratory 610998), mouse anti-Rab3 monoclonal antibody (BD Transduction Laboratory 610379), and chicken anti-Liprin1-α polyclonal antibody (Sigma GW21470) were used as a primary antibody.

Statistical analysis- All data accumulated under each condition from at least three independent experiments are expressed as means ± S.E.M. Student's t-test or ANOVA followed by Fisher's test was employed.

Table 5 Antisense and sense PCR primers used in real-time PCR or RT-PCR analysis.

Species	Gene	Orientation	Pair of primers for PCR (5' to 3')
Mouse (for real-time PCR)	RIM1	Sense	GTTGGAGGTTGAGGTTATCAGAGCCCGGAG
		Antisense	GACGAACTTTCCAGTGATGATTGGGAAGC
	RIM2	Sense	GACAGCTGGAGGTAGAAATCATCCG
		Antisense	GAACCATCCAATCACCATGTTGGATAG
	RIM3	Sense	GTACCAGCAAGCTCTGCTCTTTGATG
		Antisense	GCCGGTGACTGCAGCACTCAGGTCCAGCTCG
	RIM4	Sense	GCTCGAAGACACTGCCAGCTGCCTATATCAAG
		Antisense	AGGACTCGAGCCACGCCCATGAACTG
	18S ribosomal RNA	Sense	GAGGTAGTGACGAAAAATAACAAT
		Antisense	TTGCCCTCCAATGGATCCT
		Antisense (Reverse Transcript)	GAGCTGGAATTACCGCGGCT
Rat (for RT-PCR)	RIM1	Sense	CAGCATCAACAGTTATAGCTCGG
		Antisense	CATCCAATCACCATGCTGGATAG
	RIM2	Sense	GGATCACAAATCCTTTATGGGAGTGG
		Antisense	CACAGGATGGCTCTTTATCCCTAGAC
	RIM3	Sense	GGATCACAAGTGCTTCATGGGTATGG
		Antisense	GGGTAAGGGGTCCAGAAGGTCATGGAG
	RIM4	Sense	GGAAACTACGGACGAATGGAGCGGAAG
		Antisense	GGGCCCCACGGTGCTCTCGAGGGACAGCTG
	β-actin	Sense	TTCTACAATGAGCTGCGTGTGGC
		Antisense	CTCATAGCTCTTCTCCAGGGAGGA
	GAPDH	Sense	ATCACCATCTTCCAGGAGCGAG
		Antisense	CAACGGATACATTGGGGGTAGG

References

1. Sheng, M. and Hoogenraad, C. C. (2007) *Annu. Rev. Biochem.* **76**, 823–847
2. Ohtsuka, T., Takao-Rikitsu, E., Inoue, E., Inoue, M., Takeuchi, M., Matsubara, K., Deguchi-Tawarada, M., Satoh, K., Morimoto, K., Nakanishi, H., and Takai, Y. (2002) *J. Cell Biol.* **158**, 577–590
3. Zhai, R. G. and Bellen, H. J. (2004) *Physiology (Bethesda)* **19**, 262–270
4. Südhof, T. C. (2004) *Annu. Rev. Neurosci.* **27**, 509–547
5. Schoch, S. and Gundelfinger, E. D. (2006) *Cell Tissue Res.* **326**, 379–391

6. Wojcik, S. M. and Brose, N. (2007) *Neuron* **55**, 11–24

7. Stanley, E. F. (1993) *Neuron* **11**, 1007–1011

8. Sheng, Z. H., Rettig, J., Takahashi, M., and Catterall, W. A. (1994) *Neuron* **13**, 1303–1313

9. Bezprozvanny, I., Scheller, R. H., and Tsien, R. W. (1995) *Nature* **378**, 623–626

10. Neher, E. (1998) *Neuron* **20**, 389–399

11. Wadel, K., Neher, E., and Sakaba, T. (2007) *Neuron* **53**, 563–575

12. Kiyonaka, S., Wakamori, M., Miki, T., Uriu, Y., Nonaka, M., Bito, H., Beedle, A. M., Mori, E., Hara, Y., De Waard, M., Kanagawa, M., Itakura, M., Takahashi, M., Campbell, K. P., and Mori, Y. (2007) *Nat. Neurosci.* **10**, 691–701

13. Catterall, W. A. and Few, A. P. (2008) *Neuron* **59**, 882–901

14. Tsien, R. W., Ellinor, P. T., and Horne, W. A. (1991) *Trends Pharmacol. Sci.* **12**, 349–354

15. Takahashi, T. and Momiyama, A. (1993) *Nature* **366**, 156–158

16. Wheeler, D. B., Randall, A., and Tsien, R. W. (1994) *Science* **264**, 107–111

17. Catterall, W. A. (1998) *Cell Calcium* **24**, 307–323

18. Ertel, E. A., Campbell, K. P., Harpold, M. M., Hofmann, F., Mori, Y., Perez-Reyes, E., Schwartz, A., Snutch, T. P., Tanabe, T., Birnbaumer, L., Tsien, R. W., and Catterall, W. A. (2000) *Neuron* **25**, 533–535

19. Zhong, H., Yokoyama, C. T., Scheuer, T., and Catterall, W. A. (1999) *Nat. Neurosci.* **2**, 939–941

20. Maximov, A., Südhof, T. C., and Bezprozvanny, I. (1999) *J. Biol. Chem.* **274**, 24453–24456

21. Maximov, A. and Bezprozvanny, I. (2002) *J. Neurosci.* **22**, 6939–6952

22. Spafford, J. D. and Zamponi, G. W. (2003) *Curr. Opin. Neurobiol.* **13**, 308–314

23. Nishimune, H., Sanes, J. R., and Carlson, S. S. (2004) *Nature* **432**, 580–587

24. Kang, M., Chen, C., Wakamori, M., Hara, Y., Mori, Y., and Campbell, K. P. (2006) *Proc. Natl. Acad. Sci. U.S.A.* **103**, 5561–5566

25. Mori, Y., Friedrich, T., Kim, M. S., Mikami, A., Nakai, J., Ruth, P., Bosse, E., Hofmann, F., Flockerzi, V., Furuichi, T., Mikoshiba K., Imoto K., Tanabe T., and Numa S. (1991) *Nature* **350**, 398–402

26. Bichet, D., Cornet, V., Geib, S., Carlier, E., Volsen, S., Hoshi, T., Mori, Y., and De Waard, M. (2000)

Neuron **25**, 177–190

27. Varadi, G., Lory, P., Schultz, D., Varadi, M., and Schwartz, A. (1991) *Nature* **352**, 159–162
28. Lacerda, A. E., Kim, H. S., Ruth, P., Perez-Reyes, E., Flockerzi, V., Hofmann, F., Birnbaumer, L., and Brown, A. M. (1991) *Nature* **352**, 527–530
29. Béguin, P., Nagashima, K., Gonoi, T., Shibasaki, T., Takahashi, K., Kashima, Y., Ozaki, N., Geering, K., Iwanaga, T., and Seino, S. (2001) *Nature* **411**, 701–706
30. Hibino, H., Pironkova, R., Onwumere, O., Rousset, M., Charnet, P., Hudspeth, A. J., and Lesage, F. (2003) *Proc. Natl. Acad. Sci. U.S.A.* **100**, 307–312
31. Vendel, A. C., Terry, M. D., Striegel, A. R., Iverson, N. M., Leuranguer, V., Rithner, C. D., Lyons, B. A., Pickard, G. E., Tobet, S. A., and Horne, W. A. (2006) *J. Neurosci.* **26**, 2635–2644
32. Wang, Y., Okamoto, M., Schmitz, F., Hofmann, K., and Südhof, T. C. (1997) *Nature* **388**, 593–598
33. Wang, Y. and Südhof, T. C. (2003) *Genomics* **81**, 126–137
34. Kaeser, P. S., Kwon, H., Chiu, C. Q., Deng, L., Castillo, P. E., and Südhof, T. C. (2008) *J. Neurosci.* **28**, 13435–13447
35. Liang, F., Zhang, B., Tang, J., Guo, J., Li, W., Ling, E. A., Chu, H., Wu, Y., Chan, Y. G., and Cao, Q. (2007) *J. Comp. Neurol.* **503**, 501–510
36. Wang, Y. J., Sugita, S., and Südhof, T. C. (2000) *J. Biol. Chem.* **275**, 20033–20044
37. Betz, A., Thakur, P., Junge, H. J., Ashery, U., Rhee, J. S., Scheuss, V., Rosenmund, C., Rettig, J., and Brose, N. (2001) *Neuron* **30**, 183–196
38. Coppola, T., Magnin-Luthi, S., Perret-Menoud, V., Gattesco, S., Schiavo, G., and Regazzi, R. (2001) *J. Biol. Chem.* **276**, 32756–32762
39. Schoch, S., Castillo, P. E., Jo, T., Mukherjee, K., Geppert, M., Wang, Y., Schmitz, F., Malenka, R. C., and Südhof, T. C. (2002) *Nature* **415**, 321–326
40. Stanley, E. F. and Goping, G. (1991) *J. Neurosci.* **11**, 985–993
41. Forsythe, I. D., Tsujimoto, T., Barnes-Davies, M., Cuttle, M. F., and Takahashi, T. (1998) *Neuron* **20**, 797–807

42. Johnson, S., Halford, S., Morris, A. G., Patel, R. J., Wilkie, S. E., Hardcastle, A. J., Moore, A. T., Zhang, K., and Hunt, D. M. (2003) *Genomics* **81**, 304–314

43. Miki, T., Kiyonaka, S., Uriu, Y., De Waard, M., Wakamori, M., Beedle, A. M., Campbell, K. P., and Mori, Y. (2007) *Channels (Austin)* **1**, 144–147

44. Castillo, P. E., Schoch, S., Schmitz, F., Südhof, T. C., and Malenka, R. C. (2002) *Nature* **415**, 327–330

45. Fourcaudot, E., Gambino, F., Humeau, Y., Casassus, G., Shaban, H., Poulain, B., and Lüthi, A. (2008) *Proc. Natl. Acad. Sci. U.S.A.* **105**, 15130–15135

46. Lachamp, P. M., Liu, Y., and Liu, S. J. (2009) *J. Neurosci.* **29**, 381–392

47. Calakos, N., Schoch, S., Südhof, T. C., and Malenka, R. C. (2004) *Neuron* **42**, 889–896

48. Schoch, S., Mittelstaedt, T., Kaeser, P. S., Padgett, D., Feldmann, N., Chevaleyre, V., Castillo, P. E., Hammer, R. E., Han, W., Schmitz, F., Lin, W., and Südhof, T. C. (2006) *EMBO J.* **25**, 5852–5863

49. Weimer, R. M., Gracheva, E. O., Meyrignac, O., Miller, K. G., Richmond, J. E., and Bessereau, J. (2006) *J. Neurosci*. **26**, 8040–8047

50. Gracheva, E. O., Hadwiger, G., Nonet, M. L., and Richmond, J. E. (2008) *Neurosci. Lett*. **444**, 137–142

51. Ozaki, N., Shibasaki, T., Kashima, Y., Miki, T., Takahashi, K., Ueno, H., Sunaga, Y., Yano, H., Matsuura, Y., Iwanaga, T., Takai, Y., and Seino, S. (2000) *Nat. Cell Biol.* **2**, 805–811

52. Wong, F. K. and Stanley, E. F. (2010) *J. Neurochem.* **112**, 463–473

53. Niidome, T., Teramoto, T., Murata, Y., Tanaka, I., Seto, T., Sawada, K., Mori, Y., and Katayama, K. (1994) *Biochem. Biophys. Res. Commun.* **203**, 1821–1827

54. Wakamori, M., Yamazaki, K., Matsunodaira, H., Teramoto, T., Tanaka, I., Niidome, T., Sawada, K., Nishizawa, Y., Sekiguchi, N., Mori, E., Mori, Y., and Imoto, K. (1998) *J. Biol. Chem.* **273**, 34857–34867

55. Zhu, L. and Altmann, S. W. (2005) *Anal. Biochem.* **345**, 102–109

56. Kagawa, T., Ikenaka, K., Inoue, Y., Kuriyama, S., Tsujii, T., Nakao, J., Nakajima, K., Aruga, J., Okano, H. and Mikoshiba, K. (1994) *Neuron* **13**, 427–442

57. Itakura, M., Misawa, H., Sekiguchi, M., Takahashi, S., and Takahashi, M. (1999) *Biochem. Biophys.*

Res. Commun. **265**, 691-696

58. Tsuboi, T. and Fukuda, M. (2006) *J. Cell. Sci.* **119**, 2196–2203
59. Nishida, M., Nagao, T., and Kurose, H. (1999) *Biochem. Biophys. Res. Commun.* **262**, 350–354
60. Patzel, V., Rutz, S., Dietrich, I., Köberle, C., Scheffold, A., and Kaufmann, S. H. E. (2005) *Nat. Biotechnol.* **23**, 1440–1444
61. Koga, T., Kozaki, S., and Takahashi, M. (2002) *Brain Res.* **952**, 282–289
62. Castellano, A., Wei, X., Birnbaumer, L., and Perez-Reyes, E. (1993) *J. Biol. Chem.* **268**, 3450–3455
63. Castellano, A., Wei, X., Birnbaumer, L., and Perez-Reyes, E. (1993) *J. Biol. Chem*. **268**, 12359–12366
64. Ruth, P., Röhrkasten, A., Biel, M., Bosse, E., Regulla, S., Meyer, H. E., Flockerzi, V., and Hofmann, F. (1989) *Science* **245**, 1115–1118
65. Hullin, R., Singer-Lahat, D., Freichel, M., Biel, M., Dascal, N., Hofmann, F., and Flockerzi, V. (1992) *EMBO J.* **11**, 885–890
66. Plummer, M. R., Logothetis, D. E., and Hess, P. (1989) *Neuron* **2**, 1453–1463
67. Liu, H., Felix, R., Gurnett, C. A., De Waard, M., Witcher, D. R., and Campbell, K. P. (1996) *J. Neurosci.* **16**, 7557–7565
68. Gebhart, M., Juhasz-Vedres, G., Zuccotti, A., Brandt, N., Engel, J., Trockenbacher, A., Kaur, G., Obermair, G. J., Knipper, M., Koschak, A., and Striessnig, J. (2010) *Mol. Cell. Neurosci*., in press
69. Shibasaki, T., Sunaga, Y., Fujimoto, K., Kashima, Y., and Seino, S. (2004) *J. Biol. Chem.* **279**, 7956–7961
70. Hibino, H., Pironkova, R., Onwumere, O., Vologodskaia, M., Hudspeth, A., and Lesage, F. (2002) *Neuron* **34**, 411–423
71. De Waard, M., Pragnell, M., and Campbell, K. P. (1994) *Neuron* **13**, 495–503
72. Richards, M. W., Leroy, J., Pratt, W. S., and Dolphin, A. C. (2007) *Channels (Austin)* **1**, 92–101
73. Liu, T.-T., Kishimoto, T., Hatakeyama, H., Nemoto, T., Takahashi, N., and Kasai, H. (2005) *J. Physiol. (Lond.)* **568**, 917–929
74. Westenbroek, R. E., Hoskins L., and Catterall, W. A. (1998) *J. Neurosci.* **15**, 6319–6330

75. Craig, P. J., McAinsh, A. D., McCormack, A. L., Smith, W., Beattie, R. E., Priestley, J. V., Yip, J. L., Averill, S., Longbottom, E. R., and Volsen, S. G. (1998) *J. Comp. Neurol.* **397**, 251–267

76. Hanson J. E. and Smith Y. (2002) *J. Comp. Neurol.* **442**, 89–98

77. Llinás, R., Sugimori, M., Lin, J. W., and Cherksey, B. (1989) *Proc. Natl. Acad. Sci. U.S.A.* **86**, 1689–1693

78. Randall, A. and Tsien, R. W. (1995) *J. Neurosci.* **15**, 2995–3012

79. Sather, W. A., Tanabe, T., Zhang, J., Mori, Y., Adams, M. E., and Tsien, R. W. (1993) *Neuron* **11**, 291–303

80. Jun, K., Piedras-Rentería, E. S., Smith, S. M., Wheeler, D. B., Lee, S. B., Lee, T. G., Chin, H., Adams, M. E., Scheller, R. H., Tsien, R. W., and Shin, H. S. (1999) *Proc. Natl. Acad. Sci. U.S.A.* **96**, 15245–15250

81. Fletcher, C. F., Tottene, A., Lennon, V. A., Wilson, S. M., Dubel, S. J., Paylor, R., Hosford, D. A., Tessarollo, L., McEnery, M. W., Pietrobon, D., Copeland, N. G., and Jenkins, N. A. (2001) *FASEB J.* **15**, 1288–1290

82. Toru, S., Murakoshi, T., Ishikawa, K., Saegusa, H., Fujigasaki, H., Uchihara, T., Nagayama, S., Osanai, M., Mizusawa, H., and Tanabe, T. (2000) *J. Biol. Chem.* **275**, 10893–10898

83. Saegusa, H., Wakamori, M., Matsuda, Y., Wang, J., Mori, Y., Zong, S., and Tanabe, T. (2007) *Mol. Cell. Neurosci.* **34**, 261–270

84. Llinás, R. and Sugimori, M. (1980) *J. Physiol. (Lond.)* **305**, 197–213

Chapter 3

Functional impacts of Munc18-1 on the gating properties of voltage-dependent Ca^{2+} channels.

Abstract

Interaction of voltage-dependent Ca^{2+} channels (VDCCs) with associated proteins regulates coupling of VDCCs with upstream and downstream cellular events. Here, we demonstrate a previously unknown interaction between two components of the presynaptic active zone, Munc18-1 and VDCCs, which controls neurotransmitter release in mammalian neurons. Munc18-1 was found to selectively associate with VDCC β_{1a}-, β_3-, and β_{4b}-subunit to modulate gating properties of P/Q-type VDCCs. Thus, Munc18-1 promoted inactivation of β_3-, and β_{4b}-containing VDCC, and slowed activation of β_{1a}-, β_3-, and β_{4b}-containing VDCC. These findings lead the author to hypothesize that munc18-1 may allow synaptic vesicles to become docked and /or ready for fusion in the vicinity of VDCC without exposing fusion machinery to robust Ca^{2+} entry.

Introduction

Protein complexes play essential roles in various cellular responses including neurotransmission via synapses in the nervous system. In central synapses, postsynaptic density is established by protein complexes containing neurotransmitter receptors, signaling and cytoskeletal proteins, and scaffolding proteins such as PSD-95 (1), while active zones are formed by cytomatrix and other proteins responsible for neurotransmitter release from presynaptic nerve terminals (2–6). For Ca^{2+} influx upon membrane potential depolarization to evoke neurotransmitter release, efficient coupling of VDCCs to protein machineries such as soluble N-ethylmaleimide-sensitive factor attachment protein receptor (SNARE) mediating fusion of neurotransmitter-containing vesicles with presynaptic membranes is critical (7–13). Thus, it is extremely important to identify protein associations and their functional significance in understanding neurotransmission.

Multiple types of VDCCs are distinguished on the basis of biophysical and pharmacological properties (14). In neurons, high voltage-activated (HVA) VDCC types such as N-, P/Q-, R-, and L-types are essential for neurotransmitter release from presynaptic terminals (15–17). Furthermore, presynaptic Ca^{2+} channels were considered to serve as the regulatory node in a dynamic, multilayered signaling network that exerts short-term control of neurotransmission in response to synaptic activity (13). Biochemically, VDCCs are known as heteromultimeric protein complexes composed of the pore-forming α_1 and auxiliary subunits α_2/δ, β, and γ (18). The α_1-subunit, designated as Ca_V, is encoded by ten distinct genes, whose correspondence with functional types has largely been elucidated (14, 18). VDCC complexes are primarily known for their association with presynaptic and postsynaptic proteins including syntaxin, 25-kD synaptosomal protein (SNAP-25), synaptotagmin, CASK and Munc18-1-interacting protein (Mint) via interactions with the α_1-subunit (8, 9, 19–24). It was traditionally believed that anchoring Ca^{2+} channels close to the Ca^{2+} microdomain-dependent release machinery was the main reason for the physical interactions between channels and synaptic proteins, however in recent years, it is becoming clear that these proteins additionally regulate channel activity. β-subunits interact with α_1 from the cytoplasmic side to enhance functional channel trafficking to the plasma membrane (25, 26) and to modify multiple kinetic properties (27, 28).

Association with other proteins has been also revealed for β-subunits (12, 29, 30, 31). Considering the cytoplasmic disposition of β-subunits, it is intriguing to investigate whether β-subunits are involved in targeting specific subcellular machinery to VDCC complexes at presynaptic active zones for neurotransmitter release through as yet unidentified protein interactions.

Munc18-1 has been found to be the prevailing mammalian neuronal orthologue of *c. elegans unc-18* (32), widely distributed (33), present at active zones (34) and essential for transmitter release from presynaptic nerve terminals in nematode worm (35), drosophila flys (36) and mice (37, 38). Munc18-1 null mutant mice show no evidence of any neurotransmission (38), and there is also a severe impairment of dense core granule exocytosis in their adrenal chromaffin cells (39). Munc18-1 binds to syntaxin 1 with multiple binding modes. Mode 1 is a well-characterized interaction of Munc18-1 with syntaxin 1 in its closed conformation (40). Mode 2 involves interaction of Munc18-1 with the extreme N-terminus of syntaxin 1. Mode 3 involves interaction of Munc18-1 with assembled SNARE complex. The latter mode requires mode 2 to be achievable, but it is not known if both modes occur at the same time. While the interaction of Munc18-1 with syntaxin 1 must reflect an important biological function, this is unlikely to be its only role in neurosecretion. Indeed, it has been suggested that Munc18-1 is also involved in the docking of secretory vesicles (38, 41). This hypothesis supported both by peptide injection into the squid giant synapse (42) and observations on knockouts and mutants of Unc-18 in *c.elegans* (35) or Munc18-1 in mouse anterior pituitary (43) and chromaffin cells (44). Current evidence suggests that Munc18-1 influences all of the steps leading to exocytosis, including vesicle recruitment, tethering, docking, priming, and membrane fusion (45).

A recent study provided evidence for the direct binding of Munc18-1 to the presynaptic calcium channel α_1-subunit (46). However, the physiological significance of this interaction and the effect of Munc18-1 on VDCC currents were remain elusive. Here we demonstrate a previously unknown molecular interaction between Munc18-1 and VDCC β-subunits, both of which are essential presynaptic active zone protein. Munc18-1 selectively associated with the VDCC β_{1a}-, β_3-, and β_{4b}-subunit to modulate gating properties of P/Q-type VDCCs. Munc18-1 promoted inactivation of β_3-, and β_{4b}-containing VDCC, and slowed activation of β_{1a}-, β_3-, and β_{4b}-containing VDCC.

Results

VDCC β-subunits directly interact with Munc18-1

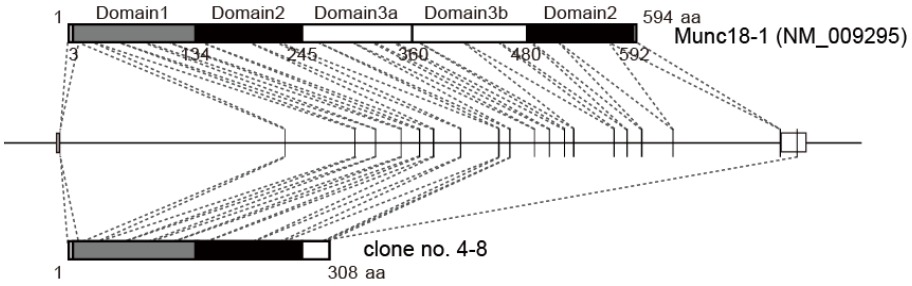

Fig. 1 The schematic representation of two splicing variants of the Munc18-1 domains.

To identify β-subunit interacting proteins that regulate presynaptic active zone organization, we performed yeast two-hybrid screening with a mouse brain complementary DNA library using the full-length rat β_{4b}-subunit as a bait. The β_4-subunit was chosen because spontaneous β_4 mutant *Cacnb4lh* (lethargic) mice have clear neurological defects suggesting that β_4-containing VDCCs are physiologically significant in the brain. Screening identified a clone (no. 4-8) encoding a minor variant of mouse Munc18-1 protein (Fig. 1). This variant contained 1–305 amino acid of reported Munc18-1 (Genbank accession NM_009295) and unique three amino acids (PLQ). Subsequent yeast two-hybrid assays using β_{4b} mutants showed that residues 22–203, containing the Src homology 3 (SH3) domain were required for the interaction of β_{4b} with the Munc18-1 (no. 4-8) (Fig. 2 *A*). β_{1a} and β_3, but not β_{2a}, also interact with Munc18-1 (no. 4-8). To determine the interaction between a major variant of Munc18-1 (NM_009295) and β-subunit, pulldown assays were performed. In vitro pulldown assays using glutathione-S-transferase (GST) fusion constructs of β-subunits revealed that Munc18-1 (NM_009295) had boud to β_{1a}, β_3, and β_{4b}-subunits, but not β_{2a}-subunit (Fig. 2*B*). Coimmunoprecipitation experiments also revealed an association between recombinant VDCC β-subunits and EGFP-tagged Munc18-1 (NM_009295) in HEK293T cells (Fig. 2*C*). Munc18-1 shows higher affinity to β_{1a}, β_3, and β_{4b}-subunits compared to β_{2a}-subunit. This is consistent with the results of yeast two-hybrid assays and GST-pulldown assays.

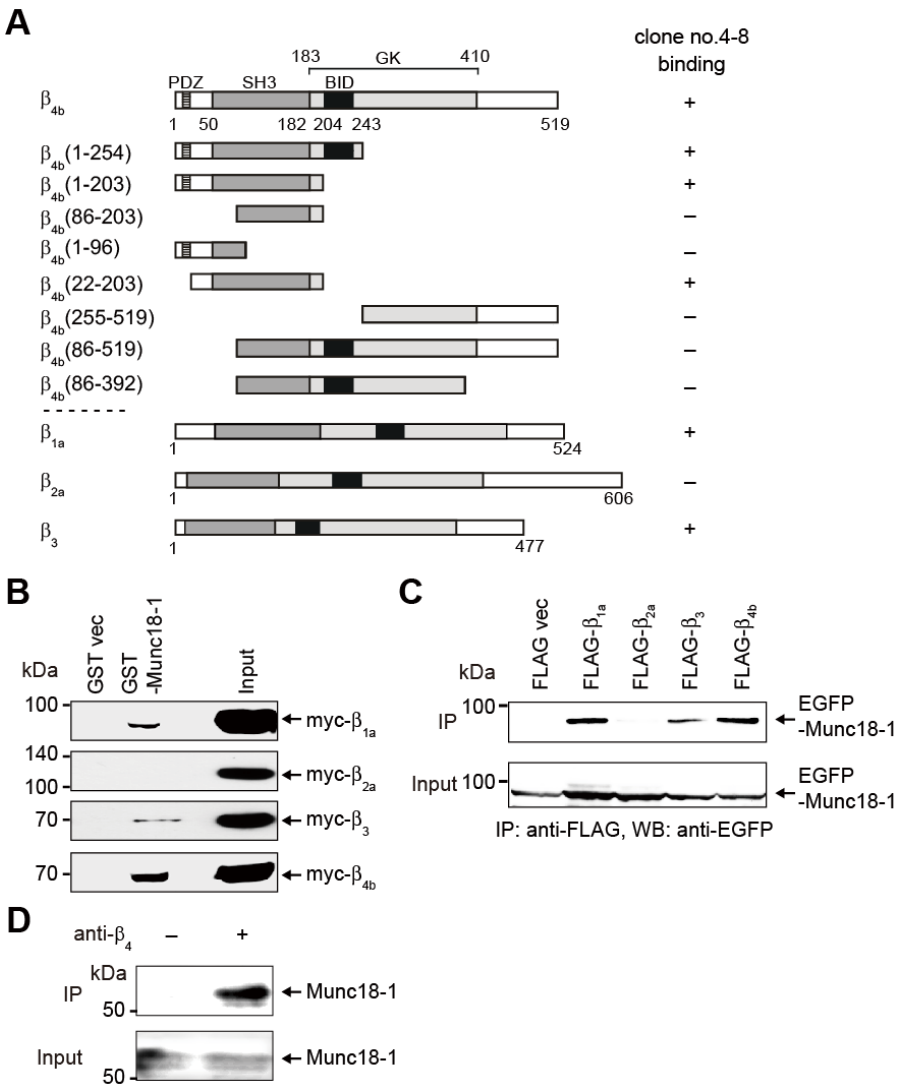

Fig. 2 Direct interaction of Munc18-1 with VDCC β-subunits. *A*. Mapping of Munc18-1-binding sites on β_{4b} by the yeast two-hybrid assay. β-subunit constructs in bait vectors were tested with Munc18-1 (no. 4-8) in the prey vector. *B*. Pulldown assay of β-subunits with GST fusion Munc18-1 constructs. GST fusion proteins immobilized on glutathione-Sepharose beads are incubated with cell lysates obtained from myc-β-transfected HEK293T cells. Bound proteins are analyzed by WB using an antibody for myc. *C*. Interactions of recombinant FLAG-tagged β-subunits and Munc18-1 in HEK293T cells. The interactions are evaluated by immunoprecipitation (IP) with antibody for FLAG, followed by WB with an antibody for GFP. *D*. Coimmunoprecipitation of Munc18 with the β_4 subunit. IP using an antibody for β_4 and subsequent WB for Munc18-1 was carried out on a crude synaptic membrane (CSM) from mouse brain.

Furthermore, in immunoprecipitation analysis of the CSM fraction solubilized with 1% digitonin-containing buffer, Munc18-1 was found to be coimmunoprecipitated with VDCC β_4-subunit (Fig. 2*D*). Thus, Munc18-1 physically associate with native β_4-subunit in the crude synaptic membrane (CSM) from the mouse brain. These results suggest direct protein-protein interactions between Munc18-1 (NM_009295) and β-subunits other than β_{2a}.

Functional effects of Munc18-1 on P/Q-type VDCC currents.

To elucidate the functional significance of direct interaction between Munc18-1 and VDCC β, we examined whole-cell Ba^{2+} currents through recombinant P/Q-type VDCC expressed as $\alpha_1\alpha_2/\delta\beta$ complexes containing the BI-2 variant of $Ca_V2.1$ (25) and various β-subunits in baby hamster kidney (BHK) cells. Prominent effects of Munc18-1 on P/Q-type VDCC currents were observed in parameters of voltage-dependent inactivation of VDCC complexes containing β_{4b}. The kinetics and voltage dependence of inactivation was significantly accelerated and shifted toward hyperpolarizing potentials by Munc18-1 (Fig. 3*A*, *B* and Table 1). VDCC containing the β_3-subunit showed a shift of voltage dependence of inactivation toward hyperpolarizing potentials without the acceleration of inactivation. Munc18-1 did not affect the inactivation parameters of VDCC containing the β_1- and β_{2a}-subunits. Thus, the promotive effect on voltage-dependent inactivation is dependent on the subtype of the β-subunit. Munc18-1 also modulated activation kinetics of P/Q-type VDCC in β-subunit dependent manner (Fig. 4). The activation time constant ($\tau_{activation}$) obtained by fitting the activation time course of inward currents with single exponential was "bell-shaped" when plotted against different voltages. As for P/Q-type VDCC containing β_1-subunit, Munc18-1 significantly decelerated activation at –15 mV,

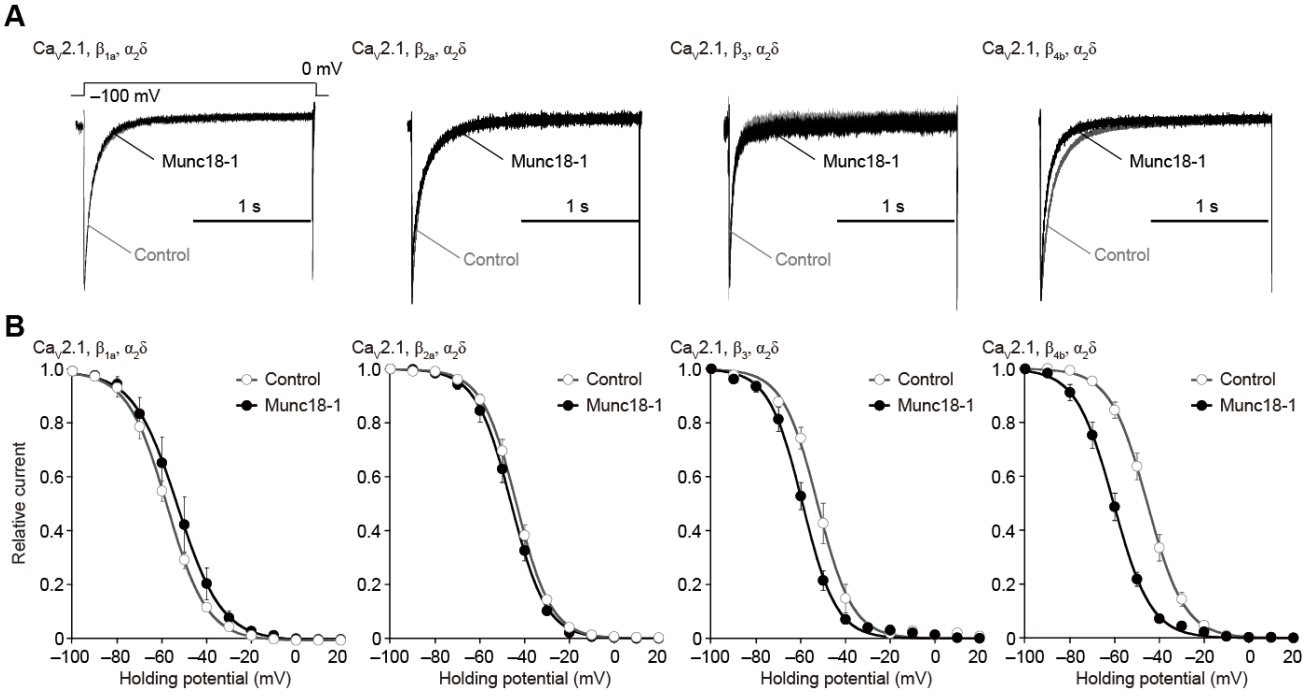

Fig. 3 Effects of Munc18-1 on the inactivation properties of recombinant neuronal VDCCs. *A.* Inactivation of P/Q-type $Ca_V2.1$ currents in BHK cells. The peak amplitudes before and after coexpression of Munc18-1 constructs were normalized for Ba^{2+} currents elicited by 2-s pulses to 0 mV from a holding potential (V_h) of –100 mV. *B.* Inactivation curves for $Ca_V2.1$ in BHK cells expressing α_2/δ and different β subunits. See Table 1 for statistical significance of the differences.

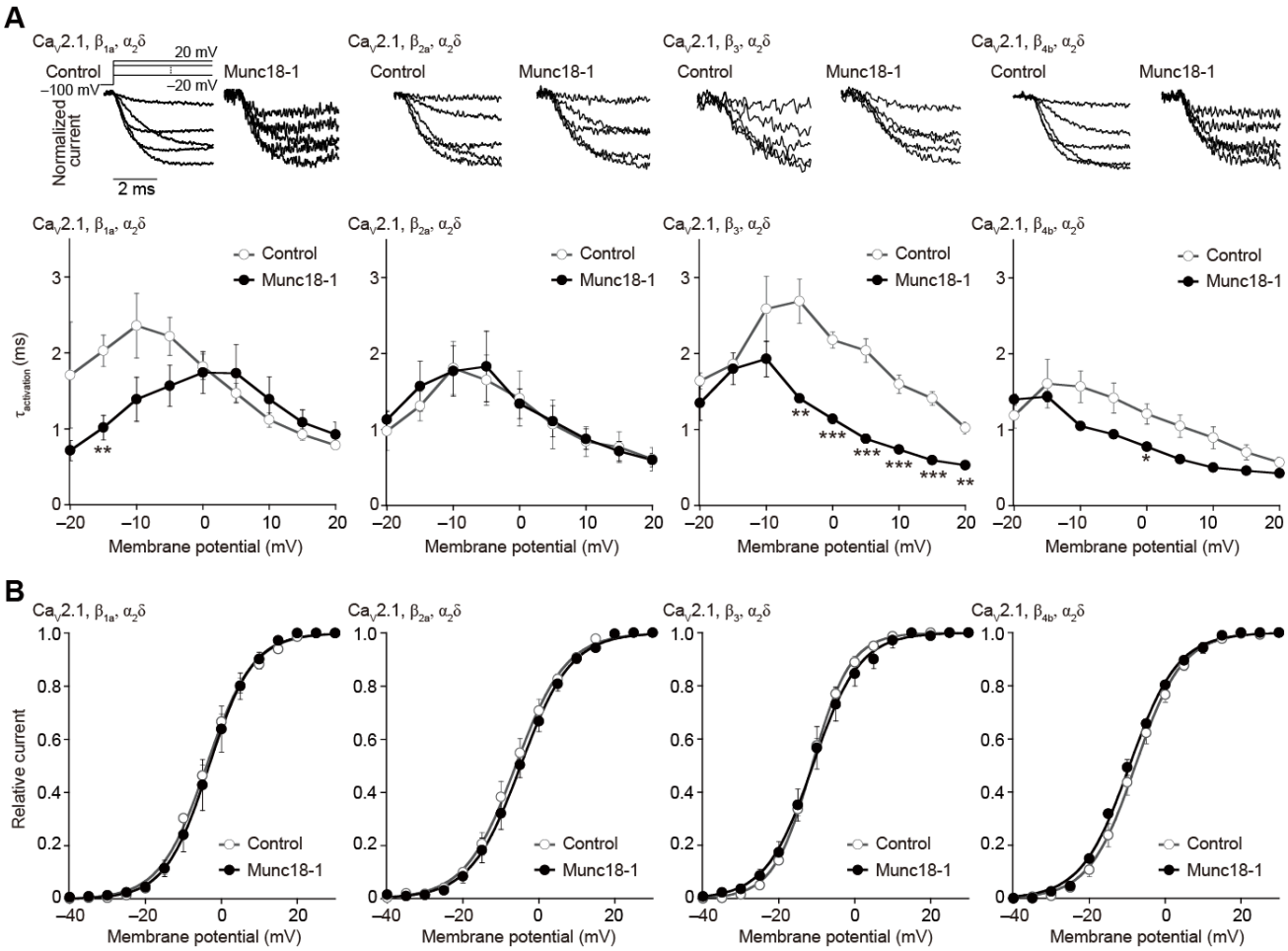

Fig. 4 Effects of Munc18-1 on the activation properties of P/Q-type $Ca_V2.1$. *A.* Activation kinetics of P/Q-type $Ca_V2.1$ currents in BHK cells expressing α_2/δ and β_{1a}-subunit. Top, families of representative Ba^{2+} currents. Currents evoked by 5-ms step depolarization from –20 to 20 mV in 10-mV increments from a V_h of –100 mV are displayed. Bottom, activation time constants plotted as a function of test potential. The activation phases are well fitted by single exponential function at all potentials. $\tau_{activation}$ are obtained from currents elicited by 5-ms step depolarization from –20 to 20 mV in 5-mV increments from a V_h of –100 mV. $^{*}P < 0.05$, $^{**}P < 0.01$, $^{***}P < 0.001$ versus vector. *B.* Activation curves of P/Q-type $Ca_V2.1$ currents. Tail currents elicited by repolarization to –60 mV after 5-ms test pulses from –40 to 30 mV are used to determine activation curves. See Table 1 for statistical significance of the differences.

and activation showed the slowest speed at –10 mV and 0 mV in control and Munc18-1 transfected cells,

respectively. As for the β_3-subunit, Munc18-1 significantly decelerated activation over –5 mV, and activation showed the slowest speed at –5 mV and –10 mV in control and Munc18-1 transfected cells, respectively. For the β_4-subunit, Munc18-1 significantly decelerated activation at 0 mV. As for β_{2a}-subunit, Munc18-1 did not show any modulation in activation speeds. Regardless of β subunits, Munc18-1 failed to exert significant effects on the voltage-dependence of activation (Fig. 4*B*, and Table 1).

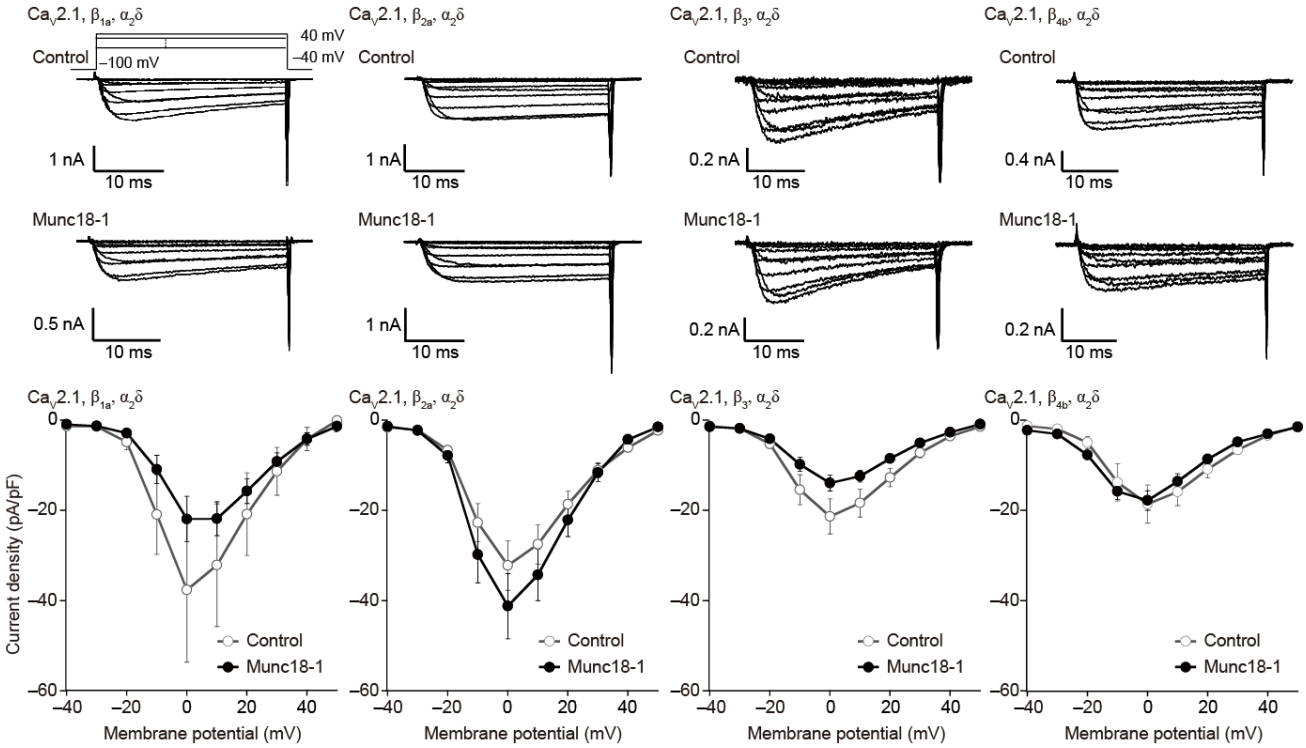

Fig. 5 Effects of Munc18-1 on the current density-voltage (*I-V*) relationships of P/Q-type Ca$_V$2.1. Top, representative traces for Ba^{2+} currents on application of test pluses from –40 mV to 40 mV with 10-mV increments from a V_h of –100 mV. Bottom, *I-V* relationships of Ca$_V$2.1. See Table 1 for statistical significance of the differences.

Munc18-1 did not show significant effects on current density-voltage (*I-V*) relationships, but VDCC containing β_3 subunit was apt to be decreased by co-expression of Munc18-1 (Fig. 5, and Table 1).

Table 1. Effects of Munc18-1 on current density, activation, and inactivation of $Ca_V2.1$.[1)]

Subunit combination		Current density[2)] (pA / pF)	Activation parameters		Inactivation parameters	
			$V_{0.5}$ (mV)	k (mV)	$V_{0.5}$ (mV)	k (mV)
$Ca_V2.1$	Vector	–37.7 ± 1.6 (5)	–3.5 ± 0.7 (4)	6.3 ± 0.1 (4)	–57.8 ± 1.5 (4)	–8.9 ± 0.7 (4)
+ β_{1a}	Munc18-1	–22.0 ± 5.0 (6)	–2.8 ± 1.8 (4)	6.1 ± 0.2 (4)	–52.7 ± 3.6 (6)	–8.8 ± 0.4 (6)
$Ca_V2.1$	Vector	–32.2 ± 5.5 (17)	–6.2 ± 1.3 (8)	6.1 ± 2.4 (8)	–46.3 ± 1.7 (16)	–6.9 ± 0.2 (16)
+ β_{2a}	Munc18-1	–41.1 ± 7.2 (12)	–4.9 ± 1.4 (8)	6.2 ± 0.3 (8)	–43.8 ± 1.3 (9)	–7.3 ± 0.1 (9)
$Ca_V2.1$	Vector	–21.3 ± 3.9 (16)	–5.0 ± 0.3 (8)	11.3 ± 0.6 (8)	–52.2 ± 2.0 (7)	–7.2 ± 0.5 (7)
+ β_3	Munc18-1	–13.9 ± 1.7 (9)	–5.6 ± 0.2 (6)	11.0 ± 1.8 (6)	–59.4 ± 1.6 (6)*	–7.4 ± 0.5 (6)
$Ca_V2.1$	Vector	–18.5 ± 4.2 (5)	–5.7 ± 1.5 (12)	6.7 ± 1.1 (12)	–49.9 ± 1.8 (14)	–7.5 ± 0.3 (14)
+ β_{4b}	Munc18-1	–17.7 ± 2.2 (5)	–8.6 ± 0.5 (4)	6.9 ± 0.2 (4)	–60.8 ± 1.7 (5)***	–7.9 ± 0.4 (5)

1) $^{*}P < 0.05$, $^{**}P < 0.01$, $^{***}P < 0.001$ versus vector.

2) Ba^{2+} currents evoked by depolarizing pulse to 0 mV from a V_h of –100 are divided by capacitance.

3) Numbers of cells analyzed are indicated in the parenthesis.

Discussion

The present investigation revealed physical associations of Munc18-1 with VDCC β-subunits. In vitro binding assays and coimmunoprecipitation experiments identified protein complexes formed by direct interactions of VDCC β-subunits with α_1-subunits and with Munc18-1 (Fig. 2*A*, *B*, *C*). Munc18-1 physically associate with native β_4-subunit in the CSM from the mouse brain (Fig. 2*D*). The interactions between Munc18-1 and VDCC β-subunits reduces the availability of P/Q-type Ca^{2+} channels and slows their activation kinetics in β-subunit-dependent manner (Figs. 3, 4)

Previous reports have demonstrated functional impacts of syntaxin, SNAP-25 and synaptotagmin on VDCCs through their physical association with the 'synprint' region in the II-III linker of α_1-proteins (9, 19, 22). It has also been reported that Munc18-1 associates with the synprint directly and with C terminus indirectly via Munc 18 interacting protein (Mint) (47). However, VDCC complex containing the β_{2a}-subunit, which can not bind to Munc18-1 (Fig. 2), did not show any modulation by Munc18-1 (Figs. 3, 4, and 5). This result supports the idea that modulation of VDCC by Munc18-1 may be dependent on β-subunit-mediated association rather than the synprint- or Mint- mediated one.

Munc18-1 has a functional impact on the gating of Ca^{2+} channels. It reduces the availability of P/Q-type Ca^{2+}

channels at a neuronal resting potential near –75 mV and slows their activation kinetics in β-subunit-dependent manner. Assuming that our findings are applicable to nerve terminals, where Munc18-1 and β_3 and/or β_4 subunit are very abundant, Munc18-1 would be expected to strongly inhibit presynaptic Ca^{2+} entry. These modulations do not appear to be advantageous for Ca^{2+} triggered fusion, but would produce the desirable effect of reducing Ca^{2+} influx in the absence of docked synaptic vesicles. The author hypothesized that Munc18-1 may allow synaptic vesicles to become docked and/or ready for fusion around VDCC without exposing fusion machinery to robust Ca^{2+} entry. The authors previously reported that Rab3-interacting molecule (RIM), which associate with synaptic vesicle protein Rab3, markedly inhibit voltage-dependent inactivation of VDCC via interaction with β-subunit. Modulation by RIM is advantageous for Ca^{2+} triggered fusion. Similar reciprocal regulation of VDCC by SNAP-25, syntaxin and synaptotagmin has been reported (48). These three presynaptic proteins associate to 'synprint' region in P/Q-type VDCC α_{1A}-subunit. Inhibitory effect of SNAP-25 was reversed by syntaxin and synaptotagmin, because of competitive displacement of SNAP-25 from 'synprint' region. Finally, the author speculates that the reduction of Ca^{2+} influx by Munc18-1 might be relieved and exchanged for increase of Ca^{2+} influx by RIM following the docking of a synaptic vesicle. Reciprocal regulation of Ca^{2+}-channel activity by Munc18-1 and RIM would ensure that Ca^{2+} entry could efficiently initiate synaptic transmission by restring the full activity of only those presynaptic Ca^{2+}-channels associated with a synaptic vesicle through SNARE-protein interactions.

Materials and Methods

cDNA cloning and construction of expression vectors- Munc18-1 (GenBank accession no. NM_009295) were cloned from mouse brain Marathon-Ready cDNA (Clontech) using PCR, and were subcloned the EGFP-tagged vector pEGFPC1 (Clontech), and the pIRES2-EGFP (Clontech). Rat β_{4b} (GenBank accession no. XM_215742) was subcloned into the FLAG-tagged vector pCMV-tag2 (Stratagene), the myc-tagged vector pCMV-tag3 (Stratagene).

Production of glutathione S-transferase (*GST) fusion proteins and recombinant β_4-subunit proteins*- For

production of GST fusion proteins for Munc18-1, cDNA for a Munc18-1(NM_009295) construct and cDNA for GST were subcloned together into the pET23 vector (Novagen). The Rosetta strain (Novagen) of *Escherichia coli* was transformed by the expression vectors, and protein expression/purification was performed according to the manufacturer's instruction (Novagen). These proteins were stored at –80 °C.

GST-pulldown assay and coimmunoprecipitation in HEK293T cells- HEK293T cells were cultured in Dulbecco's modified Eagle's medium (DMEM) containing 10% fetal bovine serum, 30 units/ml penicillin, and 30 μg/ml streptomycin. Forty-eight h after transfection, HEK293T cells were solubilized in NP-40 buffer (150 mM NaCl, 50 mM Tris, 1% NP-40, and protease inhibitors), and then centrifuged at 17400 × *g* for 20 min. For the pulldown assay, the cell lysate was incubated with glutathione-Sepharose beads bound with purified fusion proteins at 4 °C, and then the beads were washed with NP-40 buffer. The proteins retained on the beads were characterized by western blotting (WB) with anti-GFP antibody (Clontech 632460). For coimmunoprecipitation, the cell lysate was incubated with anti-FLAG M2 monoclonal antibody (Sigma F3165), and then the immunocomplexes were incubated with protein A-agarose beads (Santa Cruz), and the beads were washed with NP-40 buffer. Immunoprecipitated proteins were detected by WB with anti-β_4 antibody (12).

Biochemistry of native neuronal VDCC complexes- To obtain CSM fraction, subcellular fractionation was performed based on the previously described method (24), with slight modification. Whole mouse brains (8 g) were homogenized in a homogenization buffer containing 4 mM HEPES, 0.32 M sucrose, 5 mM EDTA, 5 mM EGTA, and protease inhibitors (pH 7.4). Cell debris and nuclei were removed by centrifugation at 800 × g for 10 min. The supernatant (S1) was centrifuged at 9,000 × g for 15 min to obtain crude synaptosomal fraction as pellet (P2). The supernatant was stored as S2. The crude synaptosomes were resuspended in the homogenization buffer and centrifuged at 10,000 × g for 15 min. The washed crude synaptosomes were lysed by hypoosmotic shock in water, rapidly adjusted to 1 mM HEPES/NaOH (pH 7.4), and stirred on ice for 30 min. After centrifugation of the lysate at 25,000 × g for 20 min, the pellet was resuspended in 0.25 M buffered sucrose. The synaptic membranes were then further enriched through a discontinuous sucrose gradient containing 0.8/1.0/1.2 M sucrose. After centrifugation at 65,000 × g for 2 h, the CSM fraction was collected from 1.0/1.2 M sucrose interface. Synaptic membrane proteins were extracted from the CSM with solubilization buffer containing 50 mM Tris, 500 mM NaCl, a mixture of protease inhibitors, and 1% digitonin (Biosynth) (pH 7.4). After centrifugation at 40,000 × g for 37 min, supernatant was diluted with a buffer

containing 50 mM Tris and 1% digitonin to adjust NaCl concentration to 150 mM and incubated overnight at 4 °C. After centrifugation at 8,000 × g for 15 min, the supernatant was incubated with protein A-agarose coupled to anti-β_4 antibody (12). Immunoprecipitated proteins were subjected to WB with anti-Munc18-1 monoclonal antibody (BD Transduction Lab 610336).

Cell culture and cDNA expression in BHK cells- BHK6-2 cell line stably expressing $Ca_V2.1$, α_2/δ and β_{1a} was described previously (49). BHK6-2 cells were cultured in DMEM containing 10% fetal bovine serum, 30 units/ml penicillin, and 30 μg/ml streptomycin. Transfection of cDNA plasmids was carried out using Effecten Transfection Reagent (QIAGEN). The cells were subjected to electrophysiological measurements 48 h after transfection.

Current recordings- The whole-cell mode of the patch-clamp technique was carried out at 22–25 °C with EPC-9 (HEKA Elektronic) patch-clamp amplifier as previously described (50). Patch pipettes were made from borosilicate glass capillaries (1.5 mm outer diameter, 0.87 mm inner diameter; Hilgenberg) using a model P-87 Flaming-Brown micropipette puller (Sutter Instrument Co.). The patch electrodes were fire-polished. Pipette resistance ranged from 2 to 3.5 megohm when filled with the pipette solutions described below. The series resistance was electronically compensated to > 60%, and both the leakage and the remaining capacitance were subtracted by –P/4 method. Currents were sampled at 100 kHz after low pass filtering at 8.4 kHz (3 db) in the experiments of activation kinetics, otherwise sampled at 20 kHz after low pass filtering at 3.0 kHz (3 db). Data was collected and analyzed using the Pulse v8.77 (HEKA Elektronic). An external solution contained (in mM): 3 $BaCl_2$, 155 tetraethylammonium chloride (TEA-Cl), 10 HEPES, and 10 glucose (pH 7.4 adjusted with tetraethylammonium hydroxide (TEA-OH)) for BHK cells, and 10 $BaCl_2$, 153 TEA-Cl, 10 HEPES, and 10 glucose (pH 7.4 adjusted with TEA-OH) for PC12 cells. The pipette solution contained (in mM): 95 CsOH, 95 aspartate, 40 CsCl, 4 $MgCl_2$, 5 EGTA, 2 disodium ATP, 5 HEPES and 8 creatine phosphate (pH 7.2 adjusted with CsOH).

Voltage-dependence of inactivation- To determine the voltage-dependence of inactivation (inactivation curve) of VDCCs, Ba^{2+} currents were evoked by 20-ms test pulse to 5 mV after the 10-ms repolarization to –100 mV (–80 mV for PC12) following 2-s V_h displacement (conditioning pulse) from –100 mV to 20 mV (from –80 mV to 20 mV for PC12) with 10-mV increments. Amplitudes of currents elicited by the test pulses were normalized to those elicited by the test pulse after a 2-s V_h displacement to –100 mV (–80 mV for

PC12). The mean values were plotted against potentials of the 2-s V_h displacement. When the inactivation curve was monophasic, the mean values were fitted to the single Boltzmann's equation: $h(V_h) = (1-a)+a/\{1+\exp[(V_{0.5}-V_h)/k]\}$, where a is the rate of inactivating component, $V_{0.5}$ is the potential to give a half-value of inactivation, and k is the slope factor.

Voltage-dependence of activation- Tail currents were elicited by repolarization to –60 mV after 5-ms test pulse from –40 to 30 mV with 5-mV increments. Currents were sampled at 100 kHz after low pass filtering at 8.4 kHz. Amplitude of tail currents were normalized to the tail current amplitude obtained with a test pulse to 30 mV. The mean values were plotted against test pulse potentials, and fitted to the Boltzmann's equation: $n(V_m) = 1/\{1+\exp[(V_{0.5}-V_m)/k]\}$, where V_m is membrane potential, $V_{0.5}$ is the potential to give a half-value of conductance, and k is the slope factor.

Reference

1. Sheng, M. and Hoogenraad, C. C. (2007) *Annu. Rev. Biochem.* **76**, 823–847
2. Ohtsuka, T., Takao-Rikitsu, E., Inoue, E., Inoue, M., Takeuchi, M., Matsubara, K., Deguchi-Tawarada, M., Satoh, K., Morimoto, K., Nakanishi, H., and Takai, Y. (2002) *J. Cell Biol.* **158**, 577–590
3. Zhai, R. G. and Bellen, H. J. (2004) *Physiology (Bethesda)* **19**, 262–270
4. Südhof, T. C. (2004) *Annu. Rev. Neurosci.* **27**, 509–547
5. Schoch, S. and Gundelfinger, E. D. (2006) *Cell Tissue Res.* **326**, 379–391
6. Wojcik, S. M. and Brose, N. (2007) *Neuron* **55**, 11–24
7. Stanley, E. F. (1993) *Neuron* **11**, 1007–1011
8. Sheng, Z. H., Rettig, J., Takahashi, M., and Catterall, W. A. (1994) *Neuron* **13**, 1303–1313
9. Bezprozvanny, I., Scheller, R. H., and Tsien, R. W. (1995) *Nature* **378**, 623–626
10. Neher, E. (1998) *Neuron* **20**, 389-399
11. Wadel, K., Neher, E., and Sakaba, T. (2007) *Neuron* **53**, 563–575
12. Kiyonaka, S., Wakamori, M., Miki, T., Uriu, Y., Nonaka, M., Bito, H., Beedle, A. M., Mori, E., Hara, Y., De Waard, M., Kanagawa, M., Itakura, M., Takahashi, M., Campbell, K. P., and Mori, Y. (2007) *Nat. Neurosci.* **10**, 691–701
13. Catterall, W. A. and Few, A. P. (2008) *Neuron* **59**, 882–901
14. Tsien, R. W., Ellinor, P. T., and Horne, W. A. (1991) *Trends Pharmacol. Sci.* **12**, 349–354
15. Takahashi, T. and Momiyama, A. (1993) *Nature* **366**, 156–158
16. Wheeler, D. B., Randall, A., and Tsien, R. W. (1994) *Science* **264**, 107–111
17. Catterall, W. A. (1998) *Cell Calcium* **24**, 307–323
18. Ertel, E. A., Campbell, K. P., Harpold, M. M., Hofmann, F., Mori, Y., Perez-Reyes, E., Schwartz, A., Snutch, T. P., Tanabe, T., Birnbaumer, L., Tsien, R. W., and Catterall, W. A. (2000) *Neuron* **25**, 533–535
19. Zhong, H., Yokoyama, C. T., Scheuer, T., and Catterall, W. A. (1999) *Nat. Neurosci.* **2**, 939–941
20. Maximov, A., Südhof, T. C., and Bezprozvanny, I. (1999) *J. Biol. Chem.* **274**, 24453–24456
21. Maximov, A. and Bezprozvanny, I. (2002) *J. Neurosci.* **22**, 6939–6952

22. Spafford, J. D. and Zamponi, G. W. (2003) *Curr. Opin. Neurobiol.* **13**, 308–314

23. Nishimune, H., Sanes, J. R., and Carlson, S. S. (2004) *Nature* **432**, 580–587

24. Kang, M., Chen, C., Wakamori, M., Hara, Y., Mori, Y., and Campbell, K. P. (2006) *Proc. Natl. Acad. Sci. U.S.A.* **103**, 5561–5566

25. Mori, Y., Friedrich, T., Kim, M. S., Mikami, A., Nakai, J., Ruth, P., Bosse, E., Hofmann, F., Flockerzi, V., Furuichi, T., Mikoshiba K., Imoto K., Tanabe T., and Numa S. (1991) *Nature* **350**, 398–402

26. Bichet, D., Cornet, V., Geib, S., Carlier, E., Volsen, S., Hoshi, T., Mori, Y., and De Waard, M. (2000) *Neuron* **25**, 177–190

27. Varadi, G., Lory, P., Schultz, D., Varadi, M., and Schwartz, A. (1991) *Nature* **352**, 159–162

28. Lacerda, A. E., Kim, H. S., Ruth, P., Perez-Reyes, E., Flockerzi, V., Hofmann, F., Birnbaumer, L., and Brown, A. M. (1991) *Nature* **352**, 527–530

29. Béguin, P., Nagashima, K., Gonoi, T., Shibasaki, T., Takahashi, K., Kashima, Y., Ozaki, N., Geering, K., Iwanaga, T., and Seino, S. (2001) *Nature* **411**, 701–706

30. Hibino, H., Pironkova, R., Onwumere, O., Rousset, M., Charnet, P., Hudspeth, A. J., and Lesage, F. (2003) *Proc. Natl. Acad. Sci. U.S.A.* **100**, 307–312

31. Vendel, A. C., Terry, M. D., Striegel, A. R., Iverson, N. M., Leuranguer, V., Rithner, C. D., Lyons, B. A., Pickard, G. E., Tobet, S. A., and Horne, W. A. (2006) *J. Neurosci.* **26**, 2635–2644

32. Hata, Y., Slaughter, C. A., and Südhof, T. C. (1993) *Nature* **366**, 347-351

33. Rizo, J. and Südhof, T. C. (2002) *Nat. Rev. Neurosci.* **3**, 641-653

34. Okamoto, M., Matsuyama, T., and Sugita, M. (2000) *Eur. J. Neurosci.* **12**, 3067-3072

35. Weimer, R. M., Richmond, J. E., Davis, W. S., Hadwiger, G., Nonet, M. L., and Jorgensen, E. M. (2003) *Nat. Neurosci.* **6**, 1023-1030

36. Halachmi, N. and Lev, Z. (1996) *J. Neurochem.* **66**, 889-897

37. Jahn, R. (2000) *Neuron* **27**, 201-204

38. Verhage, M., Maia, A. S., Plomp, J. J., Brussaard, A. B., Heeroma, J. H., Vermeer, H., Toonen, R. F., Hammer, R. E., van den Berg, T. K., Missler, M., Geuze, H. J., and Südhof, T. C. (2000) *Science* **287**, 864-869

39. Voets, T., Toonen, R. F., Brian, E. C., de Wit, H., Moser, T., Rettig, J., Südhof, T. C., Neher, E., and Verhage, M. (2001) *Neuron* **31**, 581-591

40. Misura, K. M., Scheller, R. H., and Weis, W. I. (2000) *Nature* **404**, 355-362, Burkhardt, P., Hattendorf, D. A., Weis, W. I., and Fasshauer, D. (2008) *EMBO J.* **27**, 923-933

41. Weimer, R. M., Richmond, J. E., Davis, W. S., Hadwiger, G., Nonet, M. L., and Jorgensen, E. M. (2003) *Nat. Neurosci*. **6**, 1023-1030

42. Dresbach, T., Burns, M. E., O'Connor, V., DeBello, W. M., Betz, H., and Augustine, G. J. (1998) *J. Neurosci*. **18**, 2923-2932

43. Korteweg, N., Maia, A. S., Verhage, M., and Burbach, J. P. H. (2004) *Eur. J. Neurosci* **19**, 2944-2952

44. Toonen, R. F., Kochubey, O., de Wit, H., Gulyas-Kovacs, A., Konijnenburg, B., Sørensen, J. B., Klingauf, J., and Verhage, M. (2006) *EMBO J* **25**, 3725-3737

45. Burgoyne, R. D., Barclay, J. W., Ciufo, L. F., Graham, M. E., Handley, M. T. W., and Morgan, A. (2009) *Ann. N. Y. Acad. Sci.* **1152**, 76-86

46. Chan, A. W., Khanna, R., Li, Q., and Stanley, E. F. (2007) *Channels (Austin)* **1**, 11-20

47. Maximov, A. and Bezprozvanny, I. (2002) *J. Neurosci* 22, 6939-6952

48. Zhong, H., Yokoyama, C. T., Scheuer, T., and Catterall, W. A. (1999) *Nat. Neurosci.* **2**, 939-941

49. Niidome, T., Teramoto, T., Murata, Y., Tanaka, I., Seto, T., Sawada, K., Mori, Y., and Katayama, K. (1994) *Biochem. Biophys. Res. Commun.* **203**, 1821–1827

50. Wakamori, M., Yamazaki, K., Matsunodaira, H., Teramoto, T., Tanaka, I., Niidome, T., Sawada, K., Nishizawa, Y., Sekiguchi, N., Mori, E., Mori, Y., and Imoto, K. (1998) *J. Biol. Chem.* **273**, 34857–34867

Chapter 4

TRPM1 is a component of the retinal ON bipolar cell transduction channel in the mGluR6 cascade.

Abstract

An essential step in intricate visual processing is the segregation of visual signals into ON and OFF pathways by retinal bipolar cells (BCs). Glutamate released from photoreceptors modulates the photoresponse of ON BCs via metabotropic glutamate receptor 6 (mGluR6) and G protein (Go) that regulates a cation channel. However, the cation channel has not yet been unequivocally identified. Here, we report a mouse TRPM1 long form (TRPM1-L) as the cation channel. We found that TRPM1-L localization is developmentally restricted to the dendritic tips of ON BCs in colocalization with mGluR6. TRPM1 null mutant mice completely lose the photoresponse of ON BCs but not that of OFF BCs. In the TRPM1-L-expressing cells, TRPM1-L functions as a constitutively active nonselective cation channel and its activity is negatively regulated by Go in the mGluR6 cascade. These results demonstrate that TRPM1-L is a component of the ON BC transduction channel downstream of mGluR6 in ON BCs.

Introduction

Segregation of visual signals into ON and OFF pathways originates in BCs, the second order neurons in the retina (1, 2). ON and OFF BCs express metabotropic glutamate receptors, mGluR6, and ionotropic glutamate receptors (iGluRs), respectively, on their dendrites (3-5). Reduction of glutamate released from photoreceptors by light stimulation depolarizes ON BCs and hyperpolarizes OFF BCs (6-8) mediated through respective glutamate receptors. The mGluR6 couples to a heterotrimeric G -protein complex, Go (9, 10). Signals require Goα which ultimately closes a downstream nonselective cation channel in ON BCs (6, 9, 11-13). However, this transduction cation channel in ON BCs has not been identified, despite intensive investigation. In our screen to identify functionally important molecules in the retina, we found that TRPM1 is predominantly expressed in retinal BCs. Most members of the TRP superfamily, which are found in a variety of sense organs, are non-voltage gated cation channels (14-16). The founding member of the TRP family was discovered as a key component of the light response in Drosophila photoreceptors (17). TRPM1, also known as melastatin, was the first member of the melanoma-related transient receptor potential (TRPM) subfamily to be discovered (18, 19). TRPM1 is alternatively spliced, resulting in the production of a long form (TRPM1-L) and a short N-terminal form devoid of transmembrane segments (TRPM1-S) (18, 20). Although mouse TRPM1-S was previously identified as melastatin, mouse TRPM1-L has not been identified (18). The distinct physiological and biological functions of TRPM1 still remain elusive, though some recent evidences including us suggested that TRPM1 might contribute to retinal BC function (21-23). Here we show that TRPM1-L is the transduction cation channel of retinal ON BCs in the downstream of mGluR6 cascade.

Results

Isolation of mouse TRPM1-L

We identified a mouse TRPM1-L cDNA that corresponds to the human TRPM1 long form (20). The mouse TRPM1-L encodes a predicted 1622-amino-acid protein, containing six transmembrane domains, a pore region, and a TRP domain as do other major TRP family members (Fig. 1*A*). Northern blot analysis revealed the presence of both TRPM1-L and -S transcripts in the retina, however, only the latter was detected in the skin. In situ hybridization (ISH) (Fig. 1*B–E*) showed the presence of substantial TRPM1-L transcripts in the inner nuclear layer (INL) at postnatal stages (Fig. 1*B*, *D*). Although significant TRPM1-L expression was not detected in the RPE (Fig. 1*B*, red arrow), strong TRPM1-S signals were observed in the RPE from embryonic stages to early postnatal stages (Fig. 1*C*, red arrow). Faint TRPM1-S signals were detected in the INL after postnatal day 8 (P8) (Fig. 1*E*). Immunostaining with anti-Chx10 antibody, a pan-BC marker, showed that TRPM1-L signals were located in BCs in the adult retina (Fig. 1*F*).

Localization of TRPM1-L on dendritic tips of ON BCs

Next, we raised an antibody against TRPM1-L and examined the localization of TRPM1-L (Fig. 1*G–L*). At P14, TRPM1-L was found diffusely in BC somata (Fig. 1*G*). At one month after birth (1M), TRPM1-L localized to the dendritic tips in the outer plexiform layer (OPL) (Fig. 1*H*, arrows and stars). To identify the subtypes of BCs expressing TRPM1-L, we co-immunostained 5 BCs with anti-TRPM1 antibody and several adult retinal BC markers (Fig. 1*I–L*). Punctated TRPM1-L signals were localized at the tips of Goα- as well as mGluR6-expressing dendrites (Fig. 1*I*, *J*). We also co-immunostained TRPM1-L with PNA that binds to glycoconjugates associated with the cell membrane and the intersynaptic matrix of cone terminals. The continuous punctated TRPM1-L signals appeared in register with the PNA signals, suggesting that TRPM1-L is localized adjacent to cone photoreceptors as well as to rod photoreceptors (Fig. 1*K*, indicated by stars). Actually, TRPM1-L was not expressed in photoreceptor terminals because the punctuated TRPM1-L signals did not co-localize with bassoon, a marker for the presynaptic photoreceptor structures (Fig. 1*L*). We did not observe distinct co-localization of TRPM1-L with OFF-BC markers.

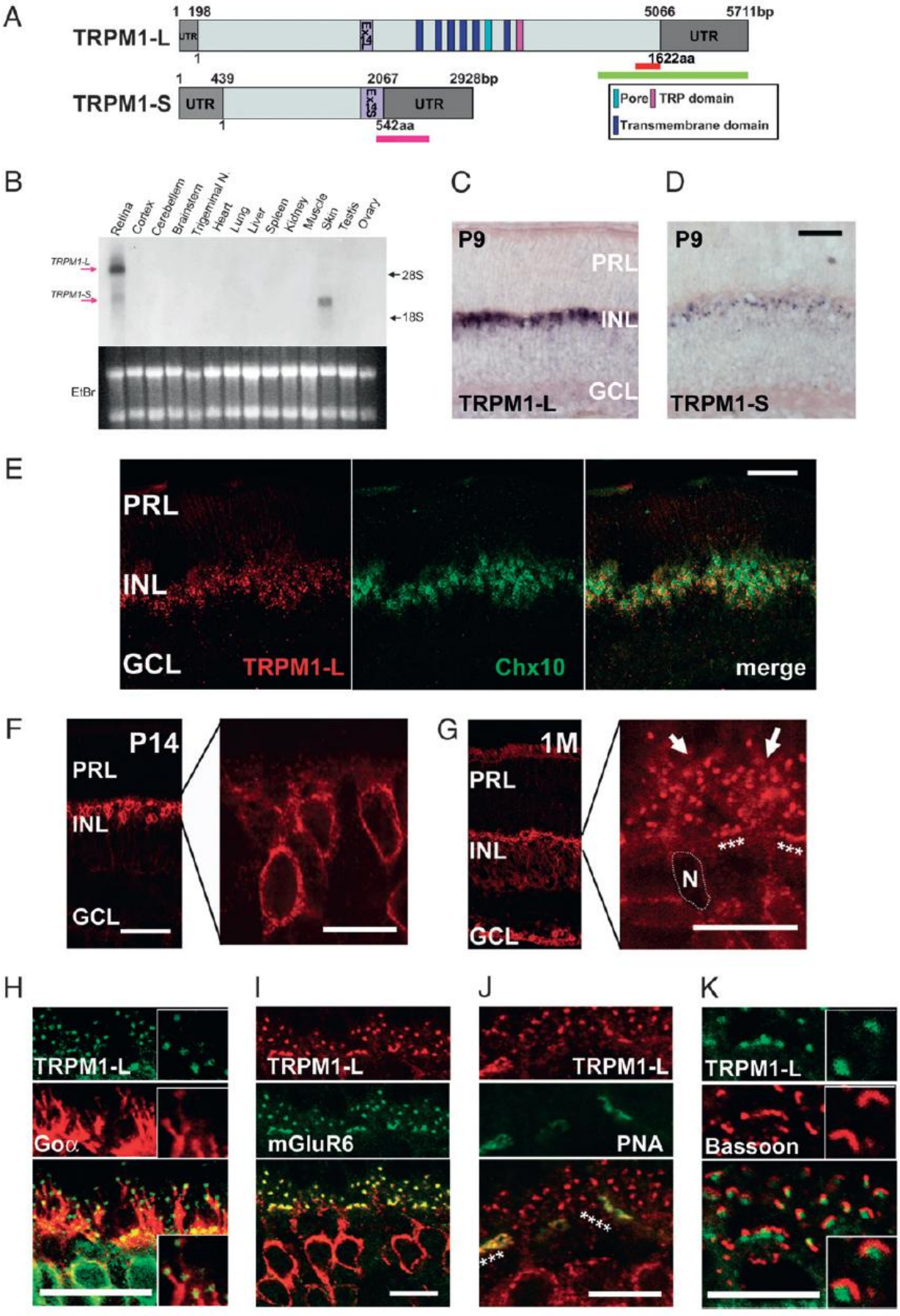
A
TRPM1-L
1 198
5066
5711bp
UTR
UTR
1622aa
TRPM1-S
1 439
2067
2928bp
UTR
UTR
542aa
Pore
TRP domain
Transmembrane domain
B
Retina
Cortex
Cerebellem
Brainstem
Trigeminal N.
Heart
Lung
Liver
Spleen
Kidney
Muscle
Skin
Testis
Ovary
TRPM1-L
TRPM1-S
28S
18S
EtBr
C
P9
PRL
INL
GCL
TRPM1-L
D
P9
TRPM1-S
E
PRL
INL
GCL
TRPM1-L
Chx10
merge
F
P14
PRL
INL
GCL
G
1M
PRL
INL
GCL
N
H
TRPM1-L
Goα
I
TRPM1-L
mGluR6
J
TRPM1-L
PNA
K
TRPM1-L
Bassoon

Fig. 1. The molecular analysis and expression of mouse TRPM1-L. ***A***. Schematic diagrams of full-length mouse TRPM1-L and TRPM1-S genes and their ORFs. Light gray boxes represent ORF, and light purple boxes indicate exon 14 (L and S). Green and pink bars indicate sequences used for TRPM1-L- or TRPM1-S-specific probes, respectively. The red bar indicates amino acid sequence used for generating anti-TRPM1-L antibody. ***B***. Northern blot analysis of mouse TRPM1 transcription in adult mouse tissues. The sizes of TRPM1-Land TRPM1-S transcripts are ≈6 kb and 3 kb, respectively. Both TRPM1-L and -S transcripts were detected in the retina; however, only the TRPM1-S transcript was detected in the skin. (Lower) Ethidium bromide staining of RNA. Each lane contains ≈10 μg of total RNA. Trigeminal N., trigeminal nucleus. ***C***, ***D***. ISH analysis of mouseTRPM1in the postnatal retina. TRPM1-L-specific signal was detected in the INL at P9 (***C***). TRPM1-S was detected in the INL at P9 (***D***). PRL, photoreceptor layer; INL, inner nuclear layer; GCL, ganglion cell layer. (Scale bar: 100 μm.) ***E***. ISH of TRPM1-L mRNA and following immunostaining of anti-Chx10 antibody, a pan-BC marker. (Scale bar: 50 μm.) ***F***, ***G***. Immunostaining with an antibody against TRPM1-L exhibited TRPM1-L signals in cell bodies of retinal BCs at P14 (***F***) and at dendritic tips of retinal BCs (stars and arrows) at 1M (***G***). N, nucleus of a BC. (Scale bars: 50 μm.) ***H–K***, Confocal images of OPLs double-labeled with anti-TRPM1-L antibody and other retinal markers. TRPM1-L-positive puncta were localized at the tips of Goα distribution (***H***). TRPM1-L-positive puncta were colocalized with mGluR6 staining (***I***). Continuous puncta marked with TRPM1-L were colocalized with PNA (stars) (***J***). TRPM1-L-positive puncta were surrounded by synaptic ribbons stained with bassoon (***K***). (Scale bars: 10 μm.)

TRPM1–L is required for visual transmission

To address a possible role of TRPM1 in ON BC function, we generated TRPM1 null mutant (TRPM1$^{-/-}$) mice by targeted gene disruption (Fig. 2*A*). We used Southern blots to confirm the exons 4-6 deletion (Fig. 2*B*). Northern blot analysis showed that no substantial transcripts were detected in TRPM1$^{-/-}$ retinas (Fig. 2*C*). Although TRPM1-S is expressed in the skin, TRPM1$^{-/-}$ mice were indistinguishable from wild-type (WT) littermates in appearance, including coat color. In TRPM1$^{-/-}$ mice, immunoreactivity to TRPM1-L was essentially undetectable (Fig. 2*D*). In contrast, no substantial reduction of retinal BC markers including Chx10, Goα and mGluR6 was observed in TRPM1$^{-/-}$ mouse retinas at 1M (Fig. 2, *E–G*, Figs. S5D and S11). The retinal tissue structure of TRPM1$^{-/-}$ mice showed no substantial abnormality 6 (data not shown). Electron microscopy analysis showed no substantial differences in the ribbon synapses in the ONL and INL between WT and TRPM1$^{-/-}$ mouse retinas (Fig. 2, *H* and I).

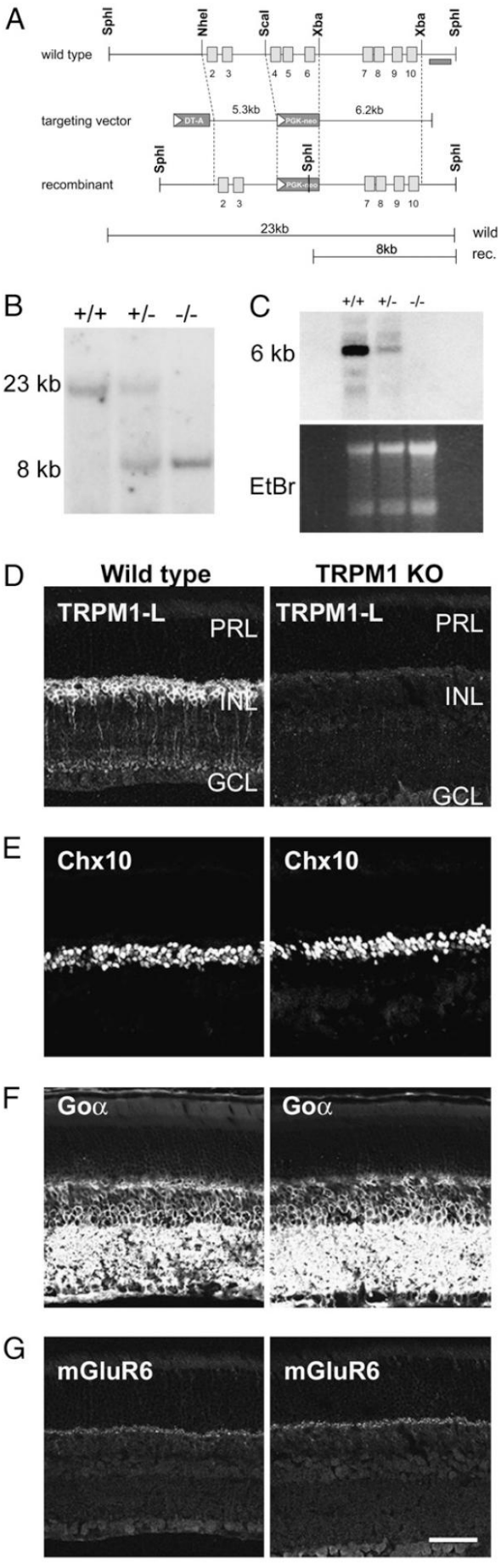

Fig. 2. Generation of TRPM1$^{-/-}$ mouse by targeted gene disruption. ***A***. Strategy for the targeted deletion of TRPM1 gene. The open boxes indicate exons. Exons 4–6 were replaced with the PGK-neo cassette. The probe used for Southern blot analysis is shown as a dark bar. ***B***. Southern blot analysis of genomic DNA. SphI-digested genomic DNA was hybridized with a 3′ outside probe, detecting 23-kb WT and 8-kb mutant bands. ***C***. Northern blot analysis of total RNA extracted from the retina derived from WT, TRPM1$^{+/-}$, and TRPM1$^{-/-}$ mice using cDNA probe derived from exons 3–9. ***D–G***. Immunostaining of WT and TRPM1$^{-/-}$ retinal sections at 1 M. The TRPM1-L signal in the INL of WT mouse retina disappeared in the TRPM1$^{-/-}$ mouse retina (***D***). Immunohistochemical analysis using antibodies to Chx10 [pan-BC nuclei marker (***E***)], Goα [ON BC dendrite marker (***F***)], and mGluR6 [ON BC dendrite tip marker (***G***)] showed no obvious difference between WT and TRPM1$^{-/-}$ mice retinas. PRL, photoreceptor layer; INL, inner nuclear layer; GCL, ganglion cell layer. (Scale bar: 50 μm.)

TRPM1–L Is Required for the Photoresponse of ON BCs.

To address a possible role of TRPM1 in ON BC function, we generated TRPM1 null mutant ($TRPM1^{-/-}$) mice by targeted gene disruption (Fig. 2*A*). We used Southern blots to confirm the exons 4–6 deletion (Fig. 2*B*). Northern blot analysis showed that no substantial transcripts were detected in $TRPM1^{-/-}$ retinas (Fig. 2*C*). Although TRPM1-S is expressed in the skin, $TRPM1^{-/-}$ mice were indistinguishable from wild-type (WT) littermates in appearance, including coat color. In $TRPM1^{-/-}$ mice, immunoreactivity to TRPM1-L was essentially undetectable (Fig. 2*D*). In contrast, no substantial reduction of retinal BC markers including Chx10, Goα, and mGluR6 was observed in $TRPM1^{-/-}$ mouse retinas at 1 month (Fig. 2 *E–G*).

To examine whether TRPM1-L can function as a transduction cation channel in rod and cone ON BCs, we applied whole-cell recording techniques to BCs in mouse retinal slices (Fig. 3). Under the whole-cell voltage clamp, light stimulation induced an inward current in ON BCs of WT mice (Fig. 3*A*, WT), reflecting the opening of transduction cation channels via mGluR6 deactivation (11, 13, 24, 25). On the other hand, neither rod BCs nor cone ON BCs of $TRPM1^{-/-}$ mice evoked photoresponses (Fig. 3*A*, TRPM1 KO). Collected data showed significant differences in the amplitude of photoresponses between WT and $TRPM1^{-/-}$ mice (Fig. 3B). Membrane current fluctuations of ON BCs in the dark were much smaller in $TRPM1^{-/-}$ mice than in WT mice (Fig. 3*A*), suggesting that there are no functional transduction cation channels in ON BCs of $TRPM1^{-/-}$ mice (Fig. 3*C*). On the other hand, light stimulation of cone OFF BCs in both WT and $TRPM1^{-/-}$ mice evoked photoresponses (Fig. 3*D*). We detected no significant differences in either the amplitude of the light responses (Fig. 3*E*) or the time for half-maximal amplitude after the light was turned off ($T_{1/2}$) (Fig. 3*F*).

Characterization of whole-cell currents via recombinant TRPM1

Ionic currents in TRPM1-trasnfected CHO cells at a holding potential (V_h) of −60 mV were measured under the whole-cell voltage clamp. A ramp pulse from +80 mV to −100 mV (V_h = −60 mV) was applied through a recording pipette filled with a Cs^+-based solution every five seconds to obtain a current-voltage (*I-V*) relationship in a divalent cation-free Na^+-based bath solution. Amplitude of the inward current at −100 mV was plotted against time to examine the effects of glutamate and $NMDG^+$. In the CHO cells expressing mGluR6, Goα and TRPM1, constitutively active inward currents were observed. In these cells, the ramp pulses revealed a linear *I-V* relationship with reversal potential (V_{rev}) of ~0 mV (0.92 mV, n = 15), indicating that, like most TRP channels, TRPM1 may be a nonselective cation channel (Fig. 4*A*). In fact, replacement of extracellular cations with $NMDG^+$ resulted not only in the suppression of the current but also in a shift of

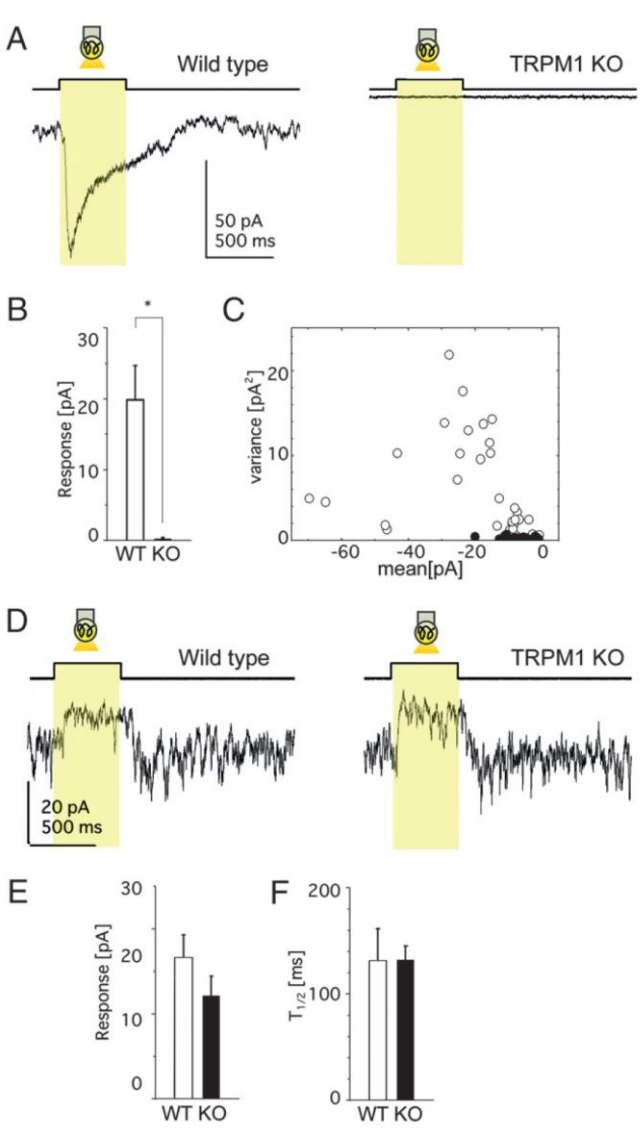

Fig. 3. TRPM1-L is essential for ON BC photoresponses. ***A–C***. Data from ON BCs in the retinal slice preparation. ***A***. Photoresponses of ON BCs from WT (Left) and TRPM1$^{-/-}$ (Right) mice (holding potential at –62 mV). Each trace illustrates the average of three responses. ***B***. Mean ± SEM of photoresponses from WT (15 cells, 12 mice) and TRPM1$^{-/-}$ (9 cells, 8 mice) mice. *, P < 0.05. ***C***. The variance against the mean (the leak current not subtracted) of the dark membrane current fluctuations obtained from WT (open circles: 34 traces, 15 cells) and TRPM1$^{-/-}$ (filled circles: 26 traces, 9 cells) mice. ***D–F***. Data from OFF BCs in the retinal slice preparation. ***D***. Photoresponses of OFF BCs from WT (Left) and TRPM1$^{-/-}$ (Right) mice under similar recording conditions as in A. Each trace illustrates the average of tworesponses. Nosignificant difference in the response amplitude (WT, 5 cells; TRPM1$^{-/-}$, 6 cells) (***E***) or in the time for half-maximal amplitude after the termination of light stimulation ($T_{1/2}$) (WT, 5 cells; TRPM1$^{-/-}$, 6 cells) (***F***).

V_{rev} toward hyperpolarizing potential (ΔV_{rev} = –23.7 mV, n = 15) (Fig. 4*A*). In addition, constitutively active currents were detected in the TRPM1 expressing cells even with the replacement of extracellular cations with either Na^+, K^+, Ca^{2+}, or Mg^{2+}, supporting the idea that TRPM1 is a nonselective cation channel (Fig. 4*C*). In contrast, a whole-cell current was not detected in Goα-transfected CHO cells stably expressing mGluR6 but not TRPM1 (n = 11) (Fig. 4*A*). In accordance with the previous report about human TRPM1 using Ca^{2+} imaging, our results suggest that TRPM1 functions as a constitutively active cation channel (21).

Characterization of single-channel currents via recombinant TRPM1

Single-channel recordings were performed in the outside-out patch mode of patch clamp measurement (Fig. 5). A current was measured and analyzed at –60 mV using a divalent cation-free K^+-based bath solution and a

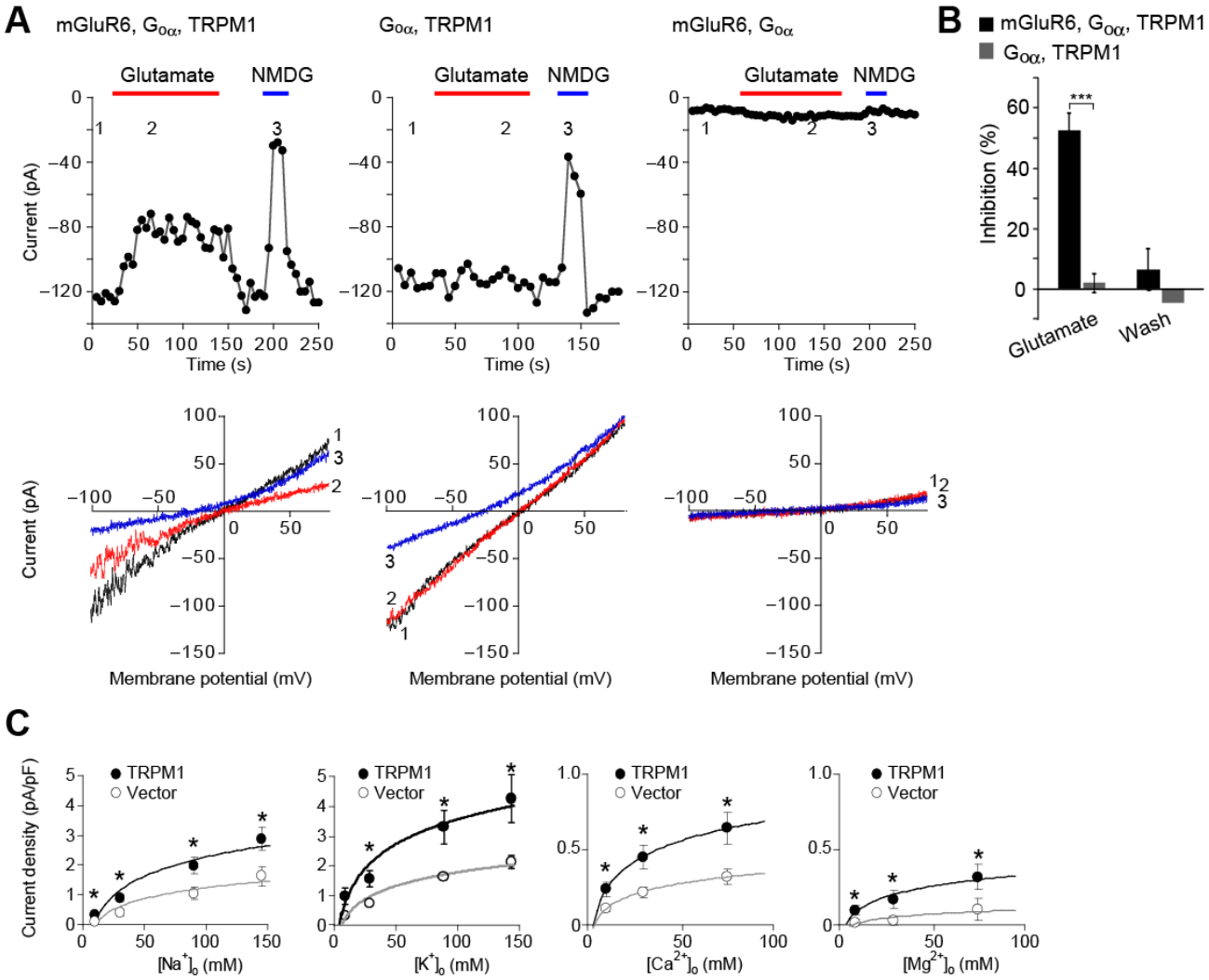

Fig. 4 Functional coupling between TRPM1-L and mGluR6.

A. mGluR6 activation inhibits cationic currents by TRPM1 expressed in CHO cells. Upper panels show effects of 1 mM glutamate on whole-cell currents recorded at −100 mV in cells expressing different combinations of constructs as indicated above each plot. Voltage ramp was applied every five seconds to measure *I-V* relationships (lower panels). Red and blue horizontal bars indicate the timing of 1-mM glutamate application and replacement of extracellular Na^+ with $NMDG^+$. Lower panel shows representative *I-V* relationships of currents in response to voltage ramps (180 ms duration) from +80 mV to −100 mV (V_h = −60 mV) before (black trace, 1) and during (red trace, 2) glutamate application and during replacement of extracellular Na^+ with $NMDG^+$ (blue trace, 3). Bar graphs represent suppression ratios of currents at −100 mV before and after activation of mGluR6 in CHO cells expressing mGluR6, Goα and TRPM1 (n = 15) or Goα and TRPM1-L (n = 11). Data represent the mean ± SEM. $^{***}P<0.001$. ***B***. Inhibitory effects of Goα constructs on TRPM1. Na^+ current densities obtained by subtracting whole-cell current densities in $NMDG^+$-based solution from those in Na^+-based solution at –60 mV. CHO cells are expressing different combinations of constructs or treated further with GMP-PNP or GDPβS as in the left

bar. Data represent the mean ± SEM. For statistical assessment, multiple comparisons were conducted by ANOVA, followed by the Tukey–Kramer test. n.s.; not significance. $^{*}P < 0.05$ and $^{**}P < 0.01$. ***C***. Dependence of whole-cell current densities on external Na^+, K^+, Ca^{2+}, and Mg^{2+} in TRPM1-transfected cells. Current densities were measured in extracellular solutions which were made by mixing the cation (either Na^+, K^+, Ca^{2+}, or Mg^{2+}) solution and the solution, where cations were totally replaced with $NMDG^+$, at various ratios (V_h is –50 mV). Closed circles indicate TRPM1-transfected cells, and open circles vector-transfected cells. Data points are mean ± SEM. *P < 0.05.

Cs^+-based pipette solution in mGluR6-stably expressed CHO cells transfected with both TRPM1 and Goα. Constitutively active currents, whose single-channel conductance was 76.70 pS and open probability (NP_O) was 0.48, were obtained in 41 cells out of 129 cells. These currents showed a V_{rev} of ~0 mV (6.86 mV, n = 21) (Fig. 5*B*). By contrast, similar single-channel currents were absent in cells expressing both mGluR6 and Goα but not TRPM1 (n = 32). The average amplitude of single TRPM1 channel currents measured at –60 mV using a divalent cation-free K^+-based bath solution and Cs^+-based pipette solution in TRPM1 transfected cells was –4.60 pA (n = 30), and that in 2 mM Ca^{2+} and 1 mM Mg^{2+}-containing solution was significantly reduced to –1.01 pA (n = 10) (Fig. 5*A*).

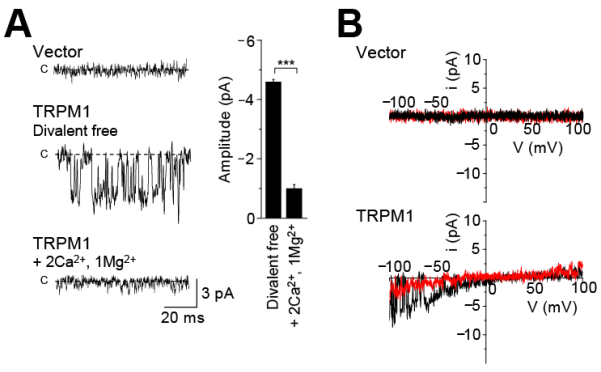

Fig. 5 Characterization of single-channel currents via recombinant TRPM1.

A. Extracellular divalent cations reduce the single-channel current amplitude of TRPM1-L in outside-out patches. Single-channel currents were recorded at –60 mV in CHO cells expressing mGluR6, Goα and TRPM1-L or control vector. Left current traces are recorded from cells transfected with vector . (top) and TRPM1-L (middle) in divalent cation-free extracellular solution or from cells transfected with TRPM1-L in 2 mM Ca^{2+}- and 1 mM Mg^{2+}-containing extracellular solution. 'C' represents the closed state. Right bar graph represents averages of single TRPM1-L channel amplitudes in divalent cation-free (n = 29) or 2 mM Ca^{2+}- and 1 mM Mg^{2+}-containing (n = 11) extracellular solution. Data represent the mean ± SEM. $^{***}P < 0.001$. ***B***. *I-V* relationships obtained from outside-out patches. Voltage ramps were applied from –100 to +100 mV (V_h=–60 mV) for 200 ms in either divalent cation-free (black traces) or 2 mM Ca^{2+} and 1 mM Mg^{2+}-containing (red traces) bath solution. CHO cells stably expressing mGluR6 were transfected transiently with TRPM1 and Goα, or vector and Goα

Functional coupling between TRPM1 and mGluR6

In CHO cells expressing mGluR6, Goα and TRPM1, constitutively active cationic currents were suppressed by the addition of 1 mM glutamate to the bath solution (Fig. 4*A*). Subsequent washout of glutamate restored the suppressed currents back to levels comparable to those prior to glutamate administration (in 15 of 22 cells). *I-V* relationships revealed that the cationic current was significantly suppressed by glutamate application. In CHO cells co-transfected with Goα and TRPM1, whole-cell currents with similar *I-V* relationships were detected. However, application of glutamate into the bath solution did not affect the whole-cell current (in 11 of 11 cells). A calculated average suppression ratio of inward current (V_h = –100 mV) by 1 mM glutamate administration was 52.7% (n = 15) in CHO cells expressing mGluR6, Goα and TRPM1, whereas the average suppression ratio in CHO cells co-expressing Goα and TRPM1 was 2.1% (n = 11) (Fig. 4*B*). The calculated suppression ratios after glutamate washout are 6.3% in CHO cells expressing mGluR6, Goα and TRPM1, and –4.5% in CHO cells expressing Goα and TRPM1, indicating that the cationic current was restored to a comparable level to that prior to glutamate application (Fig. 4*B*). These results strongly suggest that TRPM1 is the constitutively active cation channel suppressed by the mGluR6 cascade.

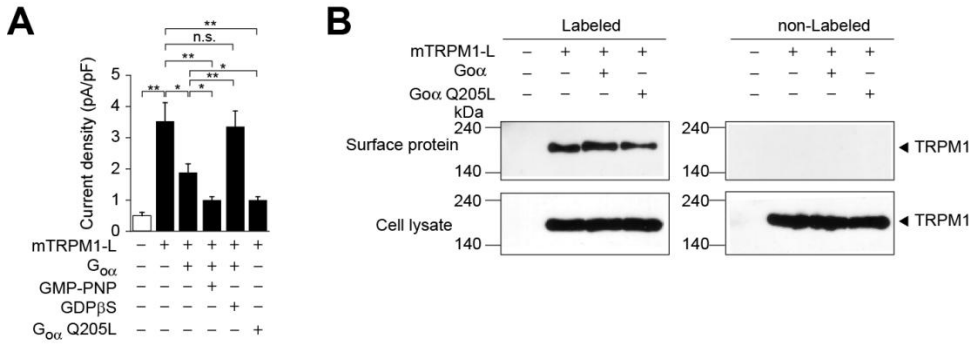

Fig. 6 Inhibitory effects of Goα constructs on TRPM1.

A. Na^+ current densities obtained by subtracting whole-cell current densities in $NMDG^+$-based solution from those in Na^+-based solution at –60 mV. CHO cells are expressing different combinations of constructs or treated further with GMP-PNP or GDPβS as in the left bar. Data represent the mean ± SEM. For statistical assessment, multiple comparisons were conducted by ANOVA, followed by the Tukey–Kramer test. n.s.; not significance. $^*P < 0.05$ and $^{**}P < 0.01$. ***B***. Cell surface expression of TRPM1. CHO cells were transfected with the constructs indicated. The cell lysate prepared after exposure to NHS-SS-biotin was incubated with streptavidin-agarose to collect cell surface proteins, and then the lysate was analyzed by Western blotting with anti-TRPM1-L antibody.

Effect of G_O activation on the whole-cell TRPM1 current

It has been debated that the mGluR6-coupled transduction channel operates in a manner similar to that of photoreceptors, in which intracellular cGMP opens the channel, and hydrolysis through phosphodiesterases (PDEs) closes the channel. Authors therefore examined whether or not TRPM1 can be activated by cGMP. However, perfusion of cGMP into TRPM1-transfected CHO cells failed to alter their whole-cell current activity, suggesting that TRPM1 is not a cGMP-gated channel (data not shown). This result agrees with several previous reports demonstrating that the transduction cation channel of the ON BC is not a cGMP-gated channel (12). Then the effect of G_o activation on the TRPM1 current was investigated by measuring a whole-cell current at V_h = −60 mV using a divalent cation-free Na^+-based bath solution and a Cs^+-based pipette solution in TRPM1-expressing CHO cells transfected either with wild type of $G_{o\alpha}$ ($G_{o\alpha}$) or a constitutively-active mutant of $G_{o\alpha}$ ($G_{o\alpha}$-Q205L). Analysis of the suppressed currents upon replacement of extracellular Na^+ with $NMDG^+$ demonstrated that the current density obtained in TRPM1-transfected cells (3.53 pA/pF, *n* = 8) was considerably larger than that in vector-transfected control cells (0.50 pA/pF, *n* = 6) and that in TRPM1- and Goα-co-transfected cells (1.89 pA/pF, *n* = 14). Furthermore, intracellular application of GMP-PNP (1 mM), an unhydrolyzable analogue of GTP, from the patch pipette to TRPM1- and Goα-co-transfected cells resulted in a remarkable decrease of current density (1.00 pA/pF, *n* = 22), whereas intracellular application of GDPβS (1 mM), an unhydrolyzable analogue of GDP, restored the current density to a level comparable to that in TRPM1-transfected cells (3.35 pA/pF, *n* = 9) (Fig. 6*A*). It was also observed that suppression of current density in TRPM1- and Goα-Q205L-co-transfected cells to a level comparable to that in TRPM1- and Goα-co-transfected cells intracellularly perfused with GMP-PNP (1.00 pA/pF, *n* = 36) (Fig. 6*A*). Authors confirmed that the expression level of TRPM1 protein was not significantly affected by Goα expression with a pull-down assay of biotinylated membrane proteins (Fig. 6*B*). These results suggest that TRPM1 channel function is negatively regulated by Go activation.

Regulation of single TRPM1 current by mGluR6 cascade

Then, in order to precisely confirm that TRPM1 channel activity is regulated via Go proteins in the mGluR6 signal cascade, regulation of single-channel currents were examined. Analyses of time-dependent changes in *NPo* demonstrated a notable suppression of *NPo* by 1 mM glutamate application and a recovery after washout (in 7 of 16 cells). The average *NPo* suppression ratio was 65.0%, and recovered to 6.5% after washout (*n* = 7) (Fig. 7*A*). These changes observed in single-channel current recordings agree well with those observed in whole-cell current recordings shown in Fig. 4*A*. In order to demonstrate more directly that TRPM1 is

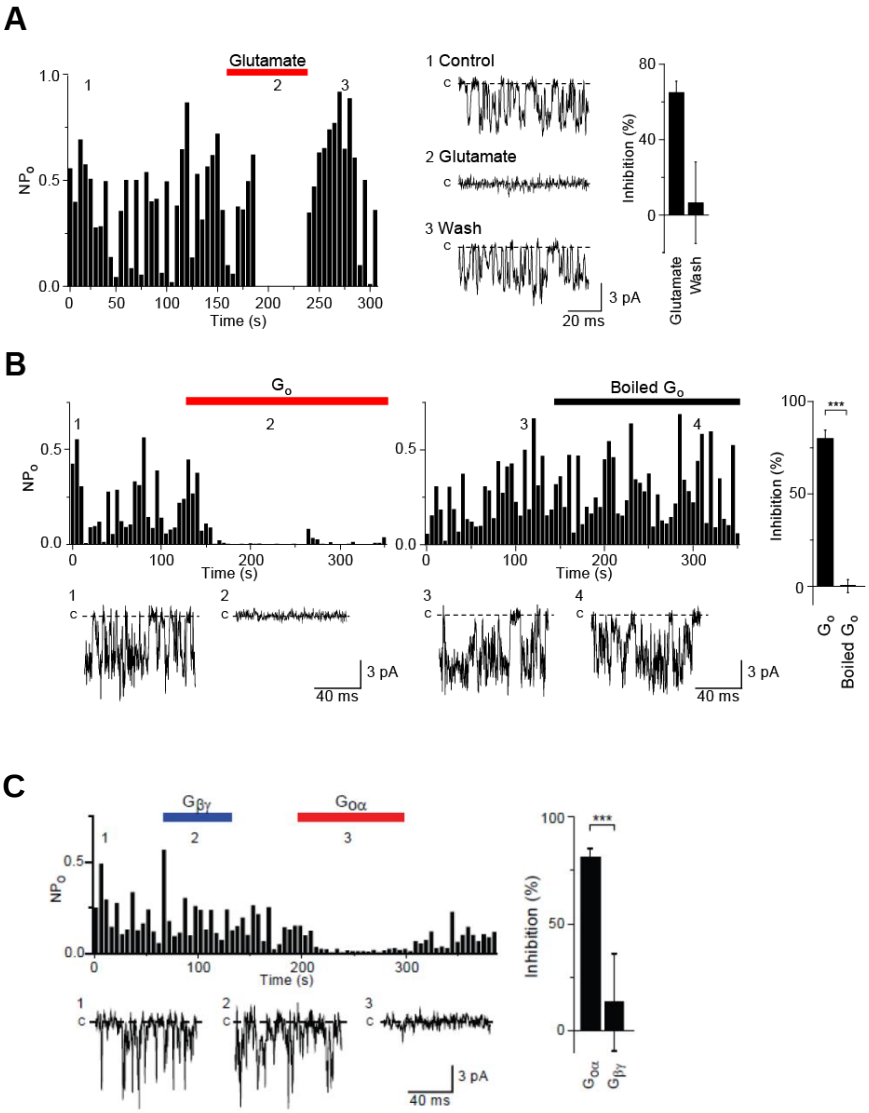

Fig. 7 Regulation of single TRPM1 current by mGluR6 cascade

A. Suppression of single TRPM1-L channel activity (NP_O) by activation of mGluR6 in excised outside-out patches. Single-channel currents were recorded at −60 mV in CHO cells expressing mGluR6, Goα and TRPM1-L. Left histogram shows the effect of glutamate application on NP_O. Red horizontal bar indicates an application of 1 mM glutamate. Middle panels show current traces before (Control, 1), during (Glutamate, 2), and after (Wash, 3) 1 mM glutamate treatment. 'C' represents the closed state. Right bar graph shows averaged *NPo* suppression ratio by glutamate application over that prior to its application. Dataesent the mean ± SEM of n =10. *B.* Inhibition of single TRPM1 channel activity (NP_O) by intracellular treatment of purified Go protein in excised inside-out patches. Single-channel currents were recorded at −60 mV in CHO cells expressing TRPM1. Activity histograms show the representative effects of 10 nM activated (Left, Go) or boiled (middle, Boiled Go) Go protein. Red and black horizontal bars indicate the application of activated and boiled Go proteins, respectively. Bottom current traces were obtained before (1,3) or during (2,4) application of Go proteins. 'C' represents the closed state. Right bar graph shows averaged NP_O suppression ratio by intracellular application of activated (n = 16) or boiled (n = 14) Go protein. Data represent the mean ± SEM. $^{***}P$<0.001. *C.* Inhibition of single TRPM1 channel activity (NP_O) by intracellular treatment of purified Gβγ protein in excised inside-out patches. Activity histograms show the representative effects of 10 nM activated Gβγ (blue bar) and Goα (red bar). Bottom current traces were obtained before (1) or during (2,3) application of G proteins. Right bar graph shows averaged NP_O suppression ratio by intracellular application of Gβγ (n = 9) or Goα (n = 9). Data represent the mean ± SEM. $^{***}P$<0.001.

regulated by Go protein,the effect of addition of the purified Go protein (22) from the intracellular side on TRPM1 activity was tested in an excised inside-out patch recordings (Fig. 7*B*). Currents were measured at –60 mV using a divalent cation-free K^+-based pipette (extracellular) solution and a Cs^+-based bath (intracellular) solution with the application of 10 nM Go protein which was activated with GMP-PNP. In TRPM1 transfected cells, we detected similar single-channel currents (–4.60 pA, n = 43) as observed in Fig.7*B*. Application of the purified Go protein gradually but strongly suppressed *NPo* (80.2%, in 16 of 16 cells) within 60 sec, whereas administration of heat-denatured 10 nM Go protein failed to suppress *NPo* (0.6%, in 14 of 14 cells) with GMP-PNP (Fig. 7*B*). Together, these results suggest that TRPM1 channel activity is negatively regulated by Go protein downstream of the mGluR6 cascade, supporting the idea that TRPM1 functions as the transduction channel downstream of mGluR6 in ON BCs.

Discussion

Recently, it was suggested that TRP channels have a possible function in retinal BCs (22, 23). Bellone et al. reported that TRPM1 may be responsible for horse congenital stationary night blindness (CSNB), from their observation that TRPM1 expression was decreased in CSNB (LP/LP) Appaloosa horses among five genes within the LP candidate region of the equine genome (22). Although mutations of TRPM1 in LP/LP horse were not identified, they even speculated that TRPM1 might be a transduction cation channel in retinal ON BCs. Shen et al. (2009) investigated whether or not TRPV1 is a retinal ON BC transduction channel. ON BCs responded to TRPV1 agonists, however, photoresponses of ON BCs in $TRPV1^{-/-}$ mice were normal. Based on the absence of the dark-adapted ERG b-wave in the Trpm1tm1Lex mutant mouse, they speculated that ON BC function would be disrupted in these mice (23). In this study, we show that TRPM1-L is essential for the light-evoked response of ON BCs and that TRPM1-L meets the criteria for the transduction cation channel as follows: (i) Immunohistochemical experiments revealed that TRPM1-L is specifically expressed in ON BCs, especially at the dendritic tips in colocalization with mGluR6. (ii) Retinal slice patch recordings from the $TRPM1^{-/-}$ mice show that photoresponses disappear in ON BCs but remain intact in OFF BCs. (iii) Application of patch clamp techniques to the TRPM1-expressing cells found that TRPM1-L is a non-selective cation channel and that the TRPM1-L activity is negatively regulated by the glutamate-activated mGluR6-Go signaling cascade.

Co-transfection of TRPM1 and Goα elicited a whole-cell current sensitive to suppression by glutamate application in CHO cells stably expressing mGluR6 (Fig. 4*A*, *B*). Co-expression of TRPM1 with constitutively activated Goα (Goα-Q205L) or with Goα in the presence of GMP-PNP resulted in significant suppression of TRPM1 channel activity (Fig. 4*B*). Furthermore, the single TRPM1 channel current was also suppressed by the application of purified Go protein from the intracellular side of the excised inside-out patch

membrane (Fig. 6*A*).

A previous report suggested that a transduction cation channel in ON BCs has linear *I-V* relationship and nonselective cation permeability properties (23). In our heterologous expression system, the TRPM1 channel showed a similar linear *I-V* relationship and similar nonselective cation permeability for Na^+, K^+, Ca^{2+}, and Mg^{2+} (Fig. 5) to that of the transduction channel in ON BCs (Fig. 3*A*). A single-channel amplitude was −0.36 pA (−60 mV, 6.0 pS) in the transduction channel in ON BCs (Fig. 4*C*, *D*), and −1.01 pA (−60 mV, 15.1 pS) in TRPM1-transfected CHO cells in a divalent cation-containing solution (Fig. 5d). According to previous reports with noise analysis, a single-channel conductance of the transduction channel in ON BCs was estimated to be 11 pS in salamanders (24), 12.5 pS in cats (7), and 5 pS (−0.3 pA at −60 mV) in mice (25). Since single-channel conductances obtained in our study for the transduction channel in ON BCs as well as in heterologous expression system bathed in a divalent cation-containing solution were close to the values reported in previous reports, TRPM1 is likely to be a component of the transduction channel in ON BCs.

Very recently, TRPM1 channel current measurements in mouse melanocytes were reported (26). The study demonstrated that TRPM1 in a heterologous expression system shows a nonselective cation channel property and a small whole-cell current density of ~2 pA/pF (−120 mV). This low current density is similar to our results obtained in the heterologous expression system (3.53 pA/pF at −60 mV). Under physiological conditions where perforated patch recordings were performed in rod BCs in mouse retinal slice preparations, *Po*max was estimated to be less than 0.5 (25). In the perforated patch recordings, intracellular concentrations of Ca^{2+} and GTP as well as other unknown factors could not be controlled. On the other hand, in whole-cell recordings of BCs isolated from the cat retina, Po_{max} was nearly 0.96 (7). In the present study, *NPo* of TRPM1 transfected cells was estimated to be 0.48. Therefore, it seems likely that the kinetics of transduction channels may be regulated not only by Go, Ca^{2+}, and GTP, but also by unidentified factors.

In mouse retinal slices, transduction channel currents of ON BCs under whole-cell voltage clamp were almost completely suppressed in the dark (7, 25, 27). On the other hand, in the co-transfected CHO cells, the inhibition ratio of TRPM1 current by mGluR6 activation measured in whole-cell and outside-out modes was 52.7% and 65.0%, respectively (Fig. 4*A*, 7*A*). The glutamate response in TRPM1 currents was observed in 15 of 22 cells in the whole-cell mode (68.2%) and in 7 of 16 cells in the outside-out mode (43.8%). These differences between ON BCs and our recombinant expression system may derive from a difference in efficiency of coupling between receptors and channels. Our heterogonous expression system may lack unknown factors that efficiently couple mGluR6 with TRPM1 in ON BCs, which may lead to certain populations of TRPM1 molecules becoming uncoupled from receptors. Particularly, in the outside-out patch

membranes, which failed to respond to glutamate, receptors can be absent. In this context, it is important to note that a direct application of purified Go protein suppressed single TRPM1 currents in all inside-out patch membranes (in 16 of 16 cells), and the inhibition ratio of NP_O in the inside-out mode was higher (80.2%) than that in the whole-cell and outside-out modes (Fig. 7*B*).

Since our purified Go protein preparation mainly contained Goα, TRPM1 is likely to be regulated through a membrane-delimited mechanism mainly by Goα. On the other hand, it was reported that G-protein-coupled inwardly rectifying potassium (GIRK) current was activated by Gβγ subunits (28). In activation of GIRK, Giα was suggested not only to function as a donor of Gβγ but also to promote Gβγ modulation by anchoring receptors and channels (29, 30). Based on these previous observations, it should be noted that there is a possibility that Goα affected Gβγ which derives from the CHO cell membrane eventually suppressing the TRPM1 activity. In addition, the author cannot exclude the possibility that our Go preparation contained an undetectable trace level of Gβγ. Furthermore, unknown factors may be involved in transmission of the Goα signal to TRPM1 on the cell membrane.

In conclusion, we clearly demonstrate that TRPM1-L is a component of the transduction cation channel in the mGluR6 cascade of retinal ON BCs.

Materials and Methods

Molecular Cloning and Construction of Mouse TRPM1-L Expression Vector.

We screened the UniGene databases by Digital Differential Display (DDD) and found UniGene Cluster Mm.58616, which contains ESTs (expressed sequence tags) enriched in the eye and the skin. Represented EST sequences encoded TRPM1-S (melastatin, trpm1 short form). We screened a mouse P0-P3 retinal cDNA library using a 1,703-bp fragment of the mouse melastatin cDNA (283-1991 bp of #AF047714) and isolated the mouse TRPM1 long form (TRPM1-L). TRPM1-L cDNA was subcloned into a modified pCAGGS vector (31).

Immunohistochemistry.

Mouse eye cups were fixed, cryoprotected, embedded, frozen, and sectioned 20 μm thick. For immunostaining, we used the following primary antibodies: anti-Goα antibody (mouse monoclonal, Chemicon, #MAB3073), anti-bassoon antibody (mouse monoclonal, Stressgen, #VAM-PS003), and anti-Chx10 antibody [rabbit polyclonal, our production (32)].

Antibody Production.

A cDNA encoding a C-terminal portion of mouse TRPM1-L (amino acid 1554–1622, TRPM1-L-C) was subcloned into pGEX4T-1 (Amersham). We confirmed, either by immunohistochemistry or Western blotting, that the signals detected by this antibody in the retina disappeared in TRPM1$^{-/-}$ mice. The antibody against mGluR6 was raised in Guinea Pigs with synthetic peptides [KKTSTMAAPPKSENSEDAK] (853-871, GenBank #NP_775548.2). We confirmed that the signals detected by this antibody in the retina disappeared in mGluR6$^{-/-}$ mice and by preincubation with 5.7 μg/mL synthetic peptides as molar ratio 1:100 with antibody.

Generation of TRPM1-Null Mutant Mice.

We deleted exons 4–6 of the TRPM1 gene to produce the targeting construct for the targeted gene disruption of TRPM1. The linearized targeting construct was transfected into TC1 embryonic stem cell line (33).

Retinal Slice Preparation and Recordings.

Adult (postnatal day < 28) 129Sv/Ev (WT) mice were dark adapted for ≈20 min, and retinal slices were prepared as described in ref. 34. At the end of perforated patch recordings, the patch membrane was ruptured to introduce Lucifer yellow from the patch pipette into the cell and then its morphology was examined by epifluorescence microscopy (35–37). The extracellular solution contained 120 mM NaCl, 3.1 mM KCl, 2 mM CaCl2, 1 mM MgSO4, 23 mM NaHCO3, 0.5 mM KH2PO4, and 6 mM D-glucose (pH adjusted to 7.6 with 95% O2/5% CO2 at 36°C). The pipette solution for recordings consisted of 105 mM CsCH3SO3, 0.5 mM CaCl2, 5 mM EGTA, 20 mM Hepes, 10 mM TEA-Cl, 5.5 mM MgCl2, 5 mM ATP disodium salt, 0.5 mM GTP disodium salt, and 0.25% Lucifer yellow dipotassium salt (pH adjusted to 7.6 with CsOH). For perforated patch recordings, 0.5 mg/mL amphotericin B (Sigma) was added to the pipette solution. The retinal slice was diffusely illuminated (2.3 × 104 photons·μm−2·s−1) by a light-emitting diode (emission maximum at 520 nm) from underneath the recording chamber.

Recombinant expression and current recording in CHO cells.

Chinese hamster ovary (CHO) cells were cultured in Dulbecco's modified Eagle's medium (DMEM) containing 1% L-proline, 10% fetal bovine serum, 30 units/ml penicillin, and 30 μg/ml streptomycin under a 95% air-5% CO_2 atmosphere at 37 °C. CHO cell lines stably expressing mGluR6 were described previously (38). Transfection of cDNA plasmids was carried out using FugeneHD (Roche) according to the

manufacturer's instructions. The cells were subjected to electrophysiological measurements 48-72 hrs after transfection.

Whole-cell current recordings.

Whole-cell and patch recordings were performed on CHO cells at room temperature (22-25 °C) with EPC-9 (Heka Electronic) or Axopatch 200B (Axon Instruments) patch-clamp amplifier as previously described (39). The patch electrodes prepared from borosilicate glass capillaries had a resistance of 2 MΩ for whole-cell recordings and 7 MΩ for single-channel recordings. Currents were sampled at 20 kHz after low pass filtering at 3.0 or 5.0 kHz. PULSE (version 8.8; Heka Electronic) or pCLAMP (version 10.0.2; Axon Instruments) software was used for command pulse control, data acquisition, and analysis. For whole-cell recordings, the Na^+-based bath solution contained (in mM) 145 NaCl, 10 HEPES, and 10 D-glucose (pH adjusted to 7.4 with NaOH, and osmolality adjusted to 320 mosmol/kgH_2O with D-mannitol). The pipette solution contained (in mM) 145 CsCl, 2.86 $CaCl_2$, 1 $MgCl_2$, 5 EGTA, and 10 HEPES (pH adjusted to 7.4 with CsOH, and osmolality adjusted to 300 mosmol/kgH_2O with D-mannitol). The free Ca^{2+} concentration of this solution was calculated to be 200 nM as computed with Maxchelator[25]. In some experiments, the pipette solution also contained 1 mM nonhydrolyzable GTP analog, guanylyl-imidodiphosphate (GMP-PNP) (Sigma) or 1 mM nonhydrolyzable GDP analog, guanosine 5'-0-(2-thiodiphosphate) (GDPβS) (Sigma). Suppression ratio (%) in Fig. 5a was calculated according to the following equation; Suppression ratio (%) = $100\times\{1-(I_{Glu}-I_{NMDG})/(I_{Ctl}-I_{NMDG})\}$ where I_{Ctl} and I_{Glu} are whole-cell current observed before and during 1 mM glutamate application at −100 mV, respectively. I_{NMDG} represents the current observed during N-methyl-D-glucamine ($NMDG^+$)-replacement of extracellular cations with $NMDG^+$. For determination of a cation current, the basic extracellular solution contained (in mM) 145 NMDGCl, 10 HEPES, and 10 D-glucose (pH adjusted to 7.4 with NMDGOH, and osmolality adjusted to 320 mosmol/kgH_2O with D-mannitol) was used, and the external $NMDG^+$ was replaced with the appropriate amount of Na^+, K^+, Ca^{2+}, or Mg^{2+} to give various concentrations of cations (monovalent cations; 10, 30, 90, 145 mM, divalent cations; 10, 30, 72.5 mM). As for determination of a K^+ current, 10 mM TEACl was added to extracellular solutions. The pipette solution contained (in mM) 145 CsCl, 2.86 $CaCl_2$, 1 $MgCl_2$, 5 EGTA, and 10 HEPES (pH adjusted to 7.4 with CsOH, and osmolality adjusted to 300 mosmol/kg H_2O with D-mannitol). The free Ca^{2+} concentration of this solution was calculated to be 200 nM as computed with Maxchelator (39).

Single-channel current recordings.

Single-channel recordings were performed in the excised inside-out or outside-out configuration. Activity plots of open probability (NP_O, N is the number of channels in the patch, P_O is the single-channel open probability) recorded from inside-out and outside-out patches, as calculated for a series of 500-ms test pulses to −60 mV, and plotted as a vertical bar on the activity histogram. The NP_O of single-channels was calculated by dividing the total time spent in the open state by the total time of continuous recording (500 ms) in the patches containing active channels. The amplitude of single-channel currents was measured as the peak-to-peak distance in Gaussian fits of the amplitude histogram. For outside-out recordings, the extracellular side was exposed to a bath solution containing (in mM) 140 KCl, 10 HEPES, and 5 D-glucose (pH adjusted to 7.4 with KOH, and osmolality adjusted to 320 mosmol/kgH_2O with D-mannitol). To observe the effects of extracellular divalent cations, 2 mM $CaCl_2$ and 1 mM $MgCl_2$, were added to bath solution. The pipette solution was composed of (in mM) 145 CsCl, 2.86 $CaCl_2$, 1 $MgCl_2$, 5 EGTA, and 10 HEPES (pH adjusted to 7.4 with CsOH, and osmolality adjusted to 300 mosmol/kgH_2O with D-mannitol). Suppression ratio (%) in Fig. 5c was calculated according to the following equation; Suppression ratio (%) = $100\times\{1-NP_{O\ Glu}/NP_{O\ Ctl}\}$, where $NP_{O\ Ctl,}$ and $NP_{O\ Glu}$ indicate mean NP_O of 6 traces obtained before and during 1 mM glutamate application, respectively. For inside-out recordings, the intracellular side was exposed to a Cs^+-based bath solution consisting of (in mM) 145 CsCl, 2.86 $CaCl_2$, 1 $MgCl_2$, 5 EGTA, and 10 HEPES (pH adjusted to 7.4 with CsOH, and osmolality adjusted to 300 mosmol/kgH_2O with D-mannitol), and an extracellular (pipette) solution that contained (in mM) 140 KCl, 10 HEPES, and 5 D-glucose (pH adjusted to 7.4 with KOH, and osmolality adjusted to 320 mosmol/kgH_2O with D-mannitol) was used. Purified Go protein was activated by 100 nM GMP-PNP for 30 min at 4 °C (Go), or denaturated by boiling for 10 min at 95 °C (Boiled Go) prior to use. Suppression ratio (%) in Fig. 5e was calculated according to the following equation; Suppression ratio (%) = $100\times\{1-NP_{O\ Go}/NP_{O\ Ctl}\}$, where $NP_{O\ Ctl,}$ and $NP_{O\ Go}$ indicate mean NP_O of 6 traces obtained before and during activated or boiled Go protein application.

References

1. Gariano, R. F. and Gardner, T. W. (2005) *Nature* **438**, 960-966
2. DeVries, S. H. and Baylor, D. A. (1993) *Cell* **72** Suppl, 139-149
3. Nakanishi, S., Nakajima, Y., Masu, M., Ueda, Y., Nakahara, K., Watanabe, D., Yamaguchi, S., Kawabata, S., and Okada, M. (1998) *Brain Res. Brain Res. Rev* **26**, 230-235

4. Nomura, A., Shigemoto, R., Nakamura, Y., Okamoto, N., Mizuno, N., and Nakanishi, S. (1994) *Cell* **77**, 361-369
5. Haverkamp, S., Grünert, U., and Wässle, H. (2001) *J. Comp. Neurol* **436**, 471-486
6. Morigiwa, K. and Vardi, N. (1999) *J. Comp. Neurol* **405**, 173-184
7. de la Villa, P., Kurahashi, T., and Kaneko, A. (1995) *J. Neurosci* **15**, 3571-3582
8. Masu, M., Iwakabe, H., Tagawa, Y., Miyoshi, T., Yamashita, M., Fukuda, Y., Sasaki, H., Hiroi, K., Nakamura, Y., and Shigemoto, R. (1995) *Cell* **80**, 757-765
9. Euler, T., Schneider, H., and Wässle, H. (1996) *J. Neurosci* **16**, 2934-2944
10. Weng, K., Lu, C., Daggett, L. P., Kuhn, R., Flor, P. J., Johnson, E. C., and Robinson, P. R. (1997) *J. Biol. Chem* **272**, 33100-33104
11. Vardi, N. (1998) *J. Comp. Neurol* **395**, 43-52
12. Nawy, S. (1999) *J. Neurosci* **19**, 2938-2944
13. Dhingra, A., Jiang, M., Wang, T., Lyubarsky, A., Savchenko, A., Bar-Yehuda, T., Sterling, P., Birnbaumer, L., and Vardi, N. (2002) *J. Neurosci* **22**, 4878-4884
14. Shiells, R. A. and Falk, G. (1990) *Proc. Biol. Sci* **242**, 91-94
15. Ramsey, I. S., Delling, M., and Clapham, D. E. (2006) *Annu. Rev. Physiol.* **68**, 619-647
16. Clapham, D. E. (2003) Nature 426, 517-524
17. Owsianik, G., Talavera, K., Voets, T., and Nilius, B. (2006) *Annu. Rev. Physiol.* **68**, 685-717
18. Montell, C. (2001) *Sci. STKE* **2001**, re1
19. Duncan, L. M., Deeds, J., Hunter, J., Shao, J., Holmgren, L. M., Woolf, E. A., Tepper, R. I., and Shyjan, A. W. (1998) *Cancer Res.* **58**, 1515-1520
20. Kraft, R. and Harteneck, C. (2005) *Pflugers Arch* **451**, 204-211
21. Xu, X. Z., Moebius, F., Gill, D. L., and Montell, C. (2001) *Proc. Natl. Acad. Sci. U.S.A* **98**, 10692-10697
22. Asano, T., Semba, R., Ogasawara, N., and Kato, K. (1987) *J. Neurochem* **48**, 1617-1623
23. Nawy, S. (2000) *J. Neurosci* **20**, 4471-4479
24. Attwell, D., Mobbs, P., Tessier-Lavigne, M. & Wilson, M. (1987) *J. Physiol.* **387**, 125-161
25. Sampath, A. P. and Rieke, F. (2004) *Neuron* **41**, 431-443
26. Oancea, E., Vriens, J., Brauchi, S., Jun, J., Splawski, I., and Clapham, D. E. (2009) *Sci Signal* **2**, ra21
27. Hasegawa, J., Obara, T., Tanaka, K., and Tachibana, M. (2006) *Neuron* **50**, 63-74
28. Logothetis, D. E., Kurachi, Y., Galper, J., Neer, E. J., and Clapham, D. E. (1987) *Nature* **325**, 321-326
29. Peleg, S., Varon, D., Ivanina, T., Dessauer, C. W., and Dascal, N. (2002) *Neuron* **33**, 87-99

30. Rubinstein, M., Peleg, S., Berlin, S., Brass, D., and Dascal, N. (2007) *J. Physiol.* (Lond.) **581**, 17-32
31. Niwa H., Yamamura K., Miyazaki J. (1991) *Gene* **108**, 193-199
32. Koike, C., Nishida, A., Akimoto, K., Nakaya, M., Noda, T., Ohno, S., and Furukawa, T. (2005) *J. Neurosci*. **25**, 10290-10298
33. Deng, C., Wynshaw-Boris, A., Zhou, F., Kuo, A., and Leder, P. (1996) *Cell* **84**, 911-921
34. Matsui, K., Hasegawa, J., and Tachibana, M. (2001) *J. Neurophysiol*. **86**, 2285-2298
35. Ghosh, K. K., Bujan, S., Haverkamp, S., Feigenspan, A., and Wässle, H. (2004) *J. Comp. Neurol*. **469**, 70-82
36. Berntson, A. and Taylor, W. R. (2000) *J. Physiol. (Lond.)* **524**, 879-889
37. Euler, T. and Masland, R. H. (2000) *J. Neurophysiol*. **83**, 1817-1829
38. Cayouette, S., Lussier, M. P., Mathieu, E. L., Bousquet, S. M. & Boulay, G. Exocytotic insertion of TRPC6 channel into the plasma membrane upon Gq protein-coupled receptor activation. J Biol Chem 279, 7241-7246 (2004).
39. Wakamori, M. et al. Single tottering mutations responsible for the neuropathic phenotype of the P-type calcium channel. J Biol Chem 273, 34857-34867 (1998).
40. Berlin, J. R., Bassani, J. W., and Bers, D. M. (1994) *Biophys. J.* **67**, 1775-1787

General Conclusion

The first three chapters carried out to reveal physiological role of novel VDCC complexes and suggested novel function of the VDCC β subunit as a node of presynaptic protein assembly. The last chapter describes the functional characterization and regulatory mechanism of postsynaptic Ca^{2+} channel in retinal bipolar cells.

RIM1 confers sustained activity and neurotransmitter vesicle anchoring to presynaptic Ca^{2+} channels

The molecular organization of presynaptic active zones is important for the neurotransmitter release that is triggered by depolarization-induced Ca^{2+} influx. We demonstrated a previously unknown interaction between presynaptic active zone components, RIM1 and voltage-dependent Ca^{2+} channels (VDCCs), that controls neurotransmitter release. RIM1 associated with VDCC β-subunits via its C terminus to markedly suppress voltage-dependent inactivation among different neuronal VDCCs. Consistently, in pheochromocytoma neuroendocrine PC12 cells, acetylcholine release was significantly potentiated by the full-length and C-terminal RIM1 constructs, but membrane docking of vesicles was enhanced only by the full-length RIM1. Thus, RIM1 association with β in the presynaptic active zone supports release via two distinct mechanisms: sustaining Ca^{2+} influx through inhibition of channel inactivation, and anchoring neurotransmitter-containing vesicles in the vicinity of VDCCs.

Rab3-interacting molecule γ isoforms lacking the Rab3-binding domain induce long-lasting currents but block neurotransmitter vesicle-anchoring in voltage-dependent P/Q-type Ca^{2+} channels

Physiological function has not been elucidated yet for RIM3 and RIM4, which exist only as short γ isoforms (γ-RIMs) carrying the C-terminal C_2B-domain common to RIMs but not Rab3-binding region and other structural motifs present in α-RIMs including RIM1α. Here we demonstrate that γ-RIMs also exert prominent suppression on VDCC inactivation via direct binding to β-subunits. In neuron-like pheochromocytoma PC12 cells, this common functional feature allows native RIMs to enhance acetylcholine secretion, whereas γ-RIMs are uniquely different from α-RIMs in blocking localization of neurotransmitter-containing vesicles near the plasma membrane. As α-RIMs, γ-RIMs are widely distributed in central neurons. The results suggest that sustained Ca^{2+} influx through suppression of VDCC inactivation by RIMs is a ubiquitous property of neurons, while the extent of vesicle-anchoring to VDCCs at plasma membrane may depend on the competition of α-RIMs with γ-RIMs for VDCC β-subunits.

Functional impacts of Munc18-1 on gating properties of voltage-dependent Ca^{2+} channels.

Assembly of voltage-dependent Ca^{2+} channels (VDCCs) with associated proteins regulates coupling of VDCCs with upstream and downstream cellular events. Here, we demonstrate a previously unknown interaction between two components of the presynaptic active zone, Munc18-1 and VDCCs, that controls neurotransmitter release in mammalian neurons. Munc18-1 selectively associated with VDCC β_{1a}-, β_3-, and β_{4b}-subunit to modulate gating properties of P/Q-type VDCCs. Munc18-1 promoted inactivation of β_3-, and β_{4b}-containing VDCC, and slowed activation of β_{1a}-, β_3-, and β_{4b}-containing VDCC. The author hypothesized that munc18-1 may allow synaptic vesicles to become docked and /or ready for fusion around VDCC without exposing fusion machinery to robust Ca^{2+} entry.

Functional characterization of TRPM1 as a component of the retinal ON bipolar cell transduction channel in the mGluR6 cascade

An essential step in intricate visual processing is the segregation of visual signals into ON and OFF pathways by retinal bipolar cells (BCs). The release of glutamate from photoreceptors modulates the photoresponse of ON BCs via metabotropic glutamate receptor 6 (mGluR6) and G-protein (Go) that regulate a cation channel. For a long time, the transduction channel in ON BCs had not been identified. Recently, it was reported that *TRPM1* is the candidate of the ON BC transduction channel. *TRPM1* null mutant mice completely lose the photoresponse of ON BCs. However, this hypothesis was not convincing, because functional characterization of TRPM1 has not been reported. Authors succeeded the whole-cell and single-channel recording of TRPM1 recombinantly expressed in CHO cells, which revealed the character of TRPM1 as a constitutively active non-selective cation channel. Furthermore, the TRPM1 channel activity is negatively regulated by activated Go in the mGluR6 cascade. These results suggest that TRPM1 is likely to be a component of the ON BC transduction channel.

– List of Publications –

1. **RIM1 confers sustained activity and neurotransmitter vesicle anchoring to presynaptic Ca^{2+} channels.**

   Shigeki Kiyonaka, Minoru Wakamori, Takafumi Miki, **Yoshitsugu Uriu**, Mio Nonaka, Haruhiko Bito, Aaron M Beedle, Emiko Mori, Yuji Hara, Michel De Waard, Motoi Kanagawa, Makoto Itakura, Masami Takahashi, Kevin P Campbell & Yasuo Mori.

   Nat. Neurosci. **10**, 691-701 (2007). **(Chapter 1)**

2. **Rab3-interacting molecule γ isoforms lacking the Rab3-binding domain induce long-lasting currents but block neurotransmitter vesicle-anchoring in voltage-dependent P/Q-type Ca^{2+} channels.**

   Yoshitsugu Uriu, Shigeki Kiyonaka, Takafumi Miki, Masakuni Yagi, Satoshi Akiyama, Emiko Mori, Akito Nakao, Aaron M. Beedle, Kevin P. Campbell, Minoru Wakamori, and Yasuo Mori.

   J. Biol.Chem. in press (2010). **(Chapter 2)**

3. **Functional impacts of Munc18-1 on gating properties of voltage-dependent Ca^{2+} channels.**

   Yoshitsugu Uriu, Shigeki Kiyonaka, Hiroshi Nakajima, Yoshinori Takada, Yuji Hara, Minoru Wakamori, and Yasuo Mori.

   Manuscript in preparation. **(Chapter 3)**

4. **TRPM1 is a component of the retinal ON bipolar cell transduction channel in the mGluR6 cascade.**

   Chieko Koike, Takehisa Obara, **Yoshitsugu Uriu**, Tomohiro Numata, Rikako Sanuki, Kentarou Miyata, Toshiyuki Koyasu, Shinji Ueno, Kazuo Funabiki, Akiko Tani, Hiroshi Ueda, Mineo Kondo, Yasuo Mori, Masao Tachibana, and Takahisa Furukawa.

   Proc. Natl. Acad. Sci. U. S. A. **107**, 332-337 (2010). **(Chapter 4)**

– Other Publications –

1. **Mutation associated with an autosomal dominant cone-rod dystrophy CORD7 modifies RIM1-mediated modulation of voltage-dependent Ca^{2+} channels.**

   Takafumi Miki, Shigeki Kiyonaka, **Yoshitsugu Uriu**, Michel De Waard, Minoru Wakamuri, Kevin P. Campbell and Yasou Mori.

   Channels (Austin) **1**, 144-147 (2007).

2. **Rim2α determines docking and priming states in insulin granule exocytosis.**

   Takao Yasuda, Tadao Shibasaki, Kohtaro Minami, Harumi Takahashi, Akira Mizoguchi, **Yoshitsugu Uriu**, Tomohiro Numata, Yasuo Mori, Jun-ichi Miyazaki, Takashi Miki, and Susumu Seino

   Cell Metabolism in press (2010).

– List of Japanese Publications –

1. **神経伝達物質放出におけるCa^{2+}チャネル複合体形成の生理的意義** ***Physiological role of presynaptic Ca^{2+} channel complexes on neurotransmitter release.***

   清中茂樹，**瓜生幸嗣**，三木崇史，森泰生

   生化学 **80**, 658-661 (2008).

2. **多様な感受性を示す陽イオンチャネルTRP** ***Structures and variable functions of TRP channels.***

   沼田朋大，香西大輔，高橋重成，加藤賢太，**瓜生幸嗣**，山本伸一郎，金子雄，眞本達生，森泰生

   生化学 **81**, 962-983 (2009)